



Dissertation  
submitted to the  
Combined Faculty of Mathematics, Engineering and Natural Sciences  
of Heidelberg University, Germany  
for the degree of  
Doctor of Natural Sciences

Put forward by  
NICO WINKEL  
born in: Boppard, Rheinland-Pfalz, Germany  
Oral examination: 21.10.2024



# Pathways to Supermassive Black Hole Growth

Resolving Gas Flows and Black Hole Mass Scaling Relations  
in AGN Host Galaxies

Referees:

Dr. Knud Jahnke

Prof. Dr. Jochen Heidt



# Zusammenfassung

Supermassereiche Schwarze Löcher (SMBHs) mit mehreren Millionen bis Milliarden Sonnenmassen befinden sich im Zentrum der meisten, wenn nicht aller, massereichen Galaxien, einschließlich der Milchstraße. Verschiedene Skalierungsbeziehungen zwischen der Schwarzlochmasse ( $M_{\text{BH}}$ ) und den Eigenschaften der Wirtsgalaxie deuten auf eine gemeinsame Entwicklung hin. Ein entscheidender Faktor für diese Beziehungen könnten die Phasen sein, in denen SMBHs große Mengen an Gas akkretieren, was sich in Form von leuchtkräftigen Aktiven Galaxienkernen (AGNs) zeigt. Man geht davon aus, dass der Gastransport zum SMBH durch Prozesse in der Wirtsgalaxie gesteuert wird, während eine Rückkopplung durch den AGN die Entwicklung der Galaxie wiederum beeinflusst. Während solche Prozesse in den Zentren nahegelegener AGNs mit niedriger Leuchtkraft beobachtet wurden, haben deren geringe Akkretionsraten nicht wesentlich zum Wachstum von SMBHs im Univerum beigetragen. Um die Prozesse zu entschlüsseln, die tatsächlich für die Entwicklung von SMBHs und ihren Wirtsgalaxien relevant sind, müssen die Kernregionen von AGNs mit hohen spezifischen Akkretionsraten untersucht werden.

In dieser Arbeit zeige ich, wie 3D spektroskopische Beobachtungen mit hoher räumlicher Auflösung genau dazu genutzt werden können. Neue Daten, aufgenommen mit dem Narrow-Field-Mode des MUSE-Instruments am Very Large Telescope der ESO, enthüllen einen beeindruckenden, 300 Parsec großen Sternentstehungsring nahe des Galaxienzentrums von Mrk 1044. Die Kinematik des ionisierten Gases und die Spiralstruktur deuten darauf hin, dass die Sternentstehung Material zum AGN treibt. Eine spektro-astrometrische Analyse zeigt einen kompakten Ausfluss von ionisiertem Gas, was darauf hindeutet, dass der AGN sich in einem frühen Entwicklungsstadium befindet. In NGC 4593 enthüllen ALMA Beobachtungen große Mengen molekularen Gases, das von den Skalen der Wirtsgalaxie bis in die Einflussosphäre des Schwarzen Loches reicht. In Kombination mit MUSE NFM Daten untersuche ich die Effizienz der Sternentstehung, die Gaskinematik und die Massenflussraten und diskutiere verschiedene Mechanismen, die diese Art von Gastransport ermöglichen könnten. Schließlich präsentiere ich eine neue Kalibrierung der Beziehung zwischen  $M_{\text{BH}}$  und der stellaren Geschwindigkeitsdispersion  $\sigma_*$  der Wirtsgalaxie. Durch die Kombination unabhängig gemessener  $M_{\text{BH}}$  mit Integralfeldspektroskopie von VLT/MUSE und Keck/KCWI kann ich

erstmalig zeigen, dass AGNs und inaktive Galaxien denselben zugrundeliegenden Skalierungsbeziehungen folgen. Das stellt einen entscheidenden Baustein für die Messung von Schwarzwlochmassen in AGNs im entfernten Universum dar.

Die Fortschritte in den Beobachtungsmethoden und Analysetechniken, die in dieser Arbeit genutzt wurden sind eine Blaupause für die Untersuchung der Verbindung zwischen leuchtkräftigen AGNs und ihren Wirtsgalaxien. Aufbauend auf den Pilotstudien von Mrk 1044 und NGC 4593 werden ab Herbst 2024 neue Beobachtungen beginnen. Ihr Ziel ist es, die Gastransportprozesse in Quasaren, den leuchtkräftigen AGNs, umfassend zu entschlüsseln und damit die Grundlage für die Forschung der kommenden Jahre zu legen.

# Abstract

Supermassive black holes (SMBHs) with masses ranging from millions to billions of times that of the Sun exist at the centres of most massive galaxies, including our Milky Way. Various scaling relations between SMBH mass ( $M_{\text{BH}}$ ) and host galaxy properties suggest a coevolution between them. A key factor in establishing these relations may be the periods during which SMBHs accrete significant amounts of gas, a process that manifests as luminous Active Galactic Nuclei (AGNs). The transport of gas towards the SMBH is believed to be regulated by processes within the host galaxy, while feedback from the AGN influences the galaxy's evolution in return. While such processes have been resolved in the centres of nearby low-luminosity AGNs, their low accretion rates are insufficient to grow a SMBH. To better understand the processes driving the growth of SMBHs and their host galaxies across cosmic time, it is essential to study AGNs with high specific accretion rates.

In this thesis, I demonstrate how high-spatial-resolution 3D spectroscopic observations are used to achieve this goal. The ionized gas kinematics and spiral morphology suggest that star formation drives material toward the AGN. A spectroastrometric analysis reveals a parsec-scale ionized gas outflow, indicating that the AGN is in an early stage of evolution. In NGC 4593, ALMA observations uncover abundant molecular gas extending from the kpc-scale galaxy bar into the BH sphere of influence. Combined with MUSE NFM data, I analyse the star formation efficiency, gas kinematics, and mass inflow rates, discussing various mechanisms that may enable this AGN feeding mode. Finally, I present a recalibration of the relation between  $M_{\text{BH}}$  and host galaxy stellar velocity dispersion  $\sigma_*$ . By combining independently measured  $M_{\text{BH}}$  with unprecedented integral-field spectroscopic data from Keck/KCWI, VLT/MUSE and VLT/VIMOS, I demonstrate for the first time that AGNs and quiescent galaxies follow the same underlying scaling relations, providing a baseline for measuring SMBH masses across cosmic time.

The advancements in observational methods and analysis techniques utilised in this work offer a blueprint for studying the connection between luminous AGNs and their host galaxies. Building on these pilot studies, new observations aimed at a comprehensive census of gas flows in nearby quasars will begin in October 2024, laying the groundwork for future research.



## Acknowledgements

Looking back on the last four years, it's hard to believe how quickly time has flown by. There is a long list of people I would like to thank, without whom this journey would not have been possible. First, I would like to thank Bernd Husemann, who provided me with fascinating data, technical advice and scientific background to start this PhD project, and taught me during the early stages of my PhD. I am also grateful to Knud Jahnke, who stepped in as my supervisor without hesitation, helped me develop my projects, and offered careful advice when difficult decisions had to be made. My sincere thanks go to Hans-Walter Rix for believing in my future career steps. I would also like to thank my examination committee members, Joachim Wambsganß, Werner Aeschbach, and especially Knud Jahnke and Jochen Heidt, for reviewing this thesis. A special thanks to Vardha Bennert. Despite the nine-hour time difference between Heidelberg and California, you were an indispensable mentor to me. Your trust, patience, scientific insight, and general advice made the last three years of my PhD much richer. To my close friends with whom I've shared so much: Evert, Eric, Verena, Sebastian, and Max, who were all in the same boat when we started this journey four years ago — I wouldn't want to miss a single one of the highs and lows we've experienced together. I will always remember our dinner parties, skiing trips, hiking adventures, bike tours, and the unforgettable retreats. Your support and friendship mean everything to me.

Zuletzt möchte ich meiner lieben Familie danken. Ihr habt nie an mir gezweifelt, sondern mich immer dabei unterstützt meinen Träumen zu folgen. Ich bin unfassbar froh, dass es euch gibt.

# Contents

1	INTRODUCTION	4
1.1	Active Galactic Nuclei	4
1.1.1	A Brief History	4
1.1.2	AGN Unification Models	7
1.1.3	SMBH Properties from Type 1 AGN Spectra	9
1.2	AGN Host Galaxies	11
1.2.1	AGN Feeding	11
1.2.2	AGN Feedback	13
1.2.3	Open Questions in AGN Feeding and Feedback	18
1.3	Black Hole Mass - Host Galaxy Scaling relations	20
1.3.1	Quiescent Galaxies	21
1.3.2	Active Galaxies	23
1.4	Objectives and Outline of This Work	25
2	CIRCUMNUCLEAR STAR FORMATION IN MRK 1044	28
2.1	Introduction	28
2.2	Data	31
2.2.1	Observations and Data Reduction	31
2.2.2	Optical Imaging	32
2.2.3	IFU Optical Observations	32
2.2.4	Deblending the AGN and Host Emission	35
2.3	Analysis and Results	41
2.3.1	Fitting the Stellar Continuum and the Ionized Gas Emission	42
2.3.2	Mapping the Emission Line Properties	44
2.3.3	Kinematic Modeling	52
2.4	Discussion	59
2.4.1	Star Formation as Potential Driver for AGN Fueling	59
2.4.2	Chemical Enrichment of the CNE	63
2.4.3	On the Black Hole Feeding Mechanism	64
2.5	Summary and Conclusions	66
3	A COMPACT OUTFLOW IN MRK 1044	71
3.1	Introduction	71

---

3.2	Observations and Data Reduction . . . . .	74
3.3	Analysis and Results . . . . .	75
3.3.1	Optical AGN Spectrum . . . . .	75
3.3.2	Spectroastrometry . . . . .	78
3.3.3	The Spatially Resolved Outflow . . . . .	81
3.3.4	Radio Emission . . . . .	83
3.3.5	Ly- $\alpha$ Absorption . . . . .	85
3.4	Discussion . . . . .	87
3.4.1	Nuclear Excitation Mechanism . . . . .	87
3.4.2	Exploring a Geometric Model for the Unresolved Outflow Component . . . . .	90
3.4.3	Outflow Energetics and Mass Outflow Rates . . . . .	92
3.4.4	Origin of Mrk 1044's Radio Emission . . . . .	95
3.4.5	Outflow Expansion from Nuclear to Galaxy Scales . . . . .	96
3.4.6	Mrk 1044 - A Young AGN . . . . .	100
3.5	Summary and Conclusions . . . . .	103
3.6	Appendix . . . . .	105
3.6.1	Size of the Resolved Outflow H0 . . . . .	105
3.6.2	Geometric Expanding Shell Model . . . . .	106
4	GAS INFLOW IN NGC 4593 . . . . .	114
4.1	Introduction . . . . .	114
4.2	Data . . . . .	116
4.2.1	ALMA Imaging . . . . .	116
4.2.2	Optical 3D Spectroscopy . . . . .	116
4.3	Analysis and Results . . . . .	118
4.3.1	Spectral Synthesis Modelling . . . . .	118
4.3.2	Star Formation Rates . . . . .	119
4.3.3	Kinematic Modelling . . . . .	121
4.3.4	Torques from the Self-Gravitating Gas Spiral . . . . .	124
4.3.5	Time Evolution of the Torque Field . . . . .	126
4.4	Discussion . . . . .	129
4.4.1	Star Formation Along the Single-arm Spiral . . . . .	129
4.4.2	The Torquing Mechanism . . . . .	132
4.4.3	Consequences for SMBH Growth . . . . .	132
4.5	Summary and Conclusions . . . . .	133

4.6	Appendix . . . . .	135
4.6.1	Tilted-ring Modelling of the Stellar and Ionised Gas Rotation . . . . .	135
5	UNIFIED BLACK-HOLE-MASS-HOST-GALAXY SCALING RELATIONS IN ACTIVE AND QUIESCENT GALAXIES . . . . .	140
5.1	Introduction . . . . .	140
5.2	Sample Selection . . . . .	145
5.2.1	AGN Sample . . . . .	145
5.2.2	Quiescent Galaxy Sample . . . . .	148
5.3	Observations and Data Reduction . . . . .	148
5.3.1	IFU Observations . . . . .	148
5.3.2	HST Imaging . . . . .	154
5.4	Analysis . . . . .	155
5.4.1	Surface Photometry . . . . .	155
5.4.2	AGN Parameters . . . . .	158
5.4.3	Spectral Synthesis Modeling . . . . .	159
5.4.4	Host-Galaxy Stellar Kinematics . . . . .	162
5.4.5	Dynamical Masses . . . . .	170
5.4.6	Fitting the $M_{\text{BH}}$ Scaling Relations . . . . .	171
5.5	Results and Discussion . . . . .	171
5.5.1	Host-galaxy Morphologies . . . . .	171
5.5.2	The $M_{\text{BH}}$ Scaling Relations of Quiescent Galaxies . . . . .	175
5.5.3	The $M_{\text{BH}}$ Scaling Relations of AGNs . . . . .	176
5.5.4	Controlling Selection Effects . . . . .	183
5.5.5	The Virial Factor $f$ . . . . .	188
5.5.6	Uniform $M_{\text{BH}}$ Scaling Relations of Active and Quiescent Galaxies: Consequences . . . . .	189
5.6	Summary . . . . .	189
5.7	Appendix . . . . .	192
5.7.1	AGN Spectral Fitting . . . . .	192
5.7.2	The Importance of AGN-host Deblending . . . . .	195
5.7.3	Spatially Resolved vs. Aperture-integrated $\sigma$ . . . . .	196
5.7.4	Stellar Kinematics from Different IFU Datasets . . . . .	199
5.7.5	Stellar Kinematics from Fitting Different Diagnostic Features . . . . .	201
5.7.6	Effect of Aperture Size on Aperture-integrated $\sigma$ . . . . .	201
5.7.7	Comparing Stellar and SSP Libraries . . . . .	203

5.7.8 Comparing Spectral Synthesis Modeling Codes . . .	205
6 SUMMARY AND OUTLOOK	209
6.1 Summary and Interpretation of Main Results . . . . .	209
6.2 Future Prospects . . . . .	211
6.2.1 BH-mass-host-galaxy Scaling Relations . . . . .	211
6.2.2 Resolving the Role of NLS1s in AGN Evolution . . .	213
6.2.3 The VLT Large Programme TENSION-QSO: A Comprehensive Census of Gas Flows in Nearby Quasars . . . . .	217
6.3 Closing . . . . .	221
LIST OF FIGURES	225
LIST OF TABLES	226
LIST OF PUBLICATIONS	227
BIBLIOGRAPHY	229



---

# Introduction

# Abstract

Active Galactic Nuclei (AGNs) have been intensively studied over the last few decades. Not only have they provided strong evidence for the existence of supermassive black holes (SMBHs) at the centres of galaxies, but they also appear crucial for galaxy formation and evolution in the Universe. Since the discovery of AGNs in the 1960s, research has focused on understanding the accretion of matter onto SMBHs and the detailed structure of AGNs to explain the various observational signatures across the entire electromagnetic spectrum. Although this topic continues to be actively studied, the primary focus of AGN research has shifted in the last two decades towards understanding how AGNs interact with their host galaxies and influence each other's evolution. This introduction sets the scientific framework for this dissertation, providing a concise overview of the fundamental topics necessary to follow the content presented. It includes a brief overview of the AGN phenomenon, our current understanding of their connection to host galaxies, and the ongoing efforts to address open questions by studying gas flows and black hole mass - host galaxy scaling relations across cosmic time.

# Chapter 1 | Introduction

## 1.1 Active Galactic Nuclei

### 1.1.1 A Brief History

Supermassive black holes have long captivated both public interest and the sustained attention of the astronomical community. Strong observational evidence supports the existence of an SMBH in our own galaxy, the Milky Way – a groundbreaking discovery by Andrea M. Ghez, Reinhard Genzel and their research teams, which was recognised with the 2020 Nobel Prize in Physics. More recently, in 2022, the Milky Way’s central black hole was directly imaged by the Event Horizon Telescope Collaboration. This follows the first-ever direct image of a supermassive black hole (SMBH), the SMBH located in the galaxy M87 at the centre of the Virgo Cluster ([Event Horizon Telescope Collaboration et al., 2019](#)). However, observations of related phenomena date back to the early 20th century. In 1909, Edward Fath identified emission lines in the spectra of NGC 1068 and Messier 81, and in 1918, Heber Curtis discovered the famous jet in Messier 87, describing it as “*a curious straight ray [...] connected with the [galaxy] nucleus*”. Further studies revealed unusual high-excitation emission lines in the spectra of certain galaxies (e.g., [Humason, 1932](#); [Mayall, 1934](#)), but their origin remained elusive for another three decades.

A crucial step forward happened in 1943, when Carl K. Seyfert made the groundbreaking observation that some galaxies exhibit unusual morphologies, characterised by extremely bright, stellar-like nuclei that are sources of very broad emission lines. From the 1950s onward, objects exhibiting these characteristics were collectively summarised under the term Active Galactic Nucleus (AGN). Active galaxies were later empirically classified into two subclasses based on their emission-line characteristics ([Khachikian & Weedman, 1974](#)). Seyfert 1 galaxies are distinguished by broad permitted emission lines with a Full Width at Half Maximum (FWHM) greater than  $2000 \text{ km s}^{-1}$ . They also display highly ionised, narrow forbidden emission lines ( $\text{FWHM} < 1000 \text{ km s}^{-1}$ ) and a featureless power-law contribution from thermal emission. In contrast, Seyfert 2

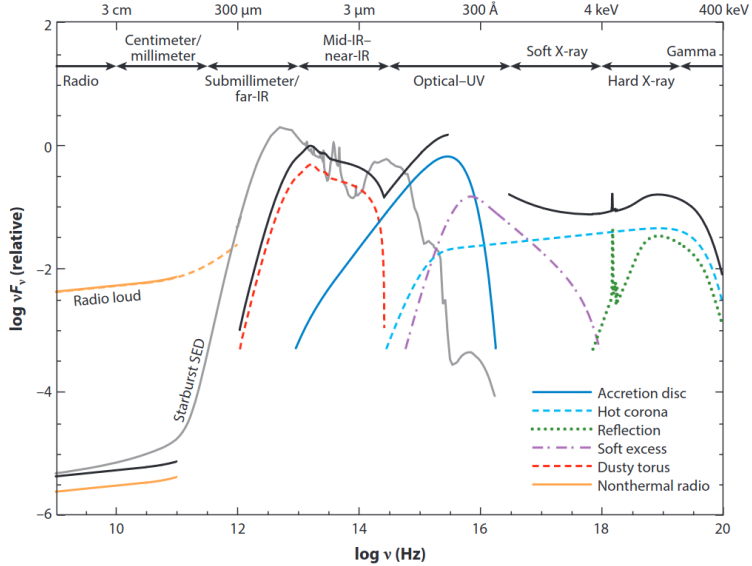


Figure 1.1: A schematic depiction of an AGN spectral energy distribution (SED). Coloured lines represent individual components that originated from different AGN structures (see Fig. 1.2). The mm-to-far-infrared SED is typically considered to have a small contribution on the overall galaxy SED, except in the case of extremely luminous quasars and strong jetted AGN. Apart from that, AGNs emit across the entire electromagnetic spectrum, with the main emission originating from the AGN accretion disc peaking in the ultraviolet. Image adapted from [Hickox & Alexander \(2018\)](#), originally published in [Harrison et al. \(2014\)](#).

galaxies lack the broad emission lines and the power-law continuum. A small fraction of Seyfert galaxies exhibit characteristics of both types, leading to the later introduction of intermediate classes ([Osterbrock & Koski, 1976](#)).

Around that time, remarkably strong extragalactic radio sources were also identified (e.g., [Baade & Minkowski, 1954](#); [Matthews & Sandage, 1963](#)). Depending on their optical counterparts, they were classified as either radio galaxies or, if they exhibited optical characteristics similar to Seyfert 1s, they were called quasi-stellar radio sources (quasars). Similar point-like objects that were detected optically but lacking associated radio

emission were termed quasi-stellar objects (QSOs, Schmidt, 1963). Given that QSOs and quasars<sup>1</sup> were known from their redshifts to be of extragalactic origin, and if their underlying host galaxies could be detected, they were regarded as higher-luminosity analogues of Seyfert 1 galaxies (Kristian, 1973). The powering mechanism of AGNs was subject to great discussion (Pacholczyk & Weymann, 1968). The variability of the broad-line emission, from a few hours to several years, set strong constraints on its spatial extent. This region could not be larger than a few parsecs. The huge energy needed to produce their luminosity on such small scales left only one viable explanation for the AGN phenomenon: gas accretion onto a supermassive black hole.

Thus, a direct consequence of the AGN powering mechanism is the existence of BHs<sup>2</sup> with several million to billion solar masses in the centres of galaxies. AGNs can emit across the entire electromagnetic spectrum, with each domain corresponding to a different spatial and energy regime, and different physical processes that produce the radiation (see Fig. 1.1 and Padovani et al. 2017 for a review). Since their discovery, AGNs have been intensively studied to gain a deeper understanding of their nature. In the late 1960s, AGNs were observed for the first time in X-rays (Bowyer et al., 1970; Giacconi et al., 1974). It was quickly established that X-ray emission is not only ubiquitous in AGNs but also accounts for a significant portion of their luminosity (Elvis et al., 1978). Their X-ray radiation is primarily produced via inverse Compton scattering by a hot electron corona, probing the innermost regions of the AGN, just 2-20 gravitational radii away from the black hole (e.g., Haardt & Maraschi, 1991). Nowadays it is well-established that AGNs are complex in their appearance. Therefore, multi-wavelength observations are essential for identifying the physical processes at work and obtaining a comprehensive understanding of the AGNs' structure.

---

<sup>1</sup>Nowadays the terms QSO and quasar are used interchangeably, as the underlying mechanism is thought to be the same.

<sup>2</sup>While we know of the existence of stellar mass black holes through, for example, X-ray binaries and gravitational waves, throughout this thesis, the abbreviation BH will be used synonymously with supermassive black holes.

### 1.1.2 AGN Unification Models

After their discovery, more and more phenomena related to AGNs were discovered. These included optically violent variable quasars and BL Lacertae objects, summarised under the term "Blazars" (Angel & Stockman, 1980), and radio-loud and radio-quiet quasars, just to mention a few. The so-called unified models of AGNs are attempts to explain the wide variety of different types of AGNs by the same underlying phenomena, with only minor differences, such as the viewing angle or the presence of radio emission, distinguishing the AGN classes (Antonucci, 1993; Urry & Padovani, 1995). In the classic model, the central accreting SMBH is surrounded by a sub-parsec scale, geometrically thin, optically thick accretion disc. This disc is heated by gravitational pressure, producing high gas temperatures emitting thermal blackbody radiation. Magnetic field interactions and Compton scattering provide non-thermal contributions to the spectrum of the accretion disc, amplifying its emission in various wavelengths domains. The powerful accretion disc illuminates the surrounding broad-line region (BLR), wherein clouds move on roughly Keplerian orbits. An optically thick, parsec-scale "torus" of dust and gas can shield the view of the BLR and accretion disc, with the obscuration depending on the inclination with respect to the observer's line of sight. Consequently, high-excitation emission lines from the narrow-line region gas (NLR) at larger distances from the centre remain unobscured, which results in the observational distinction between Seyfert 1 and 2 galaxies as well as between quasars and radio galaxies (Fig. 1.2, left panel).

While the Unified Model of AGN has been quite successful, its simplistic assumptions had to be refined over time. The "receding torus" model (Lawrence, 1991) posits that the inner radius of the torus is defined by the dust sublimation temperature, which increases with AGN luminosity. As a consequence, the covering factor by which the BLR is obscured should decrease as AGN luminosity increases, which is observationally confirmed (e.g., Treister et al., 2008; Lusso et al., 2013). Additionally, theoretical considerations from Krolik & Begelman (1988) suggest that the torus is clumpy rather than continuous, which was confirmed observationally in the meantime (Tristram et al., 2014; Isbell et al., 2021), and which led to more sophisticated versions of the AGN unification model (see right panel of Fig. 1.2). However, several open questions persist (see Netzer, 2015, for a review), for instance, the wide range of covering factors observed at

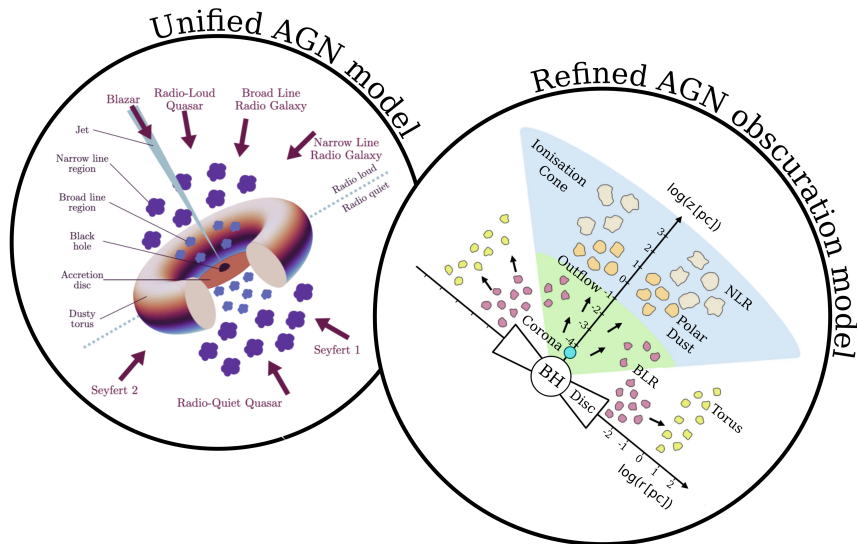


Figure 1.2: *AGN unification models*. The left panel illustrates the classic AGN unification model, which still offers substantial descriptive power for explaining the various observed AGN types. In this model, the broad-line region (BLR) clouds are illuminated by the accretion disc surrounding the SMBH, from which relativistic jets can be launched. Depending on the observer’s viewpoint, the BLR may be obscured by a continuous dust torus. The right panel presents an updated version of the obscuration model. In this version, the dust torus and polar dust are clumpy, and so are AGN-driven outflows, which occur across multiple gas phases and spatial scales. Figures are adapted from Emma L. Alexander (left) and Ramos Almeida & Ricci (2017) (right panel).

fixed AGN luminosity (see Hickox & Alexander, 2018, for a review), and why the obscured fraction depends on waveband used to select the AGN (Merloni et al., 2014; Stalevski et al., 2016). Furthermore, the AGN unification model still not addresses the the redshift-evolution of the obscured fraction, AGN luminosity distribution, and possible connections to host galaxies. Especially in mergers, AGNs seem to behave differently compared to those in secularly evolving host galaxies, which is explained in more detail in Sect. 1.2.

### 1.1.3 SMBH Properties from Type 1 AGN Spectra

As a direct gateway to the BLR, the spectrum of unobscured (type 1) AGNs provides crucial diagnostics for inferring properties of the circumnuclear region of AGNs. For instance, the radius of the broad-line region  $R_{\text{BLR}}$  can be determined using "reverberation mapping" (RM) in AGNs whose BLR signal shows sufficient time variability. In the framework of the AGN unification model, the BLR emission-line flux varies in response to changes in the continuum light from the BH accretion disc. This response is delayed because it takes time for the light to travel from the accretion disc to the broad-line region, causing the emission lines to "reverberate" after the continuum varies. In this picture, a time lag can be interpreted as the physical distance corresponding to the size of the BLR (Blandford & McKee, 1982; Peterson, 1993). Assuming virial motions of the BLR gas clouds, the mass of the central BH is given by

$$M_{\text{BH}} = f \frac{R \Delta v^2}{G} = f \times \text{VP} \quad (1.1)$$

where  $R$  is the radius of the BLR,  $\Delta v$  is the rms velocity of the BLR gas clouds,  $G$  is the gravitational constant, and VP is the virial product. In practice,  $\Delta v$  can be measured from the width of the broad emission lines, and  $R$  from the time lags which are measured via the cross-correlation function<sup>3</sup> Furthermore, the virial factor  $f$ , a parameter describing the BLR geometry and kinematics, is required and calibrated on local AGNs (see Sect. 1.3).

Beyond that, the RM method has revealed a remarkably tight correlation between  $R_{\text{BLR}}$  and the continuum luminosity (" $R$ - $L$  relation") as measured from e.g.,  $L_{5100}$ , the emission-line free continuum at 5100 Å (Bentz et al., 2013; U et al., 2022; Woo et al., 2024). It is typically parameterised as

$$\log(R_{\text{BLR}}/\text{lt day}) = K \cdot \alpha \log(\lambda L_{\lambda}(5100 \text{ \AA})/10^{44} \text{ erg s}^{-1}) \quad (1.2)$$

with best-fitting values of  $K = 1.46$  and slope  $\alpha = 0.45$  from SDSS-RM (Fonseca Alvarez et al., 2020). When combined with the assumption of virialised BLR clouds, the  $R$ - $L$  relation can be used to estimate the BH

---

<sup>3</sup>The cross-correlation function identifies the time lag by measuring the similarity between two time series as one is shifted relative to the other.

mass  $M_{\text{BH}}$  based on the width of the broad lines, and the continuum luminosity via eq. 1.1. Both quantities, broad line width and continuum luminosity, are straightforward to measure from a single spectrum of type 1 AGNs. As such, the so-called "single-epoch" method has become the standard technique to homogeneously measure  $M_{\text{BH}}$  across cosmic time (Shen et al., 2008; Shen & Liu, 2012).

On a different note, reverberation mapping provides direct tests of the Unification Model by constraining the structure and kinematics of the BLR. To achieve this, precise velocity-resolved broad-line lags must be measured, demanding intensive monitoring with frequent sampling. Empirical modelling of the cross-correlation function then provides a characterisation of the overall morphology and kinematics of the broad-line-emitting gas (Pancoast et al., 2014; Williams & Treu, 2022). Although the angular size of the BLR is generally too small to be resolved directly, advances in interferometry with VLTI/GRAVITY have recently provided independent comparisons (GRAVITY Collaboration et al., 2018, 2020, 2021, 2024). For the handful of AGNs analysed with both RM and interferometry, the measured BLR parameters generally align (GRAVITY Collaboration et al., 2024), supporting the cloud model used to parameterise the BLR structure (Pancoast et al., 2014).

More characteristics of type 1 AGN spectra were explored by Boroson & Green (1992) through a principal component analysis of various QSO parameters. Their study revealed that a single primary vector, the so-called Eigenvector 1 (EV1), explains most of the observed scatter of the AGN parameters (see also Yip et al., 2004). EV1 describes the anti-correlation between the broad Fe II emission and the [O III] $\lambda$  5007 emission-line strength, therefore connecting BLR with NLR properties, which is not straightforward to interpret. Hu (2008) discovered that the broad Fe II lines in type 1 SDSS QSOs are typically redshifted relative to the broad Balmer lines, implying that the Fe-emitting gas is inflowing into the BLR. Given the correlation of Fe-strength with the Eddington ratio  $\lambda_{\text{Edd}} = L_{\text{bol}}/L_{\text{Edd}}$ , this inflow would necessitate substantial shielding from AGN radiation pressure. Absorption of ionising photons could be achieved by the high Fe II column densities, which indeed are found to increase with increasing Eddington ratio (Sameshima et al., 2011). This finding supports the suggestion that the NLR covering factor, i.e., what fraction of the NLR gas is directly exposed to the BLR continuum, is highly variable between

AGNs, and may be the primary driver of [O III] line strength (Baskin & Laor, 2005; Ludwig et al., 2009). This explanation provides a physical argument for the correlation observed in EV1. Another hypothesis describes an evolutionary scenario (Mathur, 2000; Grupe, 2004): AGNs with strong Fe II and high Eddington ratios might be younger AGNs in which accretion-disc winds and associated NLR would be more compact. This would lead to faster outflows and higher gas densities, prone to collisional de-excitation of forbidden lines, explaining the relative faintness of [O III] with respect to the broad H $\beta$  component. To summarise, the EV1 relation provides important insights into the physical mechanisms between the observed spectral properties of NLR and BLR. Understanding the underlying physical drivers is essential for constraining the detailed structure of AGNs and evolutionary implications.

## 1.2 AGN Host Galaxies

### 1.2.1 AGN Feeding

A long-standing question related to the AGN phenomenon is what physical processes ignite their nuclear activity. The prevailing idea is that gas accretion from the host galaxy provides the material necessary to fuel the central engine. However, since this gas is typically distributed on kiloparsec scales, several orders of magnitude in distance must be bridged to reach the black hole's gravitational sphere of influence (SoI) and, ultimately, the black hole's accretion disc. Along the way, the gas is exposed to a series of heating and cooling processes, shocks from stars or the AGN, gravitational torques, and collisions with other gas clouds. Moreover, the ionising radiation, whose radiation pressure counteracts the gas inward motion, varies substantially between different AGNs: Typical AGN bolometric luminosities range  $L_{\text{bol}}$  ranging from  $10^{42} \text{ erg s}^{-1}$  to  $10^{48} \text{ erg s}^{-1}$ . As a result, gas transport towards the AGN is not only a multi-scale problem but also a multi-phase one, observable in atomic, cold molecular, warm molecular, and ionised gas phases (see Storchi-Bergmann & Schnorr-Müller 2019 for an overview of diagnostic tools).

Since the absolute mass accretion rates of AGNs span several orders of magnitude, it is likely that a series of different processes are at work. As for secular processes, galaxy spiral arms can transport gas from the

outer regions to the bulge. Additionally, galactic bars induce slow-acting gravitational torques that continuously redistribute angular momentum (Sellwood & Wilkinson, 1993; Kormendy & Kennicutt, 2004a), resulting in steady radial gas migration through bar dust lanes (Sormani et al., 2023). Inflowing gas often stalls near or just below the inner Lindblad resonance on scales of a few hundred parsecs, where nuclear discs, spirals, and intense star formation are commonly observed (Buta & Combes, 1996; Mazzuca et al., 2008; Comerón et al., 2010). Further inward, additional gravitational torques from non-axisymmetric stellar potentials, such as nuclear ovals or bars, can lead to angular momentum loss and subsequent radial gas transport (García-Burillo et al., 2009; Davies et al., 2014). Given the abundance of cold gas within the inner few hundred parsecs of AGNs (Wada et al., 2009; Mazzalay et al., 2013; Lelli et al., 2022), chaotic cold accretion via inelastic collisions between condensed gas clouds may also play a significant role (Li & Bryan, 2014; Gaspari & Sądowski, 2017). Moreover, hydrodynamic simulations by Kim & Elmegreen (2017) indicate that frequently observed nuclear spirals are signatures of star-formation induced shocks, and produce a net gas inflow.

Measuring exact gas mass inflow rates close to AGNs is challenging, as these rates are typically derived from small-amplitude residuals of the dominant kinematic moment. As the signal from the inflowing component is often weak, it is easily outshone by emission from the AGN or an outflow. In the case of nearby low-luminosity (low- $L$ ) AGNs, circumnuclear gas inflow rates have been measured for individual AGNs, ranging from 0.01-15  $M_{\odot}/\text{yr}$  (Haan et al., 2009; Davies et al., 2009; Müller Sánchez et al., 2009; Combes et al., 2014; Lelli et al., 2022). Given that this inflowing gas also significantly contributes to star formation near the AGN (Rosario et al., 2018; Mallmann et al., 2018), and that additional angular momentum transport is required to move the gas further into the black hole’s sphere of influence, it remains an open question whether such inflow rates can sustain an AGN cycle of  $10^7$ - $10^8$  yr (Hickox et al., 2014), even for such relatively small BH mass accretion rates.

Fuelling the most luminous quasars requires strong gas instabilities, which can happen in galaxy interactions and major galaxy mergers. The strong tidal forces occurring during mergers can lead to large amounts of gas flowing towards galaxy centres, often accompanied by bursts of star formation. This explains why most luminous quasars are found in

strongly interacting galaxies (Urrutia et al., 2008; Treister et al., 2012). However, strong interactions are not a necessary criterion for luminous quasars: quasars hosted by largely undisturbed disc galaxies are observed at  $z \sim 1$  (Cisternas et al., 2011b),  $z \sim 2$  (Kocevski et al., 2012; Schawinski et al., 2012; Mechtley et al., 2016), and beyond (Ding et al., 2022; Walter et al., 2022). The global connection between AGNs and strong galaxy interactions has been discussed extensively (see for example Koss et al. 2010; Silverman et al. 2011; Ellison et al. 2011 vs. Cisternas et al. 2011b; Villforth et al. 2014, 2017). Addressing the question of how important mergers really are for the global AGN population is complicated by (i) the different timescales of mergers vs. AGN activity (Hickox et al., 2014), (ii) the obscured AGN fraction in galaxy mergers (Weston et al., 2017; Hickox & Alexander, 2018), and (iii) biases in the samples selected from different wavebands (Padovani et al., 2017). Accounting for these effects where possible, studies of AGN demographics have concluded that the bulk of cosmic SMBH growth in the last 10 Gyr is not associated with major mergers (Kocevski et al., 2012; Mechtley et al., 2016). This suggests that secular mechanisms must play a crucial role for fuelling AGN at the highest accretion rates.

### 1.2.2 AGN Feedback

The enormous amount of energy released during the AGN phase has been considered important for influencing galaxy evolution since the discovery of AGNs. However, it was not until the late 1990s that groundbreaking observations sparked a surge of scientific interest in what is now known as AGN feedback. First, it was observed that the gas temperatures in the interstellar medium (ISM) of elliptical galaxies were higher than expected, suggesting that a heating mechanism was required to account for the lower gas cooling rates, which were attributed to AGNs (Binney & Tabor, 1995; Ciotti & Ostriker, 1997). Second, correlations between various host galaxy properties and black hole mass  $M_{\text{BH}}$  were discovered (Magorrian et al., 1998; Gebhardt et al., 2000; Ferrarese et al., 2001, see also Sect. 1.3). Early semi-analytical models of galaxy evolution explained these correlations through AGN-driven gaseous outflows interacting with their host galaxies (Silk & Rees, 1998a). Third, it was recognised that in both semi-analytical models and hydrodynamic simulations of galaxy evolution, star formation and black hole growth resulted in runaway growth. To prevent

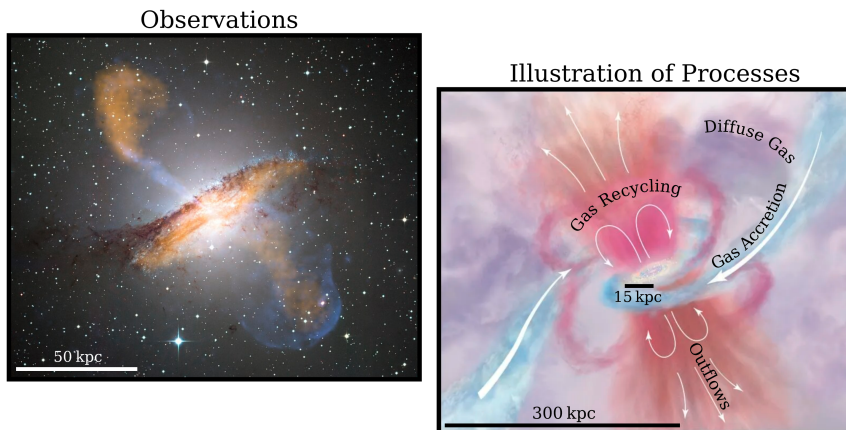


Figure 1.3: *Observations and illustration of how AGN impact galaxies and their surroundings.* The left panel features Centaurus A, a prime example of a nearby starburst galaxy that also hosts an AGN. The composite image captures the various processes associated with AGNs: sub-mm observations reveal lobes (orange), while relativistic jets are observable in X-rays (blue), injecting energy into and out of the surrounding host galaxy (the dust lanes and stellar light). The right panel illustrates different routes of the galactic gas flows. Galaxies evolve not in isolation but by redistributing and ejecting their gas through outflows (pink). While these outflows can be star-formation-driven, AGNs also play a significant role. The diffuse gas halo (purple) likely contains gas from both sources, mixed over time and eventually recycled back into the galaxy’s central bulge (red, very centre) and gaseous disc (blue). Image Credit: (left) ESO/WFI; MPIIR/ESO/APEX/A.Weiss et al.; NASA/CXC/CfA/R.Kraft et al., (right) adapted from [Tumlinson et al. \(2017\)](#).

such a runaway scenario, AGN feedback was invoked to regulate both processes at the high-mass end of the galaxy stellar mass function ([Benson et al., 2003](#); [Springel et al., 2005](#)). To this day, AGN feedback remains a key ingredient in state-of-the-art cosmological hydrodynamic simulations, playing a critical role in regulating star formation efficiencies and self-regulating black hole growth to reproduce the observed stellar mass and black hole mass functions across cosmic time ([Dubois et al., 2012](#); [Vogelsberger et al., 2014](#); [Gaspari et al., 2020](#)).

Centaurus A, shown in Fig. 1.3, is a nearby AGN that is one of the foremost examples a radio-loud AGN, showcasing a multitude of physical processes and spatial scales that must be considered for describing AGN feedback. To address the complexity and assess which processes are truly important for galaxy evolution, Heckman & Best (2014) suggested that AGNs can be broadly categorised into two groups. The first group, the radiative-mode AGNs, emits most of their energy in the form of electromagnetic radiation, which results directly from matter accreting through a central, optically thick accretion disc. This group corresponds to the observed population of Seyfert galaxies and QSOs. Approximately 10% of AGNs fall into the second group, referred to as "mechanical-mode" or "jet-mode" AGNs. These AGNs are radiatively inefficient ( $\lambda_{\text{Edd}} \lesssim 0.01$ ) but are radio-loud, characterised by the presence of highly collimated, relativistic radio jets. This straightforward yet simplistic classification has served as the basis for implementing AGN feedback in many state-of-the-art cosmological hydrodynamic simulations (see Habouzit et al. 2022 for a concise overview). For example, the IllustrisTNG simulations employ a black hole mass-dependent Eddington ratio threshold to determine whether a black hole provides feedback in the form of isotropic heating ("thermal mode") or directed momentum kicks ("kinetic mode"). As a result, in TNG simulations, black hole feedback is only relevant for black holes with masses  $M_{\text{BH}} \gtrsim 10^{8.2} M_{\odot}$ , and galaxy quenching primarily occurs through kinetic energy injection that pushes gas out of the galaxy halo (Weinberger et al., 2017; Terrazas et al., 2020). Similarly, HorizonAGN (Dubois et al., 2012) and SIMBA (Anglés-Alcázar et al., 2017) use a two-mode feedback model, whereas EAGLE simulations rely on a single-mode model that uses stochastic thermal energy injection from the AGN (Booth & Schaye, 2009). While such AGN feedback prescriptions may be successful in capturing their cumulative effects in cosmological simulations, they do not address how the energy is expelled, where and how it couples to the host galaxy, or whether it locally suppresses or even enhances star formation.

The astronomical community has dedicated significant effort over the last decade to identify the exact physical mechanisms of AGN feedback and their relevance to galaxy formation and evolution. Observations support kinetic-mode winds as a mechanism for expelling gas from the galaxy in the form of molecular gas outflows (Feruglio et al., 2010; Veilleux et al.,

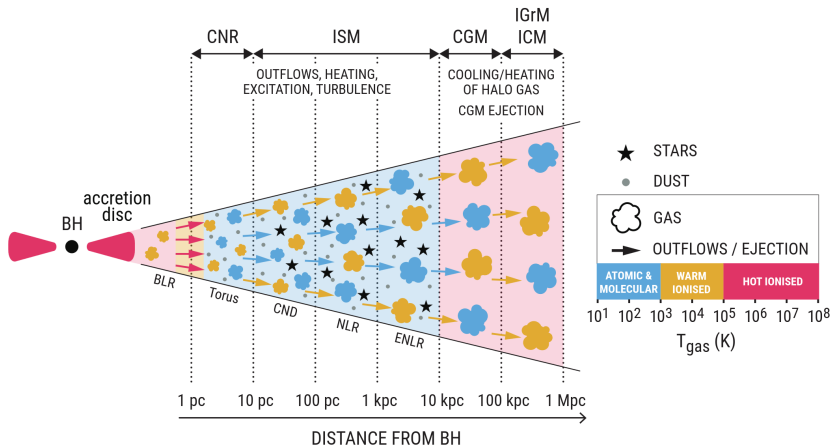


Figure 1.4: *Overview of spatial scales and temperature ranges relevant for AGN Feedback.* Gas on all scales occurs in various phases and temperature (colour coding). Via AGN-driven outflows, the BH can affect gas properties from the circumnuclear region (CNR) all the way to the circumgalactic medium (CGM) and the intragroup and intracluster medium (IGrM/ICM). This large range in spatial scales naturally corresponds to an equivalently large range in temporal scales. Figure adapted from [Harrison & Ramos Almeida \(2024\)](#).

2013; Cicone et al., 2014) and ionised gas outflows (Crenshaw et al., 2010; Villar-Martín et al., 2011; Woo et al., 2016; Rupke et al., 2017). Mapping the ionised gas outflow kinematics on kpc scales through long-slit or integral-field spectroscopic (IFU) observations of bright optical emission lines such as  $[\text{O III}]\lambda\lambda 4690, 5007$  or  $\text{H}\alpha$  has emerged as a powerful technique. Outflow velocities and energetics can be determined from the line shapes: While the strong narrow component is typically measured to be at rest within the galaxy frame, a fast-moving blue-shifted wing component is often detected and interpreted as an outflow. Based on this technique, several AGN surveys have specifically aimed at getting a comprehensive understanding of AGN-host interactions, such as KASHz ([Harrison et al., 2016](#)), AGNIFS ([Riffel et al., 2017](#)), KONA ([Müller-Sánchez et al., 2018](#)), MAGNUM ([Mingozzi et al., 2019](#)), SUPER ([Circosta et al., 2018](#)), and QFeedS ([Jarvis et al., 2021](#)). Moreover, the X-ray selected BAT AGN

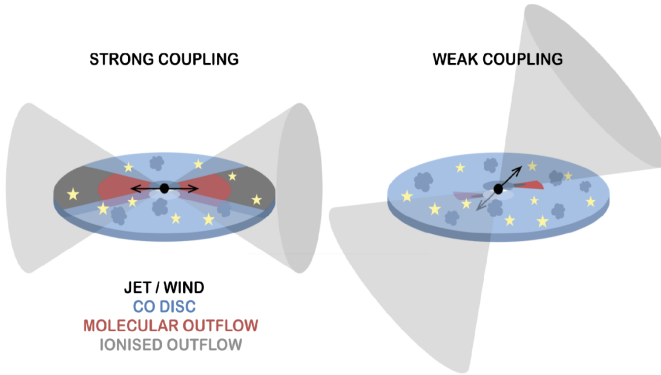


Figure 1.5: *Examples of strong and weak coupling of outflows and the galactic disc.* A jet, wind or ionised outflow may have a high or low inclination with respect to the molecular gas disc. If interacting, the ionised outflow may entrain a molecular gas (observed as molecular gas outflows) or heat the gas to temperatures where it effectively suppresses star formation. While these processes have been resolved in some nearby low- $L$  Seyferts, it is largely unexplored for AGNs with high specific mass accretion rates. Figure adapted from Ramos Almeida et al. (2022).

Spectroscopic Survey (Koss et al., 2017) and the spectroscopically-selected Close AGN Reference survey (Husemann et al., 2022, CARS) have each created multi-dimensional, pan-chromatic datasets that enable the study of these processes that occur across various temperature and spatial scales (see Fig.1.4). In these surveys, ionised outflows of several nearby Seyfert galaxies are resolved down to scales of several tens of parsecs. Their low luminosity and proximity allow for detailed mapping of outflow morphologies, velocities, and energetics (e.g., Kakkad et al., 2023). One important result is that orientation of the AGN with respect to the host galaxy disc matters for the efficiency of energy-coupling (Cresci et al., 2015; Husemann et al., 2019; Smirnova-Pinchukova et al., 2022, see also Fig. 1.5). However, the current AGN phase seems to only have subtle impact on galaxy-scale star formation rates. Furthermore, ionised outflows of lower- $L$  Seyferts are generally more compact than first expected (Singha et al., 2022), suggesting that the effect of outflows may be limited to the sub-kiloparsec scales around the AGN. However, the AGN radiation field ionises gas in

the so-called extended narrow line region (ENLR). The ENLR size scales with  $M_{\text{BH}}$ , which could be interpreted as proxy for the AGN lifetime (Husemann et al., 2022). As outflow energetics tend to scale with AGN luminosity (Fiore et al., 2017; Kakkad et al., 2022), AGNs with higher accretion rates represent the most interesting sites for studying the imprint of feedback from radiative-mode AGNs.

### 1.2.3 Open Questions in AGN Feeding and Feedback

#### Outflow Energetics in Luminous AGNs

While the centres of nearby low- $L$  AGN host galaxies are easy to access observationally, their mass outflow rates may be small and are unlikely to have a lasting impact on their host galaxies (Venturi et al., 2018; Shimizu et al., 2019). In contrast, QSOs accrete mass at substantially higher rates and their feedback is much more likely to have a meaningful impact on the host galaxy. Compared to low- $L$  AGNs, the structure of the QSO’s BH accretion flow, from where the outflows are launched, are dominated by different processes (Giustini & Proga, 2019; Sadowski & Gaspari, 2017). Not only does this imply a strong dependence of the outflow launching mechanism with  $\lambda_{\text{Edd}}$  (Best & Heckman, 2012; Rennehan et al., 2023), but also that the coupling of the QSO-driven winds with the surrounding ISM at 10 pc to 10 kpc-scale becomes more efficient at high  $\lambda_{\text{Edd}}$  (Gaspari et al., 2012; Hopkins et al., 2016). Observationally, QSO outflow mass rate have been found to be much higher (Fiore et al., 2017) compared to those in low- $L$  AGNs. However, with typically  $>1$  kpc resolution, the outflow geometry is often unconstrained, and missing diagnostic lines to infer the electron density  $n_e$  has left more than one order of magnitude uncertainty in their energetics (e.g., Villar-Martín et al., 2016; Davies et al., 2020). Moreover, beam-smearing caused by low spatial resolution introduces a complex morpho-kinematic coupling, which has led to a great debate about outflow sizes, velocities and outflow rates on kpc scales (Villar-Martín et al., 2016; Tadhunter et al., 2018). As outflows are predicted to have the greatest impact on their host galaxies in AGNs with high accretion rates, resolving the galaxy centres around luminous AGNs is a pressing objective. However, each of the observational challenges mentioned above becomes even more pronounced at high AGN luminosities. Not to mention, luminous AGNs are rare in the local Universe. In other

words, resolving the physics of energetic outflows is not only complicated given technical challenges, but also due to the small number of nearby luminous AGNs in which the spatial scales could be observed.

### Host Galaxy Conditions for Near-Eddington BH Accretion

With unprecedented data taken with JWST, numerous luminous quasars at high redshift were recently discovered. Their existence has further amplified a challenge in the field: To explain the quasars' luminosities, it requires SMBHs of several billion solar masses already a few 100 Myr after the Big Bang (Eilers et al., 2023; Wang et al., 2023; Maiolino et al., 2024, e.g.). Regardless of the nature of the initial BH seeds (which is currently topic of great discussion), there must have been an epoch in the early Universe when BHs accreted at or above the Eddington limit for timescales of several 100 Myr (see Fig.1.6). However, such sustained near-Eddington accretion rates are not observed anywhere in the Universe and in stark contrast with current models of AGN accretion. Although several recent studies suggest that the  $R-L$  relation may have a turnoff at luminosities driven by high Eddington ratios, implying that the SMBH masses of the highest-redshift quasars may be slightly overestimated, a significant tension remains (Du et al., 2018; Martínez-Aldama et al., 2019; Dalla Bontà et al., 2020a, see also Sect. 1.1.3).

To constrain the nature of the BH seeds and explain how they were able to grow so quickly, the accretion physics must be better understood. Since the centres of the earliest quasar host galaxies will remain observationally inaccessible, this must be done in the nearby Universe. We have promising low-redshift equivalents to fast-growing lower-mass SMBHs in the form of Narrow-Line Seyfert 1 (NLS1) galaxies. With their extreme BH accretion rates close to the Eddington limit ( $\lambda_{\text{Edd}} \sim 1$ ), the central engines of NLS1s are prototypical of the high-redshift AGN population currently being discovered by JWST. However, the properties of NLS1s are not well understood; they cannot be explained by inclination effects, nor do they fit in the AGN unification model. As a result, their place within the overall AGN population has remained unclear for the past four decades.

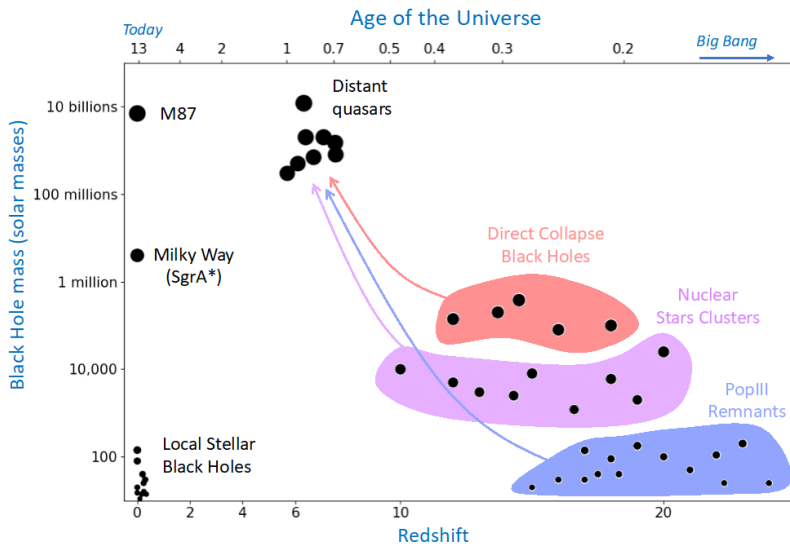


Figure 1.6: *Illustration of accretion history of high- $z$  quasars in the early Universe.* Luminous quasars are currently being discovered out to redshifts of  $z = 7$  and higher when the age of the Universe was less than a Gyr. As these quasars are powered by SMBH masses of several billion solar masses, it requires initial BH seeds to accrete close to the Eddington limit for several 100 Myr. Several types of initial BH seeds are discussed, including massive Population III stars, nuclear star clusters or direct collapse BHs. While more massive seeds lower the accretion rates required to bridge the gap, the BH growth is still challenging to explain with current models of AGN accretion. Credit: Roberto Maiolino, University of Cambridge.

### 1.3 Black Hole Mass - Host Galaxy Scaling relations

SMBHs are typically about three orders of magnitude smaller in mass compared to their host galaxies. Similarly, the BH gravitational SoI is roughly three orders of magnitude smaller than the extent of its host galaxy. Given that the dynamics on such small scales are decoupled from those of the

host galaxy, and considering that galaxy formation is itself a complex process, it is not immediately clear why the properties of a galaxy should be related to those of the SMBH. However, as discussed in the previous section, various AGN-driven outflows can extend to scales comparable to or beyond that of the host galaxy. Based on this observation, Silk & Rees predicted in 1998a that AGN feedback processes should produce a correlation between BH mass and the host galaxy’s stellar velocity dispersion in the form of  $M_{\text{BH}} \propto \sigma_{\star}^5$ . This correlation was shortly after discovered in local quiescent galaxies (Gebhardt et al., 2000; Ferrarese & Merritt, 2000), marking the beginning of the study of the coevolution of BHs and their host galaxies. Since then, review articles by Ferrarese & Ford (2005), Kormendy & Ho (2013), Graham (2016) and Greene et al. (2020) have cited over two thousand references, underscoring the topic’s continued relevance to the community.

### 1.3.1 Quiescent Galaxies

After a series of seminal papers, it was established that  $M_{\text{BH}}$  correlates with bulge luminosity (Kormendy & Richstone, 1995; Marconi & Hunt, 2003) and bulge stellar mass (Magorrian et al., 1998; Häring & Rix, 2004). This led to the common belief that black holes and bulges coevolve by regulating each other’s growth. Among the scaling relations,  $M_{\text{BH}}\text{-}\sigma_{\star}$  was found to be remarkably tight over many orders of magnitude, leading to the speculation that the observed scatter was primarily due to observational limitations, and that the intrinsic scatter in the relation might be close to zero (Ferrarese & Merritt, 2000). However, this proved not to be the case. Advances in observational techniques allowed for more precise constraints on the parameters of these scaling relations. Measurements of the  $M_{\text{BH}}$  became increasingly precise once the SMBH’s SoI could be spatially resolved and the stellar orbits could be modelled. On the black hole side,  $M_{\text{BH}}$  was measured with unprecedented precision via modelling the stellar orbits with within the black hole’s SoI. On the other hand, high spatial resolution HST photometry and IFU observations enabled detailed measurements of host galaxy properties across various structural sub-components. With these technical advancements and larger sample sizes, Gültekin et al. (2009) found that the scatter in these relations decreases at higher  $M_{\text{BH}}$ . This trend is driven by galaxy morphology, where spiral galaxies, compared to massive elliptical galaxies, exhibit a larger

scatter in the  $M_{\text{BH}}$ -host galaxy scaling relations. It aligns well with an alternative formation scenario proposed around that time, suggesting that the properties of black holes and their host galaxies correlate due to galaxy growth via hierarchical merging (e.g. Peng, 2007; Jahnke & Macciò, 2011).

An important lesson learned since then is that the technique used to measure host galaxy parameters significantly impacts the results. Aperture sizes in terms of galaxy effective radius are not only defined differently in the literature, but the methods for deriving aperture-integrated kinematics from individual spectra are also inconsistent. Using a standardised method, Kormendy & Ho (2013) reviewed that classical bulges are not necessary for BH formation, as BHs are also detected in pseudobulges of some disc galaxies. They further concluded that in disc galaxies, the BHs, when detected, do not correlate with the properties of the disc. However, this claim was challenged by McConnell & Ma (2013), van den Bosch (2016), and Davis et al. (2017), who found correlations with various properties of galaxy discs, including the  $M_{\text{BH}}-\sigma_*$  relation, albeit with a steeper slope. Beyond the disc-spheroid distinction, many additional dependencies of the  $M_{\text{BH}}$ -host-galaxy scaling relations have been explored, including barred vs. unbarred galaxies (Graham, 2008; Hu, 2008), pseudo-vs. classical bulges (Kormendy & Ho, 2013; Saglia et al., 2016), and late-type vs. early-type galaxies (McConnell & Ma, 2013; Sahu et al., 2019). In summary, there are plenty of nuances in the scaling relations driven by host galaxy morphology. The relation of the spheroidal components can be interpreted as an evolution driven by AGN, mergers and stellar winds, as suggested by Graham & Sahu (2023). The global  $M_{\text{BH}}-\sigma_*$  relations show an offset at the high- $M_{\text{BH}}$  end, where the brightest cluster galaxies tend to host overmassive black holes that likely formed by dry mergers of massive ellipticals (Bogdán et al., 2018; Graham, 2023). At the low-mass end, where host galaxies are spirals, the global  $M_{\text{BH}}-\sigma_*$  relation seem to broaden, which Sahu et al. (2019) explain through a mixture of different populations following intrinsically different relations. Interestingly, as the relations are studied with increasing detail, their reported intrinsic scatter  $\epsilon$  keeps increasing. For example, the scatter in the  $M_{\text{BH}}-\sigma_*$  relation has grown from  $\epsilon = 0.30$  dex (Gebhardt et al., 2000) to  $\epsilon = 0.44$  dex (Gültekin et al., 2009) and then to  $\epsilon = 0.53$  dex (Sahu et al., 2019), to name a few. This trend suggests that early studies may have underestimated their measurement uncertainties or may have targeted biased samples. The se-

lection criteria used in these studies remain an active topic of discussion: Are the  $M_{\text{BH}}$ -host galaxy scaling relations showing the complete picture, or are current measurement techniques only sensitive to the densest systems (Shankar et al. 2016; van den Bosch et al. 2015; Shankar et al. 2020 vs. Kormendy 2020)? In the latter case, the observed scaling relations might represent only the upper envelope of a much larger distribution, with a large undetected pedestal of lower-mass BHs residing in galaxies with lower stellar mass surface densities.

### 1.3.2 Active Galaxies

The  $M_{\text{BH}}$  scaling relations of AGNs are particularly interesting for various reasons. From a technical perspective, estimating BH masses in AGNs has always been challenging. The standard techniques involving spatially resolved kinematics of stars generally cannot be applied to AGNs because the strong BLR continuum severely dilutes any spectral features of the stars (Davies et al., 2006; Onken et al., 2007), and there are not many nearby AGNs for which the required spatial resolution can be achieved. Reverberation mapping (see Sect.1.1.3) offers the most promising probe of the gravitational potential of the BH, but traditional RM can only constrain  $M_{\text{BH}}$  to an unknown geometrical factor, the virial factor  $f$  (see eq. 1.1). Historically, assuming that AGNs and quiescent galaxies share the same scaling relations,  $f$  was constrained as sample-average by matching the the VP- $\sigma_*$  relation of AGNs to the  $M_{\text{BH}}$ - $\sigma_*$  relation of quiescent galaxies (e.g., Onken et al., 2004). As  $f$  is also required for estimating BH masses via the single-epoch method, this calibration formed the baseline for measuring BH masses across cosmic time.

From a scientific perspective, RM can also constrain BLR kinematics and geometry (see Sect. 1.1.3), which provides crucial tests for our understanding of the AGN structure. Furthermore, evolutionary trends of the parameters of the  $M_{\text{BH}}$ -host-galaxy scaling relations can help discern between merger-driven vs. secular formation scenarios. As the methods for measuring black hole masses in quiescent galaxies are not applicable beyond the local Universe (since the gravitational SoI is not resolvable), evolutionary studies rely on scaling relations measured in AGNs. It is worth noting that, although often implicitly assumed, there is no fundamental reason why AGNs should follow the same scaling relations as quiescent galaxies. For example, BHs in AGNs which are currently growing

at relatively high rates, may grow faster compared to the timescales over which their host galaxy properties develop. Moreover, the AGN sample might represent a biased subset in either  $M_{\text{BH}}$  or host galaxy properties, as the processes within the host galaxy that trigger AGNs are not yet fully understood (see Sect. 1.2.1).

With recent developments pushed by the GRAVITY-AGN group, and intense reverberation mapping campaigns from the Lick AGN Monitoring Project (LAMP) collaboration, it has only now become possible to independently measure  $M_{\text{BH}}$  and individual  $f$ -factors for a statistically meaningful sample of AGNs, covering a large dynamic range in  $M_{\text{BH}}$ . This breakthrough allows calibrating the  $M_{\text{BH}}-\sigma_*$  relation without the underlying assumption that quiescent galaxies and AGNs follow the same relation. In other words, for the first time, this allows for a direct test whether the initial hypothesis that AGNs and quiescent galaxies share the same underlying conditions. In this thesis, I will complement the state-of-the-art  $M_{\text{BH}}$  measurements with host galaxy properties measured from high-resolution imaging and IFU spectroscopy. These techniques enable detailed decomposition of AGNs and their host galaxies, allowing for precise measurements of  $\sigma_*$  and better characterisation of morphological features like bars and pseudobulges. High-resolution imaging addresses issues related to morphological substructures and inclination effects, while IFU spectroscopy provides spatially resolved kinematics necessary for refining the  $M_{\text{BH}}-\sigma_*$  relation and reducing biases introduced by rotational broadening and aperture effects. Based on these detailed measurements, we have a solid foundation for testing the 'classical' approach of using a sample-average  $f$ , and to assess whether the assumptions underlying the single-epoch method for measuring  $M_{\text{BH}}$  across cosmic time are well-grounded in the AGN  $M_{\text{BH}}$ -range explored so far.

## 1.4 Objectives and Outline of This Work

In this introduction, the fundamental ideas and open questions necessary to understand this thesis have been outlined. More detailed introduction to the topics will be given in each introduction preceding the respective chapters. The overarching goals of this thesis can be summarised as follows:

1. Constraining the BH fuelling and feedback processes in the circumnuclear regions of type 1 AGNs accreting at high specific rates.
2. The first spatially resolved calibration of  $M_{\text{BH}}-\sigma_*$  of AGNs with independently measured BH masses.

For each of the objectives, I use state-of-the-art 3D spectroscopic data to study the host galaxy near the unobscured AGN. In Chapter 2, I present and analyse IFU data, which allow me to map the circumnuclear star formation in the nearby NLS1 galaxy Mrk 1044. Chapter 3 reports the detection of a compact AGN-driven ionised gas outflow in the same galaxy. In Chapter 4, I present optical IFU data along with ALMA CO observations of the molecular gas in the centre of NGC 4593, aiming to identify the radial gas transport mechanism. Chapter 5 presents the calibration of the AGN  $M_{\text{BH}}-\sigma_*$  and  $M_{\text{BH}}-M_{\text{bulge,dyn}}$  relations, pushing the limits of measuring stellar kinematics close to the centres of luminous type 1 AGNs. Finally, in Chapter 6, I review the conclusions drawn from this work, evaluate them in the context of recent progress in the literature, and discuss future perspectives based on these findings.

---

# Tracing the circumnuclear star formation in the super-Eddington NLS1 Mrk 1044

This chapter has been adapted from [Winkel et al. \(2022\)](#), published in *Astronomy & Astrophysics*. The project was supervised by Dr. Bernd Husemann who led the data proposal and acquisition, while I led the data reduction and analysis. The interpretation of the results was supported by the CARS collaboration.

N. Winkel<sup>1</sup>, B. Husemann<sup>1</sup>, T. A. Davis<sup>2</sup>, I. Smirnova-Pinchukova<sup>1</sup>,  
V. N. Bennert<sup>3</sup>, F. Combes<sup>4</sup>, M. Gaspari<sup>5</sup>, K. Jahnke<sup>1</sup>, J. Neumann<sup>6</sup>,  
C. P. O’Dea<sup>7</sup>, M. Pérez-Torres<sup>8,9</sup>, M. Singha<sup>7</sup>, G. R. Tremblay<sup>10</sup>, H. W. Rix<sup>1</sup>

<sup>1</sup>Max-Planck-Institut für Astronomie, Königstuhl 17, D-69117 Heidelberg, Germany

<sup>2</sup>Cardiff Hub for Astrophysics Research & Technology, Cardiff University, CF24 3AA, UK

<sup>3</sup>Physics Department, CalPoly, San Luis Obispo, CA 93407, USA

<sup>4</sup>LERMA, Observatoire de Paris, NRS, Sorbonne Univ., Paris, France

<sup>5</sup>Princeton University, 4 Ivy Lane, NJ 08544-1001, USA

<sup>6</sup>University of Portsmouth, Burnaby Road, Portsmouth, PO1 3FX, UK

<sup>7</sup>University of Manitoba, Winnipeg, MB R3T 2N2, Canada

<sup>8</sup>IAA, Glorieta de las Astronomía s/n, 18008 Granada, Spain

<sup>9</sup>Departamento de Física Teórica, Universidad de Zaragoza, E-50009 Zaragoza, Spain

<sup>10</sup>CfA| Harvard & Smithsonian, 60 Garden St., Cambridge, MA 02138, USA

## Abstract

The host galaxy conditions for rapid supermassive black hole growth are poorly understood. Narrow-line Seyfert 1 (NLS1) galaxies often exhibit high accretion rates and are hypothesized to be prototypes of active galactic nuclei (AGN) at an early stage of their evolution. We present adaptive optics (AO) assisted VLT MUSE NFM observations of Mrk 1044, the nearest super-Eddington accreting NLS1. Together with archival MUSE WFM, data we aim to understand the host galaxy processes that drive Mrk 1044’s black hole accretion. We extracted the faint stellar continuum emission from the AGN-deblended host and performed spatially resolved emission line diagnostics with an unprecedented resolution. Combining both MUSE WFM and NFM-AO observations, we used a kinematic model of a thin rotating disk to trace the stellar and ionized gas motion from 10 kpc galaxy scales down to  $\sim 30$  pc around the nucleus. Mrk 1044’s stellar kinematics follow circular rotation, whereas the ionized gas shows tenuous spiral features in the center. We resolve a compact star-forming circumnuclear ellipse (CNE) that has a semi-minor axis of 306 pc. Within this CNE, the gas is metal-rich and its line ratios are entirely consistent with excitation by star formation. With an integrated star formation rate of  $0.19 \pm 0.05 M_{\odot} \text{yr}^{-1}$ , the CNE contributes 27% of the galaxy-wide star formation. We conclude that Mrk 1044’s nuclear activity has not yet affected the circumnuclear star formation. Thus, Mrk 1044 is consistent with the idea that NLS1s are young AGN. A simple mass budget consideration suggests that the circumnuclear star formation and AGN phase are connected and the patterns in the ionized gas velocity field are a signature of the ongoing AGN feeding.

# Chapter 2 | Tracing the Circumnuclear Star Formation in the Super-Eddington NLS1 Mrk 1044

## 2.1 Introduction

Active galactic nuclei (AGN) accreting with high Eddington ratios are often classified as narrow-line Seyfert 1 (NLS1) galaxies. NLS1s offer an unobscured view of the broad-line region (BLR), such that their optical spectra exhibit both emission lines originating from the high-density BLR and from the low-density narrow-line region (NLR). As opposed to broad-line Seyfert 1s (BLS1s), both permitted and forbidden emission lines are narrow ( $\text{FWHM}(\text{H}\beta) < 2000 \text{ km s}^{-1}$ , Goodrich 1989). NLS1s often exhibit weak [O III] emission ( $[\text{O III}]/\text{H}\beta < 3$ , Osterbrock & Pogge 1985) and strong Fe II emission from the BLR. This locates them at the extreme end of the Eigenvector 1 relation (EV1, Boroson & Green, 1992; Sulentic et al., 2000), which is believed to be driven by the Eddington ratio.

The relative narrowness of the broad lines in NLS1 is usually interpreted as a result of smaller rotational velocities of ionized gas clouds in the BLR. Thus, the inferred central black-hole (BH) masses of NLS1 are small ( $10^6 - 10^8 M_{\odot}$ , e.g., Zhou et al. 2006; Rakshit et al. 2017). Although "narrow" broad lines could also be produced by inclined BLR disks in conventional BLS1s (Baldi et al., 2016), inclination-independent BH mass estimates (e.g., Du et al., 2014, 2015; Wang et al., 2014; Pan et al., 2018; Berton et al., 2021) and the host morphologies of NLS1s (Krongold et al., 2001; Järvelä et al., 2017, 2018; Berton et al., 2019) suggest genuinely low BH masses.

Previous studies have found that NLS1s systematically lack large-scale diffuse radio emission (Komossa et al., 2006; Gliozzi et al., 2010; Doi et al., 2013; Lister et al., 2016), and AGN-ionized gas on kiloparsec scales in contrast to BLS1s which suggests little to no AGN activity in their recent past (e.g., Husemann et al., 2008). It is often speculated that NLS1s represent the early stages of the AGN life cycle where the fueling of the

central super-massive black hole (SMBH) is not yet affected by feedback processes from the host galaxy (Mathur, 2000; Collin & Kawaguchi, 2004).

Although NLS1s share the same classification based on their optical spectra, they exhibit fairly heterogeneous properties. Only a few are detected in the radio among which the dominating emission mechanism ranges from AGN-dominated composite and to host-dominated (Järvelä et al., 2021). Among the AGN-dominated ones, some show traces of extended jets detected in the radio, reaching distances of tens of kiloparsecs from the nucleus. In individual NLS1 galaxies, relativistic jets powered by the central engine have been found (Yuan et al., 2008; Foschini, 2011; Foschini et al., 2015) as well as blazar-like phenomena such as high brightness temperature, a double-humped spectral energy distribution, or gamma-ray emission (Romano et al., 2018; Paliya et al., 2019; Komossa, 2018). X-ray observations have shown that NLS1s exhibit fast variability on typical timescales of less than one day (Boller, 2000), which is expected for the small BH masses and high accretion rates (Ponti et al., 2012).

One of the open questions regarding the place of NLS1s among the AGN population is the origin of the exceptionally bright Fe II emission from their BLR. The high metallicity is difficult to explain from a galaxy evolution perspective as it requires substantial star formation (SF) to enrich the material in the accretion disk. At redshifts around  $z \sim 1$ , star-forming galaxies are more likely to host rapidly growing, radiatively efficient AGN despite having similar gas fractions and star formation efficiencies as their non-SF counterparts (Nandra et al., 2007; Goulding et al., 2014). This suggests that both galaxy-scale SF and the AGN phase are triggered by the same secular processes. At intermediate and low redshifts, however, the accretion becomes radiatively inefficient and mostly mechanical (Hickox et al., 2009). Furthermore, the following are a matter of discussion: how gas is channeled from the galactic scales down to the subparsec scales of the circumnuclear accretion disk, how the gas transport affects the SF and its spatial distribution in the host, and what is the main driver of such transport (e.g., turbulent mixing, inelastic collisions, and gravitational torques; see Gaspari et al. 2020 for a review).

The host galaxies of NLS1s are predominantly classified as disk galaxies and often possess pseudo-bulges (Crenshaw et al., 2003). They often exhibit enhanced SF in their nuclear regions (Deo et al., 2006) and only a few of them show signs of major mergers or interaction (Ohta et al., 2007).

Therefore, the gas transport toward the galaxy center requires an internal process to prolong SF and AGN accretion. This idea is further supported by the frequent presence of pseudo-bulges in NLS1 host galaxies (Orban de Xivry et al., 2011), which are formed from secular processes (Kormendy & Kennicutt, 2004a). These asymmetries can develop circumnuclear spiral structures (Maciejewski, 2004) and enable radial gas migration (Sakamoto et al., 1999; Sheth et al., 2005).

Local AGN in which circumnuclear SF has been resolved have low Eddington ratios (e.g., Esquej et al., 2014; Ramos Almeida et al., 2014; Ruschel-Dutra et al., 2017; Esparza-Arredondo et al., 2018; Knapen et al., 2019) and they may therefore have been caused by different fueling mechanisms than accretion-mode NLS1s. The situation is further complicated by the difficulty to observe close to their unobscured nucleus. It requires an accurate deblending of the AGN emission that is broadened by the instrumental point spread function (PSF) and the faint host emission. Moreover, the NLS1 population is heterogeneous (Komossa et al., 2006; Järvelä et al., 2017) and low-redshift NLS1s are rare, which makes a statistical evaluation of their host galaxy properties challenging. Given the diversity among NLS1s and their complex behavior, their classification by their optical classification alone probably does not reflect the underlying physical mechanisms. We therefore need detailed studies of individual objects to explain their characteristics on the BH - host galaxy interaction.

Mrk 1044 is a classic example of a NLS1 and one of the nearest super-Eddington accreting AGN. It is a radio-quiet, luminous ( $L_{\text{bol}} = 3.4 \times 10^{44} \text{ erg s}^{-1}$ ) NLS1 at  $z = 0.0162$  (Husemann et al., 2022). Its central engine is powered by a BH with a reverberation mapped mass of  $M_{\text{BH}} = 2.8 \times 10^6 M_{\odot}$  (Du et al., 2015). Numerous studies have confirmed Mrk 1044's high accretion rate with Eddington fractions  $\lambda_{\text{Edd}} = L_{\text{bol}}/L_{\text{Edd}}$  that range from 1.2 (Husemann et al., 2022) up to 16 (Du et al., 2015). Although Mrk 1044 is a bright X-ray source (Dewangan et al., 2007), it shows no signs of AGN-driven hot outflows in the form of extended X-ray emission (Powell et al., 2018). The luminous central region, however, shows frequency-dependent variability and an X-ray excess that is likely caused by relativistic Compton scattering from a high-density accretion disk (Mallick et al., 2018). In a recent study, Krongold et al. (2021) used XMM-Newton observations to identify an ultra-fast outflow with a mul-

tivelocity, multiphase structure originating at the scales of the accretion disk.

On galaxy scales, Mrk 1044 has a barred spiral morphology (Deo et al., 2006) with an estimated H I mass of  $2.6 \times 10^9 M_{\odot}$  (König et al., 2009) and H<sub>2</sub> mass of  $4 \times 10^8 M_{\odot}$  (Bertram et al., 2007). Powell et al. (2018) have identified three concentric star-forming rings. The outer ring at  $\sim 7$  kpc is likely to be associated with spiral arms in a rotating disk, whereas the inner star-forming region has not been resolved in earlier studies. Although Mrk 1044 is an extensively studied nearby NLS1, a complete picture of the host galaxy processes and how they affect its AGN activity is still missing. In this work we present adaptive-optics (AO) assisted optical integral field spectroscopic (IFU) observations of Mrk 1044 to study the ionized properties and explore the kinematic signatures of the BH - host galaxy interaction at unprecedented spatial resolution. Throughout this paper, we assume a flat  $\Lambda$ CDM cosmology with  $H_0 = 70 \text{ km s}^{-1} \text{ Mpc}^{-1}$ ,  $\Omega_M = 0.3$ , and  $\Omega_{\Lambda} = 0.7$ . In this paper,  $1''$  corresponds to 0.333 kpc at the redshift of Mrk 1044 and the associated luminosity distance is 70.0 Mpc.

## 2.2 Data

### 2.2.1 Observations and Data Reduction

For this study we use the integral field spectroscopic data acquired with the Multi Unit Spectroscopic Explorer (MUSE, Bacon et al., 2010, 2014) at the Very Large Telescope (VLT). The unprecedented spatial resolution and spectral coverage of the adaptive-optics assisted narrow field mode (NFM-AO) allowed us to map the host galaxy emission line properties and kinematics of both stellar and gas components down to a resolution of 89 mas (30 pc). In order to gain a complete picture of the physical processes on different spatial scales, we combined them with the IFU data from the Close AGN Reference Survey (CARS, Husemann et al., 2022) and a high resolution broadband image acquired with the UVIS instrument on the Hubble Space Telescope (HST).

## 2.2.2 Optical Imaging

Mrk1044 has been imaged with HST under the program ID 12212 using WFC3/UVIS in the F547M filter. We collected the archival image from the Hubble Legacy Archive<sup>1</sup>. The field of view (FOV) spans  $3.66' \times 3.56'$  with a spatial resolution of  $0''.067$  at  $6000\text{\AA}$  as reported in the WFC3 Instrument Handbook.

## 2.2.3 IFU Optical Observations

### VLT MUSE WFM

As part of CARS (Husemann et al., 2022)<sup>2</sup>, Mrk1044 has been observed with the wide field mode (WFM) of the MUSE instrument. The data were reduced using the standard ESO pipeline v.2.8.1 (Weilbacher et al., 2012, 2020) as described in Husemann et al. (2022). The resulting data cube has a FOV of  $62''.7 \times 63''.5$  with a sampling of  $0''.2$  per pixel and a seeing-limited resolution of  $1''.03$ . Along the wavelength axis, it extends from  $4750\text{\AA}$  to  $9300\text{\AA}$  with a spectral resolution of  $\sim 2.5\text{\AA}$  that slightly varies over the spectral range (Bacon et al., 2017; Gu erou et al., 2017).

### VLT MUSE NFM-AO

We observed Mrk1044 with the AO-assisted NFM of the MUSE Integral Field Unit under the program 0103.B-0349(A). The data were acquired on 23 Aug 2019, 24 Aug 2019, and 28 Sep 2019. The 12 exposures have an integration time of 550s each and were dithered by a small angle to minimize the imprint of cosmic rays and flat-fielding artifacts. We used the MUSE pipeline v2.8.3-1 together with the graphical user interface ESO Reflex v2.11.0 to execute the EsoRex Common Pipeline Library reduction recipes.

For WFM data, the reduction pipeline performs a differential atmospheric refraction (DAR) correction that is based on a theoretical prediction (Weilbacher et al., 2020). However, the correction is poor for observations in the NFM since the performance of the hardware build-in atmospheric dispersion correction (ADC) is insufficient. In order to correct for the remaining wavelength-dependent atmospheric refraction, we

<sup>1</sup><https://hla.stsci.edu/>

<sup>2</sup><https://cars.aip.de/>

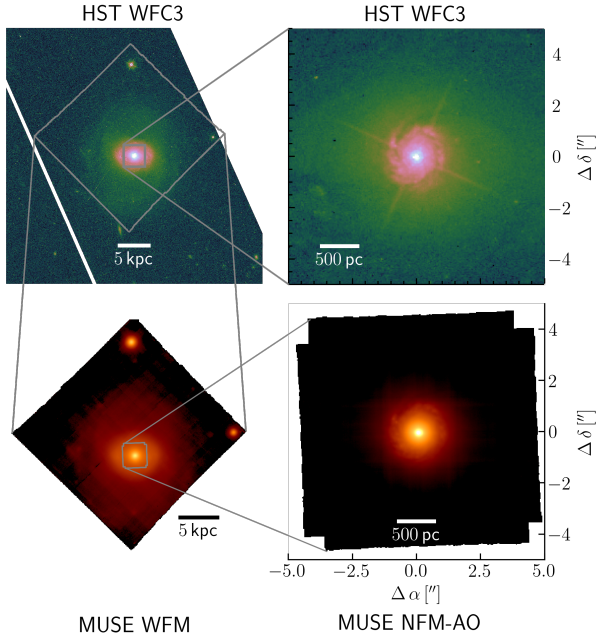


Figure 2.1: *Mrk 1044* IFU and imaging observations. We show the comparison of the FOV HST WFC3/UVIS in the F547M filter (left), VLT MUSE WFM (center), and VLT MUSE NFM-AO (right). The two images from MUSE are white-light images which were created by integration over the wavelength axis. Both WFC3/UVIS and MUSE WFM have a FOV that covers the host galaxy beyond its effective radius of its disk  $r_e = 7.14 \pm 0.04$  kpc (Wang et al., 2014), whereas MUSE NFM-AO only captures the innermost  $3.1 \times 3.2$  kpc.

used a 2D Moffat model<sup>3</sup> to measure the AGN position of the individual exposures after the sky correction (`muse_scipost`). To remove the wavelength-dependence, we subtracted the wavelength-dependent coordinate offset in the PIXTABLE files. Fig. 2.2 demonstrates the procedure for one example exposure. After the correction, the residual variation of

<sup>3</sup>The AO-induced PSF is not well described by a 2D Moffat profile (see Sect. 2.2.4), especially far from the center. However, to get an estimate of the data quality, it is a sufficiently accurate model.

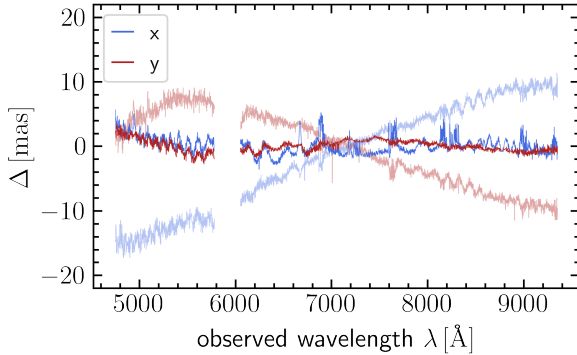


Figure 2.2: *Wavelength-dependent AGN position on the detector plane before (transparent) and after (opaque) correcting for differential atmospheric refraction.* The wavelength range around 5890 Å has been blocked by a dichroic in the optical path to avoid contamination and saturation of the detector by the strong sodium emission from the AO laser.

the quasi-stellar object (QSO) position across the full wavelength range is of the same order of magnitude as its scatter ( $\sim 0''.04$ ).

The spatial resolution of individual exposures depends on the wavelength-dependent performance of the AO system. The science observations taken on 24 Aug 2019 have an inferior quality compared to the remaining ones due to the atmospheric conditions during the exposures. Especially at the blue end of the spectrum where we performed most of our diagnostics, the difference in resolution is substantial. Here, the FWHM of the 2D Moffat to model the AGN PSF is larger by a factor of 3 – 4. So as to not degrade the resolution of the data cube, we therefore only combined the eight exposures taken in the night of 23 Aug 2019 and 28 Sep 2019 with `muse_exp_combine`.

The final data cube consists of  $369 \times 378$  spaxels, corresponding to a FOV of  $9''.23 \times 9''.45$  with 127,741 spectra. From the width of the telluric emission lines, we find a constant resolution of  $\text{FWHM} = 2.54 \pm 0.10 \text{ \AA}$  across the full wavelength range 4750 Å - 9350 Å, corresponding to  $160.4 \text{ km s}^{-1}$  and  $81.5 \text{ km s}^{-1}$  at the blue and the red end of the spectrum, respectively.

### 2.2.4 Deblending the AGN and Host Emission

In 3D spectroscopic observations of type 1 AGN, the light of the unresolved central QSO distributes over the host galaxy as dictated by the PSF. Due to the bright AGN and the low surface-brightness host emission, the AGN contamination is particularly strong within the small FOV of the MUSE NFM data cube (see right panel of Fig. 2.1). Disentangling the host emission from QSO contamination requires deblending in both spectral and spatial dimensions.

The AGN-host deblending process contains the following five steps: 1) estimating the PSF at the broad lines by AGN-host decomposition; 2) reconstructing the AO-shaped PSF at the broad lines with a model; 3) generating a hybrid PSF that combines the empirical PSF with the model PSF; 4) interpolating the hybrid PSF along the wavelength axis; and 5) applying an iterative AGN-host deblending procedure combining the wavelength-dependent hybrid PSF with the host galaxy surface brightness profile. In the following subsections, we describe each of the steps in detail.

#### PSF Extraction at the Broad Emission Lines

In order to separate the host emission from the QSO emission, we employed the dedicated software<sup>4</sup> `QDeblend3D` (Husemann et al., 2013). It is based on the concept that the spectrum of each spaxel is a superposition of the host spectrum and a spectrum from the central QSO that is scaled in flux according to the PSF. Since broad lines from the BLR are spatially unresolved, that is to say point-like, type 1 AGN allow one to extract the empirical PSF at each broad line available. In the following, we give a brief outline of the concept. For a detailed description of the algorithm, we refer the reader to Husemann et al. (2013).

As a first step, `QDeblend3D` scales the broad-line wings to the flux of the pseudo-continuum to obtain a PSF. The high signal-to-noise (S/N) QSO spectrum is then scaled to match the flux of the broad-line wings in each spaxel (step 1), which corresponds to a tentative QSO data cube. As a next step, the emission from the host galaxy is obtained by subtracting the QSO data cube from the original data cube. Since the initially extracted QSO spectrum is inevitably contaminated by a small fraction of host galaxy light, this leads to an over-subtraction of the host cube

---

<sup>4</sup><https://git.io/qdeblend3d>

near the center. To estimate the host contribution, `QDeblend3D` interpolates the host cube toward the central QSO position assuming a surface brightness (SB) profile. In our case, we used a constant SB profile since the over-subtracted region is small ( $\sim 0''.5$ ). The host spectrum in the central pixel is then subtracted from the tentative QSO spectrum in order to obtain an updated QSO spectrum which is used for the next iteration starting at step 1. With this procedure, we extracted the empirical PSF at  $H\beta$ ,  $H\alpha$ , and  $O\text{I}\lambda 8446 + \text{Ca}\text{II}\lambda 8498$  (see [Matsuoka et al., 2007](#)) which have a FWHM of 89, 51, and 41 mas, respectively.

### Modeling the MUSE NFM-AO PSF

Our observations of Mrk 1044 with MUSE NFM were assisted by the Ground Atmospheric Layer Adaptive Optics for Spectroscopic Imaging (GALACSI) AO system ([Ströbele et al., 2012](#)) to improve spatial resolution. The AO-shaped PSF does not follow the Moffat profile suited for seeing-limited observations. Instead, it has a peculiar shape that depends on the performance of the AO system. Here, we describe the PSF modeling for bright point-like AGN emission required for the subsequent deblending process.

The NFM-AO PSF only slowly changes with wavelength. However, since we subtracted the bright AGN emission to get the relatively faint host, small inaccuracies in the PSF model could already severely affect our analysis of the narrow host emission lines. Another problem is that the subtraction of an empirical PSF adds noise to the host data cube which dominates over the faint host emission already at small distances from the center. We are therefore interested in using a model that describes both the behavior of the NFM-AO PSF toward the faint outskirts and its wavelength dependence. An analytic model for the long-exposure AO-corrected PSF has been presented by [Fétick et al. \(2019\)](#), which is hereafter referred to as PSFAO19). They describe the phase power spectral density (PSD) with a narrow Moffat core and a wide Kolmogorov halo. The PSFAO19 model consists of five parameters (and an additional two in the asymmetric case), which include the Fried parameter  $r_0$ , the AO-corrected phase PSD background  $C$ , the Moffat amplitude  $A$ , and the Moffat scale factors  $\alpha$  and  $\beta$ . This parametrization is physically motivated by the design of the AO system. The actuators that deform the secondary mirror are separated by a pitch which sets the maximal spatial frequency

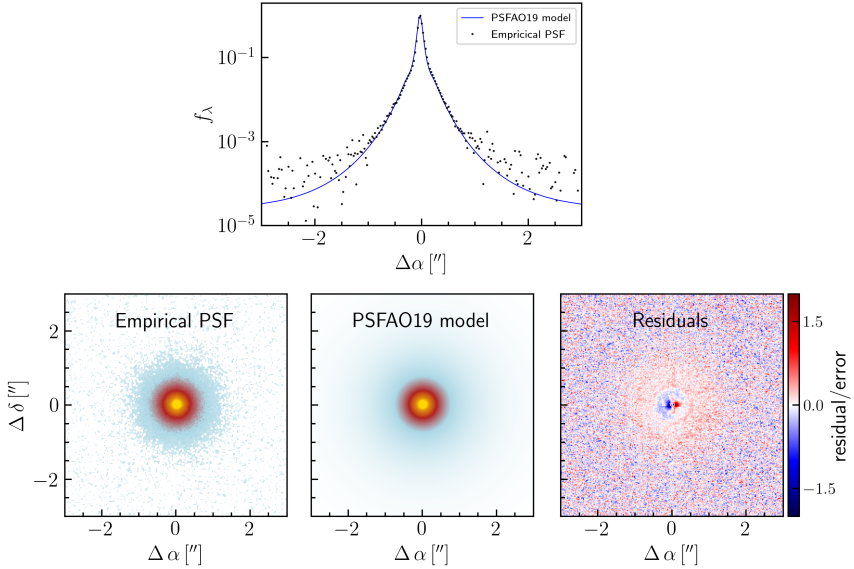


Figure 2.3: *Fitting the MUSE NFM-AO PSF.* From left to right, the panels show the empirical PSF for the broad H $\beta$  line extracted as described in Sect. 2.2.4, the corresponding PSFAO19 model, and the residual flux map. The rightmost panel shows the cross section of the PSF at the QSO position and fixed  $\delta$ . While the turbulent halo of the AO-induced PSF is well reproduced by the PSFAO19 model, the systematic errors near the center are significant compared to the relatively faint host signal.

of the phase  $f_{\text{AO}}$  which can be corrected by the AO system. Beyond this frequency, the residual phase PSD is not affected by the AO system, which leaves a residual turbulence in the PSF outskirts.

To retrieve the best-fit parameters for the empirical PSFs available, we used the PSFAO19 model that uses a Levenberg–Marquardt algorithm to minimize the  $\chi^2$  sum of the flux in the residual images. We fit the PSF over the full FOV, weighted by the inverse of the noise variance of the individual pixels. In Table 2.1 the best-fit parameters are listed. The Fried parameter  $r_0$  increases with wavelength as  $\lambda^{1.22 \pm 0.05}$  and it is consistent with the theoretical prediction  $\lambda^{6/5}$ . Since the atmospheric refraction is

Table 2.1: *Best-fit PSFAO19 model parameters at three different wavelengths.* We extracted the empirical PSFs from the data cube at each of the available broad lines.

Parameter	H $\beta$	H $\alpha$	O I $\lambda$ 8446+Ca II $\lambda$ 8498
$r_0$ [cm]	13.3	18.8	26.2
$C$ [ $10^{-3}\text{rad}^2\text{cm}^2$ ]	14.9	10.8	7.3
$A$ [ $\text{rad}^2$ ]	337	705	8
$\alpha$ [ $\text{cm}^{-1}$ ]	2.36	1.34	3.28
$r$	0.987	1.008	1.018
$\theta_R$	0.35	-0.44	-0.61
$\beta$	1.56	1.63	1.67
FWHM [mas]	88	51	40

smaller in the red (i.e., the AO system performs better), the FWHM of the PSF decreases with wavelength.

### Generating the Hybrid PSF

In contrast to the empirical PSF, the analytic model has the advantage that it does not contain noise. Thus, it does not add noise to the host cube when subtracting the PSF cube from the original data cube. This is particularly important at a large distance from the center where the host emission is faint and the S/N of the empirical PSF is low. We find that the outskirts of the PSF are well reproduced by the PSFAO19 model (see Fig. 2.3). Near the center, however, the amplitude of the residuals is  $\sim 1\%$  of flux from the AGN and therefore of the same order of magnitude as the host signal.

In order to combine the advantages of both regimes, we created a hybrid PSF. For the high S/N central regions, we used the empirical PSF, whereas the model PSF is superior at a large distance from the center. We selected the transition at the radius beyond which the azimuthally averaged S/N falls below a threshold value of 3. For H $\beta$ , H $\alpha$ , and O I+Ca II, the transition radii are located at 39, 73, and 28 px, respectively.

### Interpolation of the PSF with Wavelength

The PSF is wavelength-dependent as can be seen from Fig. 2.4. Therefore, we need to interpolate the 2D PSFs that are available for the three broad lines listed in Table 2.1.

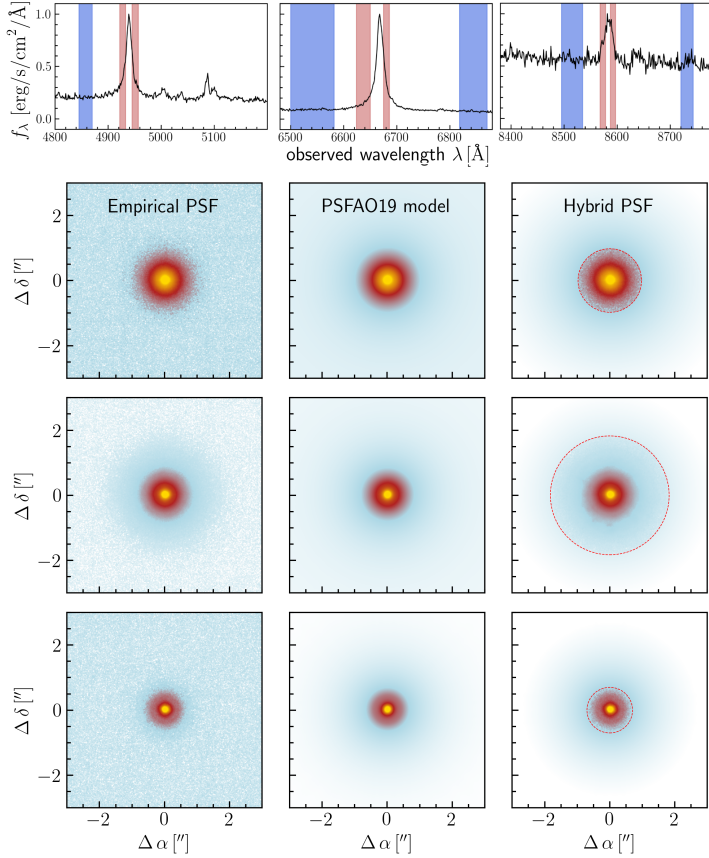


Figure 2.4: *Construction of hybrid PSF from the MUSE data cube.* The top panels show the continuum (blue) and broad-line (red) spectral regions from which the broad-line intensity was extracted. The resulting empirical PSFs with logarithmic intensity scaling are shown in the bottom panels, left column. The corresponding best-fit PSFAO19 models are shown in the third bottom second column, and the bottom third column shows the hybrid PSFs which we generated by replacing the empirical PSFs with the modeled PSFs beyond the radius where the S/N drops below a threshold value (dashed red circle).

As a first approach, we used a spline interpolation of the parameters in Table 2.1 to generate a PSF cube across the full wavelength range. However, we find that this method leaves strong residual artifacts between the broad lines at which the PSF was extracted. This indicates that not all of the PSFAO19 parameters change smoothly with wavelength and only three broad lines are insufficient to constrain the exact wavelength-dependence.

An alternative approach involves a simple yet effective pixel-by-pixel interpolation of the hybrid PSF across the full wavelength range. Since  $H\beta$  and  $O\text{I}\lambda 8446 + \text{Ca}\text{II}\lambda 8498$  are close to the edges of the MUSE wavelength range, no significant extrapolation is required. As a first step, we normalized the hybrid PSFs extracted at  $H\beta$ ,  $H\alpha$ , and  $O\text{I}\lambda 8446 + \text{Ca}\text{II}\lambda 8498$  to their peak flux. For each of the spaxels, we describe the wavelength dependence of the flux with a third-order polynomial. Consequently, the PSF cube equals the available empirical PSF at the positions of the broad lines. The interpolated PSF cube was then scaled in the central spaxel to match the flux of the QSO spectrum.

### Iterative AGN-host Deblending from the IFU data

We now want to deblend the AGN from the host emission. By construction, the PSF cube contains the faint but non-negligible emission from the host in the central pixel. Therefore, the subtraction from the original datacube causes an over-subtraction in the center. We followed the AGN-host deblending approach described in Husemann et al. (2022) where the AGN spectrum was iteratively corrected for the host galaxy contribution. Thereby we assumed a constant host galaxy surface brightness within the innermost  $0''.5$  (corresponding to  $167\text{ pc}$  or  $0.08 r_e$ ).

The result of the iterative deblending process is displayed in Fig. 2.5. The  $3''$  aperture spectra show that the point-like AGN emission contains the entire broad-line emission and little to no contribution from narrow lines. This is because Mrk 1044 AGN is so luminous that it dominates over the narrow line emission on parsec scales. The host spectrum contains the stellar absorption and the spatially extended ionized gas emission in the form of narrow absorption and emission lines, respectively.

Most of our diagnostics in the following are based on emission lines in the  $H\beta$ -[O III] window. We therefore estimate the spatial resolution for

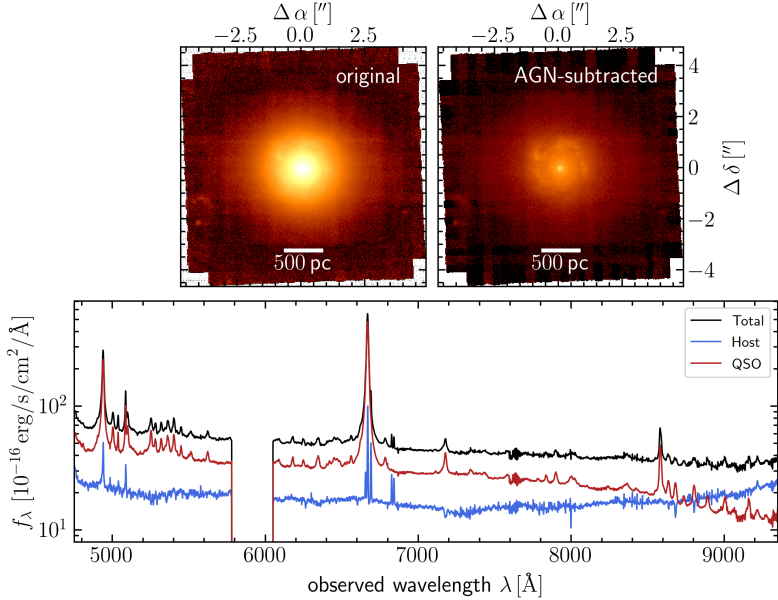


Figure 2.5: *Result of the iterative AGN-host deblending for Mrk 1044.* The bright point-like AGN emission distributes over the entire FOV of the data cube which is captured by the H $\alpha$  narrow-band images on the right. Both original (top left) and deblended host (top right) images share the same color-scaling, which demonstrates the successful deblending. The bottom panel shows the original blended spectrum (black) within a 3'' aperture centered on the QSO position. The AGN emission (red) contains the broad lines, whereas in the host galaxy spectrum (blue) only narrow emission lines are present.

the analysis from the PSF cube at H $\beta$  where the FWHM is 89 mas which corresponds to 30 pc in the galaxy system.

### 2.3 Analysis and Results

We aim to quantify the stellar and ionized gas properties from the IFU data and map them across the host galaxy. Following the AGN-host de-

blending described in the previous section, the subsequent analysis only employs the AGN-subtracted host emission.

### 2.3.1 Fitting the Stellar Continuum and the Ionized Gas Emission

For the extraction of the galaxy properties, we employed `PyParadise` (Husemann et al., 2016a, 2022) which is a publicly available<sup>5</sup> updated version of the stellar population synthesis fitting code `Paradise` (Walcher et al., 2015). It was extended by a Markov chain Monte Carlo (MCMC) algorithm to find the parameters of the line-of-sight velocity distribution (LOSVD) and a routine to fit the emission lines. The main steps involved are the following.

(1) As a first step, both the input spectra and the template library spectra were normalized by a running mean, where emission lines or strong sky line residuals were masked and linearly interpolated. This normalization has the advantage that the fitting result is less sensitive to nonphysical continuum variations caused by the wavelength interpolation of the PSF, especially near the nucleus (see Fig. 2.5).

(2) In the next step, `PyParadise` used an iterative scheme to independently determine the best-fit of the LOSVD and linear combination of simple stellar population (SSP) template spectra. Starting from an initial LOSVD guess obtained by fitting a single spectrum drawn from the template library, all spectra in the template library were convolved with the initial LOSVD guess to obtain the best-fit non-negative linear combination of template spectra. The resulting best-fit spectrum was used as input for further iterations and the two-step process of estimating the LOSVD and linear combination was repeated. For our analysis, we selected the CB09 SSP library, which is an updated version of the library presented in Bruzual & Charlot (2003a). The template metallicities range from  $[\text{Fe}/\text{H}] = -1.44$  to  $1.44$  and stellar ages from 1.7 Myr to 13 Gyr. The SSP spectra cover  $3500 \text{ \AA}$  to  $9500 \text{ \AA}$  at a spectral resolution of  $2.5 \text{ \AA}$ . Our results did not change within the uncertainties if we employed the higher-resolution SSP library from González Delgado et al. (2005).

(3) The final best-fit spectrum was denormalized and subtracted from the original spectrum.

---

<sup>5</sup><https://git.io/pyparadise>

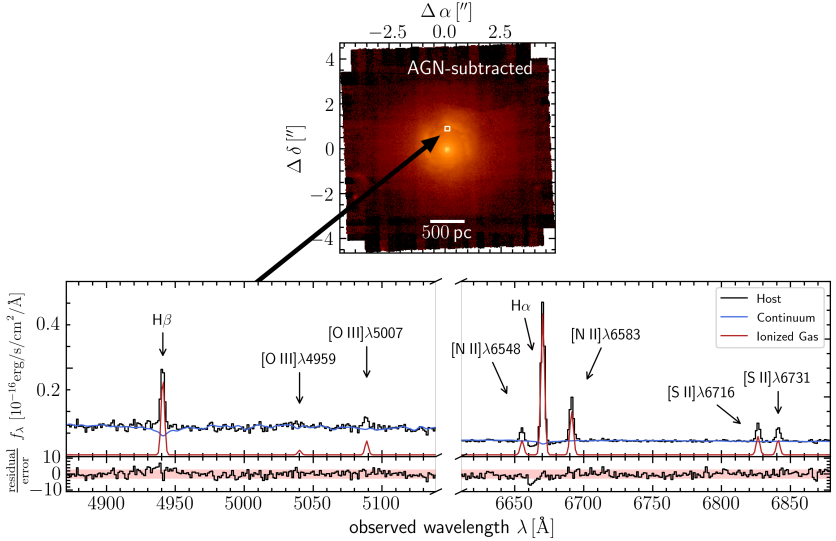


Figure 2.6: *Fitting of an example host spectrum with PyParadise.* The top panel shows an  $H\alpha$  narrow-band image of the AGN-subtracted host emission. An example  $8\times 8$ -binned spaxel is highlighted with a white square north of the nucleus. The corresponding host spectrum extracted from this aperture is shown in the bottom panel as a black line in the  $H\beta$  (left) and  $H\alpha$  window (right). Furthermore, we show the best-fit spectrum of the stellar continuum (blue) and the ionized gas contribution (red) which we obtained with PyParadise. The residuals show that the model reproduces the spectrum within the  $3\sigma$  confidence region.

(4) To model the emission lines from the residual spectrum, PyParadise used a set of Gaussian models with a common LOS velocity, taking into account the spectral resolution that is approximately constant with wavelength (see Sect. 2.2.3). For the doublet emission lines  $[N\ II]\lambda\lambda 6548,83$  and  $[O\ III]\lambda\lambda 4959,5007$ , we fixed the flux ratio to the theoretical prediction of 2.96 (Storey & Zeppen, 2000; Dimitrijević et al., 2007). Furthermore, we coupled the emission lines in radial velocity and velocity dispersion in order to increase the robustness of the flux measurement. Our results

did not change within the uncertainties if we did not kinematically tie the model parameters for emission lines with different ionization potentials.

Compared to the established pPXF software (Cappellari & Emsellem, 2004; Cappellari, 2017) which uses low-order polynomials to fit the stellar continuum, PyParadise allowed us to model the stellar absorption lines irrespective of the details of the PSF subtraction. In this way, we could robustly constrain the stellar kinematics close to the nucleus. In Fig. 2.6 we visualize an example spectrum from the MUSE data cube within a randomly selected aperture, together with the best-fit spectrum of the stellar continuum and the ionized gas emission.

For a large fraction of the spaxels, the S/N is too low to robustly model the low surface brightness emission lines and the faint stellar continuum emission. We therefore employed two spatial binning techniques that spatially coadd the spectra of the host data cube. For the stellar continuum, we used the adaptive Voronoi tessellation routine of Cappellari & Copin (2003) to achieve a minimum S/N=20 in the wavelength range  $5080 \text{ \AA} < \lambda < 5260 \text{ \AA}$ . We then modeled the binned stellar continuum spectra with PyParadise using the updated CB09 version of the evolutionary synthesis model spectra from Bruzual & Charlot (2003a) before projecting the stellar kinematics from the Voronoi grid onto the initial MUSE sampling grid. This information was then used to model the stellar emission again for each spaxel of the host data cube, but in this case keeping the stellar LOSVD parameters fixed. Finally, we spatially coadded  $2 \times 2$  and  $8 \times 8$  spaxels of the host data cube and fit the emission lines to the residual continuum spectra. The spatial binning allowed us to extract the emission line properties in regions that are more than one order of magnitude fainter than in the original data cube. We estimated the uncertainties for all emission line parameters with a Monte-Carlo approach. For a single spectrum we generated 40 artificial spectra by fluctuating the flux density within its errors. Subsequently, we conducted both stellar continuum and emission line fitting for the artificial spectra.

### 2.3.2 Mapping the Emission Line Properties

The surface brightness maps together with the velocity field and the dispersion are shown in Fig. 2.7. For the surface brightness maps, we only selected spaxels with  $S/N > 3$ , and an uncertainty of  $< 30 \text{ km s}^{-1}$  for both velocity and dispersion. For the high S/N regions, we overplotted the  $8 \times 8$

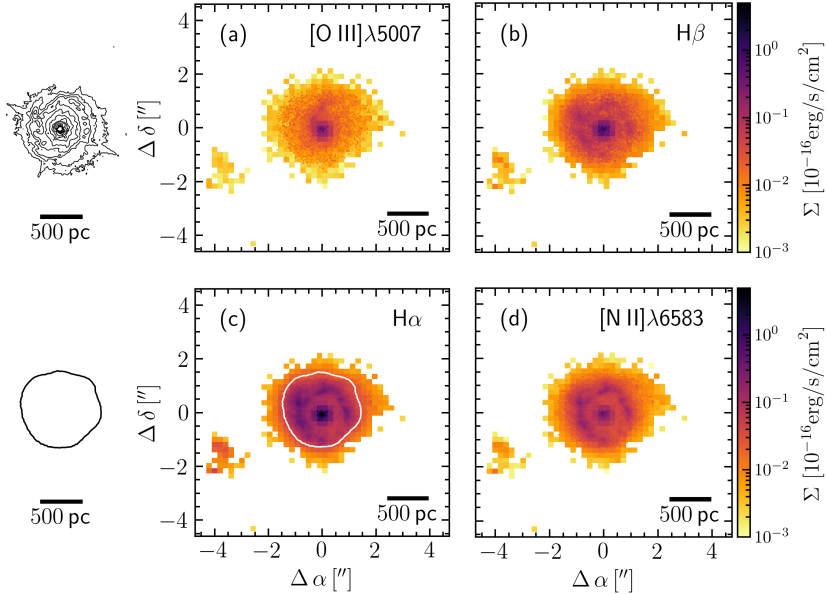


Figure 2.7: *Mapping the ionized gas properties of Mrk 1044.* The bottom-left panel contains the outer contours where  $H\alpha$  surface brightness exceeds  $3 \times 10^{-18} \text{ erg s}^{-1} \text{ cm}^{-2}$  which indicates the core region of enhanced narrow  $H\alpha$  emission. Here and in the following we show both contours as a reference for the size of the structures identified. The surface brightness maps for the prominent narrow emission lines after subtracting the AGN emission are shown in (a) - (d). The maps were spatially coadded by  $2 \times 2$  pixels and  $8 \times 8$  pixels for regions where the S/N of the emission line is  $< 3$ .

binned map with the  $2 \times 2$  binned spaxels. The emission from the narrow lines is mostly concentrated in a nearly circular patch around the nucleus. Beyond  $\sim 800$  pc from the center, the signal from the emission lines is too weak to be robustly modeled. Within the patch, we detected a pronounced ring-like structure that is present in the  $H\beta$ ,  $H\alpha$ , and  $[N II] \lambda 6583$  emission. The ring structure is most prominent in the  $H\alpha$  emission. Since the inclination of the galaxy disk is  $67^\circ$  (Powell et al., 2018), the deprojected ellipse has an axis ratio of 2.45. The size of the ring is comparable to the

extent of the luminous inner region in the HST WFC3/UVIS image, for which we show the contours in the top-left panel of Fig. 2.1.

For each of the surface brightness maps, the peak emission stems from near the nucleus. The associated high velocity and the high dispersion in that region indicate an outflowing component. We note that although the AGN-host deblending algorithm is capable of subtracting any compact emission, it is only a first-order subtraction of the point-like emission. As demonstrated by Singha et al. (2022), the region near the nucleus may require a more complicated modeling with multiple narrow line emitting structures. Here and in the following analysis, we exclude the emission from the innermost  $0''.5$  (160 pc). A detailed analysis and discussion of Mrk 1044's outflow will instead be presented in Winkel et al. (in prep.). Ignoring the high velocity and dispersion feature in the center, the velocity field exhibits a smooth rotational field across the MUSE NFM FOV. The median dispersion of  $\sigma = 34.9 \text{ km s}^{-1}$  is fairly small, indicating dynamically cold ionized gas.

### Excitation Mechanism

From the emission line ratios, the underlying excitation mechanism can be identified, that is to say SF ionization in H II regions, as well as photoionization by the hard radiation field of an AGN and low-ionization nuclear emission-line regions (LINERs). A commonly used demarcation is made in the Baldwin-Phillips-Terlevic diagram (BPT, Baldwin et al., 1981) which uses the  $[\text{O III}]/\text{H}\beta$  versus  $[\text{N II}]/\text{H}\alpha$  line ratios. The upper-right panel of Fig. 2.8 shows the BPT diagram for the  $8 \times 8$  binned spaxels. All spaxels are associated with a cloud that spreads over the star-forming domain but is elongated toward the AGN-ionized region. The scatter originates from the finite spatial resolution of 30 pc which does not allow one to resolve individual star-forming clouds. Together with the LOS projection, different ionization conditions are inevitably captured within one spaxel. Furthermore, different ISM metallicities and densities lead to the star-forming cloud occupying a large area in the BPT diagram (e.g., Smirnova-Pinchukova et al. 2022). Nonetheless, the vast majority of spaxels in the MUSE NFM FOV is consistent with excitation through SF. We therefore assume the AGN contribution in terms of ionizing radiation to be negligible.

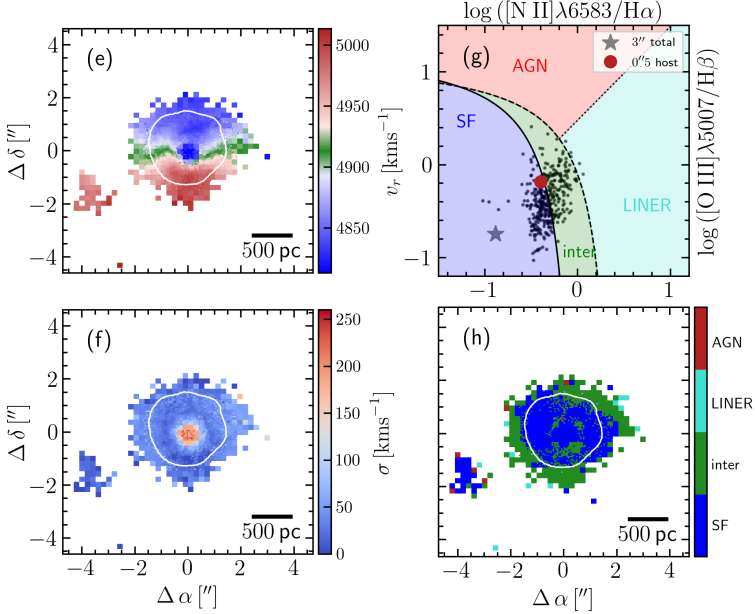


Figure 2.8: *Emission line diagnostics for the center of Mrk 1044's host galaxy.* The LOS velocity (e) and velocity dispersion (f) of Mrk 1044's ionized gas appear quiescent. Panel (g) shows the BPT diagram for Mrk 1044's central region for  $8\times 8$  spatially coadded spaxels. The gray star shows Mrk 1044's position based on its AGN-contaminated  $3''$  aperture spectrum. The empirical demarcation lines from Kauffmann et al. 2003 (continuous), Kewley et al. 2001 (dashed), and Cid Fernandes et al. 2010 (dotted) define classifications as star-forming, composite (inter), and low-ionization nuclear emission region (LINER) and AGN-ionized regions, respectively. Already the AGN-blended  $3''$  spectrum is located in the star-forming regime. For the AGN-subtracted cube, all spaxels as well as the  $0.5''$ -integrated host component are consistent with excitation by SF. Panel (h) shows the spatial distribution of the excitation mechanism. Mrk 1044 is ionized by SF, even in the immediate vicinity of its nucleus.

The spatial distribution of the excitation mechanism is shown in the bottom-right panel of Fig. 2.8. Interestingly, the spaxels classified as composite are located toward the outskirts of the bright H $\alpha$  ring. This could either be caused by evolved stars during the short yet energetic post-AGB phase which mimic the LINER emission (Binette et al., 1994; Stasińska et al., 2008), or leaking photons from HII regions plus starburst-driven shocks (Heckman, 1980; Dopita & Sutherland, 1996). More strikingly, it becomes evident that even in the very center of Mrk 1044, SF appears to be the dominant excitation mechanism in the host. Since the inner region is dominated by an outflow, we followed the procedure described in Singha et al. (2022) and used a two-component Gaussian model to fit the central 0''5-integrated host spectrum. The resulting BPT classification for the host component is consistent with the single-component analysis of the individual spaxels (see Fig. 2.8) which confirms the success of our AGN-host deblending process.

Excitation by SF close to the nucleus contradicts the findings in nearby active galaxies where the high AGN-ionization is typically found close to the nucleus (Davies et al., 2014; Richardson et al., 2014). This is particularly interesting given Mrk 1044's super-Eddington accretion rate. At such high luminosities, quasar mode feedback is expected to drive galactic scale outflows through radiation pressure from the active nucleus (Nesvadba et al., 2007; Liu et al., 2013; Ciccone et al., 2018). However, Mrk 1044's host does not exhibit any sign of interaction with the AGN photo-ionization field  $< 1$  kpc, despite the current AGN phase. If its BLR was obscured, Mrk 1044 would be identified as a star-forming galaxy. Moreover, the line ratios from the AGN-contaminated 3''-aperture spectrum clearly place Mrk 1044 in the star-forming regime (top-right panel of Fig. 2.8). There exist several examples of X-ray selected obscured AGN that appear optically inactive (XBONG galaxies, e.g., Severgnini et al., 2003; Caccianiga et al., 2007; Trump et al., 2009) and star-forming in their diagnostic line ratios (Hornschemeier et al., 2005). Castelló-Mor et al. (2012) have shown X-ray bright galaxies that are optically classified as star-forming are mostly NLS1s. This suggests that Mrk 1044 could be a prototype of many accretion-mode AGN at high redshift that are difficult to identify since their spatially unresolved narrow line ratios classify them as star-forming galaxies.

### Circumnuclear Star Formation

The star formation rate (SFR) is an important parameter for understanding the interaction between the central AGN and its host galaxy. The surface brightness maps derived in the previous section allowed us to map the current SFR surface density  $\Sigma_{\text{SFR}}$  with high spatial resolution.

As a first step, we had to correct the H $\alpha$  flux for foreground dust attenuation along the LOS. Assuming case B recombination at an electron temperature  $T_e = 10^4$  K and electron density  $n_e = 100 \text{ cm}^{-3}$ , the intrinsic Balmer ratio is 2.86 (Osterbrock, 1989). The nebular colour excess can be estimated from the Balmer decrement as

$$E(B - V) = \frac{E(\text{H}\beta - \text{H}\alpha)}{\kappa(\lambda_{\text{H}\beta}) - \kappa(\lambda_{\text{H}\alpha})} \times \log\left(\frac{F_{\text{H}\alpha}/F_{\text{H}\beta}}{2.86}\right) \quad (2.1)$$

$$= 1.97 \times \log\left(\frac{F_{\text{H}\alpha}/F_{\text{H}\beta}}{2.86}\right). \quad (2.2)$$

Here,  $\kappa(\lambda_{\text{H}\beta})$ ,  $\kappa(\lambda_{\text{H}\alpha})$  is the reddening curve for star-forming galaxies from (Calzetti et al., 2000, hereafter C00) evaluated at H $\beta$  and H $\alpha$ , respectively. Using the C00 reddening curve, the dust extinction at wavelength  $\lambda$  was connected to the colour excess by

$$A_\lambda = \kappa(\lambda) \times E(B - V) \quad (2.3)$$

$$A_{\text{H}\alpha} = (3.33 \pm 0.80) \times E(B - V). \quad (2.4)$$

With the above relation, we corrected the H $\alpha$  luminosity as

$$L_{\text{intr}}(\text{H}\alpha) = L_{\text{obs}}(\text{H}\alpha) \times 10^{\frac{A_{\text{H}\alpha}}{2.5}}. \quad (2.5)$$

Following the argument from the previous section, we assumed that all of the extinction-corrected H $\alpha$  luminosity is generated by SF ionization. We then computed the SFR using the relation from Calzetti et al. (2007) (C07), which was calibrated for nearby star-forming galaxies assuming a constant SFR over 100 Myr

$$\text{SFR}/M_\odot\text{yr}^{-1} = 5.3 \times 10^{-42} L_{\text{intr}}(\text{H}\alpha)/\text{erg s}^{-1}. \quad (2.6)$$

This calibration applies for the default two power law stellar IMF from Starburst99 (Leitherer et al., 1999). Moreover, it contains the underlying

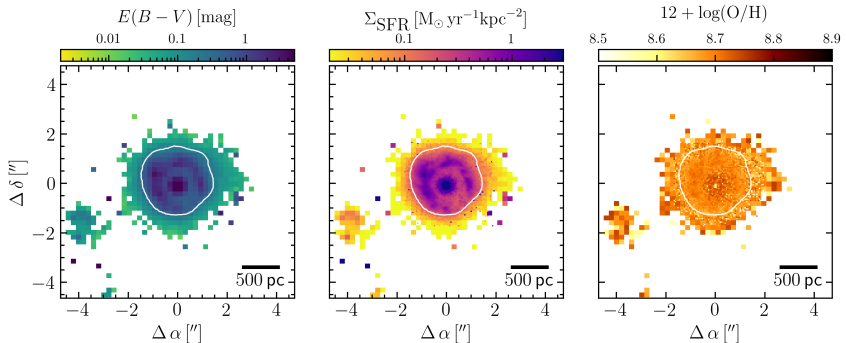


Figure 2.9: *Mapping the SFR in the vicinity Mrk 1044’s nucleus.* From left to right the panels show (1) the HST/UVIS contours, (2) Mrk 1044’s extinction map, (3) the SFR surface density and (4) the gas-phase metallicity. The contour of the  $H\alpha$  ring is over-plotted in white. While both extinction and SF are concentrated in a circumnuclear ring, the chemical composition of the ionized gas is homogeneous within the inner 1 kpc.

assumption that the ISM has solar metallicity. For a robust measure of the  $\Sigma_{\text{SFR}}$ , we imposed a minimum S/N for both  $H\beta$  and  $H\alpha$  line fluxes. Furthermore, we selected  $E(B - V) = 0$  for spaxels with  $F_{H\alpha}/F_{H\beta} < 2.86$ . After applying these criteria, the selected  $8 \times 8$  binned spaxels sampled the entire star-forming ring such that we did not lose flux when computing integrated properties of the star-forming ring.

The left panel of Fig. 2.9 shows that the extinction is particularly high in the ring of enhanced  $H\alpha$  emission. Within the  $H\alpha$  contour (and excluding the innermost 0’5, see Sect. 2.3.2), the median extinction is 0.65 mag, indicating a significant abundance of dust along the LOS. This coincides with the presence of dusty spiral absorption features in the HST WFC3 image (Fig. 2.1). As shown in the right panel of Fig. 2.9, the  $H\alpha$  ring shows a particularly high SFR surface density. The azimuthally averaged peak SFR located at a projected radius of  $r = (306 \pm 43)$  pc. Taking the galaxy inclination of  $67^\circ$  into account, the deprojected structure is an ellipse with an axis ratio of 2.45. We therefore refer to the circumnuclear region of enhanced SFR as the circumnuclear ellipse (CNE). As before,

we excluded the innermost 0".5 when computing integrated properties of the CNE.

The average  $\Sigma_{\text{SFR}}$  within the CNE is  $0.16 \pm 0.04 \text{ M}_{\odot} \text{ yr}^{-1} \text{ kpc}^{-2}$ , as computed from the integrated extinction-corrected H $\alpha$  flux. This value lies significantly above the minimum of  $10^{-3} \text{ M}_{\odot} \text{ yr}^{-1} \text{ kpc}^{-2}$  for driving galactic winds (Veilleux et al., 2005) and is typical of circumnuclear star formation bursts (Kennicutt, 1998; Kennicutt & De Los Reyes, 2021). It is comparable to the lower end of the  $\Sigma_{\text{SFR}}$  in ultra-luminous infrared galaxies (ULIRGS) that host the most powerful starbursts known (Dopita et al., 2002; Genzel et al., 2010).

For typical star-forming spiral galaxies with  $\Sigma_{\text{gas}} = 10 \text{ M}_{\odot} \text{ pc}^{-2}$ , the Kennicutt-Schmidt law predicts  $\Sigma_{\text{SFR}} = 6 \times 10^{-3} \text{ M}_{\odot} \text{ yr}^{-1} \text{ kpc}^{-2}$ . Following the same procedure as for the CNE, we used the MUSE WFM data cube to compute the galaxy-wide SFR surface density of  $\Sigma_{\text{SFR}} = (5.9 \pm 1.0) \times 10^{-3} \text{ M}_{\odot} \text{ yr}^{-1} \text{ kpc}^{-2}$ . We estimated an integrated value of  $\text{SFR}_{\text{tot}} = 0.70 \pm 0.17 \text{ M}_{\odot} \text{ yr}^{-1}$ . This value is consistent with  $\text{SFR} = 0.6 \pm 0.2 \text{ M}_{\odot} \text{ yr}^{-1}$  estimated by Smirnova-Pinchukova et al. (2022) who used the integrated IR luminosity. While the galaxy-wide value SFR places Mrk 1044 among the star-forming population, it is evident that the inner star-forming ellipse with  $\text{SFR}_{\text{CNE}} = 0.19 \pm 0.05 \text{ M}_{\odot} \text{ yr}^{-1}$  accounts for 27% of the absolute galaxy SFR.

### Metallicity of the Starforming CNE

Another important characteristic of the ionized gas is the metallicity. In contrast to the SFR, which traces short-lived ( $\sim 5 \text{ Myr}$ ) emission from H II regions, the gas-phase metallicity provides a cumulative measure for the enrichment history of the ISM. Furthermore, in- and outflows can affect the chemical composition of gas on short timescales. The gas-phase metallicity therefore provides an important diagnostic to constrain its origin and motion.

There exist several metallicity indicators that are based on the line ratios emitted by H II regions. Since Mrk 1044's star-forming CNE is completely consistent with excitation by SF, we can use strong line ratios covered by the MUSE wavelength range to estimate the gas-phase metallicity. The N2S2 index defined as  $\text{N2S2} = \log ([\text{N II}]\lambda 6583 / [\text{S II}]\lambda\lambda 6717, 31)$  has proven to be a reliable indicator for the O/H abundance ratio (Dopita et al., 2016).

We used N2S2 index calibration established in [Husemann et al. \(2019\)](#). Since the O/H abundance is significantly dependent on the empirical calibration adopted ([Kewley & Ellison, 2008](#)), we used the emission line ratios of star-forming galaxies in the SDSS DR7 value-added catalog by [Brinchmann et al. \(2004\)](#) to determine a N2S2-calibration of

$$12 + \log(\text{O}/\text{H}) = 8.960 + 0.873 \times \text{N2S2} - 0.610 \times \text{N2S2}^2. \quad (2.7)$$

We thus have a self-consistent measure based on the metallicities from [Tremonti et al. \(2004\)](#). Our results do not change within the uncertainties when we used the  $\text{O3N2} = \log\{([\text{O III}]\lambda 5007/\text{H}\beta)/([\text{N II}]\lambda 6583/\text{H}\alpha)\}$  indicator instead.

The right panel of [Fig. 2.9](#) shows the gas-phase metallicity of Mrk 1044's inner region. In contrast to the extinction and the SFR surface density, the metallicity does not exhibit a ring-like structure. Within the star-forming CNE it is fairly constant with a median value of  $12 + \log(\text{O}/\text{H}) = 9.07$ . The scatter of the O/H abundance (0.02 dex) is smaller than the scatter of N2S2-O/H relation (0.06 dex), suggesting homogeneous properties of the ISM across the CNE. For the material in the turbulent ISM of the CNE, we estimated an upper limit for the dynamical time by comparing the CNE size  $d$  ( $2\times$  the semi-minor axis) with the median ionized gas dispersion  $\sigma_{\text{gas}} = 75 \pm 2 \text{ km s}^{-1}$

$$t_{\text{dyn}}(\text{CNE}) \sim \frac{d}{\sigma_{\text{gas}}} = 8 \text{ Myr}. \quad (2.8)$$

The dynamical time estimate is comparable to the timescale of ISM enrichment by massive stars, indicating that the ISM is well mixed on  $< 1 \text{ kpc}$  scales. However, the CNE may be affected from gas in- and outflows occurring on longer timescales. We therefore interpret the constant gas-phase metallicity to be a signature of a homogeneous enrichment process through the ongoing starburst.

### 2.3.3 Kinematic Modeling

To investigate whether the gas and stellar motion are consistent with dynamically cold rotation on a circular orbit, we used a simple model to fit the 2D velocity maps extracted in [Section 2.3.1](#). We shall consider the

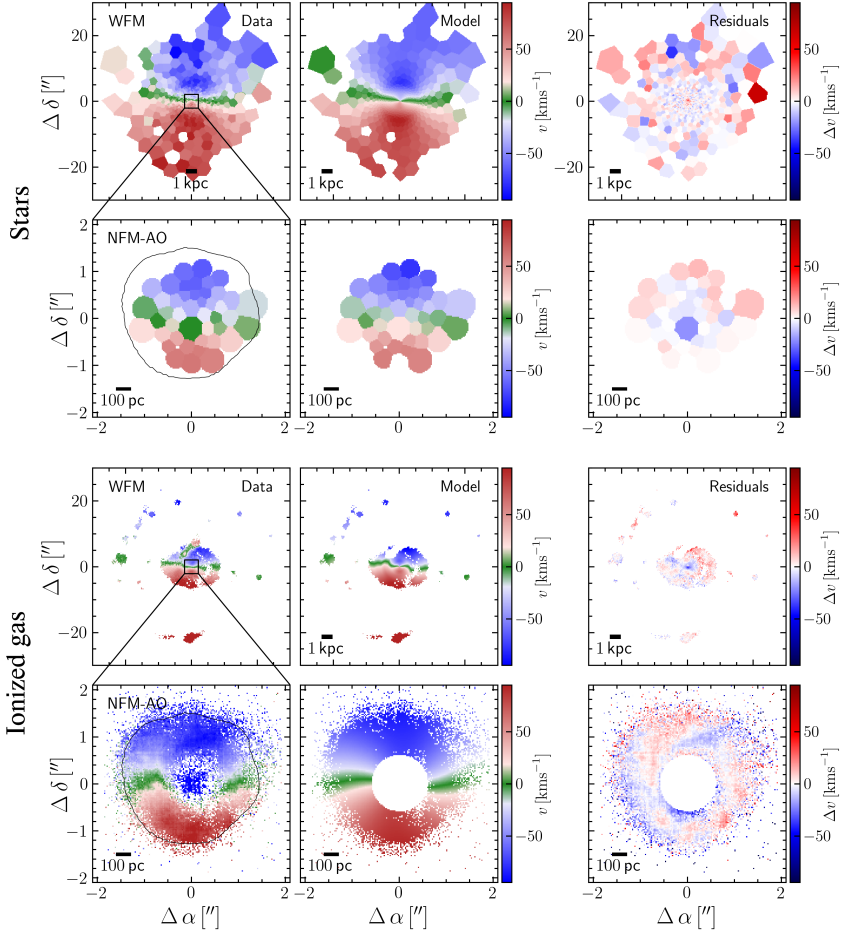


Figure 2.10: *Modeling the stellar and ionized gas velocity field.* For each ionized gas and stellar kinematics, the panels are organized as follows: From left to right, the panels show (1) Mrk 1044’s stellar and ionized gas velocity field; (2) the kinematic model of a thin rotating disk; and (3) the difference between the observed and model velocity field. Top panels show the MUSE WFM data and the bottom panels the zoom-in onto the NFM-AO data. Both the stellar and ionized gas are well reproduced by the thin rotating disks, but clumpy structures in the velocity residuals of the ionized gas are highlighted in Fig. 2.12.

first moment of the LOSVD, the intensity-weighted mean velocity, which we assume to trace the material in a thin disk. If the inclination of the system  $i$  is unknown, the projected velocity of a circular orbit in the plane of the galaxy can be expressed through the azimuthal angle  $\phi$  measured from the projected major axis in the galaxy plane:

$$v_r = v_{sys} + v \sin i \times \cos(\phi + \text{PA}) \quad (2.9)$$

$$= v_{sys} + v \sin i \times \cos\left(\arctan\left(\frac{y - y_c}{x - x_c}\right) + \text{PA}\right). \quad (2.10)$$

Here,  $v_{sys}$  is the systemic velocity, PA is the position angle of the rotation axis, and  $(x, y)$  are the Cartesian coordinates in the observed plane with the galaxy center located at  $(x_c, y_c)$ . We assumed the AGN position to be the same as the kinematic center of the circular motion. Furthermore, we adopted the inclination of the disk  $i = 67.4 \pm 4.5^\circ$  computed by Powell et al. (2018). Thus, our analytic model consists of three free parameters ( $v_{sys}, \text{PA}, v$ ) for which we determined the best-fit values using the Bayesian MCMC software `GAStimator`<sup>6</sup>. This algorithm maximizes the log-likelihood of the residuals between the observed and the model LOSVD. In order to trace the rotation curve  $v(r)$ , we sampled the FOV with concentric rings within which the model was evaluated. We chose their radial width to equal the FWHM of the PSF, that is  $1''03$  for MUSE WFM and  $89 \text{ mas}$  for NFM-AO, respectively. Finally, we assumed a smooth rotation curve by radially interpolating the parameters (PA,  $v$ ) to compute the model velocity in each pixel.

### Kinematics of the Stellar Component

Although the stars are likely to have significant pressure support, we conduct a simple experiment here by assuming purely circular motions. The stellar emission is spatially binned such that the stellar continuum reaches  $S/N \geq 20$  as described in Sect. 2.3.1. Since the bin size varies across the FOV, we discretize the model by projecting it onto the Voronoi grid and taking the average velocity within each bin. We then use this information to maximize the log-likelihood of the LOSVD.

<sup>6</sup><https://github.com/TimothyADavis/GAStimator>

The top panels of Fig. 2.10 show the stellar velocity field together with the best-fit model and the residuals. Both observations from MUSE WFM and NFM-AO show a smooth rotational pattern that ranges from the smallest resolved scales of  $\sim 100$  pc to galaxy scales  $\sim 20$  kpc. The thin rotating disk model reproduces this pattern well as we do not see systematic extended structures in the residual map. This indicates that the stellar velocity field is largely unperturbed, justifying our initial (simplistic) assumption of circular orbits for the stellar rotation. Approaching the center, the stars have decreasing rotational velocity  $v$ , while the PA stays constant. This is compatible with the quiescent rotating velocity field of a disk galaxy that is dominated by the gravitational potential of the host galaxy alone.

### Kinematics of the Ionized Gas

Compared to the stellar rotation, the ionized gas rotates significantly faster than the stellar component as shown in Fig. 2.11. Since the stars experience pressure support from their velocity dispersion, their motion in a disk system is not described by circular orbits. The higher rotational velocity of the ionized gas component is a reflection of this effect, the so-called asymmetric drift.

We modeled the ionized gas velocity on the native MUSE pixel sampling since the velocities measured from the high S/N emission lines are well constrained. Since the high velocity gas in the center is clearly not associated with the rotating disk of the host, we used a circular aperture to mask the pixels in the innermost  $0''.5$ . Furthermore, the ionized gas velocity field captured by MUSE WFM exhibits an arc-shaped stream perpendicular to the galaxy disk that stretches from 1.3-4 kpc. Powell et al. (2018) suggest that this "bloom" was first ejected by the high star formation surface density in Mrk 1044's CNE. Since it does not corotate with the galaxy disk, we also excluded this feature from the model.

Apart from the two features that we manually excluded, the ionized gas velocity field appears quiescent, indicating an undisturbed rotational motion. The bottom-right panels of Fig. 2.10 show that on galaxy scales, the ionized gas is surprisingly well described by the disk rotation. Only within the innermost 1 kpc did we detect spatially extended structures in the velocity residuals that coincide with the location of the star-forming CNE. We highlight these extended structures in Fig. 2.12, where the ionized

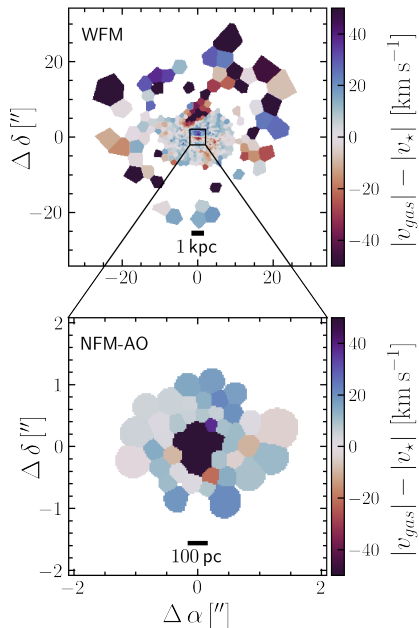


Figure 2.11: *Difference between Mrk 1044’s gas and stellar velocity field.* MUSE WFM is shown in the top panel, data from NFM-AO in the bottom panel. Except for the high velocity bloom that stretches  $\sim 5''$ - $15''$  north from the center, the gas rotates faster than the gravitationally driven motion of the stellar component.

gas velocity residuals show both receding and approaching components with a spiral-like shape. We selected two prominent patches which were obtained from smoothing the map with a Gaussian kernel of 3 px and imposing a minimum velocity of  $\pm 3 \text{ km s}^{-1}$ . The contours of the smoothed map together with the original map are shown in Fig. 2.12. The size and orientation of the clumps coincide with the direction and extent of the spiral pattern of the dust absorption seen in the HST WFC3 image (see left panel of Fig. 2.1). The arcs reach from 400 pc to 150 pc toward the central region as highlighted in Fig. 2.12. Both regions are ionized by SF and have symmetric line shapes which indicate that the velocity residuals

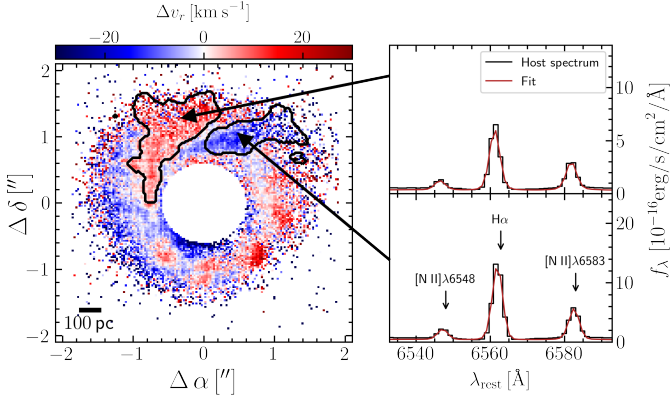


Figure 2.12: Zoom-in onto the residual gas velocity clumpy structures.  $\Delta v_r$  is shown after subtracting the rotating thin disk model. The contours highlight spaxels of the smoothed map (see text) and correspond to an approaching (blue) and receding (red) clump, respectively. The panels on the right show the rest-frame spectra of the host in the  $\text{H}\alpha + [\text{N II}]$  region, integrated over the respective patch. The emission lines have a symmetric shape and are well reproduced by the fit, indicating a genuine shift of the velocity residuals  $\Delta v_r$ .

are genuine rather than artifacts from fitting asymmetric emission lines. The approaching region has a median velocity offset of  $\Delta v_r = 5.9 \text{ km s}^{-1}$  and the receding region  $\Delta v_r = -7.0 \text{ km s}^{-1}$ . Clump-like structures are typical signatures of radial streaming motions within the disk, likely due to slow inflow in the disk plane.

Fig. 2.13 shows the radial dependence of the kinematic parameters measured with the rotating disk model. As expected for an inclined rotating disk, the rotational velocity increases with increasing distance from the center up to a maximum value of  $v_{\text{gas}} \approx 100 \text{ km s}^{-1}$  (gas) and  $v_{\star} \approx 80 \text{ km s}^{-1}$ , respectively, before the rotation curve flattens. The model also confirms that the ionized gas rotates faster at all radii as is expected due to the asymmetric drift (see Fig. 2.11).

Gadotti et al. (2020) report that the nuclear disks have larger rotational support as compared to the underlying main disk. For Mrk 1044, we recognize a velocity jump around  $\sim 200 \text{ pc}$  where both the ionized gas and the stellar rotation appear to rotate faster in the CNE. However, due to

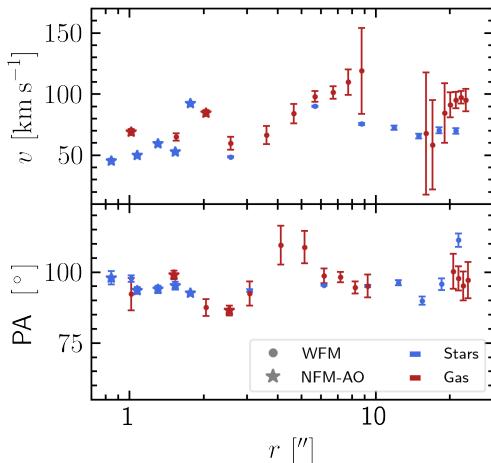


Figure 2.13: *Radial dependence of the rotating disk model parameters.* Both model parameters of the galaxy stellar (blue) and ionized gas (blue) velocity field are shown. The data points acquired from the MUSE NFM-AO observations are shown as stars and have errors smaller than the size of the symbol. The data points from MUSE WFM are shown as errorbars. From  $0''.8$  to  $25''$ , the PA of the disk-like rotation is constant and matches between ionized gas and stars. For both, the rotational velocity increases from the center up to  $\sim 6''$  before it flattens out.

the seeing-limited resolution of the MUSE WFM data of  $\text{FWHM}=1''.03$ , the rotation velocity in the innermost  $\sim 330$  pc is underestimated due to beam smearing. Only MUSE NFM-AO allows one to resolve the stellar motion on scales of the CNE, but it does not have the coverage to compare the nucleus with the galaxy on larger scales. Thus, the velocity jump could also be caused by the different resolution of MUSE WFM and NFM-AO. Within the uncertainties, the PA of the rotational axis is constant across the whole galaxy. The median values of  $\text{PA}_* = 95.2 \pm 2.4^\circ$  and  $\text{PA}_{\text{gas}} = 99.0 \pm 16.2^\circ$  indicate that both stellar and gas rotation are aligned. Altogether, Mrk 1044’s kinematics are quiescent. The smooth radial behavior of the kinematic parameters indicates that Mrk 1044 does not currently experience major interactions with a companion or external disturbances.

## 2.4 Discussion

Despite its super-Eddington accretion rate, Mrk 1044 shows an unperturbed, rotation-dominated velocity field. Moreover, there is no close companion visible in continuum light that could trigger a nuclear starburst or AGN activity. Alternatively, intrinsic processes could be responsible for the enhanced star formation activity near the nucleus.

### 2.4.1 Star Formation as Potential Driver for AGN Fueling

Contradictory results regarding the connection between SF and AGN have been reported in the literature. While some authors claim a correlation between global SFR and AGN luminosity (e.g., Bonfield et al., 2011; Rosario et al., 2012; Chen et al., 2013; Xu et al., 2015; Lanzuisi et al., 2017; Stemo et al., 2020), others find only weak or no correlation (Baum et al., 2010; Rosario et al., 2013; Azadi et al., 2015; Stanley et al., 2015, 2017). This discrepancy can partially be explained by the different timescales of SF and AGN variability and the fact that the time-delay to trigger SF is typically longer than the AGN duty cycle (Silk, 2013; Zubovas et al., 2013; Harrison et al., 2021). In addition, different spatial scales over which galaxy integrated properties are measured ( $\sim 10$  kpc) compared to the BH accretion disk ( $< 1$  pc) add further scatter to the correlation.

The importance of the distance on which AGN affect their hosts has been pointed out by Volonteri et al. (2015), who used a suite of hydrodynamical simulations to compare the BHAR with the galaxy SFR on different spatial scales. We show their results together with Mrk 1044's position in Fig. 2.14. In their simulations, Volonteri et al. (2015) describe galaxies as isolated ("stochastic" phase), during a "merger" that lasts  $\sim 0.2 - 0.3$  Gyr, or in the "remnant" phase. Their simulations predict that, in contrast to the works by Mullaney et al. (2012) and Chen et al. (2013), the galaxy-wide SFR is uncorrelated with BHAR. Instead, only the nuclear ( $\sim 100$  pc) SFR correlates with BHAR. Mrk 1044 is in-line with this prediction. We have shown that on galaxy scales, the star-forming CNE contributes a significant part of the total SFR which pushes Mrk 1044 into the merger regime. On nuclear scales, however, the CNE in Mrk 1044 follows the  $\text{SFR}_{100 \text{ pc}}\text{-BHAR}$  correlation. Volonteri et al. (2015) further find that nuclear SFR and BHAR variations have similar amplitudes and both vary on similar timescales.

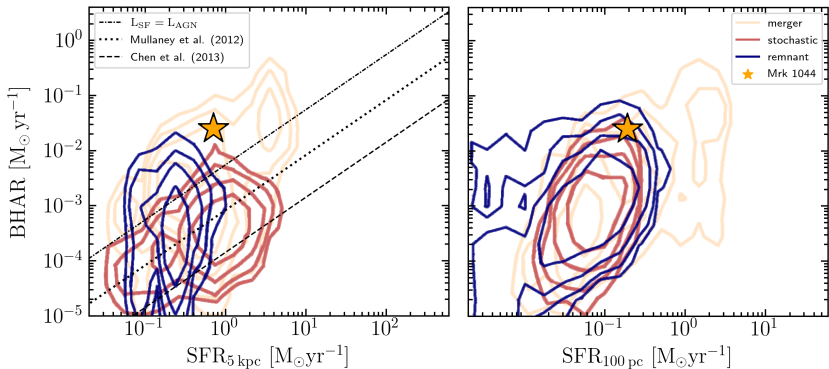


Figure 2.14: Comparison of Mrk 1044’s BHAR and SFR on different spatial scales with theoretical predictions. The contours are taken from Volonteri et al. (2015) and describe the BHAR during a merger (blue), stochastic (red), and remnant (yellow) phase, respectively. The lines represent the relations between galaxy-scale SFR and BHAR from Mullaney et al. 2012 (mass-selected galaxies, dotted line) and Chen et al. 2013 (star-forming galaxies, dashed). The dash-dotted line marks the line that separates AGN- and SF-dominated regions. On galaxy scales, Mrk 1044 has a high SFR comparable to that of merging galaxies. In the center, the high SFR of Mrk 1044’s CNE follows the predicted correlation with BHAR.

These results are supported by starbursts observed in the inner regions of nearby Seyfert 1s where the starburst intensities increase with AGN luminosity and Eddington ratio (Imanishi & Wada, 2004; Davies et al., 2007; Watabe et al., 2008; Diamond-Stanic & Rieke, 2012). In this regard, Mrk 1044 represents an extreme example where the high SFR surface density coincides with a phase of strong nuclear activity. The critical question is whether both processes are physically connected.

### SFR versus BHAR

Since a substantial fraction of Mrk 1044’s galaxy-wide SF is concentrated in a circumnuclear ellipse, we want to find out whether it can explain the enhanced BHAR. Assuming that in Mrk 1044’s star-forming CNE mas-

sive stars quickly return their material to the ISM through stellar winds and supernovae (SNe), we can compare the mass fluxes from SF and BH accretion.

We would like to note that H $\alpha$  nebular emission arises from the recombination of gas ionized by O- and early-type B-stars with  $M_{\star} \gtrsim 20 M_{\odot}$  (Peters et al., 2017). Due to their short lifetime, the presence of H $\alpha$  emission implies ongoing SF within the last 5 Myr. We assume that the lifetime of the massive stars is short compared to the total duration of the present-day star formation activity, that is to say they instantaneously return their material to the ISM, except for a remnant mass  $M_r$ . We adopted the metallicity-dependent compact remnant mass function from Fryer et al. (2012, eq. 5,7 and 9). Due to the vast abundance of molecular hydrogen in the host galaxy ( $4 \times 10^8 M_{\odot}$ , Bertram et al. 2007), we assume a constant SFR that equals the present-day value of  $0.19 M_{\odot} \text{yr}^{-1}$  estimated in Sect. 2.3.2. We can express the rate of enriched material that fading stars return into the ISM as

$$\dot{M}_{\text{SNe}} = \int_{m_{\min}}^{m_{\max}} [m - M_r] \times \text{SFR} \times \xi(m) dm, \quad (2.11)$$

where  $\xi(m)$  is the initial mass function (IMF) and  $\text{SFR} \times \xi(m)$  corresponds to the birth rate of stars with mass  $m$ . We chose a minimum mass of  $m_{\min} = 8 M_{\odot}$  for stars that enrich the ISM on the relevant timescale  $\sim 10$  Myr. Further, we assumed a default Starburst99 IMF (Leitherer et al., 1999) from  $0.1 M_{\odot}$  to  $100 M_{\odot}$  and metal-rich gas ( $Z/Z_{\odot}=2$ ) to estimate the mass ejection rate from stellar winds with Eq. 2.11:

$$\dot{M}_{\text{SNe}} = 3.6 \times 10^{-2} M_{\odot} \text{yr}^{-1}. \quad (2.12)$$

Using Mrk 1044's bolometric luminosity  $L_{\text{bol}} = (1.4 \pm 0.2) \times 10^{44} \text{ erg s}^{-1}$  reported in Husemann et al. (2022) and a radiative efficiency of  $\eta = 0.1$ , we estimated the black hole accretion rate (BHAR)

$$\dot{M}_{\text{BH}} = \frac{L_{\text{bol}}}{\eta c^2} = 2.5 \times 10^{-2} M_{\odot} \text{yr}^{-1}. \quad (2.13)$$

Under the above assumptions, the present-day net mass flux from stellar winds and SNe in the CNE exceeds the current BHAR by a factor of 1.5. Since we have not made a geometric assumption, comparing both

quantities requires that all stellar ejecta remain within the CNE and that they are channeled toward the accretion disk, which may not be the case in reality. We also note that choosing a higher  $\eta$  that is typical of high accretion rates (Ohsuga et al., 2005; McKinney et al., 2015) reduces the BHAR. Nonetheless, our simple model supports the scenario where the SF in the circumnuclear ellipse drives the high accretion rate of Mrk 1044.

### Lifetime of the CNE Star Formation

The abundance of dense molecular gas from which the stars are formed correlates with the BHAR (Izumi et al., 2016; Shanguan et al., 2020). Theoretical models suggest a physical connection between molecular gas abundance and BHAR on scales of a few 100 pc down to the accretion disk, independent of galaxy-scale processes (Umemura et al., 1997; Thompson et al., 2005; Kumar & Johnson, 2010).

We can estimate the maximum duration of the BH growth at the current rate by assuming a closed box model. The mass evolution of the gaseous disk with the cold gas mass  $M_{\text{H}_2}$  is given by

$$\dot{M}_{\text{H}_2} = \dot{M}_{\text{SNe}} - \dot{M}_{\text{BH}} - \text{SFR}. \quad (2.14)$$

Assuming that the cold gas content  $M_{\text{H}_2} = 4 \times 10^8 M_{\odot}$  (Bertram et al., 2007) will be entirely accreted onto the BH, the maximum duration of the gas accretion is

$$\frac{M_{\text{H}_2}}{\dot{M}_{\text{H}_2}} = \frac{M_{\text{H}_2}}{\dot{M}_{\text{SNe}} - \dot{M}_{\text{BH}} - \text{SFR}} \quad (2.15)$$

$$= 1.5 \text{ Gyr}. \quad (2.16)$$

With this simplistic estimate, the central BH of Mrk 1044 will have consumed its entire pristine cold gas reservoir after 1.7 Gyr with a final mass  $M_{\text{BH}} = 4 \times 10^8$  that equals the present-day HI mass. However, we already see a spatially resolved outflowing component in the ionized gas kinematics (see Fig. 2.8). Neglecting in- and outflows from the CNE might therefore not be a robust assumption. Using the BH mass - extended narrow line region size relation from Husemann et al. (2022), the expected timescale for an AGN-driven outflow to propagate through the CNE is  $\sim 10^{4.5}$  yr, which is well below the time that the BH requires for significant mass

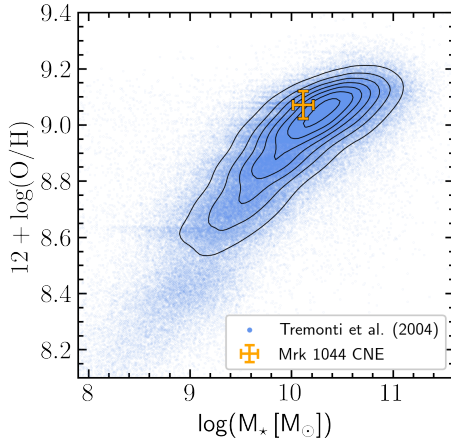


Figure 2.15: *Mrk 1044*'s gas-phase metallicity relative to the mass-metallicity relation from Tremonti et al. (2004). Compared to star-forming galaxies with a similar stellar mass, Mrk 1044's CNE has a higher metallicity by 0.11 dex.

growth. Furthermore, it is questionable whether the strong AGN phase will affect the host galaxy star formation activity through AGN feedback. Due to the proximity of the CNE near the active nucleus, the energy input, irrespective of the coupling mechanism, would first affect the SF in the CNE before it would propagate through the entire host galaxy. The presence of ongoing SF so close to the nucleus means that Mrk 1044's BH fueling is a recent event. A detailed discussion on Mrk 1044's AGN-driven outflow and its future impact on the host galaxy SFR will be presented in Winkel et al. (in prep.)

### 2.4.2 Chemical Enrichment of the CNE

Using UV spectra obtained with HST Imaging Spectrometer, Fields et al. (2005a) identified two outflowing absorbing systems that escape from Mrk 1044's center. From the column densities of O IV, N V, and HI measured with the Far Ultraviolet Spectroscopic Explorer, Fields et al. (2005b) estimated their metallicity to be at least five times solar. Such high metal abundances are difficult to explain in a galaxy evolution context.

Fig. 2.15 shows that, compared to the overall star-forming galaxy population, Mrk 1044's star-forming CNE has a gas-phase metallicity that is higher than average by 0.11 dex. This result is in agreement with the unperturbed velocity field, as we do not see signs of an external gas reservoir that could fuel Mrk 1044's center with fresh metal-poor gas. Instead, the high SFR suggests that Mrk 1044 is currently diverging from the mass-metallicity relation. The CNE size and its enrichment state are well in agreement with the TIMER studies of nuclear disks and nuclear rings (Bittner et al., 2020). With an approximate bar size that is  $\sim 5$  kpc (see Fig. 2.1), Mrk 1044 fits well into the correlation between the nuclear disks' size and bar size (Gadotti et al., 2020), which suggests a secular bar-driven formation of the CNE.

### 2.4.3 On the Black Hole Feeding Mechanism

We have shown above that the mass ejection rate from dying stars in Mrk 1044's circumnuclear star-forming region is comparable to the current BHAR. Furthermore, the high metal abundances in the CNE and the accretion disk suggests that the gas has the same origin. To provide both the ongoing SF and the AGN with material, there must be efficient gas channeling from galaxy scales toward the center. In the following, we discuss the secular host galaxy processes that could trigger the radial gas migration.

Since the ionized gas corotates with the galaxy disk, the gas transport toward the center must be accompanied by a significant loss of angular momentum. One ingredient to achieve this is to increase the turbulence in the ISM which allows the gas to dissipate its angular momentum. There have been several disk-internal processes suggested that induce turbulence. For example, SN explosions and stellar winds deposit energy into a pressure-supported circumnuclear gas disk. The higher turbulence increases the effective kinetic viscosity, that is to say it enables a more efficient angular momentum transfer (Kawakatu & Wada, 2008; Wutschik et al., 2013). For Mrk 1044, the high SFR in the circumnuclear ellipse could be a reflection of this process.

Another process has been suggested for collisional disks where the cold gas could radially migrate toward the galaxy center via chaotic cold accretion (CCA, e.g., Gaspari et al., 2019). The circular motion is

perturbed by recurrent collisions between cold gas cells which reduces their angular momentum and thus enables radial mass transport toward the center. In this way, CCA can rapidly boost inflow rates from the galaxy meso-scale ( $\sim 100$  pc) down to the micro-scale ( $<1$  pc, [Gaspari et al. 2017](#)). Independent of how it is injected into the rotating disk, turbulence allows the gas to dissipate its angular momentum and radially migrate toward the galaxy center. The enhanced SF seen in Mrk 1044's CNE could either be a result of gravitational instabilities within the self-gravitating eccentric disk or vice versa.

Other astrophysical processes may further boost the angular momentum transport. The strong eccentricity of Mrk 1044's CNE suggests that its formation is driven by a galaxy-scale process. Furthermore, Mrk 1044's host morphology is not that of a bona fide barred spiral. As is visible in the left panels of [Fig. 2.1](#), the inner  $\sim 500$  pc are dominated by dusty spiral arms and they are slightly elongated from the southeast to the northeast. The spiral arms are surrounded by a tenuous bar with a semi-major axis of  $\sim 2$  kpc which, in contrast, stretches in the east-west direction. On the largest scales up to  $\sim 15$  kpc, the galaxy outskirts exhibit a spiral structure once more which is elongated in the north-south direction. Due to its peculiar host morphology, the gas migration toward Mrk 1044's central engine could be driven by angular momentum transport through gravitational torques ([Shlosman et al., 1990](#)). The minor axis of the CNE coincides with the orientation of the bar and is therefore likely a resonant ring that typically forms at the inner Lindblad resonances (ILR). At that location of the ILR, the gas-flow toward the center is slowed down and it accumulates in a reservoir ([Combes, 1996](#); [Comerón et al., 2010](#)). This is supported by the enhanced SF within Mrk 1044's circumnuclear ellipse which is likely the reflection of a gas repository.

At smaller distances than 100 pc from the center, large-scale torques become inefficient and disk instabilities are required to transport gas down to scales of the accretion disk ("bars within bars," [Shlosman et al., 1989a](#)). Hydrodynamic simulations from [Hopkins & Quataert \(2010a\)](#) show that this process would explain the high SFR through the formation of circumnuclear molecular gas clumps. This means that gas accretion and SF are self-regulating and can coexist in an inhomogeneous, gravitationally unstable disk ([Vollmer et al., 2018](#); [Schartmann et al., 2018](#)). In this

scenario, the gas may only be partially converted into stars since the advection timescale is shorter than the SF timescale (Thompson et al., 2005). Therefore, the radial gas transport allows for efficient channeling to the accretion disk, which would explain Mrk 1044’s high accretion rate. As the motion of the stellar component is driven by the gravitational potential alone, the angular momentum transport only affects the gas component.

For Mrk 1044, we see a possible signature of this process in the spiral trails in the ionized gas velocity field (Fig. 2.12). The majority of galaxy spiral arms are trailing (e.g., Pasha & Smirnov, 1982; Puerari & Dottori, 1992), which can be explained with swing amplification of density waves that are directed inward (Toomre, 1981; Athanassoula et al., 2009). Thus, the deviation from circular rotation likely traces the radial gas migration toward Mrk 1044’s galaxy center. On the other hand, the ionized gas contributes a small fraction of the supply for the SMBH compared to the cold molecular gas (e.g., Gaspari et al., 2017). While the ionized gas is accelerated by momentum injection through radiation and winds from SNe, the dense inner regions of molecular clouds might be shielded from both and its motion remain unperturbed. However, in a CCA scenario, the molecular gas is expected to inherit part of the galaxy-scale kinematics via the top-down condensation, hence leading to tighter phase correlations (Gaspari et al., 2018). Overall, we require high angular resolution of the molecular gas kinematics in Mrk 1044’s central region to understand the detailed gas feeding toward the accretion disk, in particular to unveil the cooler phases.

## 2.5 Summary and Conclusions

In this work, we have presented new MUSE NFM-AO observations of the nearby unobscured NLS1 galaxy Mrk 1044. The deblending of the AGN from the host emission enabled us to extract the host galaxy properties with unprecedented resolution. We have mapped the host galaxy stellar velocity field and the emission line properties in Mrk 1044’s central kiloparsec. Furthermore, we have used a kinematic model to identify structures that deviate from a quiescent rotating disk. Our key results are the following.

- A large fraction (27%) of the galaxy-wide SF is concentrated in a compact star-forming CNE with  $\Sigma_{\text{SFR}} = 0.16 \pm 0.04 \text{ M}_{\odot} \text{ yr}^{-1} \text{ kpc}^{-1}$ , a semi-minor axis of  $306 \pm 43 \text{ pc}$ , and an axis ratio of 2.45. Within the CNE, the optical emission line ratios are entirely consistent with excitation by SF. Surprisingly, we do not find signs of extended photo-ionized gas emission, despite Mrk 1044's high accretion rate.
- From 30 kpc down to  $\sim 100 \text{ pc}$ , both stellar and ionized gas follow the quiescent kinematic pattern of a rotating thin disk. In the velocity fields, there are no signs of a major interactions with a companion.
- Within the compact CNE, the ionized gas exhibits clumpy streams with  $\sim 100 \text{ pc}$  extent that deviate from rotation with the disk, potentially contributing to the SMBH feeding. Their projected LOS velocity is on the order of  $10 \text{ km s}^{-1}$ .
- The gas-phase metallicity within the star-forming CNE is above the expected value from the mass-metallicity relation.
- The estimated mass ejection rate from massive stars exceeds the current BHAR.

Our results suggest that the circumnuclear SF is connected to the high accretion rate of Mrk 1044's central BH. It remains unclear, however, if the SF drives Mrk 1044's BH accretion or if both share an underlying process that triggers them at the same time. Very long baseline interferometric observations of Mrk 1044's nuclear region have been conducted recently with the Atacama Large Millimeter/submillimeter Array (ALMA). The information on the molecular gas abundance and distribution will help to understand the fueling of Mrk 1044's central engine. However, to constrain the initial process driving the rapid BH growth in NLS1, a comparative study of nearby BLS1s and NLS1s with high spatial resolution is required.

---

# A parsec-scale multi-phase outflow in the super-Eddington NLS1 Mrk 1044

This chapter is based on work published in [Winkel et al. \(2023\)](#) in *Astronomy & Astrophysics*. I am the primary developer of the spectroastrometric analysis tool `Siēna`<sup>3D</sup>, which played a crucial role in this project. The analysis, discussion, and interpretation of the results were conducted with the support of Dr. Bernd Husemann, Dr. Mainak Singha and the CARS collaboration.

N. Winkel<sup>1</sup>, B. Husemann<sup>1</sup>, M. Singha<sup>2</sup>, V. N. Bennert<sup>3</sup>, F. Combes<sup>4</sup>,  
T. A. Davis<sup>5</sup>, M. Gaspari<sup>6</sup>, K. Jahnke<sup>1</sup>, R. McElroy<sup>7</sup>, C. P. O’Dea<sup>2</sup>, and  
M. A. Pérez-Torres<sup>8,9,10</sup>

<sup>1</sup>Max-Planck-Institut für Astronomie, Königstuhl 17, D-69117 Heidelberg, Germany

<sup>2</sup>University of Manitoba, Winnipeg, MB R3T 2N2, Canada

<sup>3</sup>Physics Department, CalPoly, San Luis Obispo, CA 93407, USA

<sup>4</sup>LERMA, Observatoire de Paris, CNRS, Sorbonne Univ., Paris, France

<sup>5</sup>Cardiff Hub for Astrophysics Research & Technology, Cardiff University, CF24 3AA, UK

<sup>6</sup>Princeton University, 4 Ivy Lane, Princeton, NJ 08544-1001, USA

<sup>7</sup>The University of Queensland, St. Lucia, QLD 4072, Australia

<sup>8</sup>IAA-CSIC, Glorieta de la Astronomía s/n, E-18008 Granada, Spain

<sup>9</sup>Universidad de Zaragoza, Pedro Cerbuna 12, E-50009 Zaragoza, Spain

<sup>10</sup>European University Cyprus, Diogenes street, Engomi, 1516 Nicosia, Cyprus

## Abstract

The interaction between active galactic nuclei (AGNs) and their host galaxies is scarcely resolved. Narrow-line Seyfert 1 (NLS1) galaxies are believed to represent AGN at early stages of their evolution and to allow one to observe feeding and feedback processes at high black hole accretion rates. We aim to constrain the properties of the ionised gas outflow in Mrk 1044, a nearby super-Eddington accreting NLS1. Based on the outflow energetics and the associated timescales, we estimate the outflow’s future impact on the ongoing host galaxy star formation on different spatial scales. We applied a spectroastrometric analysis to observations of Mrk 1044’s nucleus obtained with the adaptive-optics-assisted narrow field mode of the VLT/MUSE instrument. This allowed us to map two ionised gas outflows traced by [O III], which have velocities of  $-560 \pm 20 \text{ km s}^{-1}$  and  $-144 \pm 5 \text{ km s}^{-1}$ . Furthermore, we used an archival spectrum from the Space Telescope Imaging Spectrograph on HST to identify two Ly- $\alpha$  absorbing components that escape from the centre with approximately twice the velocity of the ionised gas components. Both [O III] outflows are spatially unresolved and located close to the AGN ( $< 1 \text{ pc}$ ). They have gas densities higher than  $10^5 \text{ cm}^{-3}$ , which implies that the BPT diagnostic cannot be used to constrain the underlying ionisation mechanism. We explore whether an expanding shell model can describe the velocity structure of Mrk 1044’s multi-phase outflow. In the ionised gas emission, an additional outflowing component, which is spatially resolved, is present. It has a velocity of  $-211 \pm 22 \text{ km s}^{-1}$  and a projected size of  $4.6 \pm 0.6 \text{ pc}$ . Our kinematic analysis suggests that significant turbulence is present in

the interstellar medium around the nucleus, which may lead to a condensation rain, potentially explaining the efficient feeding of Mrk 1044's AGN. Within the innermost  $0.5''$  (160 pc), we detect modest star formation hidden by the beam-smearred emission from the outflow. We estimate that the multi-phase outflow was launched  $< 10^4$  yrs ago. Together with the star formation in the vicinity of the nucleus, this suggests that Mrk 1044's AGN phase started only recently. The outflow carries enough mass and energy to impact the host galaxy star formation on different spatial scales, highlighting the complexity of the AGN feeding and feedback cycle in its early stages.

# Chapter 3 | A Parsec-Scale Multi-Phase Outflow in the Super-Eddington NLS1 Mrk 1044

## 3.1 Introduction

Supermassive black holes (SMBHs) in the hearts of galaxies are believed to interact with their host galaxy. The enormous amount of energy released by an active galactic nucleus (AGN) is injected into the interstellar medium (ISM) where it effectively delays the gas cooling. This deprives the galaxy of its cold gas reservoir (Zubovas & King, 2012) and eventually leads to star formation (SF) quenching, an effect that is referred to as ‘negative feedback’. Such AGN-induced negative feedback is an important ingredient to reproduce galaxy properties in cosmological hydrodynamical simulations (e.g. Crain et al., 2015; Dubois et al., 2016; Weinberger et al., 2017) and semi-analytic models (e.g. Somerville et al., 2008; Fontanot et al., 2020). In contrast, AGNs have also been suggested to locally promote the SF in its host galaxy by enhancing the gas pressure in the ISM (‘positive feedback’, Silk, 2013; Cresci et al., 2015).

The physical mechanisms through which AGN feedback acts are poorly constrained by observations. Open questions include when and how much energy is released during the AGN phase, how the energy is transported from the accretion disc to galaxy scales, and how it couples to the surrounding ISM. One important signature of AGNs are powerful outflows, which are a product from the energy released by the accreting SMBH and its interaction with the ISM. Such AGN-driven outflows have a multi-phase nature. In the X-ray, they can be identified in the form of fast radiation-driven winds, which originate from scales of the BH accretion disc (Tombesi et al., 2010; Gofford et al., 2013; Tombesi et al., 2013). However, atomic, molecular, and ionised gas outflows are typically observed at distances from parsecs up to several kilo-parsecs from the galaxy centre. Ionised outflows are often identified from the systematically asymmetric emission line shape of [O III] $\lambda\lambda$ 4960,5007. The blue shoulder is usually interpreted as a bi-conical outflow of AGN-ionised gas where the receding side is obscured by dust from the host galaxy (e.g. Heckman et al., 1981;

Bischetti et al., 2017; Bae & Woo, 2016; Wylezalek et al., 2020). Both observations (Silk & Rees, 1998a; King, 2003; Holt et al., 2006, 2008; Ciccone et al., 2014) and hydrodynamical simulations (e.g. Di Matteo et al., 2005; Gaspari et al., 2020) suggest that multi-phase outflows represent a key channel through which the AGN feedback acts on the host galaxy. Moreover, such feedback can significantly stimulate turbulent condensation, leading to gas precipitation and chaotic cold accretion (CCA; e.g. Gaspari et al. 2019).

Due to the compactness of the AGN-dominated region from which the outflows are launched, it is still a matter of debate how the evolution of the central BH impacts the host galaxy on different scales. An increasing number of studies provide a detailed and spatially resolved analysis of ionised gas outflows in local AGNs (e.g. Greene et al., 2011; Husemann et al., 2016a; Revalski et al., 2018; Venturi et al., 2018; Husemann et al., 2019; Riffel et al., 2020). One big challenge is to determine the outflow location, orientation, and intrinsic size. The works of Greene et al. (2011); Liu et al. (2013); Harrison et al. (2014) and McElroy et al. (2015) have suggested that galaxy-scale outflows might be prevalent in the majority of luminous AGNs. In contrast, a recent study by Singha et al. (2022) has shown that among the luminous AGNs in the representative sample of the Close AGN Reference Survey (CARS, Husemann et al., 2022), a large fraction (64%) of them have ionised gas outflows with an extent of less than 100 pc. This disagreement can partially be explained by beam smearing in seeing-limited observations (Husemann et al., 2016b; Villar-Martín et al., 2016; Davies et al., 2019). Another problem is that the inferred outflow properties such as electron density, masses, and kinetic energies are poorly constrained as they depend on the outflow geometry, which is often unknown in luminous type 1 AGNs (e.g. Rakshit & Woo, 2018).

Constraining the fundamental spatial, energy, and timescales is crucial to understand how AGN-driven multi-phase outflows are launched and how they couple to the host galaxy ISM. For AGNs in the Sloan Digital Sky Survey (SDSS), Mullaney et al. (2013) and Woo et al. (2016) have shown that outflows occur more frequently in AGNs with a high Eddington ratio. In this regime, radiation pressure from the accretion disc couples to the dense ISM and can drive the outflow (Fabian, 2012), suggesting that ionised gas outflows are launched during the AGN phase. Among

the general AGN population, narrow line Seyfert 1 (NLS1) galaxies show low BH masses at high accretion rates (e.g. Boroson 2002; Grupe et al. 2010, review by Komossa & Xu see review by 2007a). NLS1s often host ultra-fast outflows (UFOs) (e.g. Gupta et al., 2013; Parker et al., 2017; Reeves et al., 2018; Kosec et al., 2018; Reeves & Braito, 2019; Xu et al., 2022). Furthermore, NLS1s are located at the extreme end of the Eigenvector 1 (EV1) correlation, which involves the widths and strengths of [O III] $\lambda$ 5007, H $\beta$ , and Fe II emission lines (Boroson & Green, 1992). Wang et al. (1996) extended the EV1 plane by the soft X-ray photon index where NLS1s typically exhibit a prominent, soft X-ray excess (Gliozzi & Williams, 2020). The EV1 correlation is thought to be primarily driven by the Eddington ratio (Sulentic et al., 2000), which suggests that there might be a connection between the BH accretion rate and the launching mechanism of a multi-phase outflow. For a comprehensive understanding, we need to resolve the multi-phase outflow both spatially and in its kinematic components.

In this work we present a detailed analysis of the ionised gas outflow in the centre of Mrk 1044. Mrk 1044 is a nearby, luminous ( $L_{\text{bol}} = 3.4 \times 10^{44} \text{ erg s}^{-1}$ , Husemann et al. 2022) NLS1 with a stellar mass of  $\log(M_*/M_\odot) = 9.92_{-0.12}^{+0.17}$  (Smirnova-Pinchukova et al., 2022). Its central engine is powered by a BH with a reverberation mapped mass of  $M_{\text{BH}} = 2.8 \times 10^6 M_\odot$  (Du et al., 2015). Mrk 1044 shows a soft X-ray excess, which Mallick et al. (2018) explained by relativistic reflections from a high density accretion disc. From the several narrow absorption lines that are present in Mrk 1044's XMM-Newton spectra, Krongold et al. (2021) identified four kinematically distinct UFOs. Their velocity and density structure suggest that the two light absorbers may originate from the same multi-phase outflow.

The results presented in this work are based on the analysis of Mrk 1044's host galaxy presented in Winkel et al. (2022, hereafter Paper I) where we found that the host galaxy SF is concentrated in a circumnuclear ellipse (CNE) at  $\sim 300$  pc from the centre. Furthermore, we detected tentative signatures of ionised gas channelling towards the centre, which might be a signature of ongoing BH fuelling. Despite the high BH accretion rate, the host galaxy does not exhibit any signs of disturbance even at a short distance from the nucleus ( $\sim 160$  pc). Based on the velocity field of the stellar component, we have constrained Mrk 1044's systemic velocity

to  $cz = 4913.4 \pm 0.2 \text{ km s}^{-1}$ , corresponding to a redshift of  $z = 0.0164$ . In the very centre of Mrk 1044, we detected a spatially resolved ionised gas component that is blue-shifted, which indicates an ionised gas outflow. In this work we use optical IFU data, UV spectroscopic data, and radio imaging to constrain the properties of Mrk 1044's multi-phase outflow. Combining the observations, we aim to attain a detailed understanding of the outflow location, geometry, and its physical driver. Throughout this paper we assume a flat Lambda cold dark matter cosmology with  $H_0 = 70 \text{ km s}^{-1} \text{ Mpc}^{-1}$ ,  $\Omega_M = 0.3$ , and  $\Omega_\Lambda = 0.7$ . In this framework,  $1''$  corresponds to  $333 \text{ pc}$  at the galaxy redshift, where Mrk 1044's associated luminosity distance is  $70.0 \text{ Mpc}$ .

## 3.2 Observations and Data Reduction

### Optical IFU Observations

We use integral field spectroscopic data obtained with the adaptive optics assisted narrow field mode (NFM-AO) of the Multi Unit Spectroscopic Explorer (MUSE, [Bacon et al., 2010, 2014](#)) at the Very Large Telescope (VLT). The data reduction is described in Paper I. The reduced data cube consists of  $369 \times 378$  spaxels, corresponding to a FOV of  $9''23 \times 9''45$ . The spectral resolution is almost constant with a full width at half maximum (FWHM) of  $2.54 \pm 0.10 \text{ \AA}$  across the entire wavelength range  $4750 \text{ \AA} - 9350 \text{ \AA}$  corresponding to  $160.4 \text{ km s}^{-1}$  and  $81.5 \text{ km s}^{-1}$  at the blue and the red end of the spectrum, respectively. In Paper I we describe the modelling of the adaptive-optics-shaped point spread function (PSF) using a hybrid approach between the empirical PSF and the analytical PSFAO19 model from [Fétick et al. \(2019\)](#). The spatial resolution measured from the PSF extracted at the broad  $\text{H}\beta$  emission is  $89 \text{ mas}$  which corresponds to  $30 \text{ pc}$  in the galaxy system. We have deblended the AGN from the host emission in an iterative process that is described in Paper I. In this work, we aim to extract the properties of the outflow from the original data cube that contains the blended emission from the AGN and the host.

### UV Spectroscopy

We employ an archival UV spectrum of Mrk 1044 that was acquired with the Space Telescope Imaging Spectrograph (STIS) on the Hubble Space

Telescope (HST). This data has first been presented in [Fields et al. \(2005a\)](#) where the authors identified two outflowing absorbers with super-solar metallicity. Since we have a robust measure of Mrk 1044’s systemic velocity from the stellar rotational field, we re-analyse the outflow kinematics. We retrieve the archival data from the Hubble Legacy Archive<sup>1</sup> and stack the two data sets o8k4010-50 and o8k4010-60 taken with the G140M grating. The target was observed on UTC 2003 June 28 with the 52X0.2 aperture centred on Mrk 1044’s nucleus. The two spectra were acquired with an exposure time of 1294 s and 1440 s respectively and have a resolution of 0.053 Å/px. The stacked spectrum extends from 1194.57 Å to 1249.10 Å with a central wavelength of 1222 Å.

### Radio Imaging

Mrk 1044 has been observed with Karl G. Jansky Very Large Array (VLA) in the C-band (6 GHz) on October 30, 2016 and X-band (10 GHz) on January 15, 2017. The JVLA observations were taken in the A configuration which has a maximum baseline of 36.4 km and a minimum baseline of 0.68 km. The A configuration observations are sensitive to emission on scales up to 9'' in C-band and up to 5''3 at X-band. The three C-band scans have an integration time of 245 s each resulting in a total integration time 735 s. The two X-band scans have an integration time of 325 s each. Together with two existing additional scans (330 s), the X-band has a total integration time of 1310 s. 3C48 and 3C138 were used as flux density calibrators. We reduced the JVLA data using the Common Astronomy Software Applications (CASA, [McMullin et al., 2007](#)) pipeline version 6.2.1.7 and the dedicated CASA tools for VLA observations.

## 3.3 Analysis and Results

### 3.3.1 Optical AGN Spectrum

In order to understand the ISM properties of Mrk 1044’s outflow on nuclear scales, we aim to extract the ionised gas kinematic components present in the innermost few parsecs. In Paper I we have described the iterative deblending of AGN and host emission. For the following analysis we use

---

<sup>1</sup><https://hla.stsci.edu/>

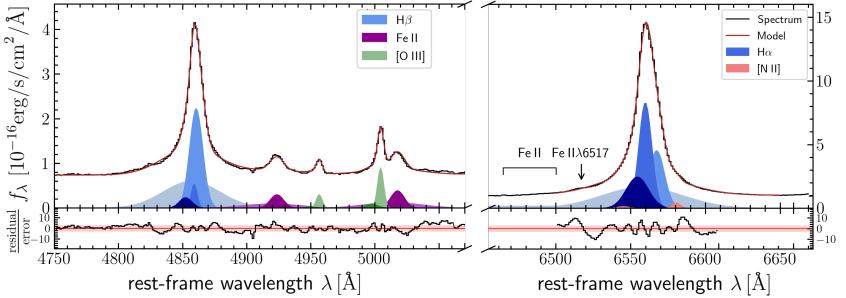


Figure 3.1: *Modelling Mrk 1044's AGN spectrum.* The H $\beta$ -[O III] region is shown left, and H $\alpha$ -[N II] region in the right panel. To reproduce the observed spectrum (black) we use a multi-Gaussian model for H $\beta$  (blue), [O III] (green), Fe II (purple), H $\alpha$  (blue, right panel) and [N II] (red). The best-fit spectrum is shown as a red line and well reproduces the prominent emission lines, including the blue shoulder of the [O III] narrow line.

the AGN spectrum from the deblended AGN data cube which contains the point-like emission from Mrk 1044's nucleus exclusively. Due to the finite width of the PSF, it probes the innermost 30 pc around the nucleus. The spectrum in the observed frame is shown in Fig. 3.1 for both the H $\beta$ + [O III] and the H $\alpha$ + [N II]+ [S II] regions. It exhibits prominent emission lines H $\beta$ /H $\alpha$  and [O III] $\lambda\lambda$ 4959,5007 and especially from Fe II, whereas the [N II] $\lambda\lambda$ 6548,6583 doublet is barely visible.

We simultaneously model the AGN spectrum in the H $\beta$ + [O III] and the H $\alpha$ + [N II] region. Our model consists of several Gaussian components and a linear approximation of the local continuum in each of the windows. To reproduce the H $\beta$  and H $\alpha$  line shape, we require a broad+medium component and a narrow core component. The broad and medium component both have a kinematically tied component in the prominent broad Fe II  $\lambda\lambda$ 4924,5018 doublet. For the forbidden doublet emission lines [N II] $\lambda\lambda$ 6548,6583 and [O III] $\lambda\lambda$ 4959,5007 we couple the flux ratios to the theoretical prediction of 2.96 (Storey & Zeippen, 2000; Dimitrijević et al., 2007). To reproduce the narrow [O III] line shape we require an additional blue-shifted 'wing' component which has a kinematically tied counterpart in H $\beta$  and H $\alpha$ . To find the best-fit parameters of the model we minimise the  $\chi^2$  of the residuals with a Levenberg-Marquardt algorithm. We

Table 3.1: *Best-fit parameters from modelling Mrk 1044's AGN spectrum.* The left columns list the emission lines in the  $H\beta$ -[O III] region, the right column the  $H\alpha$ + [N II] region. Velocities and dispersion are computed in the galaxy rest-frame. Lines that are listed together are kinematically coupled. Furthermore, we have kinematically tied the wing component between  $H\beta$ + [O III] and  $H\alpha$ . In each of the strong lines, the core component has a velocity that is significantly different from zero.

component	line	$v_r$ [km s <sup>-1</sup> ]	$\sigma$ [km s <sup>-1</sup> ]
H $\beta$ window			
broad	H $\beta$ +Fe II	-272 $\pm$ 11	1349 $\pm$ 14
medium	H $\beta$ +Fe II	-48 $\pm$ 4	281 $\pm$ 2
core	H $\beta$ + [O III]	-144 $\pm$ 5	165 $\pm$ 17
wing	H $\beta$ + [O III]	-560 $\pm$ 20	251 $\pm$ 31
H $\alpha$ window			
broad	H $\alpha$	-232 $\pm$ 13	1232 $\pm$ 13
medium	H $\alpha$	206 $\pm$ 87	212 $\pm$ 48
core	H $\alpha$ + [N II]	-140 $\pm$ 7	180 $\pm$ 12
wing	H $\alpha$	-560 $\pm$ 20	251 $\pm$ 31

estimate the uncertainties of the parameters by modelling 1000 artificial spectra generated from the  $1\sigma$  flux density errors in the AGN spectrum. We note that the identification of the components in the emission line spectrum can also be reproduced with software packages that involve a Fe II-template to account for the strong Fe II contribution in the  $H\beta$ -[O III] window. However, the systematic uncertainty of the optional Fe II template provides a poorer description of the AGN spectrum than our multi-Gaussian model, especially in the [O III] region where we perform most of our diagnostics. We note further that the results presented in the following do not change within the uncertainties if the emission from ions with different ionisation potentials are not kinematically coupled. In particular, the results do not change qualitatively if we release the kinematic coupling between the  $H\beta$  and [O III] components and the  $H\alpha$ -wing and [N II] components respectively.

Fig. 3.1 shows that the AGN spectrum in both spectral regions is well reproduced by our four component model. Considering the high signal-to-noise ratio (S/N), also the  $H\alpha$  line shape is well-reproduced close to its centre. The broad wings, however, are contaminated by the broad Fe II $\lambda$ 6517, He I emission and Fe Complex (c.f. Fig.7 Véron-Cetty et al.,

Table 3.2: *Spectroastrometric measurement for the spatial offset between the kinematic components.* By construction, the broad H $\beta$  and H $\alpha$  components are located at the AGN position.

component	offset [mas]	offset [pc]
H $\beta$ broad	0.00 $\pm$ 0.54	0.00 $\pm$ 0.19
[O III] core	0.67 $\pm$ 0.54	0.23 $\pm$ 0.19
[O III] wing	0.91 $\pm$ 1.22	0.31 $\pm$ 0.42
H $\alpha$ broad	0.00 $\pm$ 0.05	0.00 $\pm$ 0.02
[N II] core	0.66 $\pm$ 1.09	0.23 $\pm$ 0.40

2004) which are not included in our model. The kinematic parameters of the best-fit model of the AGN spectrum are summarised in Table 3.1. Both H $\alpha$ + [N II] and H $\beta$ + [O III] narrow core components have radial velocities significantly smaller than zero by  $v_r(\text{H}\beta + [\text{O III}]) = -144 \pm 5 \text{ km s}^{-1}$  and  $v_r(\text{H}\alpha + [\text{N II}]) = -140 \pm 7 \text{ km s}^{-1}$ , indicating that the region from which the narrow line emission emerges is moving towards the observer. In addition to the blue-shifted narrow core component, we detect a wing component in the H $\beta$  and [O III] emission with a velocity shift of  $-560 \pm 20 \text{ km s}^{-1}$ . This feature is often recovered in AGN spectra and is typically interpreted as an ionised gas outflow moving towards the observer, where the receding side is obscured by dust around the nucleus (e.g. Heckman et al., 1981; Boroson, 2005; Zakamska et al., 2003; Woo et al., 2016).

### 3.3.2 Spectroastrometry

After having identified two outflowing systems in both Mrk 1044’s H $\beta$ - and [O III] emission, we now aim to constrain their location and spatial extent. For this purpose, we have developed the Spectroastrometric analysis tool for Ionized gas Emission in Nearby AGN (Siena3D, Winkel & Singha, 2022). Siena3D locates and traces kinematic components in 3D spectroscopic observations with high precision, using a spectroastrometric approach (for discussion see Bailey, 1998; Gnerucci et al., 2010, 2011). The software package is available on GitHub<sup>2</sup> under a OSI<sup>3</sup> approved licence. The concept behind Siena3D is described in Singha et al. (2022) where the technique has been applied and tested for the entire CARS sam-

<sup>2</sup><https://github.com/nicowinkel/Siena3D>

<sup>3</sup><https://opensource.org/licenses>

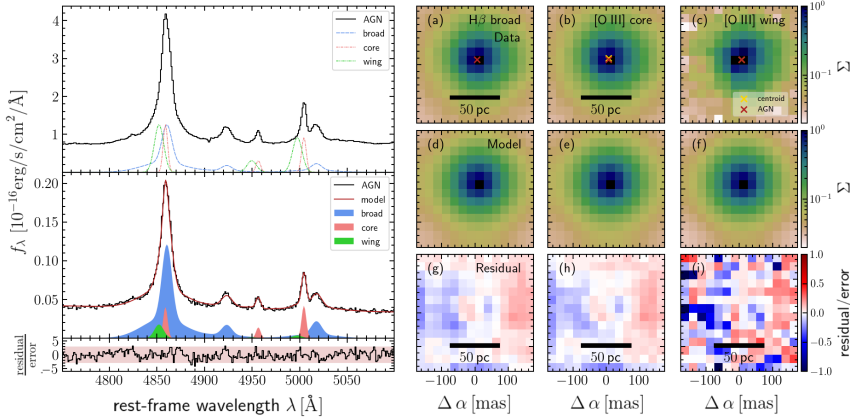


Figure 3.2: *Spectroastrometric analysis of Mrk 1044's central region using the original MUSE NFM-AO data cube.* The left panels show an arbitrary example spectrum that is picked from the small window around the nucleus shown in the panels on the right. To fit the spectrum, we keep the kinematics and line ratios of the kinematics fixed to that of the components found in the AGN spectrum. The panels on the right show the surface brightness within the central 150 mas for the kinematic components where the flux maps are normalised to their peak flux. Here we only show the measure light distribution from the BLR  $H\beta$  (left),  $[O\ III]$ -wing (middle), and narrow  $[O\ III]$ -core (right) component. From top to bottom the maps show the 2D light distributions, the best-fit model of the PSF and the residual maps. The red cross indicates the PSFAO19 fit to the BLR  $H\beta$ . The green and white crosses indicate the centroids for the PSFAO19 models to the surface brightness maps of the  $[O\ III]$ -wing and core respectively, in which the amplitude and position of the Moffat model were varied only. The offset of both  $[O\ III]$  core and wing component from the AGN position are smaller than 0.1 px.

ple of nearby unobscured AGNs. Here, we give a brief description of the concept.

(1) As a first step, we use the kinematic components identified in the AGN spectrum to generate normalised base spectra (top left panel of Fig. 3.2). All emission lines that belong to the kinematic components are combined in the respective base spectrum. Their flux ratios and kinematics are tied to what we measured in the highest signal-to-noise spaxel.

This step involves the assumption that both line ratios and kinematics are constant throughout the structure that is traced (e.g. a compact fast moving ionised gas cloud or the BLR).

(2) In the next step, we use the base spectra to fit the spaxels in a  $14 \times 14$  pixel ( $0''.35 \times 0''.35$ ) aperture around the AGN position using a non-negative least squares optimiser. For one arbitrary spaxel, the best-fit model together with the contribution from the components are shown in the bottom left panel of Fig. 3.2. Our results do not depend on the exact size of the aperture, since the high S/N core of the PSF (FWHM=1.6 px to 3.6 px) is captured entirely.

(3) From the best-fit model, we map the flux that originates from the individual kinematic components. We fit the PSF to the light distributions to locate their centroids relative to the AGN position. For this task we adopt the hybrid PSF model that involves the empirical PSF and the analytic PSFAO19 model for the adaptive-optics-shaped PSF measured in Paper I, using the analytic model from Fétick et al. 2019.

(4) Finally, we evaluate whether the light distribution deviates from a point-like emission to test whether the component has an intrinsic extended that is spatially resolved. The methodology is described in Appendix 3.6.1 where we constrain the projected extent of a resolved component (see Sect. 3.3.3).

The precision by which different components can be kinematically and spatially disentangled depends on multiple parameters including the size and sampling of the PSF, the accuracy of the PSF model, the spectral resolution, the velocity offset between the kinematic components and the S/N of the emission lines and their dispersion. In order to estimate the systematic uncertainty of our method specific to our data set, we have generated a set of mock data cubes by simulating the emission line profiles at different velocities, locations and sizes. We manually displaced the [O III]-wing component while keeping the location of the broad and core components fixed. At the S/N of [O III] core and wing component, the offset of both can be detected down to 0.1 px, corresponding to 2.5 mas or 0.85 pc in the galaxy system. Furthermore, we have simulated spatially resolved structure by convolving the PSF with a Gaussian kernel. For Mrk1044 we can constrain the intrinsic extent of the outflow down to a size of 0.2 px (1.7 pc). At smaller scales, the precision is limited by the

relatively low S/N of the wing component that is blended with the core component in each of the emission lines [O III] $\lambda\lambda$ 4959,5007.

For the Mrk 1044, the result of the spectroastrometric measurement in the H $\beta$ -[O III]-region is shown in Fig. 3.2, with the corresponding centroid positions listed in Table 3.2. The broad component originates from the  $\mu$ pc-scale BLR that is unresolved and follows the PSF light profile by construction. Therefore, the residual maps of the broad component reflect the systematic uncertainty of the PSF. But also the residuals of the [O III]-core and wing component show no extended structure. Neither [O III] outflowing component has an intrinsic extent that is larger than 0.2 px (1.7 pc). Furthermore, both core and wing component are located at the exact AGN position within the systematic uncertainties. We therefore conclude that neither of the [O III]-outflows have a projected distance from the nucleus that is larger than 0.85 pc.

### 3.3.3 The Spatially Resolved Outflow

During the analysis of the star-forming CNE in Paper I, we have reported a high surface brightness spot in the centre that is present after subtracting the AGN emission. In the following we refer to this feature as H0 as it is most pronounced in H $\alpha$  and H $\beta$  surface brightness maps. The left panel of Fig. 3.3 shows that in the host data cube the feature is constrained to the innermost 0''.5. In Paper I the analysis with a single Gaussian emission line model yielded blue-shift of  $-140 \text{ km s}^{-1}$  and a peak velocity dispersion that is significantly higher than that of the CNE ( $\sigma = 234 \pm 9 \text{ km s}^{-1}$ , see fig. 7 in Paper I). The high velocity-offset with respect to the galaxy systemic velocity suggests that the ionised gas is outflowing. We detect the gas in each of the narrow emission lines H $\beta$ , [O III], H $\alpha$  and [N II] whereas we cannot trace a significant component [S II] given the low spectral signal-to-noise of the spatially resolved analysis.

Although the outflow appears circularly symmetric, it is not an artefact from the PSF subtraction. To better understand this we recall the PSF subtraction process. H $\alpha$  and H $\beta$  are the wavelengths at which we have extracted the empirical PSF. By definition, the empirical PSF contains all the point-like emission. After the PSF cube construction, our PSF subtraction method is an iterative routine to clean the host emission from the AGN contamination. Since we interpolate the PSF between H $\alpha$  and H $\beta$ , an inaccurate PSF model would cause much stronger residual features

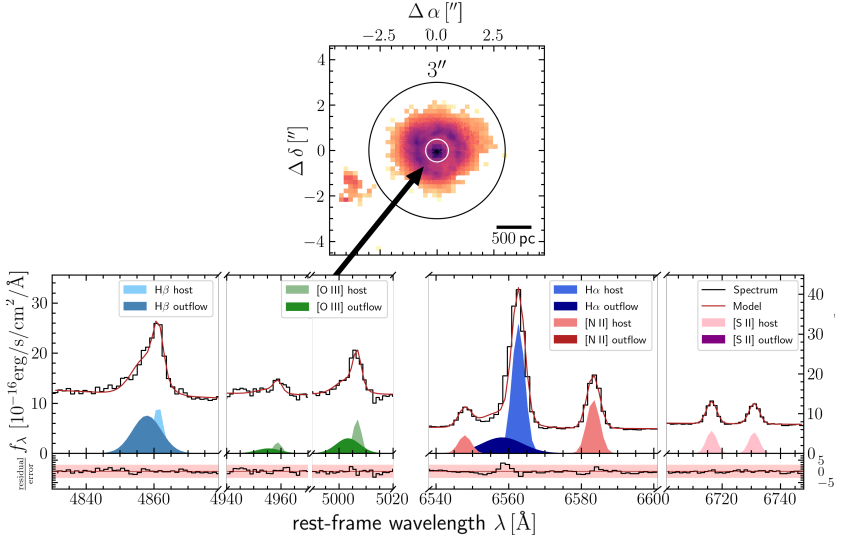


Figure 3.3: *Origin of the forbidden [S II] emission in Mrk 1044's centre.* The top panel shows the H $\alpha$  surface brightness map where the H0 outflow is located the central 0''.5. The bottom panel shows the two component model for the inner 0''.5 integrated spectrum where we fixed the host and outflow kinematics to what we found from the 3'' integrated spectrum. For the outflow, we do not find a significant contribution of [S II] and [N II] suggesting that the gas density lies above their critical densities.

at wavelengths at which the empirical PSF was not directly measured, that is [O III]. Furthermore, the central feature is present after each iteration of the PSF subtraction process. In particular, it is present after the first iteration where the host-contaminated AGN-spectrum is subtracted. The circularly symmetric surface brightness profile can thus be explained by a compact source together with the effect of beam smearing. To understand the origin of this spatially resolved outflow, we constrain its extent as described Appendix 3.6.1. Our analysis yields a projected intrinsic extent of  $0.55 \pm 0.10$  px, corresponding to  $4.6 \pm 0.6$  pc in the galaxy frame.

### Multi-component Analysis

The spectrum around the nucleus is a superposition of the emission from the host and that of the spatially resolved outflow H0. The two signals stem from intrinsically distinct structures, potentially located at different regions in the galaxy and having different ionisation conditions. To disentangle and analyse their signal, we follow the methodology described in [Singha et al. \(2022\)](#), which contains the following steps:

First, we fitted  $H\beta + O\text{ III}\lambda\lambda 4959,5007$  with a two-component (host and outflow) Gaussian model each in a within a  $3''$  aperture. This gives us a robust estimate of the integrated host and outflow kinematic parameters.

We then fitted each of the  $H\beta + [O\text{ III}]\lambda\lambda 4959,5007$  and  $H\alpha + [N\text{ II}]\lambda\lambda 6548,83 + [S\text{ II}]\lambda\lambda 6716,31$  with the two-component model, this time keeping the kinematic parameters fixed to the values retrieved in step 1. Furthermore, we couple the line ratios among the  $[O\text{ III}]$  and  $[N\text{ II}]$  doublet lines to the theoretical prediction of 2.96 ([Storey & Zeippen, 2000](#); [Dimitrijević et al., 2007](#)). Due to the relatively low S/N of the blended emission lines, this task could only be performed on the  $0''.5$ -integrated spectrum.

The result of the process is shown in [Fig. 3.3](#). Each of the strong emission lines is detected at a  $>3\sigma$  confidence level with their kinematic parameters listed in [Table 3.3](#). Except for the high signal-to-noise centre of the  $H\alpha$  emission line, the residual spectrum is uniformly distributed around zero, with a scatter of  $0.22\sigma$  (FWHM), where  $\sigma$  is the formal uncertainty from the AGN-blended cube. We conclude that the multi-Gaussian model provides a good description of the nuclear host spectrum. We detect a wing component that is present in  $H\beta$ ,  $H\alpha$  and  $[O\text{ III}]$  exclusively. In contrast, the corresponding wing components in  $[N\text{ II}]$  and  $[S\text{ II}]$  are faint or missing such that we could only estimate upper flux limits. We constrain and discuss the underlying ionisation mechanism from the emission line ratios in [Sect. 3.4.1](#).

#### 3.3.4 Radio Emission

The EVLA broad-band images in the C- and X-band are shown in [Fig. 3.4](#). The peak frequencies are located at 5 GHz (C-band) and 10 GHz (X-band). At these frequencies, we detect the AGN with a peak flux of  $758 \pm 19 \mu\text{Jy}/\text{beam}$  (C-band) and  $496 \pm 10 \mu\text{Jy}/\text{beam}$  (X-band). The ra-

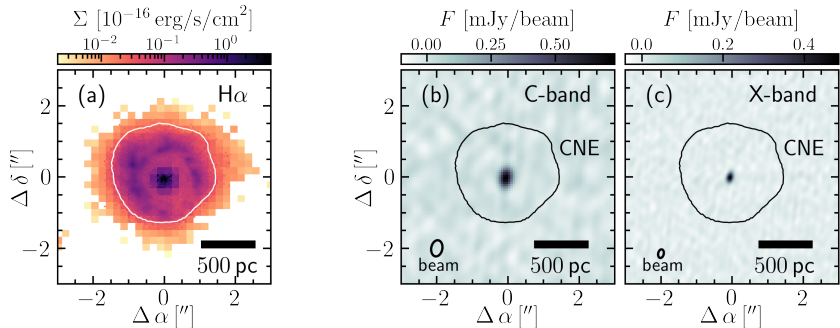


Figure 3.4: *Mrk 1044*'s nuclear region seen in the optical and radio emission. Panel (a) shows the surface brightness map of the H $\alpha$  narrow line emission extracted as described in Paper I. The panels on the right show the broad-band EVLA images of the radio emission in the C-band (b) and X-band (c) with the corresponding FWHM-contour of the beam shown in the lower left corner respectively. The contours of the star forming CNE encompassing the nucleus are shown as black contours (see Paper I). In both C- and X-band the nuclear radio emission is unresolved by VLA.

radio emission appears to be concentrated in the beam aperture in both bands. To quantify the size of the source, we use the CASA routine `imfit` to measure the AGN emission within a 10 px radius from the centre which is sufficient to capture the source's entire emission. We find that the source is spatially unresolved by VLA and the centroid of its radio emission matches the location of the AGN within the uncertainties. Its integrated flux density amounts  $714 \pm 32 \mu\text{Jy}$  in the C-band and  $484 \pm 18 \mu\text{Jy}$  in the X-band respectively. Assuming that the spectrum between 5 GHz and 10 GHz is described by a power law  $S_\nu \propto \nu^\alpha$ , we estimate the spectral index from the flux density. Its uncertainty depends both on the statistical error from thermal noise of the image and the systematic uncertainties  $\sqrt{\sigma_{\text{rms}}^2 + \sigma_{\text{sys}}^2}$ . Combining both, we use eq. (1) from sect. 3.2 from [Ramírez-Olivencia et al. \(2022\)](#) to estimate the uncertainty throughout our calculation. From *Mrk 1044*'s integrated flux densities we obtain a spectral index of  $\alpha_{\text{int}} = -0.56 \pm 0.23$ , whereas using the peak flux densities yields  $\alpha_{\text{peak}} = -0.61 \pm 0.16$ . Both values are consistent with

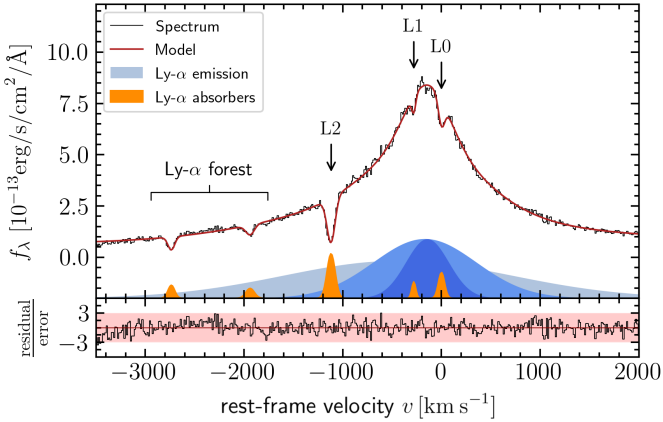


Figure 3.5: *Modelling Mrk 1044’s UV spectrum in the Ly- $\alpha$  window.* We use a multi-Gaussian model for the Ly- $\alpha$  emission (blue), and the absorbing systems (orange). The best-fit model (red line) reproduces the spectrum (black line) well in the selected wavelength range. Since the Ly- $\alpha$  systems L1 and L2 are accompanied by high metallicity absorption lines at the same velocity (Fields et al., 2005a), the absorbing clouds must be local to the galaxy.

each other, indicating once more that the source is spatially unresolved by VLA. As discussed by Ramírez-Olivencia et al. (2022), the peak flux is not affected by the systematic uncertainty from the different beam sizes between the C- and the X-band. We therefore consider the more robust result to be  $\alpha_{\text{peak}}$  and adopt its value for the following analysis.

### 3.3.5 Ly- $\alpha$ Absorption

Fields et al. (2005a) have identified two outflowing systems in Mrk 1044’s UV spectrum from Ly- $\alpha$ , NIV $\lambda$ 1239,43 and CIV $\lambda$ 1549,51 absorption. Using the line strengths and a photo-ionisation model they estimated several times solar metallicities for both absorbing clouds and concluded that the absorbers were ejected from the BLR local to the galaxy. In contrast to Fields et al. (2005a), we have used a kinematic model of a thin rotating disc to describe the stellar rotation in Paper I. This represents a robust measure for the galaxy systemic velocity  $cz = 4913.4 \pm 0.2 \text{ km s}^{-1}$  which

Table 3.3: *Summary of the outflowing systems.* The only component that we spatially resolve are the H $\alpha$  and H $\beta$  core components in the AGN spectrum (Fig. 3.1). Their kinematic parameters listed here correspond to those of the core component of the two-component 0''5 integrated two-component fit described in Sect. 3.4.1. The [O III] emitters O1 and O2 are spatially unresolved. Their maximum offset and size equals the systematic uncertainty of our measurement. For the Ly- $\alpha$  absorbers, the spatial extent is not constrained.

System	detection	location [pc]	extent [pc]	$v_r$ [km s $^{-1}$ ]	$\sigma$ [km s $^{-1}$ ]
H0	H $\beta$ , H $\alpha$ , [O III]	<2.1	$4.6 \pm 0.6$	$-211 \pm 22$	$218 \pm 7$
O1	H $\beta$ , H $\alpha$ , [O III]	<0.85	<1.7	$-144 \pm 5$	$165 \pm 17$
O2	H $\beta$ , H $\alpha$ , [O III]	<0.85	<1.7	$-560 \pm 20$	$251 \pm 31$
L1	Ly- $\alpha$	-	-	$-278 \pm 43$	$17 \pm 6$
L2	Ly- $\alpha$	-	-	$-1118 \pm 2$	$41 \pm 5$

allows for a self-consistent comparison between Mrk 1044's AGN, outflow and host galaxy properties after re-analysing the kinematics of the two UV absorbing systems.

We model Mrk 1044's UV spectrum in the Ly- $\alpha$ -window using a set of Gaussians and a linear approximation of the continuum. To reproduce the broad emission line shape, we require three components whereas a single Gaussian is sufficient to model the absorption line shapes. To find the best-fit parameters, we use the same technique that is described in Sect. 3.3.1. The result of this process is shown in Fig. 3.5. For the absorbers that we employ for the following discussion, the kinematic parameters for the individual components are listed in Table 3.3. The broad component appears blue-shifted in the spectrum since Ly- $\alpha$  is a resonant line where the photons gain momentum by scattering on the fast-moving BLR clouds. Another reason might be that the BLR geometry might not be entirely symmetric. If the receding side of the BLR is obscured by dust, the observed Ly- $\alpha$  emission line is skewed towards the blue.

There are two absorbers with velocities  $-1937 \pm 6$  km s $^{-1}$  and  $-2736 \pm 4$  km s $^{-1}$  which can be explained by foreground extinction from the Ly- $\alpha$  forest (Fields et al., 2005a). The different systematic velocity explains the nature of the Ly- $\alpha$  absorbing system L0 that is located at the galaxy rest-frame with  $v_r(\text{L0}) = 0.9 \pm 3.8$  km s $^{-1}$ . Most importantly, we recover the two outflowing systems L1 and L2 for which we measure systematically higher velocities for the absorbing features compared to Fields et al.

(2005a). Both systems are local to the galaxy as they show corresponding absorption from N V and C IV. We measure the outflow velocity of the absorbing systems L1 and L2 as  $v_r(\text{L1}) = -278 \pm 43 \text{ km s}^{-1}$  and  $v_r(\text{L2}) = -1118 \pm 2 \text{ km s}^{-1}$ , respectively.

## 3.4 Discussion

There are multiple outflowing systems present in Mrk 1044's outflow, both in optical emission and UV absorption. In Table 3.3 we summarise their kinematic properties and their distance from the nucleus. In the following we discuss the ionised gas excitation mechanism close to the galaxy nucleus and limitations of the diagnostics. Furthermore, we discuss whether we can link the different outflow velocities between [O III]-emitters and Ly- $\alpha$ -absorbers using a geometric model. Finally, we estimate the mass outflow rates and energetics and discuss the future impact of the multi-phase outflow on the host galaxy star formation.

### 3.4.1 Nuclear Excitation Mechanism

In Paper I we have shown that Mrk 1044 has a high star formation rate that is concentrated in a circumnuclear ellipse (CNE). The 3''-integrated emission line ratios have shown that all spaxels in Mrk 1044's CNE are located in the star forming regime. But also in the very centre at the location of the outflow, the line ratios seem to favour SF as the dominant excitation mechanism. However, after disentangling the host emission from the resolved outflow H0, a closer look onto the forbidden line ratios suggests that the situation is more complicated.

#### Nuclear Star Formation Hidden by the Outflow

From the multi-component model of the central region in Sect. 3.3.3 we compile the BPT diagnostic diagram that is shown in Fig. 3.6. It contains the data from the spatially resolved 8 $\times$ 8 co-added spaxels that belong to the star-forming CNE (see Paper I) together with the 0''5-integrated values for the host and outflow component. By definition, the host component is located in the galaxy rest-frame. It occupies the same area as the resolved CNE-spaxels. Although the host component may contain

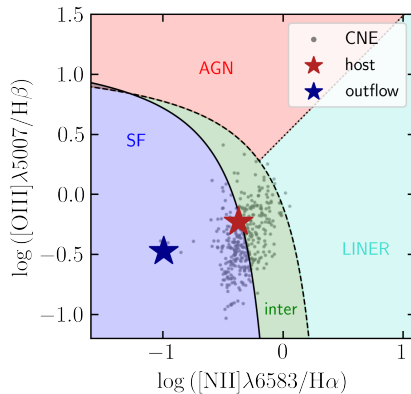


Figure 3.6: *BPT diagnostics of the extended outflow H0*. The grey data points correspond to the  $8 \times 8$  co-added spaxels that belong to the star-forming CNE (see Paper I). The stars represent the two components that are present in the  $0''.5$ -integrated spectrum that is shown in Fig. 3.3. The host component (red star) is consistent with SF-classification of the line ratios recovered in the CNE. For the outflowing component (blue star), both  $[\text{O III}]$  and  $[\text{N II}]$  emission might be suppressed due to collisional de-excitation in the high density gas. The BPT classification of the outflow as SF-ionised might therefore be misleading.

a significant amount of beam-smearred emission from the CNE, the host  $[\text{S II}]$  emission peaks in the centre, which implies that it cannot be beam-smearred emission alone. Thus, even within the central  $0''.5$  there must be gas present at relatively low densities  $n_e < 4 \times 10^3 \text{ cm}^{-3}$  the critical density of  $[\text{S II}]$  (De Robertis & Osterbrock, 1986)).

Combining the above findings, it indicates that the host galaxy star-formation in the CNE is not limited to the distance of  $\sim 300 \text{ pc}$  from the nucleus. It extends down to  $< 0''.5$  ( $< 160 \text{ pc}$ ) from Mrk 1044’s nucleus, but is heavily blended by the beam-smearred emission of the ionised gas outflow. Following the same procedure as in Winkel et al. (2022), we use the  $0''.5$ -integrated line flux from the host galaxy to estimate the  $\text{SFR} = 5_{-3}^{+5} \times 10^{-2} M_{\odot} \text{ yr}^{-1}$  that is ‘hidden’ by the beam-smearred emission from the luminous ionised gas outflow.

### High Outflow Gas Densities

Compared to the host components, the line fluxes associated with the outflowing 'wing'-component H0 have a larger systematic uncertainty in the region around the narrow  $\text{H}\alpha + [\text{N II}]$ . This is caused by the blended emission from host and outflow components between  $[\text{N II}]$  and  $\text{H}\alpha$  and the relatively low signal-to-noise. While we detect the  $[\text{O III}]$ -wing, the kinematically corresponding  $[\text{N II}]$  emission is weak such that we could only estimate an upper limit from the level of the spectral noise (see Sect. 3.3.3). The strong line ratios appear to unambiguously locate Mrk 1044's ionised gas outflow in the SF regime of the BPT diagnostic. We argue, however, that the BPT-classification of the outflow is misleading.

The total ionised gas mass ejected by the outflow from  $< 4.6 \text{ pc}$  is  $10^3 M_{\odot} \text{yr}^{-1}$ . Comparing with the relation for SF-driven outflows, the mass outflow rate exceeds the prediction by four orders of magnitude (Fluetsch et al., 2019; Stuber et al., 2021, see also Sect. 3.4.3). We conclude that Mrk 1044's outflow cannot be star-formation driven but must be powered by the radiation field of the luminous AGN. In this scenario, however, the AGN photo-ionisation is expected to dominate the emission line ratios.

A physical explanation that resolves the contradiction might be related to the compactness of the outflow. Considering that it has not yet expanded to host-galaxy scales beyond a few pc, the entire gas must be contained in a significantly smaller volume compared to the kiloparsec-scale outflows of the extended narrow line region (ENLR). At less than a few pc distance from the nucleus we therefore expect significantly higher outflow gas densities. If it exceeds the critical density of  $[\text{N II}]$  and  $[\text{O III}]$ , the bulk of the ions collisionally de-excite and thus suppress the forbidden emission lines. Assuming an electron temperature of  $T_e = 10^4 \text{ K}$  we estimate the electron density to be between the critical densities of  $[\text{N II}]$  and  $[\text{O III}]$  respectively, that is  $8.7 \times 10^4 \text{ cm}^{-3} < n_e < 7 \times 10^5 \text{ cm}^{-3}$  (De Robertis & Osterbrock, 1986). In this scenario the BPT classification of the outflow as SF-ionised can be explained by the high gas density, even if the actual excitation mechanism is related to the AGN radiation field. Therefore, the BPT diagnostic is not a reliable tool to constrain the underlying ionisation mechanism in the presence of high density ionised gas dominating an unresolved structure. Combining the above arguments we suggest that Mrk 1044's ionised gas outflow is likely AGN-driven.

### 3.4.2 Exploring a Geometric Model for the Unresolved Outflow Component

In 3.3.1 and Sect. 3.3.5 we have described that in each [O III]-emission and Ly- $\alpha$  absorption, two spatially unresolved outflowing systems are present. A summary of the derived kinematic parameters is listed in Table 3.3. We notice that velocity ratios among the [O III]-emitters ( $v_{\text{O2}}/v_{\text{O1}} = 3.9$ ) and the Ly- $\alpha$  absorbers ( $v_{\text{L2}}/v_{\text{L1}} = 4.0$ ) are similar. Furthermore, the velocity ratios between the faster and the slower components respectively match ( $v_{\text{L2}}/v_{\text{O2}} = 2.0$ ,  $v_{\text{L1}}/v_{\text{O1}} = 1.9$ ). Motivated by this constant factor, we aim to identify the systems with each other and discuss whether the integrated [O III] emission line shape can be explained through a geometric alignment.

In order to constrain the geometry, we use a forward modelling approach to predict the shape of the [O III] emission lines based on an expanding shell geometry. We parameterise the model by the inclination  $i$  of the ionised gas outflow velocity with respect to the line-of-sight, the 'narrowness'  $\alpha/\theta_0$  that describes the radial dependence of the shells' intrinsic luminosity profile in units of the half-opening angle  $\theta_0$ , and the flux ratio between the two shells  $r$ . We use a forward modelling approach to constrain the parameters by fitting the [O III] emission line shape. A detailed description of the method is described in the Appendix 3.6.2.

The geometric model predicts highly inclined shell caps ( $i = 79 \pm 8^\circ$ ) which are centrally concentrated  $\alpha/\theta_0 = 0.2 \pm 0.1$ . Within the uncertainties, the result on the inclination is independent of the exact value of the BLR opening angle and how centrally concentrated the outflow is ( $0.01 < \alpha/\theta_0 < 1$ ).

#### Expanding Shell Model versus Dust Torus Model

The AGN unification model predicts that an active nucleus possesses a compact strong radiation source around the SMBH that is surrounded by a high velocity emission-line region, the BLR. The relatively small scatter of the half-opening angles of the AGN dust-tori of  $\sim 60^\circ$  (Ricci et al., 2017) suggests that the optical classification is a reliable indicator for the orientation of the obscuring dust torus. For Mrk 1044's multi-phase outflow, the expanding shell model fails to reproduce the [O III] emission line shape for  $i \lesssim 60^\circ$ . At larger inclination, however, the dust obscuration

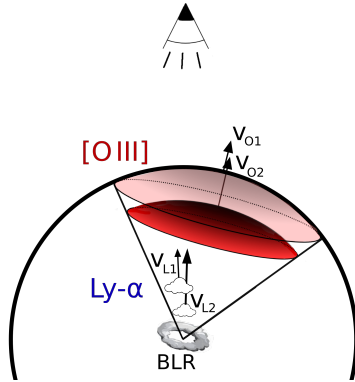


Figure 3.7: *Qualitative illustration of a possible alignment of the unresolved outflowing systems.* Combining the dust torus model with the expanding shell model, the Ly- $\alpha$  absorption cannot be spatially linked with the [O III] emitting cloud. Hence, the inclination of the system as well as the geometry of the [O III] emitting structure is unconstrained. Compared to the extended [O III] emitting region, the Ly- $\alpha$  clouds are likely to be located closer to the AGN engine due to their higher velocity.

from the torus encompassing the nucleus is expected to block the view into the BLR, which contradicts the type-1 nature of Mrk 1044.

One way to resolve the tension is that Mrk 1044's BLR obscuration may differ from the nearby low-luminosity Seyfert galaxies for which the AGN unification model was originally developed. From the Swift-Burst Alert Telescope (BAT) selected local AGN sample, Ricci et al. (2017) reported that the AGN obscured fraction is mainly determined by the Eddington ratio  $\lambda_{\text{Edd}}$ . They concluded that the main physical driver of the torus diversity is the accretion rate, which regulates the torus covering factor by means of radiation pressure. A clumpy torus (Schartmann et al., 2008; Stalevski et al., 2019) provides a more accurate description of the relationship between X-ray and mid-IR luminosities (Nenkova et al., 2008; Stalevski et al., 2012; Hönig & Kishimoto, 2017) and also been resolved for individual systems with high-resolution mid-IR imaging (e.g. Isbell et al., 2021). It is unclear whether the same orientation-based unification model involving a smooth torus is directly applicable to a highly accreting system like Mrk 1044. Nonetheless, Marin & Antonucci (2016) argued that the

probability to see a type-1 source at high inclination is almost zero. Based on the polarisation properties of AGNs in the 3CRR catalogue the authors concluded that the optical classification is a reliable indicator for the BLR orientation.

A less drastic solution for the mismatch between the inclination and Mrk1044's unobscured nucleus is to discard our toy model's rigorous assumptions on the geometry multi-phase outflow. Since we have not spatially resolved any of the components, the Ly- $\alpha$  absorbing clouds may not be linked to the [O III] emitting clouds. The different kinematics between the Ly- $\alpha$  absorbers and [O III] emitters could thus be a reflection of the inhomogeneity of the ISM on sub-pc scales regarding the ionisation conditions and the density distribution. Compared to the [O III] ionised gas, the Ly- $\alpha$  absorbers have higher velocity but smaller dispersion. This can be understood if the outflow is launched from accretion disc scales and entrains the ambient gas, thus gradually decreasing its bulk velocity while increasing the dispersion/turbulence due to the interactions with the surrounding ISM (Gaspari & Sądowski, 2017). This can also potentially trigger a CCA condensation rain (see Section 3.4.5). In an alternative interpretation, the outflow is intrinsically elongated but aligned with the line-of-sight. Due to the optically thin [O III] clouds, a velocity gradient within the medium would increase the integrated observed line width and mimic a high dispersion of the spatially unresolved structure. Both explanations favour that the [O III] emission occurs at larger distance from the nucleus than the Ly- $\alpha$  absorption. A qualitative illustration of this alignment is shown in Fig. 3.7 where the fast Ly- $\alpha$  absorbing clouds are located closer to the nucleus. We note that the inclination and geometry of the [O III] clouds remain unconstrained. For the following discussion, we therefore do not adopt the specific value that predicted by the expanding shell model.

### 3.4.3 Outflow Energetics and Mass Outflow Rates

Despite the compactness of the ionised gas outflows at present day, it will propagate through the ISM of the host galaxy. Once the shock front reaches the molecular gas from which the CNE produces stars, the outflow's energy and momentum will induce turbulence into the ISM (e.g. Wittor & Gaspari 2020). To estimate the future impact on the host galaxy star formation, we compute the current mass, energy and momentum ejec-

Table 3.4: *Outflow energetics and outflow rates.* From left to right the columns describe the quantity, the unit and the derived value for the ionised gas outflow system H0, O1 and O2 respectively. We compute the mass loading factor for the scale over which the resolved outflow is beam-smearred as well as for the integrated star forming CNE ( $\eta_{\text{CNE}}$ ) and the entire host galaxy ( $\eta_{\text{tot}}$ ) which have not yet been reached by the expanding outflow.

		H0	O1	O2
$A_{\text{H}\alpha}$	[mag]	1.5	3.7	2.2
$\log(L_{\text{H}\alpha})$	[erg s <sup>-1</sup> ]	39.3	42.4	41.5
$M_{\text{ion}}$	[10 <sup>5</sup> M <sub>⊙</sub> ]	0.01	10.5	1.2
$\dot{M}$	[M <sub>⊙</sub> yr <sup>-1</sup> ]	0.002	15	7
$\log(\dot{p})$	[dyne]	30.5	34.1	34.4
$\log(\dot{E})$	[erg s <sup>-1</sup> ]	37.6	41.0	41.8
$\eta_{0''.5}$		0.05	276	127
$\eta_{\text{CNE}}$		0.01	80	37
$\eta_{\text{tot}}$		0.005	21	10

tion rates released through the ionised gas outflow. We stress that the following derivations require an assumption about the morphology of the [O III] emitting clouds and their velocity as derived in Sect. 3.4.2. As discussed in the previous section, the Ly- $\alpha$  absorbers may not be spatially associated with the ionised gas outflow. We therefore use the velocities of the [O III]-emitters for the following derivations.

As a first step, we derive the total H $\alpha$ -flux of the outflowing components O1 and O2 by integrating over the individual components' flux maps extracted in Sect. 3.3.2. From the Balmer-decrement H $\alpha$ /H $\beta$  and the Milky Way-like attenuation curve Cardelli et al. (1989), we derive the attenuation analogously to Paper I. As described in Husemann et al. (2016a), the ionised gas mass can then be estimated from the extinction-corrected intrinsic luminosity  $L_{\text{H}\alpha}$  as

$$M_{\text{ion}} = 3.4 \times 10^6 \left( \frac{100 \text{ cm}^{-3}}{n_e} \right) \left( \frac{L_{\text{H}\alpha}}{10^{41} \text{ erg s}^{-1}} \right) M_{\odot}. \quad (3.1)$$

Due to the missing [S II] and [N II] emission (see Sect. 3.4.1), we assume a lower limit on the electron density  $n_e = 8.7 \times 10^4 \text{ cm}^{-3}$ , the critical density

of [N II]. In this way we ensure that the outflow masses and energies are not underestimated.

The estimated mass outflow rate depends on the assumed outflow morphology (Cicone et al., 2014; Veilleux et al., 2017). Since the UV absorbers have relatively low velocity dispersion, we consider thin shells to be the most probable description of the [O III] outflow morphology. However, in order to achieve a consistent comparison between our results and the scaling relations from Fiore et al. (2017), we assume a conical outflow geometry which lowers the derived values by a factor of approximately three. We compute the ionised gas mass outflow rate as

$$\dot{M}_{\text{OF,cone}} = 3 \times \left( \frac{v_{\text{OF}}}{100 \text{ km s}^{-1}} \right) \left( \frac{M_{\text{ion}}}{10^7 M_{\odot}} \right) \left( \frac{1 \text{ kpc}}{R_{\text{OF}}} \right) M_{\odot} \text{ yr}^{-1} \quad (3.2)$$

where  $v_{\text{OF}}$  is the outflow velocity and  $R_{\text{OF}}$  is the size of the homogeneously filled cone.

In addition to the mass outflow rate, we estimate the momentum injection rate  $\dot{p}_{\text{OF}} = v_{\text{OF}} \dot{M}_{\text{OF}}$  and the kinetic energy injection rate as  $\dot{E}_{\text{kin}} = 0.5 v_{\text{OF}}^2 \dot{M}_{\text{OF}}$ . Finally, we compare the SFR on different spatial scales and the mass injection rate from the AGN-driven outflow by computing the mass loading factor as  $\eta = \dot{M}_{\text{OF}}/\text{SFR}$ .

The results for each of the outflowing components are listed in Table 3.4. The energetics of Mrk 1044's outflow properties are affected by several systematic uncertainties. Especially the electron density  $n_e$  and the size of the system might underestimate each of the derived quantities, as we could only estimate lower and higher boundaries respectively. Nonetheless, the derived outflow properties hold some important implications especially for the future impact on the host galaxy discussed in Sect. 3.4.5. The two unresolved [O III] are luminous and dominate the outflow mass and energy budget by four orders of magnitude. The total kinetic energy of the outflows is  $7.3 \times 10^{41} \text{ erg s}^{-1}$  which corresponds to 0.2% of Mrk 1044's bolometric luminosity ( $3.4 \times 10^{44} \text{ erg s}^{-1}$ , Husemann et al. 2022). This favours the possibility of an energy-driven ionised gas outflow, if the photons couple with a comparable efficiency to the gas in the host galaxy ISM.

### 3.4.4 Origin of Mrk 1044's Radio Emission

Due to the radio-quiet nature of Mrk 1044 and the lack of extended radio jets, its nuclear radio emission could be produced by a multitude of processes. This includes the accretion disc coronal activity, an AGN driven wind, free-free emission from photo-ionised gas, or nuclear star formation. The radio spectra of H II regions is shaped by the free-free emission which, in the optically thin limit, produces a nearly flat radio spectrum with  $\alpha \sim -0.1$ . Together with the steep synchrotron spectrum from supernova remnants, the integrated radio emission of H II regions is expected to have a characteristic spectral index of  $\sim -0.7$  which is consistent with the observations of star-forming galaxies (Condon, 1992; Panessa et al., 2019; Pérez-Torres et al., 2021). To test whether the unresolved nuclear SFR is sufficient to produce the Mrk 1044's nuclear radio emission, we estimate the SFR from the observed radio continuum luminosity and the calibration from Murphy et al. (2011):

$$\frac{\text{SFR}}{M_{\odot}\text{yr}^{-1}} = \left[ 2.18 \left( \frac{T}{10^4 \text{ K}} \right)^{0.45} \left( \frac{\nu}{\text{GHz}} \right)^{-0.1} + 15.1 \left( \frac{\nu}{\text{GHz}} \right)^{\alpha^{\text{NT}}} \right]^{-1} \quad (3.3)$$

$$\times \frac{L_{\nu}}{10^{27} \text{ erg s}^{-1} \text{ Hz}^{-1}}.$$

Here,  $\alpha^{\text{NT}}$  corresponds to the non-thermal spectral index for which we use the value  $\alpha_{\text{peak}} = -0.61 \pm 0.16$  measured between 5 GHz and 10 GHz (see Sect. 3.3.4). Using Mrk 1044's C-band luminosity and an electron temperature of  $10^4$  K we use this relation to estimate a star formation rate of  $\text{SFR} = (0.81 \pm 0.45) \times 10^{-3} M_{\odot}\text{yr}^{-1}$ . The associated uncertainty involves both the error of our measured parameters (see Sect. 3.3.4) together with the 50 percent uncertainty from relation (3.3). Since the SFR estimated from the radio luminosity is exceeded by the  $0''.5$  unresolved SFR derived from Mrk 1044's H $\alpha$ -luminosity by one order of magnitude (see Sect. 3.4.1), we cannot exclude that the radio emission is partially produced by SF-related processes. Thus, we conclude that neither the spectral index nor the amount of flux allows us to distinguish whether Mrk 1044's radio emission originates exclusively from AGN-related processes or the nuclear star formation.

### 3.4.5 Outflow Expansion from Nuclear to Galaxy Scales

To test whether the individual components of the multi-phase outflow have the potential to reach galactic scales, we use the ‘k-plot’ diagnostic from Gaspari et al. (2018). The k-plot compares the line-of-sight (LOS) velocity dispersion with the LOS velocity shift. It is useful to assess the role of chaotic and turbulent motions in addition to laminar and bulk motions, and related key physical processes such as chaotic cold accretion (CCA) and AGN outflows. We use the pencil-beam approach, which better traces individual clouds or small-scale gas elements (e.g. Rose et al. 2019; Maccagni et al. 2021; North et al. 2021; Temi et al. 2022).

Fig. 3.8 shows how the CNE gas (black points) and nuclear components (red/green) of Mrk 1044 compare with the multi-phase k-plot retrieved via high-resolution hydrodynamical simulations (yellow 1-3 $\sigma$  contours; see Gaspari et al. 2018) and related observational sample of diverse galaxies (grey). The ionised gas in Mrk 1044 star-forming CNE with the highest velocity shows a symmetric spread of the dispersion within the 2 $\sigma$  contours. The tail towards low velocities at constant dispersion is more heavily associated with the rotating disc. Despite the dominance of rotation, several black points reside well within the 1- $\sigma$  CCA region, suggesting that such gas elements can also be prone to turbulent condensation. This is a common scenario in spiral galaxies where the turbulent Taylor number is on average above unity, hence favouring a rotating CCA (Gaspari et al. 2015).

Compared to the region the resolved data points of the rotating CNE occupy, the unresolved nuclear components separate. The faster components – O2 and L2 – are located in the 3 $\sigma$  area and are thus expected to be less affected by condensation and CCA. This suggests that their momentum is currently little dissipated by the interaction with the surrounding medium, which enables the outflows to escape at least from the high-density nuclear region. Due to their lower velocities, systems O1 and L1 are located within the 1.5 $\sigma$  yellow confidence region. This can be interpreted that such outflowing components have started to deposit their kinetic energy into the ISM, increasing the turbulence of the ambient medium and potentially stimulating an initial CCA rain.

It is interesting to note that the [O III] outflows have systematically higher velocity dispersion than the rest of the system. This can be interpreted in a few ways. On the one hand, the highly ionised outflow component could simply have a stronger intrinsic turbulence along its

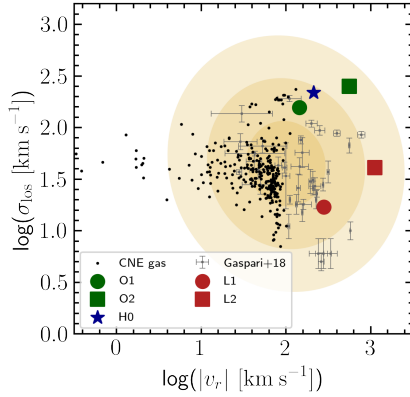


Figure 3.8: *Kinematic plot (k-plot) of the line broadening versus the line shift.* It highlights the relative importance of chaotic/turbulent motions versus laminar/bulk motions and the connected physical processes. The yellow contours show the 1-3 $\sigma$  confidence intervals for the chaotic cold accretion (CCA) feeding mode found by high-resolution hydrodynamical simulations (Gaspari et al., 2018). The grey data points indicate measurements of warm and cold condensed gas in diverse galaxies (Gaspari et al. 2018). The ionised gas of Mrk 1044’s CNE is shown as black data points. The tail towards lower velocity is mainly driven by an inclined rotating disc, with several points overlapping with the main CCA area. In contrast, the four nuclear components (red and green points) have substantially higher bulk velocity indicating that they are not kinematically associated with the disc, but rather outflowing, in particular O2 and L2 (squares). O1 and L1 appear to interact more significantly with the surrounding medium, thus being more prone to turbulent condensation.

spine, which is indicative of the entrainment of surrounding material that increases the turbulence in the ionised gas. On the other hand, it could be interpreted as a projection effect if the [O III] gas velocity is directed at a small inclination with respect to the line-of sight. In this case the [O III] emission could be affected by beam smearing as opposed to the kinematics from Ly- $\alpha$  foreground absorption. The observed [O III] line width might therefore reflect a systemic velocity gradient within the outflow and might not be interpreted as a dispersion.

---

Future Impact on the Host Galaxy

Mrk1044's outflow carries a lot of mass in the ionised gas phase. To estimate its future impact on the host galaxy, we compare the summed energetics with the scaling relations of resolved galaxy-scale outflows. The left panel of Fig. 3.9 shows that compared to other AGNs at similar luminosity, Mrk 1044's ionised gas outflow lies within the scatter of the outflowing mass - AGN bolometric luminosity correlation from Fiore et al. (2017). It is more massive by  $\sim 1$  dex than average, whereas the kinetic power is consistent with the ionised gas outflows in lower luminosity AGNs. To compare the ionised gas outflow momentum rate with the AGN radiation momentum rate  $L_{\text{bol}}/c$ , we compute the wind momentum load as  $\dot{p}_{\text{OF}}/\dot{p}_{\text{AGN}} = 3.3$ . It is consistent with the wide spread of the extended ionised gas outflows reported in Fiore et al. (2017) and close to the expectation of  $\dot{p}_{\text{OF}}/\dot{p}_{\text{AGN}} = 1$  for a momentum conserving outflow predicted by the King (2003) model. Fig. 3.9 highlights that multi-phase outflows often carry a large amount of their mass and kinetic power in the molecular gas phase, especially at low AGN luminosities (see also Fluetsch et al., 2019; Veilleux et al., 2020). We therefore expect that the AGN-driven mass injection into the host galaxy ISM is even higher if Mrk 1044's outflow is accompanied by a molecular gas outflow.

An important difference when comparing Mrk 1044 with ionised gas outflows in nearby galaxies is that they extend over different spatial scales within the host galaxy. While the relation from Fiore et al. (2017) was calibrated for ionised gas winds that extend over  $> 1$  kpc, Mrk 1044's ionised gas outflow is compact ( $< 4.6$  pc) and located close to the galaxy nucleus ( $< 2.1$  pc). Its proximity to Mrk 1044's central engine is reflected in the mass loading factor  $\eta = \dot{M}_{\text{OF}}/\text{SFR}$  which relates the SFR with the mass outflow rate. The intrinsic extent over which the galaxy property that is extracted, in this case the SFR, does affect the result dramatically, as it is shown in the third panel of Fig. 3.9. While the outflow is located at parsec-scale distance from the nucleus, the SFR can be measured in different apertures. If we compare the mass outflow rate with the SF in its immediate vicinity, that is the SF 'hidden' by the beam-smearred outflow ( $< 160$  pc, see Sect. 3.4.1),  $\eta_{0''.5} = 276$  suggests that the outflow currently dominates the ISM properties of the host galaxy on a few  $\sim 100$  pc scales. Such a high mass-loading factor is in line with the picture of a young outflow that has recently been launched by the powerful AGN. Furthermore,

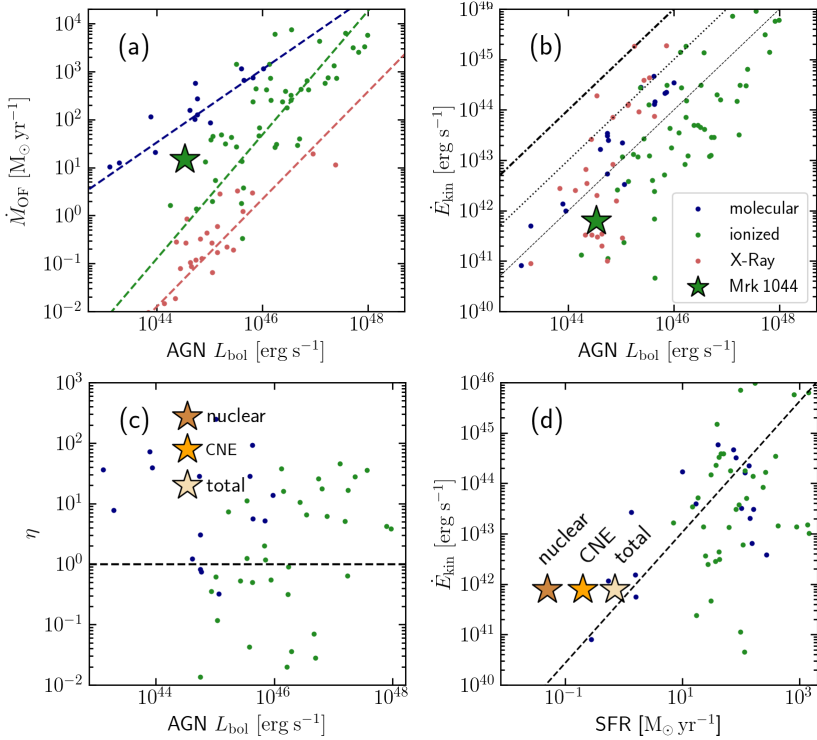


Figure 3.9: Comparing Mrk 1044’s integrated ionised gas outflow with AGN multi-phase outflow scaling relations. Coloured data points are taken from Fiore et al. (2017) and show the molecular gas outflows traced by CO, OH (blue), ionised gas outflows (green) and X-ray outflows (red). Panel (a) shows the outflowing ionised gas mass. Panel (b) shows the AGN wind kinetic power. Panel (c) shows the mass loading factor  $\eta = \dot{M}_{\text{OF}}/\text{SFR}$ . Here, the brown star represents Mrk 1044’s SF in the immediate vicinity ( $< 160 \text{ pc}$ ) from the centre, the orange point to that of the SF in the CNE and the yellow point to that of Mrk 1044’s galaxy-wide SFR. Panel (d) shows the kinetic outflow power as a function of SFR. Mrk 1044’s ionised outflow carries a lot of mass, with a mass injection into the ISM exceeds the current SFR in the immediate vicinity of the nucleus, but also compared to the galaxy-wide values.

the ionised gas outflowing mass exceeds Mrk 1044’s present day SFR, even if we compare it with the galaxy-wide SFR. However, this comparison should be regarded with caution as both quantities trace different regions of the host galaxy and the evolution of the outflow’s properties during its propagation through the ISM are largely unknown.

Since Mrk 1044’s ionised gas outflow inclination and the morphology are unconstrained, it is not clear how the outflow will impact the host galaxy. To estimate the maximum future impact on the host galaxy, we assume that the outflow is launched at large inclination relative to the galaxy rotation axis and carries its present-day mass and energy out to a few 100 pc from the nucleus. In this case it directly impacts the CNE and the galaxy disc where the host galaxy star formation is concentrated. The total mass outflow rate also exceeds the integrated star formation rate in the CNE ( $0.19 \pm 0.05 M_{\odot} \text{yr}^{-1}$ ) and the galaxy-wide SFR ( $0.70 \pm 0.17 M_{\odot} \text{yr}^{-1}$ ) by more than one order of magnitude. Mrk 1044’s multi-phase outflow may therefore have the potential to deprive the host galaxy from their molecular gas reservoir and eventually quench the host galaxy star formation. Based on the mass loading factor [Fiore et al. \(2017\)](#) argued that only powerful AGNs are able to drive the co-evolution between SMBHs and galaxies. In this interpretation Mrk 1044 would represent an uncommon example where the host galaxy evolution is regulated by the central SMBH despite the relatively low luminosity of its AGN if compared to the overall AGN population.

In the other extreme scenario the outflow is orientated perpendicular to the disc, the cold gas by which the SF in the CNE is fuelled will not be affected by the energy injection. Hence, we expect that in this case the outflow’s impact on the host galaxy is minor to none. The two extreme cases of outflow inclinations leave a wide range of possible scenarios in which the host galaxy SF may be quenched by the injection of turbulence into the ISM. Resolving the inclination of the accretion disc relative to the galaxy plane is therefore crucial to estimate the future impact of Mrk 1044’s outflow on the host galaxy.

### 3.4.6 Mrk 1044 - A Young AGN

In Paper I we have touched on the idea that Mrk 1044 as a NLS1 could be archetypal for a population of ‘young’ AGN that host a rapidly growing SMBH. There we have shown that the circumnuclear SF enriches the

ISM and shows potential signatures of ongoing BH feeding. SF is present even in the immediate vicinity of Mrk 1044’s nucleus (see Sect. 3.4.1), and might play a role in channelling the gas towards the centre as suggested by hydrodynamic simulations (Davies et al., 2007; Volonteri et al., 2015; Zhuang & Ho, 2020). Since circumnuclear SF continues to enrich the ISM and has not yet been affected by the energy injection from the expanding multi-phase outflow, this process might continue until the outflow propagates through the ISM.

To estimate a frame for the look back time at which of the ionised gas outflow was launched, we assume a constant LOS velocity by which the outflow escapes from the central engine. Since the outflow inclination cannot be robustly constrained by the geometric toy model discussed in Sect. 3.4.2, we assume that the outflow is launched perpendicular to the accretion disc. Further, we assume that the rotation axis of the accretion disc is aligned with that of the dust torus. In this case, the accretion disc inclination  $i$  of a type 1 AGN cannot be larger than the half-opening angle of the dust torus, since the torus would obscure the view to the BLR. We therefore assume Mrk 1044’s outflow inclination to be smaller than  $58^\circ$ , the median of the dust torus half-opening angle distribution (Ricci et al., 2017). From the intrinsic velocity  $v = v_{\text{LOS}}/\cos i$  and the projected distance from the nucleus  $d = d_{\text{proj}}/\sin i$  we estimate the timescale as

$$t \lesssim \frac{d_{\text{proj}}}{v_{\text{LOS}}} \tan i. \quad (3.4)$$

With the maximum projected offset from the nucleus of 0.85 pc (see Sect. 3.3.2) we infer that the two ionised gas outflow components were launched no longer than 9,900 yr (O1) and 3,500 yr (O2) ago. Using the upper limit for the location of the spatially resolved outflow H0, we estimate an upper limit for its age of  $\sim 25,000$  yr. The derived ‘age’ estimates should be regarded as an upper limit since interaction of the fast-moving ionised gas outflow with the host galaxy ISM would slow down the outflow during its expansion. Furthermore, if the outflow velocity is directed closer to the observer (i.e. at smaller inclination  $i$ ), the resulting timescale would be shorter. The picture of Mrk 1044 as a young AGN is consistent with the undisturbed kinematics that we could trace down to  $0''.5$  ( $\sim 160$  pc) from the centre (see Paper I). Furthermore, the ongoing star formation

in the CNE around Mrk 1044’s nucleus ( $\sim 300$  pc) has not been quenched by the energy injection from the multi-phase outflow. Even within the innermost 160 pc where the ionised gas outflow dominates, the integrated line ratios that belong to the host are consistent with ionisation through SF (see Sect. 3.4.1).

Since the distance of an AGN-ionised gas cloud to the AGN engine directly translates into a light travel time, the ENLR size can be interpreted as a proxy for the lifetime of a single AGN episode (Lintott et al., 2009; Keel et al., 2017; Husemann et al., 2022). At fixed luminosity, AGNs with more massive BHs would be statistically observed at much later times in their episodic phase than lighter BHs. This interpretation implies an evolutionary sequence for AGNs where systems hosting less extended ENLRs have a shorter AGN lifetime or are ‘younger’. The EV1 relation could be explained as a reflection of the time-dependence at which the AGN phase is observed. NLS1s, which are located in the tail of the EV1 relation, would represent the extreme end of the rest-frame difference between [O III]-core and systemic redshift. The interpretation of NLS1s as ‘young’ AGN would explain the relative weakness of their narrow [O III] emission lines by a combination of *i*) the absence of an AGN-ionised ENLR in the host galaxy *ii*) the compactness of the ionised gas outflow and *iii*) the high gas densities in the compact outflow (see Sect. 3.4.1). In this scenario, the prevalence of strong broad Fe II emission in the spectra of NLS1s which can be interpreted as the finite timescale on which AGN quenching is able to shut off the host galaxy star formation on nuclear scales.

Another aspect of the interpretation is that it explains Mrk 1044’s offset of the narrow [O III]-core from the galaxy systemic velocity. As we have demonstrated, the [O III]-core component is outflowing with  $-140 \text{ km s}^{-1}$  (Sect. 3.3.1) which is fundamentally different from many AGNs where the narrow [O III] traces the ENLR associated the galaxy rest-frame (e.g. Harrison et al., 2016; Husemann et al., 2022). If a young AGN drives the expanding outflow, this mismatch can be understood since the [O III]-core component traces a young structure that has a smaller intrinsic extent. Hence, the integrated narrow [O III] may trace different structures, depending on the age of the system. This implies that the outflow velocities of ‘young’ AGN cannot be estimated from the integrated emission line spectrum alone. Spatially resolving young AGN host galaxies and their

compact outflows is crucial to correctly interpret their spatial *and* kinematic structure.

A coherent picture for the recent activity of Mrk 1044’s BH growth emerges. Combining the arguments of *i*) a compact outflow, *ii*) unperturbed host kinematics and *iii*) SF-dominated radiation field in the close to the nucleus, we conclude that Mrk 1044’s AGN phase has been triggered recently. Following the idea that NLS1s host rapidly growing SMBHs at an early stage of their evolution, we predict that highly accreting AGN host galaxies with low-mass SMBHs show similar signatures close to the nucleus.

### 3.5 Summary and Conclusions

In this work we have combined IFU data from MUSE NFM-AO with the UV spectrum from HST to constrain the ionised gas properties of Mrk 1044’s outflow. We have detected two outflowing systems in both ionised gas emission and Ly- $\alpha$  absorption that are unresolved at the spatial resolution of MUSE NFM-AO. We have used a spectroastrometric approach to locate the ionised gas outflows traced by [O III] emission and estimate their energetics. Our key results are the following.

- Mrk 1044’s narrow core component O1 in which we detect H $\beta$ , H $\alpha$ , and [O III] emission is outflowing with  $v_{\text{O1}} = -144 \pm 5 \text{ km s}^{-1}$ . The [O III]-wing component O2 represents an additional component with  $v_{\text{O2}} = -560 \pm 20 \text{ km s}^{-1}$ .
- Both ionised gas outflows O1 and O2 are spatially unresolved and have a projected offset from the AGN location of smaller than 1 pc. These two outflows carry the majority of the ionised gas mass and energy and they have been launched no longer than  $\sim 10^4$  yr ago.
- Despite the compactness of Mrk 1044’s ionised gas outflow, its mass outflow rate and kinetic energy injection rate are comparable to typical AGN-driven ionised gas winds at a similar AGN luminosity. The high, present-day outflow velocity and high mass loading suggest that the outflow has the potential to expand to galaxy scales and to impact the ISM properties.

- Using a geometric toy model, we could not identify Ly- $\alpha$  absorbers with the unresolved [O III] via their kinematics. This emphasises the complex nature of the multi-phase ISM on sub-parsec scales.
- The gas densities in Mrk 1044's spatially resolved outflow H0 are above the critical density of the forbidden [S II] and [N II] line doublets, which implies that the classical BPT diagnostics cannot be used to constrain the underlying ionisation mechanism.

Our results demonstrate the importance of studying the AGN - host galaxy connection on different energy and density scales with spatially resolved observations. Although the ionised gas outflow can be identified from the AGN spectrum alone, Mrk 1044's compact multi-phase outflow stands out from well-studied examples of kiloparsec-scale extended outflows. The different outflow components, kinematics, and energetics highlight the complexity of the AGN feedback cycle, especially on the smallest galactic scales from where the outflow is launched. To better understand the role of the warm ionised gas in the immediate vicinity of accretion-mode AGNs, more IFU observations with high spatial resolution are required. Performing a similar analysis on a larger sample will help to constrain the impact of young, compact outflows on the host galaxy as well as the underlying physical mechanisms behind AGN feeding and feedback.

## 3.6 Appendix

### 3.6.1 Size of the Resolved Outflow H0

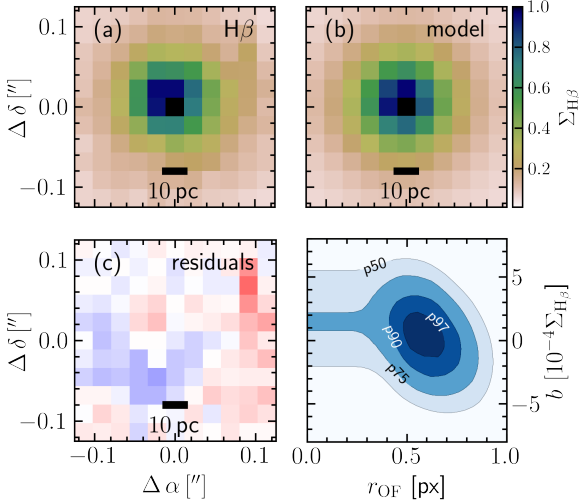


Figure 3.10: *Measuring the size of Mrk 1044’s spatially extended H $\beta$  outflow.* Panel (a) shows the flux map of the H $\beta$  outflowing component which we extracted as described in Paper I. Panel (b) shows the best-fitting model that consists of the empirical PSF convolved with a Gaussian kernel and a constant background flux. The residuals in panel (c) show that broadened PSF describes the H $\beta$  profile well. Panel (d) shows the  $\chi^2$  distribution in the parameter plane where a global minimum is present around 0.55 px (4.6 pc).

The system H0 is one of the identified ionised gas outflows’ components. It is present in the AGN-subtracted host data cube and therefore spatially resolved. In Fig. 3.10 we zoom in onto the central 0''.1 of the narrow H $\beta$  surface brightness map where the outflow flux, velocity and velocity dispersion peak. To constrain the outflow’s location and projected size, we fit the surface brightness profile with a model light distribution of an intrinsically extended source. Our model consists of (i) the empirical PSF extracted at H $\beta$  which we convolved with a Gaussian kernel  $r_{OF}$ , and

(ii) a constant background flux  $b$ . To find the best-fitting parameters, we minimise the S/N-weighted  $\chi^2$  sum of the  $H\beta$  residual flux distribution.

The best-fit model is shown in the top right panel of Fig. 3.10. It yields an intrinsic size of  $r_{\text{OF}} = 0.55 \pm 0.10$  px ( $4.6 \pm 0.6$  pc) from which we conclude that the source is spatially resolved at a  $>3\sigma$  confidence level. This extended component of the outflow is also present in  $H\alpha$  emission. Here, we follow the same method and retrieve an intrinsic projected extent of  $0.38 \pm 0.02$  px ( $3.2 \pm 0.1$  pc). Both values are consistent within the uncertainties, which suggest that both light profiles stem from the same structure. We measure the centroid of the light distribution which matches the AGN position with an uncertainty of  $0.22$  px ( $1.8$  pc). Our results are robust against choosing different spectral regions of the broad line windows for the empirical PSF extraction that is described in Paper I. Furthermore, our results do not change within the uncertainty if we use the AGN-subtracted host emission line maps presented in Paper I instead of the  $H\beta$  and  $H\alpha$  surface brightness maps that we retrieve from the spectroastrometric analysis. The former were generated from fitting the AGN-subtracted host emission with a single-Gaussian component, which is independent but fundamentally different method compared to the spectroastrometric measurement.

### 3.6.2 Geometric Expanding Shell Model

#### Constraining the Outflow Geometry

Here, we describe how we use a geometric model of two expanding shells to reproduce the  $[\text{O III}]$  emission line shape. With this model we can constrain the geometric alignment of the unresolved ionised gas outflow relative to the  $\text{Ly-}\alpha$  absorbers. The implication of the results are discussed in Sect. 3.4.2.

In contrast to the unresolved but intrinsically extended  $[\text{O III}]$  outflow, the UV spectrum only probes the line-of-sight absorption towards the high density BLR clouds. We can link the emitters and absorbers by assuming that a small fraction of the  $[\text{O III}]$ -emitting gas is also responsible for the  $\text{Ly-}\alpha$  absorption. In this scenario, the systematic velocity factor of  $\sim 2$  between  $[\text{O III}]$ -emitters and  $\text{Ly-}\alpha$ -absorbers may be the result of a projection effect.

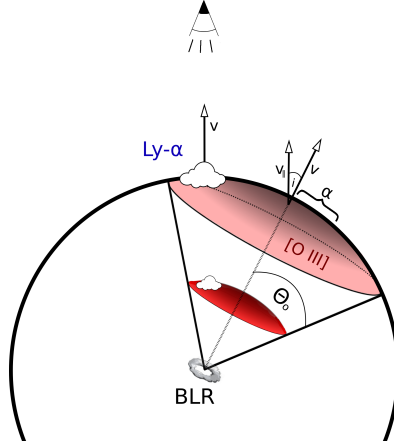


Figure 3.11: *Illustration of the expanding shell geometry.* The Ly- $\alpha$  occurs in the expanding shell, along the LOS towards the BLR with the velocity  $v$ . The [O III] emission originates from an intrinsically extended but spatially unresolved shell cap with a half-opening angle  $\theta_0$ , half-light radius  $\alpha$  and inclination  $i$ . The observer measures the integrated flux and thus measures a smaller velocity.

There exist different descriptions for outflow morphologies including uniformly filled cones (e.g. Cano-Díaz et al., 2012; Cresci et al., 2015; Fiore et al., 2017), hollow bi-cones (e.g. Müller-Sánchez et al., 2011) or thin shell structure (e.g. Rupke et al., 2005). In our case, the relatively narrow Ly- $\alpha$  absorption features have low velocity dispersion, which suggests that the absorbing structure is better described by a shell-like shock front scenario. We therefore assume that the ionised gas is distributed on two concentric shell caps with the AGN located in the origin. The shell caps expand radially with a velocity  $v$ . We further assume that the receding side is obscured by dust. Both shell caps have a half-opening angle  $\theta_0$  that is observationally constrained. Ricci et al. (2017) applied a torus model to a sample of Swift BAT AGN for which they constrained the median value of the torus half-opening angles to  $58 \pm 3^\circ$ . We adopt this value for our model, although varying  $\theta_0$  by  $\pm 10^\circ$  does not alter our results qualitatively. We assume that luminosity profile on the shell cap is centrally concentrated. We describe it by an exponential luminosity profile that declines radially with a half-light radius  $\alpha$  in units of the half-opening angle  $\theta_0$ . Thus,

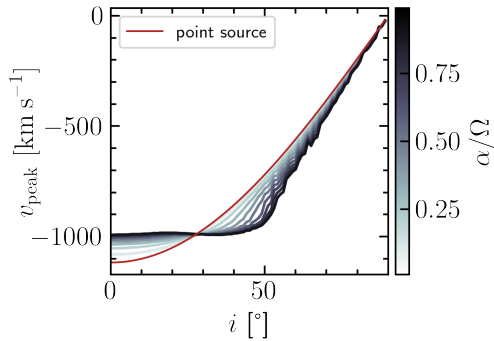


Figure 3.12: *Dependence of the emission line flux maximum corresponding velocity on inclination.* Independent of how concentrated the light profile is ( $\alpha/\theta_0$ ), the geometric model requires high inclinations of the [O III]-emitting shell to significantly reduce the peak velocity by a factor of approximately two.

$\alpha/\theta_0 = 1$  means that the half-light radius coincides with the half-opening angle. Furthermore, we include the luminosity ratio between the shells as a free parameter. An illustration of the geometric model is shown in Fig. 3.12. The two shells share the geometric parameters  $i$  and  $\alpha$ , but not for the expansion velocity  $v$  that is fixed to the measured velocity of the Ly- $\alpha$  absorbers.

### Predicting the Emission Line Shape

We use a forward-modelling approach to constrain the parameters of the expanding shell model from the [O III] $\lambda\lambda$ 4959,5007 emission lines. We predict the observed emission line shape with a numerical approach that involves the following steps.

- (1) As a first step, we sample the shell cap with  $10^5$  equidistant cells using the Fibonacci sphere algorithm<sup>4</sup>.
- (2) We incline the shell cap using a rotational coordinate transform.
- (3) For each of the cells we compute the line-of-sight velocity component and performed a binning in velocity space. This provides us with the predicted emission line shape.

<sup>4</sup>using random sampling or the golden spiral method deliver the same results

(4) To fit the rest-frame spectrum of Mrk 1044 we transform the distribution into the wavelength space using the expansion velocity of the shell together with the rest-frame wavelengths of the respective ion. With this method we generate a template of emission lines shapes, computed for a  $10^2 \times 10^2$  parameter grid with  $i = [0, 90)$  and  $\alpha = (0, 1]$ .

Since there are two emitters and absorbers respectively, our model requires a fast and a slow component. To illustrate the effect of the geometric parameters in Fig. 3.12, we show the dependence of the fast component's peak emission on the inclination of the shell caps. Higher inclinations move the peak of the line closer to the systemic velocity  $v_{\text{sys}} = 0 \text{ km s}^{-1}$ , whereas the effect of the central concentration  $\alpha/\Omega$  depends on the inclination of the system. The solution for the line shape for the slow component behaves equivalently.

To find the linear combination of the fast and slow component that fits the [O III] best, we use a non-negative least square optimisation algorithm. Since we only see the approaching side of the outflow, we only model the blue shoulder of the [O III]  $\lambda\lambda 4959, 5007$  in the with corresponding velocity range  $[v_{L2}, 0 \text{ km s}^{-1}]$ . To get an estimate of the parameters' uncertainties, we use a Monte Carlo approach. From the original AGN spectrum we generate  $10^4$  mock spectra by randomly varying the flux density within the uncertainty. From the resulting posterior distribution, we adopt half of the 16<sup>th</sup> to 84<sup>th</sup> percentile range for the parameters' uncertainties.

### The Best-Fitting Geometric Model

Using the concentrically expanding shell model, we retrieve an inclination of  $i = 79.1 \pm 8.4^\circ$ . The best-fit concentration  $\alpha/\theta_0 = 0.09 \pm 0.04$  indicates a relatively narrow ('jetted') luminosity profile. The best-fit geometric parameters have an intuitive explanation. The width of the [O III] primarily determines the concentration of the luminosity profile. Since we do not observe a double-peaked emission line, both emission lines have to be close in wavelength. This can only be achieved at high inclinations, as shown in Fig. 3.12.

Our results do not change within the uncertainties if the [O III] lines are fitted independently. Moreover, our results do not depend on how we define the 'blue shoulder', i.e. slightly adjusting the wavelength-borders around the emission line does not affect the results significantly. Introducing another geometric parameter leads to an over-fitting of the [O III]

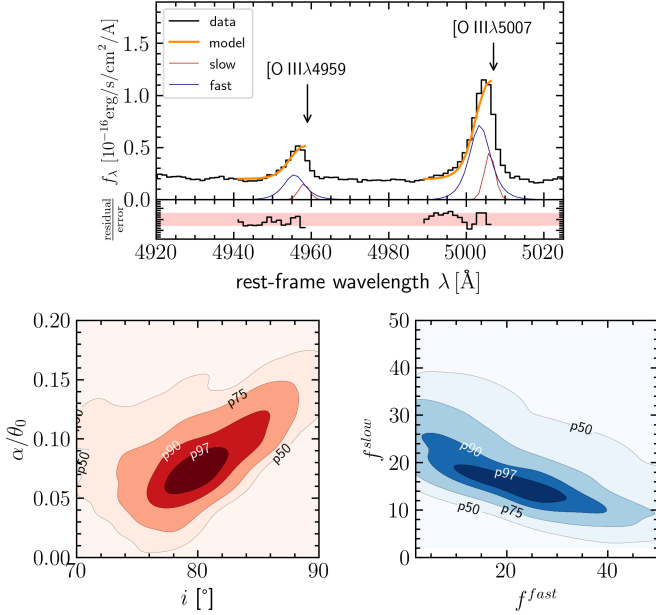


Figure 3.13: *Best-fitting model for the blue shoulder of Mrk 1044's [O III] $\lambda\lambda$ 4959,5007 emission line.* The left panel shows the AGN spectrum (black line) around the [O III] doublet emission. The best-fit model (orange line) reproduces the line shape well. Both the slow (red line) and the fast shell (blue line) contribute to the asymmetric line shape. The panels on the right show percentile regions of the posterior distribution for the geometric parameters (left) and the flux contribution (right) respectively.

emission lines given their relatively low spectral S/N. Furthermore, we have tested different parameterisations to describe the emission line profile. In particular, different geometric descriptions like that of a hollow cone (e.g. Das et al., 2006; Müller-Sánchez et al., 2011; Venturi et al., 2018) require similar inclinations to explain the [O III] line shape. We conclude that the absence of a single-peaked [O III] emission line can only be reproduced by a concentrically expanding shell model if the system is highly inclined with respect to the LOS.



---

# Resolving the gas transport mechanism in NGC 4593

This chapter summarises the current status of ongoing work. Dr. Knud Jahnke initiated the project, led the data proposal for the ALMA and MUSE NFM high-resolution datasets critical to this project and contributed to writing the introduction. Dr. Juan Antonio Fernández Ontiveros was responsible for the reduction of the ALMA dataset, while I processed the two MUSE datasets. Dr. Timothy Davis provided support for the analysis. For the evaluation of the results, I received assistance from all of the aforementioned, as well as from Dr. Françoise Combes. Our team plans to publish the results after additional testing to further strengthen our findings and their interpretation.

N. Winkel<sup>1</sup>, K. Jahnke<sup>1</sup>, J. A. Fernández Ontiveros<sup>2</sup>, T. A. Davis<sup>3</sup>, F. Combes<sup>4</sup>

<sup>1</sup>Max-Planck-Institut für Astronomie, Königstuhl 17, D-69117 Heidelberg, Germany

<sup>2</sup>CEFCA, Plaza San Juan 1, 44001 Teruel, Spain

<sup>3</sup>Cardiff Hub for Astrophysics Research & Technology, Cardiff University, CF24 3AA, UK

<sup>4</sup>LERMA, Observatoire de Paris, CNRS, Sorbonne Univ., Paris, France

## Abstract

Supermassive black holes (SMBHs) located in the hearts of galaxies grow primarily through gas accretion, visible as active galactic nuclei (AGNs). Over the past 10 billion years, most SMBH mass growth occurred in AGNs with high specific mass accretion rates. Fuelling AGNs requires substantial gas transport from kiloparsec scales down to the black hole sphere of influence. Thus far, however, a secular AGN feeding mechanism that could sustain such rates over the times scales relevant for BH growth has not been identified. After a blind search for a nearby AGN accreting at several percent of the Eddington limit, NGC 4593 has the required characteristics to resolve the associated processes in the host galaxy. We combine VLT/MUSE observations, together with ALMA observations to map NGC 4593's stellar, ionised gas and molecular gas kinematics. A prominent single-arm spiral with  $\log(M_{\text{mol}}/M_{\odot}) = 7.9 \pm 0.3$  extends over two curls from 1.3 kpc down to 100 pc from the AGN. Its centre of mass is offset from the AGN by 72 pc, causing locally and temporally varying torques. While the induced net torque budget is negative across the single arm spiral, the gas self-gravitation seems to be insufficient to explain the measured radial gas inflows of  $2.8 M_{\odot}/\text{yr}$ . With typical depletion time scales of  $\langle t_{\text{dep}} \rangle = 11 \text{ Gyr}$ , star formation along the single-arm spiral is inefficient. Instead, the gas mass inflow rates exceeds the SFR by a factor of 2, efficiently transporting gas from 1.5 kpc to the vicinity of the BH sphere of influence ( $\sim 10 \text{ pc}$ ). The observed  $m=1$  structure is indicative of an AGN feeding mode predicted by [Hopkins & Quataert \(2010b\)](#), which could represent an important missing link connecting galaxy and BH scales and potentially explain a significant fraction of cosmic SMBH growth since  $z = 2$ . While diagnosing the characteristic features is currently impossible for more distant luminous quasars, the ongoing Euclid Wide Survey will provide the data to test this hypothesis within the next two years.

# Chapter 4 | Resolving the gas transport mechanism in NGC 4593

## 4.1 Introduction

Supermassive black holes (SMBHs) are located in the hearts of massive galaxies. Their enormous mass growth over cosmic time is governed by accretion of material as manifested in bright active galactic nuclei (AGNs). To sustain the AGN phase, gas must be transported from several kiloparsec galaxy scales to the very central parsec, a process which involves multiple scales and phases. Major galaxy mergers provide an efficient channel to transport gas. They are known to trigger luminous quasar phases, i.e. AGNs with the highest specific accretion rates. However, major galaxy mergers, are often not required conditions for BH fuelling: Since cosmic noon the bulk of BH mass density growth is not associated with galaxy merging ( $z = 1$  in COSMOS, [Cisternas et al., 2011b](#)) and ( $z = 2$ , in CANDELS, [Mechtley et al., 2016](#)). In addition, half of the AGNs which dominate BH growth since  $z = 1$  ([Cisternas et al., 2011b](#)) and likely even  $z = 2$  ([Kocevski et al., 2012](#); [Cisternas et al., 2015](#)) have disc-dominated host galaxies. This implies that these galaxies had no recent strong interactions with companions. As a consequence, secular or instability processes must be responsible for gas inflow from kpc to sub-parsec scales.

The detailed galaxy-intrinsic gas transport mechanisms have been resolved in nearby low-luminosity AGNs. On galaxy scales, bars can efficiently transfer angular momentum within the galaxy disc, allowing gas to radially migrate ([Combes et al., 2014](#)). At the bar's inner Lindblad resonance (ILR), typically several 100 pc from the centre, it frequently stalls and forms a resonant ring ([Combes et al., 2019](#)). Within the ILR, bars-within-bars contribute torques ([Shlosman et al., 1989b](#)), or dynamical friction between colliding gas clouds (chaotic cold accretion, [Gaspari et al., 2015](#)). However, the processes that fuel low-luminosity AGNs are generally inefficient. The bulk of cosmic SMBH growth must have occurred in high-accretion rate AGNs, i.e. those accreting at several percent of their

Eddington limit, for which galaxy-intrinsic gas transport mechanisms that could sustain such high accretion rates are largely unexplored.

Detailed simulations have investigated torques at small scales: Already a few years ago, [Hopkins & Quataert \(2010b\)](#), HQ10 in the following, simulated the propagation of sustained gas-density instabilities in the central few 100 pc of gas-rich galaxies. Their zoom-in simulations they predicted nested structures inside the inner Lindblad resonance and co-rotation radius, which provide strong torques on gas inside the last few 10 pc through standing eccentric discs or single-armed spirals (“m=1 modes”), reaching and transporting gas all the way to sub-parsec scales. While 99% of the gas might get converted into stars along the way, a substantial mass of gas would still reach the accretion disc, sufficient to power luminous AGNs.

To detect the characteristic signatures of the m=1 mode, we have conducted a blind search imposing (a)  $M_{\text{BH}} \sim 10^7 - 10^8 M_{\odot}$ , (b) an Eddington ratio  $\lambda_{\text{Edd}}$  of several percent % and, (c) central molecular gas overdensities that could be resolved down to the BH sphere of influence. We identified NGC 4593 as one of the rare nearby (35 Mpc), luminous type 1 AGNs with a high specific BH accretion rate of  $\lambda_{\text{Edd}} = 0.08$ . Its low BH mass of  $M_{\text{BH}} = 4.47^{+3.85}_{-1.30} \times 10^6 M_{\odot}$  has been measured using various diagnostics ([Du et al., 2015](#); [Williams et al., 2018](#); [McHardy et al., 2018](#)). NGC 4593’s spiral host galaxy has a stellar mass of  $M_{\star} = 10^{10.9} M_{\odot}$ , is dominated by prominent 9.1 kpc-scale bar ([Treuthardt et al., 2012](#)). It has neutral hydrogen mass of  $M_{\text{HI}} = 10^{9.31} M_{\odot}$  ([Díaz-García et al., 2021](#)). With these properties, NGC 4593 is typical of the luminous AGN population that dominated the growth of the comic SMBH mass density growth since  $z = 1$  ([Merloni, 2004](#); [Schulze et al., 2015](#)). A single low-mass, if at all weakly interacting companion (light ratio 1:7.7, distance  $\sim 2$  disc radii ([Kollatschny & Fricke, 1985](#)), implies that the gas sub-kpc gas dynamics are dominated by processes originating from inside the galaxy rather than from an external perturber. Due to its proximity, NGC 4593’s nuclear molecular gas overdensities can be resolved from kpc galaxy scales down to the BH sphere of influence, making it an ideal target to resolve the sub-kpc scale processes down to the BH sphere of influence.

Our goal in this work is to constrain the galaxy-driven accretion processes in NGC 4593’s that contribute to providing its AGN with gas with the central two kpc, To trace the processes close to the galaxy nucleus, we combine multi-wavelength data from HST, VLT and ALMA to obtain

a panchromatic view of the AGN feeding mechanism from galaxy scales to the central few pc. Throughout this paper we assume a flat Lambda cold dark matter cosmology with  $H_0 = 70 \text{ km s}^{-1} \text{ Mpc}^{-1}$ ,  $\Omega_M = 0.3$ , and  $\Omega_\Lambda = 0.7$ .

## 4.2 Data

### 4.2.1 ALMA Imaging

The ALMA CO(2-1) imaging used in this work comes from two different observational programs. Prog.ID 2017.1.00236.S (PI: Malkan) observed NGC 4593 in a setup with lower angular resolution. Using CASA v5.4.0-70, we continuum-subtracted and reconstructed the cube at 10 km/s resolution, yielding a beam size of  $\text{bmaj} = 0''.23$  mas. In addition, our team has observed NGC 4593 under Prop.ID 2018.1.00978.S (PI: Jahnke) in a configuration with higher spatial resolution. We created a data cube merging both data sets, using a Briggs robust parameter of 0.5 favouring spatial resolution over sensitivity, and a frequency resolution that corresponds to 30 km/s. We used this merged cube for the following analysis, since it covers the molecular gas spiral structure embedded within the bar at the highest spatial resolution close to the AGN. The merged cube has an rms noise of  $\sim 0.0008 \text{ Jy/beam}$  per 30 km/s channel, corresponding to  $\Sigma_{\text{mol, gas}} \approx 0.041 \text{ M}_\odot \text{ pc}^{-2}$  per 30 km/s interval. CO conversion factors in central regions of galaxies, including ULIRGS and starbursts, are often found to be 3-5 times lower than the canonical value of the Milky Way  $\alpha_{\text{CO}}^{\text{MW}} = 4.35 \text{ M}_\odot \text{ pc}^{-2} (\text{K km/s})^{-1}$  (Downes & Solomon, 1998, 2003). Hence, we assume a constant  $\alpha_{\text{CO}} = 1/4 \alpha_{\text{CO}}^{\text{MW}}$ , as a lower limit for derived molecular gas masses (Bolatto et al., 2013).

### 4.2.2 Optical 3D Spectroscopy

NGC 4593 has been observed with MUSE in both the wide field mode (WFM) and narrow field mode (NFM) respectively. For the WFM observations collected under Prog.ID 099.B-0242(B) (PI: Carollo), reduced and calibrated data collected from the ESO Science archive. The archival data cube has a field-of-view (FoV) of  $64'' \times 65''$  with a sampling of  $0''.2$  per pixel and a seeing-limited resolution of  $1''.03$ . Its wavelength coverage

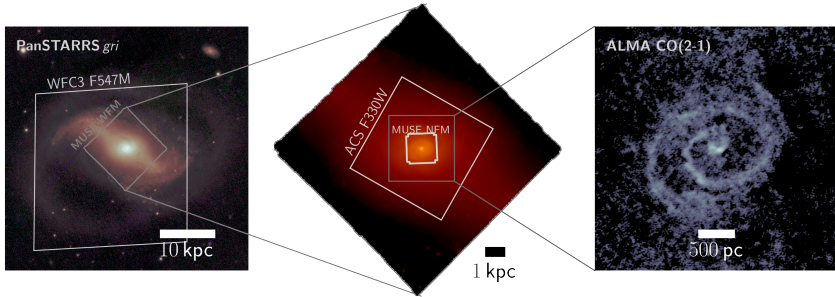


Figure 4.1: *Overview of NGC 4593's host galaxy on different spatial scales.* (Left) The PanSTARRS *gri* color images shows that a large fraction of the host galaxy disc is captured with HST/WFC3, whereas the MUSE WFM FoV of  $1' \times 1'$  only covered a fraction of the 9.1 kpc dominant bar. (Centre) The circumnuclear region is covered with optical and UV imaging from HST and 3D spectroscopy from MUSE NFM with a FoV of  $7.5'' \times 7.5''$ . (Right) ALMA Band 6 observations, here shown the moment 0 map, cover the innermost  $30''$  at the highest angular resolution of 40 mas.

extends from  $4750 \text{ \AA}$  to  $9300 \text{ \AA}$  with a spectral resolution of  $\sim 2.5 \text{ \AA}$  that increases from  $R = 1750$  ( $5000 \text{ \AA}$ ) to  $R = 3500$  ( $9300 \text{ \AA}$ ) (Bacon et al., 2017; Gu erou et al., 2017).

In addition, our team has observed NGC 4593's centre with the AO-assisted NFM of the MUSE instrument under Prog.ID 0103.B-0908(A) (PI: Jahnke). The data were acquired in service mode during the 28 Apr 2019 nights, with 8 individual exposures of 600 s each, dithered by  $0''.5$  to minimise the imprint of cosmic rays and flat-fielding artefacts. For the reduction of the data, we have used the MUSE pipeline v2.8.3 together with the graphical user interface ESO ReflEx v2.11.0 to execute the EsoRex Common Pipeline Library reduction recipes. We correct the differential atmospheric refraction as described in Winkel et al. (2022), to achieve the highest spatial resolution after combining the individual exposures. The final data cube consists of  $374 \times 367$  spaxels, corresponding to a FoV of  $9''.35 \times 9''.16$  with 137,258 spectra. From the width of the telluric emission lines, we find a constant resolution of  $\text{FWHM} = 2.54 \pm 0.10 \text{ \AA}$  across the full wavelength range  $4750 \text{ \AA} - 9350 \text{ \AA}$ , corresponding to  $160.4 \text{ km s}^{-1}$  and  $81.5 \text{ km s}^{-1}$  at the blue and the red end of the spectrum, respectively.

## Deblending AGN and Host Emission

For an accurate extraction of the emission line parameters in type 1 AGNs, it is essential to clean the extended host galaxy emission from the point-like AGN emission. This is particularly important close to the galaxy nucleus, where the AGN outshines the host galaxy by orders of magnitude. To achieve a deblending in both spatial and wavelength dimensions, we follow the approach described in Winkel et al. (2022) where the PSF-like AGN emission is extracted at the broad lines using QDeblend<sup>3D</sup> (Husemann et al., 2013). We generated a hybrid PSF model, consisting of an empirical core and an analytic model describing the low-S/N outskirts, which we then interpolated to generate 3D cubes. As a last step, we iteratively subtracted the PSF cube from the original cube. This left us with two deblended cubes; the AGN cube contains the point-like emission from the AGN including the power-law continuum and the broad line emission, whereas the host galaxy cube contains the spatially resolved emission from the host galaxy.

## 4.3 Analysis and Results

### 4.3.1 Spectral Synthesis Modelling

To extract the host galaxy stellar kinematic and emission line parameters, we used the publicly available spectral synthesis modelling code PyParadise<sup>1</sup> (Husemann et al., 2016a, 2022) and follow the procedure outlined in Winkel et al. (2022). The PSF subtraction described in Sect. 4.2.2 leaves strong non-physical continuum variations close to the AGN, artefacts for which PyParadise provides reliable solution. The fitting methodology of PyParadise and its relevance specific to the WFM and NFM data sets are outlined in Husemann et al. (2022) and Winkel et al. (2022). For NGC 4593, in brief, we first used the adaptive Voronoi tessellation routine of Cappellari & Copin (2003) to achieve a minimum stellar continuum S/N=20 in the wavelength range  $5080 \text{ \AA} < \lambda < 5260 \text{ \AA}$ . We then modelled the binned stellar continuum spectra using the updated CB09 version of the evolutionary synthesis model spectra from Bruzual & Charlot (2003a). For the next step, the emission line modelling, we tied the stellar kin-

---

<sup>1</sup><https://git.io/pyparadise>

matics to these initial measurements of the stellar kinematics, achieving robust measurements of emission line parameters. To model the emission lines, we set up `PyParadise` to use a set of Gaussian models. For the doublet emission lines [N II] $\lambda\lambda 6548,83$  and [O III] $\lambda\lambda 4959,5007$ , we fixed the flux ratio to the theoretical prediction of 2.96 (Storey & Zeppen, 2000; Dimitrijević et al., 2007). Furthermore, we coupled the emission lines in radial velocity and velocity dispersion in order to increase the robustness of the flux measurements. Our integrated flux in each of the emission lines did not change within the uncertainties if we did not kinematically tie the model parameters for emission lines with different ionization potentials. Close to the AGN, however, coupling their velocities becomes crucial for disentangling emission lines from non-physical PSF residual spectral features. Since the MUSE WFM and NFM observations were conducted under different atmospheric conditions, we analyse the two data sets independently. When both are combined for the following analysis, we degrade the spatial resolution of the NFM to match the resolution of the seeing-limited WFM observations.

### 4.3.2 Star Formation Rates

In order to estimate the star formation that occurs along NGC 4593’s single-arm spiral, we used the emission line maps, retrieved in Sect. 4.3.1. For the extinction correction of the H $\alpha$  flux, we assumed an intrinsic Balmer decrement of H $\alpha$ /H $\beta$  = 2.86, characteristic of case B recombination. We further assumed an electron temperature of  $T_e = 10^4$  K and density  $n_e = 100 \text{ cm}^{-2}$ , in which case the de-reddening can be expressed as

$$\text{H}\alpha_{\text{corr}} = \text{H}\alpha_{\text{obs}} \left( \frac{\text{H}\alpha/\text{H}\beta}{2.86} \right)^{\frac{\kappa_\alpha}{\kappa_\beta - \kappa_\alpha}} \quad (4.1)$$

$\kappa_\alpha = 2.52$ ,  $\kappa_\beta = 3.66$  (O’Donnell, 1994), and Milky Way  $R_V = 3.1$ . As a next step, we constrained the contribution of SF to the ionising H $\alpha$  flux using the Baldwin, Phillips & Terlevich (BPT) diagnostic diagram. Often, and also the case for NGC 4593, the spatially resolved line ratios form a mixing sequence in the BPT diagnostic plane, challenging an unambiguous identification of the excitation mechanism through analytical demarcation lines. For better constraining the relative contributions from SF vs. AGN ionising flux, we employed the package `Rainbow` (Smirnova-

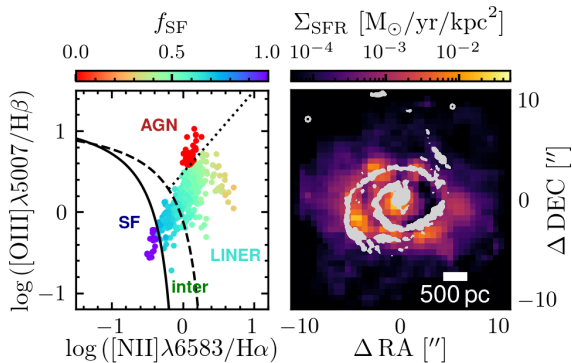


Figure 4.2: *Star formation rate across the molecular gas spiral.* The left panel shows the BPT diagnostic diagram for the combined MUSE WFM+NFM emission line maps, binned to 100 pc resolution. While the classically NGC 4593’s innermost 2 kpc occupy a mixing sequence, whose star forming fraction  $f_{\text{SF}}$  we modelled using Rainbow. The right panel shows the so-derived star formation rate surface density, overlaid with the contours of the molecular gas spiral. While the spatial distribution of  $\Sigma_{\text{SFR}}$  roughly aligns with the molecular gas, there are offsets of the order of 200 pc between the peak of both structures.

Pinchukova et al., 2022). This package relies on an empirical method based on an assembly of emission line flux ratios. It determines the posterior probability distribution through maximising a likelihood function of a model mixing sequence. The star-forming ionization fraction  $f_{\text{SF}}$  and its uncertainty are considered free parameters in the model, and are determined from the probability distribution. In practice, we used the emission line ratios of AGN and SF galaxies classified in SDSS as bases. We then identified clouds in NGC 4593 that are purely excited through AGN and SF, which lie close to the AGN in the very central 1”, and in the spiral arm, respectively.

The left panel of Fig. 4.2 shows that the majority of spaxels distribute across the mixing sequence, for which  $f_{\text{SF}}$  is a finite value  $<1$ . A large fraction of the FoV is filled with spaxels whose emission line ratios lie in the regime of low-ionisation narrow emission line regions (LINER). Since these regions coincide with low line fluxes, gas densities are likely low,

indicating that this emission predominantly arises from diffuse interstellar gas. Across the single-arm spiral, in contrast, the emission line ratios are consistent with being excited by star formation alone. Only  $< 1''$  from the galaxy centre, the hard ionisation field from the AGN takes over, and possibly shocks from outflowing gas, which shift the emission line ratios into the AGN regime. Here,  $f_{\text{SFR}}$  is considerably lower, making a robust estimation of the SFR at  $\lesssim 200$  pc from the nucleus uncertain.

The right panel of Fig. 4.2 shows the star formation rate surface density, derived from emission line ratios that were binned to a  $100 \text{ pc} \times 100 \text{ pc}$  grid. The integrated SFR across the single-arm spiral amounts  $7.0 \pm 0.2 \times 10^{-3} M_{\odot}/\text{yr}$ , with star formation rate surface densities peaking at  $\Sigma_{\text{SFR}} = 0.021 M_{\odot}/\text{kpc}^2$ . To confirm the consistency of our method, we compare the derived SFR molecular gas mass with [Díaz-García et al. \(2021\)](#), who measured  $\Sigma_{\text{mol}}^{<3.6 \text{ kpc}} = 38.10 \pm 1.42 M_{\odot}/\text{pc}^2$  and  $\Sigma_{\text{SFR}}^{<3.6 \text{ kpc}} = (6.3 \pm 0.6) \times 10^{-2} M_{\odot}/\text{kpc}^2$  from aperture-integrated CO(1–0) emission with a beam FWHM of  $\theta_{\text{beam}} = 21''5$ . Our spatially resolved measurements across the same structure yield  $\Sigma_{\text{mol}}^{3.7 \text{ kpc}} = 35.6 \pm 2.1 M_{\odot}/\text{pc}^2$ , and  $\Sigma_{\text{SFR}}^{3.7 \text{ kpc}} = (2.5 \pm 0.3) \times 10^{-3} M_{\odot}/\text{kpc}^2$ , respectively. While the molecular gas surface densities are consistent, the discrepancy between  $\Sigma_{\text{SFR}}$  can be explained through the methods: Since the SFR computed [Díaz-García et al. \(2021\)](#) is primarily based on GALEX NUV emission line fluxes, their measurement might be over-estimated due to contamination from the AGN. Similarly, if we do not apply the AGN correction factor to the H $\alpha$  emission line flux (see Sect. 4.3.2), we estimate  $\Sigma_{\text{SFR}}^{3.7 \text{ kpc}} = (1.0 \pm 0.1) \times 10^{-1} M_{\odot}/\text{kpc}^2$ , closer to what [Díaz-García et al. \(2021\)](#) reported. This discrepancy underscores the importance of correcting for AGN contamination when estimating H $\alpha$ -based star formation rates.

### 4.3.3 Kinematic Modelling

We have modelled the kinematics of the stellar and ionised gas components. The primary focus for the following analysis is on the kinematics and dynamics of the molecular gas, for which the kinematic modelling is described in the following. The modelling of the ionised gas and stellar kinematics are based on a different method, described in the Appendix 4.6.1.

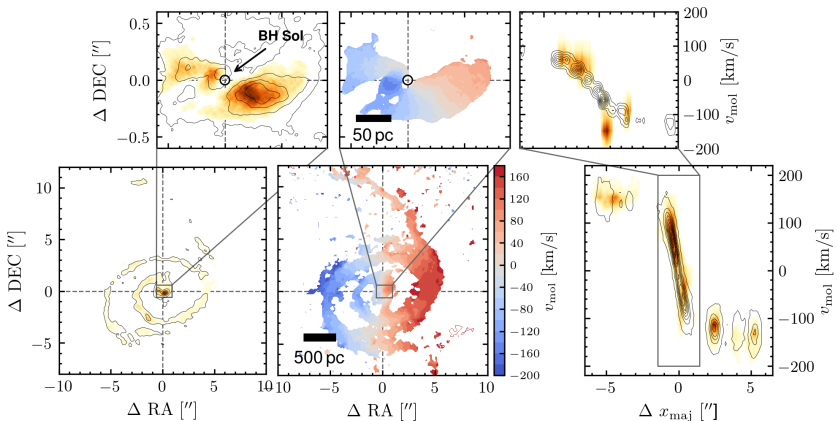


Figure 4.3: *Results of the kinematic modelling carried out with KinMS.* (Left) The left panels show the surface brightness distribution and line-of-sight velocity field of the CO(2-1) emission, for the low- (top) and high-resolution (bottom) data set respectively. The size of the BH Sol is indicated with a black circle. (Right) Position-velocity diagram along the kinematic major axis. The model includes circular rotation with radial motions, which dominate the bulk molecular gas kinematics from 1.5 kpc down to the BH Sol. For the high-spatial-resolution data set, we also include a lopsided component, to describe the bright molecular gas outflow  $\sim 50$  pc from the centre.

## Molecular Gas

For constraining the kinematics of the molecular gas, we employ the KINematic Molecular Simulation (KinMS) routines of Davis et al. (2013). More specifically, we employ `KinMS_fitter`, which uses a forward-modelling approach to infer the kinematic and dynamical parameters of the molecular gas distribution in interferometric datacubes. To account for the asymmetric flux distribution of the spiral, we use an intensity-weighted sampling generated by `skySampler`, which is a plugin to `KinMS_fitter`. The overall kinematic patterning is dominated by disc-like rotation. We therefore set up the model with an arctan-rotation curve of the form  $v(R) = 2/\pi \times v_{\text{max}} \times \arctan(R/R_{\text{turn}})$ , yielding a total of nine free parameters: The total CO flux  $F$ , the kinematic parameters describing the

Table 4.1: Results of modelling the molecular gas kinematics with *KinMS*.

Parameter	Initial guess <sup>(a)</sup>	Best-fit outer <sup>(b)</sup>	Best-fit inner <sup>(c)</sup>
$F$ [K km/s]	25	$18.92^{+0.42}_{-0.92}$	$22.94^{+0.42}_{-0.92}$
PA [°]	290	$277.6^{+1.1}_{-2.1}$	$278.0^{+1.2}_{-1.2}$
$i$ [°]	10	$48.8^{+3.9}_{-3.5}$	$47.2^{+3.9}_{-3.5}$
$x_0$ [pc]	0	$0.15^{+0.01}_{-0.02}$	$-0.15^{+0.04}_{-0.02}$
$y_0$ [pc]	0	$0.15^{+0.01}_{-0.02}$	$-0.039^{+0.01}_{-0.02}$
$\Delta v_{\text{sys}}$ [km/s]	2450	$2487.5^{+1.1}_{-1.9}$	$2487.5^{+1.1}_{-1.9}$
$\sigma_{\text{gas}}$ [km/s]	20	$20.81^{+1.40}_{-1.41}$	$21.54^{+1.40}_{-1.41}$
$R_{\text{turn}}$ ["]	1	$1.06^{+0.25}_{-0.12}$	$1.06^{+0.25}_{-0.12}$
$v_{\text{max}}$ [km/s]	200	$232.4^{+4.9}_{-11.7}$	$232.4^{+4.9}_{-11.7}$

**Notes.** <sup>(a)</sup> Initial guess for the parameters. <sup>(b)</sup> Best-fitting value from modelling the  $15'' \times 15''$  lower-resolution cube. <sup>(c)</sup> Best-fitting value from modelling the inner  $1'' \times 1''$  of the high-resolution cube.

maximum velocity  $v_{\text{max}}$  and turnover  $R_{\text{turn}}$  of the rotation curve, and the position angle PA and inclination of the disc  $i$ . The parameters  $\Delta x_0$ ,  $\Delta y_0$ , and  $\Delta v_{\text{sys}}$  describe possible offsets with respect to the assumed dynamical centre and systemic velocity, respectively. In addition, we include pure radial motions which are allowed to vary freely as a function of radius  $R$ . We set up the model parameters with uniform priors with sensible boundaries estimated from low-spatial-resolution runs of the same data set. For the final MCMC run, we generated 30,000 samples and monitored their convergence to well-sampled posterior distributions.

The best-fit *KinMS* models for NGC 4593's surface brightness and velocity fields are shown Fig. 4.3. Disc-like rotation dominates the kinematics on 1.5 kpc scales across the two curls of the single-arm spiral. Within the innermost 50 pc, a bright molecular gas outflow dominates the surface brightness, but the disc-like rotation can be traced down into the BH sphere of influence. While the low- and high-resolution data sets were fitted independently, the inferred kinematic parameters listed in Table 4.1 are consistent with each other, suggesting that a single velocity profile is sufficient to describe the molecular gas kinematics across more than two orders of magnitude in spatial scale. The analysis with *KinMS* also provides mass inflow rates as a function of distance from the centre. Empirically,

these rates are negative across the entire single-arm spiral, consistent with the morphology of the structure, which suggests radial gas migration at near-constant rates. With an average mass inflow rate of  $\dot{M} = 2.8 M_{\odot}/\text{yr}$  the single-arm spiral channels substantial amounts of molecular gas into the BH SoI, suggesting that the AGN activity could be sustained by this inflow. The gas accretion rates, timescales, and BH growth rates are discussed further in Sect. 4.4.3.

#### 4.3.4 Torques from the Self-Gravitating Gas Spiral

Due to its lopsidedness and non-axisymmetry, the molecular gas mass exerts a torques on the gas clouds assembled along its spiral arm. To assess whether this torque alone is sufficient to explain the radial gas flow retrieved with *KinMS* (see Sect. 4.3.3), we quantified the gravitational torques that using the method from [García-Burillo et al. \(2005\)](#). This method has been used in studies to estimate  $\dot{M}_{\text{gas}}$  in galaxy discs based on estimates of gravity torques on the gas and the resulting angular-momentum transport rates ([Haan et al., 2009](#); [Querejeta et al., 2016](#)). However, rather than using the stellar mass gravitational field, we use the lopsided molecular gas mass distribution as input for deriving the torque field.

As a first step, we deprojected the coordinates onto the face-on galaxy plane using an affine transformation with  $\text{PA} = 5^{\circ}$  and  $i = 38^{\circ}$ , the mean values measured in Sect. 4.3.3 for the gas disc. We used the deprojected mass surface density to map the gravitational potential  $\Phi(x, y)$  of the molecular gas spiral. This step implicitly assumes that the not-detected molecular gas mass is symmetric in azimuth so that it does not substantially contribute to the total torque budget. At each pixel, the gradient of  $\Phi(x, y)$  describes the gravitational force per unit mass  $\vec{F}(x, y)$  from which the specific torque can be derived as

$$t(x, y) = xF_y - yF_x \quad (4.2)$$

The torque map across NGC 4593's single-arm spiral is shown in the right panel of Fig. 4.4, where negative torques correspond to an effective angular momentum loss of the rotating gas. We assume that the gas column density  $\Sigma_{\text{mol}}(x, y)$  derived from the CO(2-1) line maps describes the probability of finding gas particles at this location at present. This allows us to statistically estimate the time derivative of the angular momentum

surface density  $dL_s(x, y)/dt$  by weighting  $t(x, y)$  with  $\Sigma_{\text{mol}}(x, y)$  at each pixel (see [García-Burillo et al., 2009](#)).

Estimating the radial gas flow requires the time derivative of the specific angular momentum. We derive the radial profile of the specific angular momentum loss by weighting the torque per unit mass with the gas surface density  $\Sigma_{\text{mol}}(x, y)$ , averaged over the azimuth  $\theta$ :

$$t(R) = \frac{\int_{\theta} \Sigma_{\text{mol}}(x, y) \times (xF_y - yF_x)}{\int_{\theta} \Sigma_{\text{mol}}(x, y)} \quad (4.3)$$

Furthermore, we adopt the definition of the dimensionless AGN feeding efficiency  $\Delta L/L$ , which GB05 define as the gas specific angular momentum transfer during one orbital period ( $T_{\text{rot}}$ ):

$$\frac{\Delta L}{L} = \frac{dL}{dt} \Big|_{\theta} \times \frac{1}{L} \Big|_{\theta} \times T_{\text{rot}} \frac{t(R)}{L_{\theta}} \times T_{\text{rot}} \quad (4.4)$$

Under this definition, the molecular gas angular momentum  $L_{\theta} = R \times v_{\text{rot}}$  is removed during one rotation if  $\Delta L/L = -1$ .

Finally, the radial gas mass inflow rate per unit length can be estimated from the angular momentum loss rate:

$$\frac{d^2 M}{drdt} = \frac{dL}{dt} \Big|_{\theta} \times \frac{1}{L} \Big|_{\theta} \times 2\pi R \times \Sigma_{\text{mol}}(x, y) \Big|_{\theta} \quad (4.5)$$

where  $\Sigma_{\text{mol}}(x, y) \Big|_{\theta}$  is the radial profile of the azimuthally averaged gas mass surface density. Multiplying this quantity with the shell width  $\Delta R$  provides the azimuthally-averaged local gas mass inflow rate:

$$\dot{M}(R) = \sum \frac{d^2 M}{drdt} \times \Delta R \quad (4.6)$$

We note that in our framework, the torques and mass inflow rates defined in eq. 4.3-4.6 are a result of the gas self-gravity used as input for eq. 4.2. This is fundamentally different from GB05 and many works building on that (e.g. [García-Burillo et al., 2009](#); [Haan et al., 2009](#); [Querejeta et al., 2016](#)), who derived each of the quantities based on *stellar* gravitational potential. In addition, our mass inflow rates defined in eq. 4.6 are

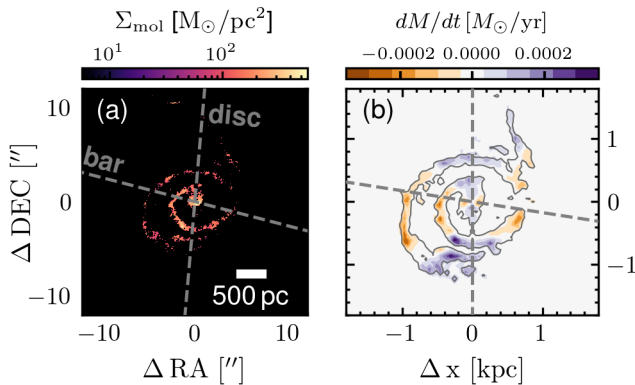


Figure 4.4: *Torque map of NGC 4593's self-gravitating molecular gas spiral.* From left to right, the panels show (a) the molecular gas mass surface density of the single-arm spiral, and (b) the spatially resolved torques that originate from the spiral's gravitational potential and act onto itself, deprojected into the frame of the spiral.

differential, i.e. describe the local mass inflow rate at radius  $R$ , rather than the volume-integrated quantity defined by GB05.

A map of the torque field resulting from the gravitational potential imposed by the molecular gas is shown in Fig. 4.4. The torques are distributed in a "butterfly pattern" García-Burillo et al. (2009), which arises from the asymmetric distribution of the gas: East and west of the centre, the torques are typically negative, whereas north and south of the centre, the torques are positive. However, these torques are not confined to change along spiral arm; since torques are sensitive to the distribution of neighbouring gas, pronounced torque gradients also exist perpendicular to the gas trail.

#### 4.3.5 Time Evolution of the Torque Field

While the torques may vary significantly as a function of position, a net negative radial torque budget is required to cause a gas inflow. Furthermore, this net torque budget should remain negative over time to produce a stable configuration. As pointed out by Lelli et al. (2022), the mass in-

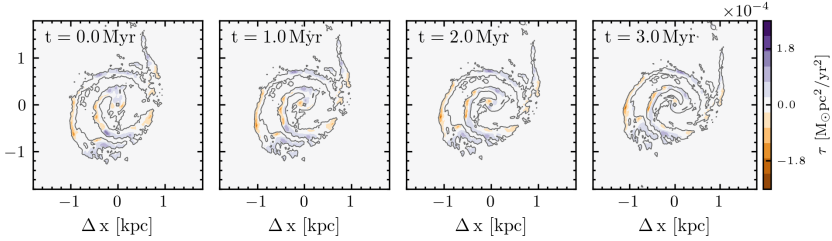


Figure 4.5: *Time-evolution of the  $m=1$  torque field.* We simulate the evolution the mass distribution as described in Sect. 4.3.5, and derive the resulting torque field. After 3 Myr, the centre of mass has rotated around the kinematic centre by  $140^\circ$ .

flow rates derived from the method outlined in the previous section, often only loosely correlate with the sign and amplitude of the radial mass transport. This is caused by the fact that the exact shape of  $t(R)$ , and thereby  $dL/L(R)$  and  $\dot{M}(R)$ , are sensitive to small changes in the underlying mass distribution. Since the morphology of the spiral is not static, these quantities should be regarded as result of the present-day  $M_{\text{mol}}$  distribution and the resulting instantaneous torque field. However, the morphology and orientation of the spiral change over time, which may impact the radial profile  $\dot{M}(R)$ . We define the radially-averaged  $\dot{M}(R)$  as the global mass inflow rate  $\dot{M}_{\text{glob}} = \langle \dot{M}(R) \rangle$ . While  $\dot{M}(R)$  might be prone to substantial short-term fluctuations, a steady radial gas transport across the spiral can only occur if  $\dot{M}_{\text{glob}}$  lies below zero for long (Myr) timescales.

To test whether the present-day net mass inflow is a short-lived configuration, we have simulated the temporal behaviour of the single-arm spiral. In practice, we set up an  $N$ -body grid based on the deprojected molecular gas mass surface density. We assume that for a short timescale, any kind of interaction between the gas particles can be neglected, and the motion of the gas particles can be approximated by via the rotation curve plus the radial migration velocity component derived in Sect. 4.3.3. For a time interval of [0 Myr, 3 Myr], the centre of mass rotates by  $140^\circ$  around the nucleus, facing the opposite orientation of the high central  $\Sigma_{\text{mol}}$  peak (Fig. 4.5). If  $m=1$ -induced net radial gas motion should compensate over time, we would expect that such a significant displacement of the gravi-

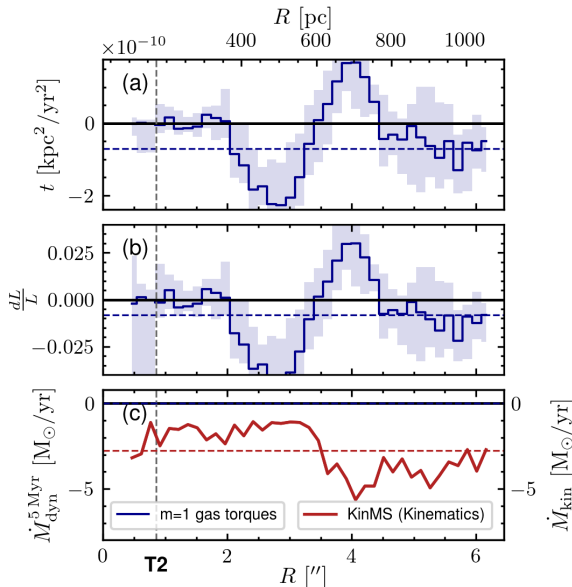


Figure 4.6: *Mass-inflow rates across NGC 4593's molecular gas spiral.* The panels, from top to bottom, depict the radial behaviour of quantities derived from the gravitational potential molecular gas distribution. T2 indicates the kinematic transition between the single-arm spiral breaks, as highlighted in Fig. 4.8. The panels show (a) Gravitational torques per unit mass. Blue lines represent  $3\text{ Myr}$ -average mass rates from gravitational torques, with the scatter shown as blue shaded regions. The radial average is shown as a dashed line. (b) The average fraction of angular momentum transferred to the gas in one rotation. (c) The molecular gas mass inflow rate derived from torques of the self-gravitating gas (blue continuous line) and empirically measured with `KinMS` kinematic modelling (red continuous line). Across the single-arm spiral, measured net mass transport,  $\dot{M}$ , is inward, with a radial average of  $\langle \dot{M}(R) \rangle = 2.8\text{ M}_\odot/\text{yr}$  (red dashed line). Although torques from the self-gravitating gas are also negative, they are an order of magnitude smaller, and their time-average is nearly zero, insufficient to explain the morphology and continuous inflow.

tating mass distribution should be reflected in the time-dependence of the global mass inflow rate. Therefore, this simplistic approach is sufficient to test how sensitive the mass inflow rates are to small displacements and deformations of the gravitating structure.

The radially evaluated properties, averaged over 3 Myr, are shown in Fig. 4.6. The torques from the self-gravitating spiral are strongest close to  $r \lesssim 500$  pc from the centre, where they change sign. This is a combined effect of the high radial gas densities around  $R \sim 500$  pc and the single-arm morphology. The radial torque budget is sensitive to the 2D distribution of the gas, and the centre of mass of the enclosed mass changes with increasing  $R$ , most drastically around  $\sim 500$  pc. The radial average over the 3 Myr-average torque profile is negative, as is the specific angular momentum loss rate  $dL/L$ . However, the amplitude of  $dL/L$  is small. A radial average of  $dL/L \sim 0.008$  suggests that the gas would require 125 orbits to lose its angular momentum. As a consequence, the resulting mass inflow rates are low (radial average  $-0.02 M_{\odot}/\text{yr}$ ) and insufficient to explain those empirically measured with  $\kappa\text{inMS}$  (radial average  $-2.8 M_{\odot}/\text{yr}$ ). Since the gas must be transported from 1 kpc to 100 pc within only a few orbits, the higher mass inflow rates measured  $\kappa\text{inMS}$  provide the better explanation for the morphology of the spiral. This result suggests that the torques from the asymmetric gas distribution alone are insufficient to explain the observed mass inflow rates.

## 4.4 Discussion

### 4.4.1 Star Formation Along the Single-arm Spiral

Not all the molecular gas in the single-arm spiral will reach the BH SoI, and eventually contribute to grow the BH. In fact, Hopkins & Quataert (2010b) predict that from the  $\sim 100$  pc scale gas only a small fraction  $< 1\%$  will reach the BH accretion disc and eventually contribute to the build-up of  $M_{\text{BH}}$ . To empirically test the efficiency by which the inflowing molecular gas forms stars, we derive  $\Sigma_{\text{mol}}$ ,  $\Sigma_{\text{SFR}}$ , and the depletion time scale  $t_{\text{dep}} = \Sigma_{\text{mol}}/\Sigma_{\text{SFR}}$ , the inverse of the star forming efficiency, along the single-arm spiral.

As a reference for the star formation efficiencies in nearby spiral galaxies, the resolved Kennicutt–Schmidt relation (rKS, Kennicutt et al., 2007;

Bigiel et al., 2008; Leroy et al., 2008; Onodera et al., 2010; Kreckel et al., 2018) provides the relation between  $M_{\text{mol}}$  and  $\Sigma_{\text{SFR}}$  on sub-kpc scales. The rKS relation has slope near to  $\sim 1$  and a dispersion of the order of  $\sim 0.2$  dex. As pointed out by Sánchez et al. (2021) and Pessa et al. (2021), the slope and scatter of the rKS vary with measurement scale. Due to the high angular resolution of the data sets,  $\sim 30$  pc for MUSE NFM and  $\sim 5$  pc for ALMA, individual star forming regions and cloud are spatially resolved. To account for the varying spatial resolution between the data sets, we project the  $\Sigma_{\text{mol}}$ , SFR and  $\Sigma_{\text{SFR}}$  maps retrieved in Sect. 4.3.2 to a common grid with  $100 \text{ pc} \times 100 \text{ pc}$  resolution. While the rKS on these scales has considerably higher scatter due to the fact that the cloud scales are still partially resolved, spatially resolving the rKS allows us to trace the star formation properties along the spiral. We note that the cloud scale and associated star formation efficiencies can vary dramatically depending on the resolution (Pessa et al., 2021). However, the qualitative behaviour of  $\Sigma_{\text{mol}}$ ,  $\Sigma_{\text{SFR}}$ , and  $t_{\text{dep}}$  remains consistent regardless of the spatial scales used for binning the maps or the width of the spiral aperture (100 pc - 400 pc) used for radial integration.

To trace the shape of the spiral, we parameterise the spatial shape of the single-arm spiral as a function of the phase  $\theta$  using a second order polynomial

$$\mathbf{r}(\theta) = \begin{pmatrix} \Delta x \\ \Delta y \end{pmatrix} = (1 - a \cdot \theta) \theta \cdot b \begin{pmatrix} \sin \theta \\ \cos \theta \end{pmatrix} \quad (4.7)$$

where  $\Delta x$  and  $\Delta y$  are the deprojected distance to the AGN in Cartesian coordinates, and  $a$  and  $b$  are free parameters. We define the spiral across the phase  $\theta = [0, 3\pi]$ , for which find best-fitting values of  $a = 0.04$  and  $b = -0.93$ . This model provides a good approximation for the shape of the spiral over two curls, starting the nucleus reaching over 1.5 curls up to the outskirts where the molecular gas structure disperses. We measure  $\Sigma_{\text{mol}}$  and  $\Sigma_{\text{SFR}}$  within 200 pc along the spiral, corresponding to  $\sim 3 \times$  the typical radial FWHM of the molecular surface mass density profile. We thereby do not only sample the highest-density regions along the "rim" of the spiral, but also cover its outskirts. This is crucial since the highest  $\Sigma_{\text{SFR}}$  spots do not perfectly align with the narrow trail of  $\Sigma_{\text{mol}}$ , potentially indicating delayed SF following the trail of the spiral arm.

Fig. 4.7 shows the radial dependency of  $\Sigma_{\text{mol}}$ ,  $\Sigma_{\text{SFR}}$  and  $t_{\text{dep}}$  across the spiral arm. We show  $d^{\text{AGN}}$ , which is the deprojected distance to

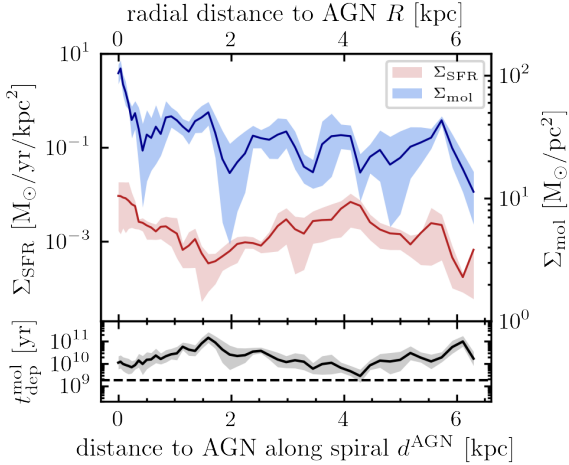


Figure 4.7: *SFR, molecular gas densities and depletion time scales along the single-arm spiral.* The top panel shows the SFR surface density  $\Sigma_{\text{SFR}}$  (red) and the molecular gas mass surface density  $\Sigma_{\text{mol}}$  (blue), as function of distance to the AGN measured along the spiral arm. While the  $\Sigma_{\text{mol}}$  is has high gas densities all across the spiral, the SF is clumped, resulting in variations of  $\Sigma_{\text{SFR}}$  by more than one order of magnitude. The bottom panel shows the molecular gas mass depletion time scale, with the dashed line marking the typical  $t_{\text{dep}}^{\text{mol}} = 1.7$  Gyr resolved in nearby spiral galaxies (Utomo et al., 2018). In the single arm spiral, it is nearly constant with a median  $\langle t_{\text{dep}}^{\text{mol}} \rangle = 11$  Gyr indicating that star formation in the single-arm spiral is remarkably inefficient.

the AGN along the morphology of the spiral arm. In addition, the secondary abscissa indicates to what deprojected galacto-centric distance  $R$  this corresponds. The average SFR surface density along the single-arm spiral peaks is  $\Sigma_{\text{SFR}} = 0.21 \pm 0.2 \text{ M}_{\odot}/\text{yr}/\text{kpc}^2$ . This is well-below the expected value of  $\text{M}_{\odot}/\text{yr}$  anticipated from the associated peak molecular gas surface density  $162 \text{ M}_{\odot}/\text{pc}^2$ , and the 100 pc-scale resolved molecular Kennicutt-Schmidt relation (Pessa et al., 2021).

#### 4.4.2 The Torquing Mechanism

In Sect. 4.3.4 we have explored whether the self-gravity of the asymmetric gas distribution may provide sufficient torques to sustain the molecular gas inflow, and explain the spiral morphology. Our preliminary conclusion drawn from the analysis is that the gas self-gravity cannot fully explain the phenomenon, or at least, it is not the only contributing factor. Constraining the underlying torquing mechanism will require further investigations. Specifically, we will test whether asymmetries in the stellar pseudobulge component may provide sufficient torques. An archival HST/NICMOS F160W image exists, covering the innermost  $1\text{ kpc} \times 1\text{ kpc}$ , which can be used for this purpose. This step will involve a careful deprojection of the 2D stellar mass surface density, enabling an analysis analogous to what we conducted in Sect. 4.3.4. Additionally, an HST/ACS HRC F330W image exists, which can be used to trace young stellar populations. Although the exposure is not particularly deep and suffers from a strong PSF in the UV (the PSF models of HRC included in `TinyTim` are poor), it may still provide enough S/N to radially trace the centre of mass of a young stellar component that could have been formed by the inflowing gas.

#### 4.4.3 Consequences for SMBH Growth

While further analysis is needed to identify the exact torquing mechanism, it is clear that the gas inflow rates are substantial. The total molecular gas in the spiral is  $\log(M_{\text{mol}}/M_{\odot}) = 7.9 \pm 0.3$ , based on a conservative conversion factor of  $1/4 \alpha_{\text{MW}}^{\text{CO}}$ . To compare this with the black hole accretion rate (BHAR), we adopt the Eddington ratio of  $\lambda = 0.08$  and  $M_{\text{BH}}$  from Sect. 4.1 and assume a radiative efficiency of  $\eta \sim 0.1$  for the optically thick, geometrically thin accretion disc typical of luminous AGNs with similar specific mass accretion rates (Davis & Laor, 2011). NGC 4593's black hole accretion rate is  $M_{\text{BH}} = 0.01 M_{\odot}/\text{yr}$ , two orders of magnitude smaller than the gas inflow rate. Still, significant angular momentum loss is required for radial migration, which could occur through gas outflows or transport of gas away from the centre. Additionally, gas may form stars along the way, further reducing the amount that actually reaches the BH SoI. Given that only a small fraction of the inflowing gas will reach the accretion disc, we make the simplistic assumption that the current mass inflow rate of  $2.8 M_{\odot}/\text{yr}^{-1}$  is necessary to sustain

the present-day BHAR. This corresponds to a timescale of 40 Myr over which the BH accretion at 8% of the Eddington rate could be sustained, resulting in a net growth of  $4 \times 10^5 M_{\odot}$ , or 10% of the current SMBH mass.

Considering that the frequency of major and minor galaxy mergers as alternative channels for BH growth is of few Gigayears in the  $z < 2$  Universe (Lotz et al., 2011), this secular feeding mode would provide relatively efficient way to fuelling BH growth. Furthermore, the gas reservoir is not expected to be depleted; simulations by e.g., Sormani et al. (2023) demonstrate that galaxy bars are effective in transporting gas from spiral arms on kiloparsec scales towards the inner end of the bar, where pseudobulges are located. In the case of NGC 4593, this is where the  $m=1$  mode takes over, suggesting that gas may remain available well beyond the estimated 40 Myr.

## 4.5 Summary and Conclusions

In this ongoing project, we investigated the origin and efficiency of a secular feeding mechanism in the barred spiral galaxy NGC 4593, which hosts a high-accretion-rate, unobscured AGN. By combining ALMA and VLT/MUSE observation, we identified a gas inflow along a prominent single-arm spiral that is present in both the cold and warm gas phases, extending from 1 kpc scales of the galaxy bar down to the BH sphere of influence. Our primary results are summarised as follows:

- The kinematics are dominated by three regimes. On the largest scales of the 9 kpc-sized galaxy bar, gas flows along the dust lanes towards the inner pseudobulge. From 1.3 kpc inward, a single-arm gas spiral extends over two coils down to  $\sim 130$  pc from the AGN, where the spiral breaks and the gas flows directly towards the BH.
- The single-armed molecular gas spiral leaves a trail of recently formed stars, with a moderate star formation rate surface density peaking at  $\Sigma_{\text{SFR}} = 0.021 M_{\odot}/\text{kpc}^2$ , and an integrated SFR of  $7.0 \times 10^{-3} M_{\odot}/\text{yr}$ . The star forming efficiency along the spiral is low, with a median depletion time scale  $\langle t_{\text{dep}} \rangle = 11$  Gyr, well-above the timescales for accretion onto the AGN.

- A steady gas flow leads to radial gas mass inflow rates of  $2.8 M_{\odot}/\text{yr}$  along the single-arm spiral. This rate is two orders of magnitude above the BH mass accretion rate estimated from AGN continuum emission.
- The mass reservoir and inflow rates across the single-arm spiral are sufficient to fuel the AGN over 40 Myr at the present rate. Sustained fuelling over such long timescales substantially contributes to the growth of NGC 4593's central SMBH: Assuming a constant BH accretion rate equal to the present-day, this process will result in a net growth of the central SMBH by 10 %.

In summary, NGC 4593 is a remarkable example of an unobscured AGN hosting a single-arm, gas-rich spiral that transports gas from galaxy scales down to the vicinity of the BH sphere of influence. While the exact torquing mechanism responsible for the  $m=1$  structure requires further investigation, it may represent an important galaxy-intrinsic AGN feeding mechanism. With gas inflow rates high enough to grow the central SMBH over the AGN duty cycle, this mechanism could significantly contribute to the growth of NGC 4593's central SMBH, provided the gas inflow and AGN accretion rates are sustained. Further investigation is needed to confirm whether torques are indeed the underlying cause and to identify the components responsible for them. Once this is achieved, it will be essential to search for similar single-arm structures in AGN-hosting galaxies to assess whether the  $m=1$  mode is a common or rare phenomenon. The ongoing Euclid Wide Survey (Euclid Collaboration et al., 2022), with its high-resolution imaging and visible-to-NIR photometry, provides a rich database for statistically constraining the prevalence of  $m=1$  spirals based on dust absorption. A census based on a sample with well-defined selection criteria, along with an analysis of the correlation between incidence and BH accretion rates, will help assess the relevance of this feeding mode for overall cosmic SMBH growth since cosmic noon.

## 4.6 Appendix

### 4.6.1 Tilted-ring Modelling of the Stellar and Ionised Gas Rotation

For the ionised gas and stellar kinematics, we employ *Kinometry* (Krajinović et al., 2006). It allows us identifying kinematic sub-components, and comparing differential behaviour between the ionised and molecular gas phase, and the stellar body of NGC 4593’s host. *Kinometry* is a generalisation of photometry to the higher moments of the line-of-sight velocity distribution (LOSVD). It performs a harmonic expansion of kinematic 2D maps along the best-fitting ellipses, thus provides also information on higher-order moments as opposed to the classical tilted ring analysis. Implicit to using modelling method is the assumption that the motion of the gas and stars is constrained to circular orbits within a thin disc.

For each the ionised gas and stellar components, we employ the two velocity maps from MUSE NFM and WFM, but analyse them independently. For the stellar velocity, we use the information from the Voronoi-grid as input, which accounts for the differential contribution from components with varying surface brightness. We achieve a similar effect for the ionised gas component by combining the velocity from the original data cube with cubes that were spatially binned by a factor of 2, 4, 8, 16 and 32. Combining the entire range of spatial bins maximises the field coverage, while guaranteeing the highest spatial resolution in the centre. To increase the robustness of the fit, we tie the kinematic centre to the position of the AGN and chose logarithmic-spaced radial bins with a minimum bin width that equals the FWHM of the respective PSF. In addition, we evaluate the model in ellipses where the spatial coverage is larger than 20%.

Fig. 4.8 shows the results of the modelling, where three distinct kinematic regimes become evident. At large scales, only covered by the stellar and ionised gas velocity fields, the host galaxy-scale 9.1 kpc bar dominates the ordered rotation. Following the bar inwards, stellar rotation drops rapidly. At  $R \sim 10$  pc ( $\sim 1.7$  kpc), the ionised gas moves significantly faster than the stellar component by 160 km/s. Although the position angle is aligned, the turn-over of the ionised gas velocity profile and the high  $k_5$  suggest that transition in the components from the galaxy-scale bar to nuclear scales. At  $1'' < R < 4''$  the molecular gas molecular gas orbits have a mean  $\langle q \rangle = 0.87 \pm 5$  deg, which corresponds to a disc inclination of

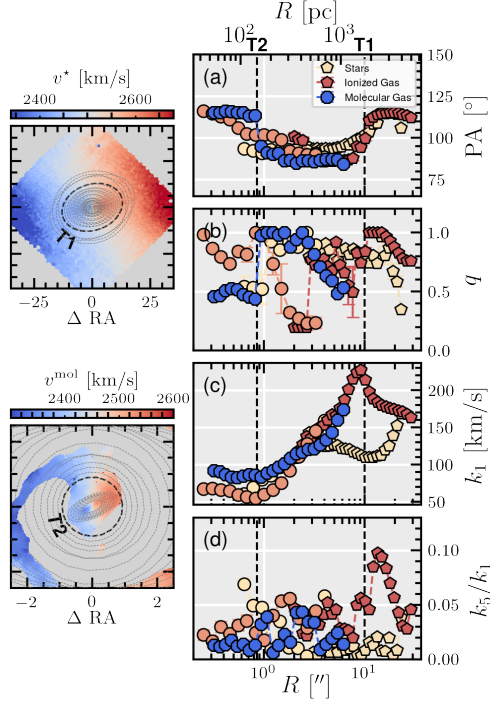


Figure 4.8: *Results of the kinematic modelling carried out with Kinemetry.* (Left) The top panel shows the stellar velocity field, the bottom panel that of the molecular gas. Over-plotted are the best-fitting ellipses along which the motion (Right) From top to bottom, the panels display (a) the PA corresponding to the orientation of the velocity profile (b) the ellipse axial ratio  $q$  (flattening) of the ellipse along which the velocity profile is measured (c) the amplitude of the bulk motions  $k_1$  corresponding to the rotation curve and (d) the higher-order term  $k_5/k_1$ , which indicates non-elliptical at large values. Profiles of the molecular gas phase, ionised gas phase and stellar rotation are shown with blue, red and yellow, respectively. A clear transition between different kinematic components is visible in each each of the velocity moments: At T1, the bar-dominated rotation transitions to the scales where the single-arm spiral shows exhibits the distinctive profile of a thin disc-rotation curve. At T2, the motion gets interrupted.

$i = (30 \pm 8)^\circ$ . In the innermost region the rotation curve turns over once again, such that the velocities rise approaching the AGN. While the stellar velocity field lacks spatial resolution in the centre, the high-S/N emission lines of the ionised gas cause beam-smearing, which dilute the velocity profile. As a consequence, the smallest scales are only well-resolved in the molecular gas phase.

---

# Unified Black Hole Mass Scaling Relations in Active and Quiescent Galaxies

This chapter is adapted from [Winkel et al. \(2024\)](#), which has been submitted for publication in *The Astrophysical Journal*. The project was initiated by Dr. Vardha N. Bennert and Dr. Bernd Husemann. The 3D spectroscopic data were obtained from various programs at the W. M. Keck Observatory and the VLT at the European Southern Observatory, one of which I led as Principal Investigator. These observations, conducted through May 2024, involved nightly observing plans developed under supervision of Dr. Bennert. Additionally, I led six observing runs related to this project at Keck II using the Keck Cosmic Web Imager instrument. Data reduction was handled by Raymond Remigio and myself. For discussion and interpretation, I received support from all of the aforementioned, as well as from colleagues in the LAMP collaboration.

Nico Winkel<sup>1</sup>, Vardha N. Bennert<sup>2,3</sup>, Raymond P. Remigio<sup>4</sup>, Tommaso Treu<sup>5</sup>,  
Knud Jahnke<sup>1</sup>, Vivian U<sup>4</sup>, Aaron J. Barth<sup>4</sup>, Matthew Malkan<sup>5</sup>, Bernd  
Husemann<sup>6,1</sup>, Xuheng Ding<sup>7</sup>, and Simon Birrer<sup>8</sup>

<sup>1</sup>Max-Planck-Institut für Astronomie, Königstuhl 17, D-69117 Heidelberg, Germany

<sup>2</sup>Physics Department, CalPoly San Luis Obispo, CA 93407, USA

<sup>3</sup>ESO, Karl-Schwarzschild-Str. 2, 85748 Garching, Germany

<sup>4</sup>Department of Physics and Astronomy, 4129 Frederick Reines Hall, UCI, CA 92697, USA

<sup>5</sup>Department of Physics and Astronomy, UCLA, 430 Portola Plaza, LA, CA 90095, USA

<sup>6</sup>EUMETSAT, Eumetsat Allee 1, 64295 Darmstadt, Germany

<sup>7</sup>School of Physics and Technology, Wuhan University, Wuhan 430072, China

<sup>8</sup>Department of Physics and Astronomy, Stony Brook University, NY 11794, USA

## Abstract

The origin of the tight scaling relation between the mass of supermassive black holes (SMBHs;  $M_{\text{BH}}$ ) and their host-galaxy properties remains unclear. Active galactic nuclei (AGNs) probe phases of ongoing SMBH growth and offer the only opportunity to measure  $M_{\text{BH}}$  beyond the local Universe. However, determining AGN host galaxy stellar velocity dispersion  $\sigma_*$ , and their galaxy dynamical masses  $M_{\text{dyn}}$ , is complicated by AGN contamination, aperture effects and different host galaxy morphologies. We select a sample of AGNs for which  $M_{\text{BH}}$  has been independently determined to high accuracy by state-of-the-art techniques: dynamical modeling of the reverberation signal and spatially resolving the broad-line region with VLTI/GRAVITY. Using IFU observations, we spatially map the host galaxy stellar kinematics across the galaxy and bulge effective radii. We find that that the dynamically hot component of galaxy disks correlate with  $M_{\text{BH}}$ ; however, the correlations are tightest on scales of the bulge. Accounting for different  $M_{\text{BH}}$  distributions, we demonstrate – for the first time – that AGNs follow the same  $M_{\text{BH}}\text{-}\sigma_*$  and  $M_{\text{BH}}\text{-}M_{\text{bulge,dyn}}$  relations as quiescent galaxies. We confirm that the classical approach of determining the virial factor  $f$  as sample-average is consistent with the average  $f$  from independent measurements. The similarity between the scaling relations of AGNs and quiescent galaxies implies that the AGN duty cycle is too short to alter BH masses on a population level. Our results strengthen the local calibration of  $f$  for measuring single-epoch  $M_{\text{BH}}$  in the distant Universe.

# Chapter 5 | Unified Black-Hole-Mass-Host-Galaxy Scaling Relations in Active and Quiescent Galaxies

## 5.1 Introduction

Supermassive black holes (SMBHs) are located in the hearts of most, if not all, massive galaxies. Their masses  $M_{\text{BH}}$  form tight correlations with various properties of their host galaxies. Prominent examples include the scaling relations between  $M_{\text{BH}}$  and bulge stellar mass (Magorrian et al., 1998; Häring & Rix, 2004), bulge luminosity (Kormendy & Richstone, 1995; Marconi & Hunt, 2003) or bulge stellar velocity dispersion  $\sigma_*$  (Ferrarese & Merritt, 2000; Gebhardt et al., 2000; Merritt & Ferrarese, 2001; Tremaine et al., 2002; Treu et al., 2004). One way to interpret these scaling relations is a coupling between the growth of SMBHs to that of their host galaxies (e.g. Ferrarese & Merritt, 2000; Kormendy & Ho, 2013), implying a causal connection between processes involved. Among the scaling relations, the  $M_{\text{BH}}-\sigma_*$  correlation stands out as particularly tight. The  $M_{\text{BH}}-\sigma_*$  relation exhibits a remarkably small intrinsic scatter of  $\sim 0.4$  dex over many orders  $M_{\text{BH}}$  and host-galaxy mass (Gültekin et al., 2009; Saglia et al., 2016; van den Bosch, 2016), providing important insights into SMBH formation scenarios, such as BH seeding models (Volonteri & Natarajan, 2009), and models for SMBH-galaxy coevolution (Robertson et al., 2006; Hopkins et al., 2006; Mo et al., 2024). Considering the tightness of the relation, and that  $\sigma_*$  is a direct tracer for dynamical mass, the  $M_{\text{BH}}-\sigma_*$  relation is often interpreted as the most direct probe for the formation and coevolution of SMBHs with their host galaxies (Tremaine et al., 2002; Beifiori et al., 2012; Saglia et al., 2016; van den Bosch, 2016; de Nicola et al., 2019; Graham, 2023). As such, the  $M_{\text{BH}}$  scaling relations for quiescent galaxies are well-established. However, any kind of evolutionary study of the  $M_{\text{BH}}$  scaling relations relies on  $M_{\text{BH}}$  measured in active galactic nuclei (AGNs).

The  $M_{\text{BH}}$  scaling relations in local AGNs are essential for various reasons. For one, broad-line (type-1) AGNs (BLAGNs) are the objects targeted in reverberation mapping (RM) studies, a unique way to determine

the mass of the SMBH. In short, RM observes variability in the accretion-disk luminosity and the time-delayed response of ionized gas in the broad-line region (BLR). While the light travel time provides constraints on the size of the BLR, Doppler-broadened emission lines give the velocity of the BLR clouds. The main uncertainties are due to the unknown geometry and kinematics of the BLR, summarized in the "virial" factor  $f$ . A sample-averaged  $f$ -value has traditionally been determined assuming that AGNs follow the same  $M_{\text{BH}}\text{-}\sigma_*$  relation as quiescent galaxies. By combining  $f$  with the empirical relation between BLR radius and luminosity (" $R$ - $L$  relation"), a single spectrum becomes sufficient for estimating  $M_{\text{BH}}$  for broad-line AGNs. This estimate is commonly referred to as the single-epoch (SE) method which enables  $M_{\text{BH}}$  measurements across the cosmic time.

Second, host galaxies build up their stellar mass, traced by  $\sigma_*$ , through secular processes on  $>10^7$  yr timescales, much longer than the duration of single AGN episodes of  $10^4$ - $10^6$  yr (Hickox et al., 2014; Schawinski et al., 2015). Despite their relatively short lifetimes, the bulk of cosmic SMBH mass growth occurs during luminous AGN phases (Merloni, 2004; Schulze et al., 2015). This implies that  $M_{\text{BH}}$  in AGNs is growing rapidly compared to the host galaxy, so that AGNs might probe a special state during the evolution of the  $M_{\text{BH}}$  scaling relations.

Third, AGNs are considered crucial for shaping the  $M_{\text{BH}}$  scaling relations. The energy from the central accretion disk can significantly affect the host galaxy by either heating the interstellar medium (ISM) or expelling cold gas, which suppresses star formation and limits the build-up of stellar mass in the bulge (Di Matteo et al., 2005; Croton, 2006; Somerville et al., 2008; Dubois et al., 2013; Harrison, 2017). These processes, collectively known as AGN feedback, can also regulate SMBH growth (Dubois et al., 2012; Massonneau et al., 2023). Although the exact timing and mechanisms of AGN feedback are still debated, these effects are expected to influence the  $M_{\text{BH}}\text{-}\sigma_*$  relation: Silk & Rees (1998b) predict a slope of  $\beta \approx 4$  for momentum-driven feedback, while energy-driven feedback should yield  $\beta = 5$  (King, 2003).

As an alternative to self-regulated SMBH growth, the hierarchical assembly of galaxy mass over cosmic time could create a non-causal link between  $M_{\text{BH}}$  and host-galaxy properties, mimicking the observed scaling relations (Peng, 2007; Hirschmann et al., 2010; Jahnke & Macciò,

2011). To achieve high stellar mass by redshift zero, a galaxy must have experienced multiple mergers, during which the central BHs also merged. If  $M_{\text{BH}}$  and host-galaxy stellar masses are randomly sampled during each merger, the central limit theorem predicts a correlation between them after several mergers. This scenario suggests that AGN feedback is not necessary for the formation of the  $M_{\text{BH}}$ -host-galaxy scaling relations over cosmic time.

All these open questions have continued to spark a large interest of the community, in particular whether the  $M_{\text{BH}}$ -galaxy scaling relations of active and inactive galaxies are identical. A series of studies have reported shallower  $M_{\text{BH}}-\sigma_*$  relations for RM AGNs, while also highlighting the challenge of extracting host-galaxy kinematics in luminous AGNs and the small dynamic range in  $M_{\text{BH}}$  (Woo et al., 2010, 2013; Park et al., 2012; Batista et al., 2017b). Woo et al. (2015) explain the initial tension by selection effects, which are sufficient to explain this flattening of the AGNs' relation. Indeed, several groups reported that  $M_{\text{BH}}-\sigma_*$  relation of AGNs and quiescent galaxies share similar slopes (e.g., Caglar et al., 2020; Shankar et al., 2019). While larger samples allow comparing the relative slopes, the offset between the  $M_{\text{BH}}-\sigma_*$  relation AGNs and quiescent galaxies remains unconstrained, because it is used to calibrate the sample-average virial factor  $f$ .

Recent advancements have enabled more robust and independent methods for measuring  $M_{\text{BH}}$  in AGNs. Compared to classical RM, velocity-resolved BLR lags from high signal-to-noise (S/N) and high-cadence spectroscopic data allow to resolve the BLR gas-flow structure (e.g., Blandford & McKee, 1982; Horne et al., 2004). For the datasets with the highest S/N, it is possible to extract more detailed properties of the BLR. However, the information is convolved with the BLR signal through the so-called transfer function, which describes the intrinsic time-delay distribution of the broad emission line (Peterson, 1993; Skielboe et al., 2015). To overcome degeneracies arising from similar BLR geometries, Pancoast et al. (2011) have introduced the Bayesian Code for AGN Reverberation and Modeling of Emission Lines (CAMEL). CAMEL provides a phenomenological description of the BLR dynamics, and thereby the inference of the BLR parameters and associated uncertainties in RM datasets. This method yielded precise and independent  $M_{\text{BH}}$  measurements, for a statistically

meaningful sample of 30 objects (e.g., Brewer et al., 2011; Li et al., 2013; Pancoast et al., 2014, 2018; Li et al., 2013; Williams et al., 2018; Williams & Treu, 2022; Villafaña et al., 2022; Bentz et al., 2022, for a recent compilation see Shen et al. 2024).

A novel third method involves spatially resolving the BLR, allowing for independent measurements of  $M_{\text{BH}}$ . What was first deemed impossible due to the small angular size of the BLR ( $\sim 10^{-4}$  arcsec) has become technically feasible with GRAVITY, the second-generation NIR beam combiner at the Very Large Telescope Interferometer (VLTI). The differential phase measures how the photo-center shifts at different wavelengths of the broad line emission compared to the continuum. Fitting the full differential phase spectra (rather than the time-resolved RM data) with a BLR model allows constraining the BLR structure and kinematics. Based the same BLR model parameterization as for CARMEL (Pancoast et al., 2014), so far six objects have robust  $M_{\text{BH}}$  from this technique (GRAVITY Collaboration et al., 2018, 2020, 2024). As this approach provides another independent method to constrain  $M_{\text{BH}}$ , this sample is complementary to the AGNs modeled with CARMEL.

In terms of host galaxy’s contribution in shaping the  $M_{\text{BH}}\text{-}\sigma_*$  relation, previous studies suggested a dependence on host morphology. Specifically, galaxies with structures like bars and pseudobulges deviate from the elliptical-only relation seen in quiescent galaxies (e.g., Graham, 2008; Hu, 2008; Gültekin et al., 2009). This morphological dependence is particularly relevant for AGNs, as  $\sigma_*$  measurements are typically based on single-aperture spectra, in which bars and pseudobulges are often unresolved (e.g., Graham et al., 2011; Woo et al., 2013). Aperture-integrated kinematics often are the only diagnostic available when covering a large dynamic range in  $M_{\text{BH}}$ . Consequently, inclination (Xiao et al., 2011; Bellovary et al., 2014), substructures (Hartmann et al., 2014) and rotational broadening from the disk contribution are likely impacting various recent calibrations of the AGN  $M_{\text{BH}}\text{-}\sigma_*$  relation, such as e.g., Woo et al. (2015); Caglar et al. (2020, 2023). Long-slit spectroscopy partially addresses this challenge by resolving the host galaxy along the slit axis. Using this technique, Bennert et al. (2015) demonstrated that  $\sigma_*$  measurements can vary by up to 40% on average across different definitions. Nevertheless, slit orientation relative to substructures, such as bars, can still dramatically impact  $\sigma_*$  (Batiste et al., 2017a). Batiste

et al. (2017b) find a 10% shallower slope for the  $M_{\text{BH}}\text{-}\sigma_*$  relation when accounting for rotational broadening in spatially resolved AGN host galaxies. However, their re-calibration is indistinguishable from that of previous studies due to a small sample of only 10 RM AGNs. Likewise, many previous studies suffered from a combination of lacking spatial resolution, poorly constrained  $M_{\text{BH}}$  and/or limited dynamic range in  $M_{\text{BH}}$  and  $\sigma_*$ . These limitations have hindered a consistent calibration of the  $M_{\text{BH}}\text{-}\sigma_*$  relation in AGNs and the determination of its intrinsic scatter and trends with AGN parameters or host-galaxy properties.

In this work, we use deep high-spectral-resolution integral-field spectroscopic (IFU) observations to spatially resolve  $\sigma_*$  across various host-galaxy components in a robust local AGN sample. High angular resolution imaging from Hubble Space Telescope (HST) will be used in a companion paper to decompose the host galaxy into its morphological components (Bennert et al., 2024, in prep.). We match the apertures for stellar kinematics extraction to the radii determined from imaging, addressing aperture effects to account for differences in galaxy morphologies, AGN luminosities, and distances. This approach ensures a consistent framework for calibrating the  $M_{\text{BH}}\text{-}\sigma_*$  across a wide range of AGN properties.

This paper is organized as follows. Sect. 5.2 covers sample selection, while Sect. 5.3 details the IFU observations and data reduction, and Sect. 5.4 the data analysis. In Sect. 5.5 we present and discuss the  $M_{\text{BH}}\text{-}\sigma_*$  relation in the context of previous work. Sect. 5.6 provides a summary. The appendix includes details on fitting procedures, comparisons of different IFU datasets, and the impact of the AGN subtraction method in our 3D spectroscopic data. Throughout this work, we have adopted  $H_0 = 67.8 \text{ km/s/Mpc}$ ,  $\Omega_{\text{m}} = 0.308$ , and  $\Omega_{\text{vac}} = 0.692$  (Planck Collaboration et al., 2016). In the following, we refer to the stellar velocity dispersion, commonly denoted as  $\sigma_*$ , as  $\sigma$ .

## 5.2 Sample Selection

### 5.2.1 AGN Sample

The core sample for this work are AGNs with velocity-resolved BLR lags that have been modeled with CAMEL. Since this technique constrains the virial factor  $f$  individually ( $f_{\text{dyn}}$ ), a major source of systematic uncertainty is eliminated compared to  $M_{\text{BH}}$  from classical RM (cRM). In other words, AGNs with dynamically modeled  $M_{\text{BH}}$  provide the most pristine sample for inferring the underlying scaling relations. Furthermore, dynamical modeling reduces the statistical uncertainties of individual measurements from  $\sim 0.4$  dex (SE) and  $\sim 0.3$  dex (cRM), to typically 0.2 dex (Pancoast et al., 2014; Villafaña et al., 2022). Thanks to a number of recent campaigns, the sample of CAMEL AGNs has grown to 30 objects (for a recent compilation see Shen et al. 2024), covering a large range in BH masses and AGN luminosities ( $\log(M_{\text{BH}}/M_{\odot}) \sim 6.4 - 8.3 M_{\odot}$ ;  $0.01 \leq z \leq 0.16$ ).

In addition, we complement the sample by AGNs whose  $M_{\text{BH}}$  has been measured from spatially resolving the BLR with VLTI/GRAVITY. This has been achieved for a total of seven objects so far (GRAVITY Collaboration et al., 2018, 2020, 2021, 2024), of which NGC 3783 and IC 4329A overlap with the CAMEL AGN sample. Of the remaining five, we include the four that have deep optical IFU observations plus broad-band HST imaging publicly available: Mrk 1239, Mrk 509, IRAS 09149-6206, 3C 273. In the following, we refer to those six objects as GRAVITY AGNs.

To further increase the range of AGN luminosities,  $M_{\text{BH}}$  and host morphologies, but without sacrificing data quality, we additionally include AGNs that have (i)  $M_{\text{BH}}$  determined from cRM, (ii) existing deep optical 3D spectroscopy and (iii) archival broad-band imaging at high angular resolution with HST. In the following, we refer to these 10 objects as cRM AGNs. In total, our extended sample consists of 44 objects: 30 CAMEL AGNs, 6 GRAVITY AGNs, and 10 cRM AGNs.

## Black Hole Masses

The black hole masses  $M_{\text{BH}}$  for the entire sample are listed in Table 5.1, with column (2) indicating the technique used for  $M_{\text{BH}}$  determination. For CAMEL and GRAVITY AGNs,  $M_{\text{BH}}$  was determined independently, without assuming the virial factor  $f$ , avoiding assumptions about BLR geometry. NGC 3783 and IC 4329A, present in both samples, have  $M_{\text{BH}}$  values consistent between both techniques. The  $M_{\text{BH}}$  from CAMEL is used for the analysis unless stated otherwise. NGC 3227 is the only AGN with  $M_{\text{BH}}$  measured using a third technique, stellar dynamical modeling, suitable for nearby galaxies where the BH sphere of influence is spatially resolved (Davies et al., 2006). The value from this method  $\log(M_{\text{BH}}/M_{\odot}) = 7.0 \pm 0.3$  agrees with the  $\log(M_{\text{BH}}/M_{\odot}) = 7.04 \pm 0.11$  from CAMEL modeling (Bentz et al., 2023a), with the latter adopted for analysis.

The cRM AGNs require assuming an  $f$ -factor to determine  $M_{\text{BH}}$ . Previous studies have used different calibrations of  $\langle f \rangle$  for deriving  $M_{\text{BH}}$ , e.g. 5.5 (Onken et al., 2004), 5.2 (Woo et al., 2010), 2.8 (Graham et al., 2011), 5.1 (Park et al., 2012), 4.3 (Grier et al., 2013), or 4.8 (Batiste et al., 2017b). For consistency, we standardize the VP by computing it from the broad H $\beta$  emission line time lag,  $\tau_{\text{cen}}^{\text{rms}}$ , and the line dispersion  $\sigma_{\text{line}}^{\text{rms}}$  via

$$\text{VP} = c\tau_{\text{cen}}^{\text{rms}} \sigma_{\text{line}}^{\text{rms}2} / G. \quad (5.1)$$

If  $\sigma_{\text{line}}^{\text{rms}}$  is unavailable, we estimate it using the relation with  $\sigma_{\text{line}}^{\text{mean}}$ , or, if both are not available,  $\text{FWHM}_{\text{line}}^{\text{mean}}$  (Dalla Bontà et al., 2020b, their table 3). We then adopt the virial factor of  $\log f = 0.65$  ( $f = 4.47$ ) from Woo et al. (2015), consistent with the average of the individual values  $\log f_{\text{dyn}} = 0.66 \pm 0.07$  determined here (see also Villafaña et al., 2023) to derive the BH masses via

$$M_{\text{BH}} = f \frac{\langle \Delta v \rangle^2 R_{\text{BLR}}}{G} \quad (5.2)$$

where  $G$  is the gravitational constant. A summary of  $M_{\text{BH}}$ , H $\beta$  time lags, line widths, and virial products is provided in Table 5.1.

# V Black-Hole-Mass-Host-Galaxy Scaling Relations in AGNs

Table 5.1: Black hole masses.

AGN Name	Sample	$\tau_{\text{rms}}^{\text{cen}}$ [d]	$\tau$ Ref.	$\sigma_{\text{line}}^{\text{rms}}$ [km s <sup>-1</sup> ]	v-ind.	VP [log $M_{\odot}$ ]	$M_{\text{BH}}$ [log $M_{\odot}$ ]	$M_{\text{BH}}$ Ref.	log $f_{\text{dyn}}$
(1)	(2)	(3)	(4)	(5)	(6)	(7)	(8)	(9)	(10)
NGC 3227	CAMEL	4.03 <sup>+0.85</sup> <sub>-0.94</sub>	B23a	1682 ± 39	B23a	6.35 <sup>+0.11</sup> <sub>-0.13</sub>	7.04 <sup>+0.11</sup> <sub>-0.11</sub>	B23a	0.72 <sup>+0.15</sup> <sub>-0.17</sub>
NGC 6814	CAMEL	6.64 <sup>+0.87</sup> <sub>-0.90</sub>	B09b	1610 ± 108	B09b	6.52 <sup>+0.11</sup> <sub>-0.12</sub>	6.42 <sup>+0.24</sup> <sub>-0.16</sub>	P14	-0.14 <sup>+0.26</sup> <sub>-0.20</sub>
NGC 4593	CAMEL	3.54 <sup>+0.76</sup> <sub>-0.82</sub>	W18	1601 ± 40	B15	6.25 <sup>+0.11</sup> <sub>-0.12</sub>	6.65 <sup>+0.27</sup> <sub>-0.15</sub>	W18	0.41 <sup>+0.25</sup> <sub>-0.20</sub>
NGC 3783	CAMEL	9.60 <sup>+0.82</sup> <sub>-0.72</sub>	B21a	1619 ± 137	B21a	6.69 <sup>+0.13</sup> <sub>-0.11</sub>	7.45 <sup>+0.07</sup> <sub>-0.10</sub>	B21b	0.82 <sup>+0.12</sup> <sub>-0.15</sub>
	GRAVITY	-	-	-	-	-	7.40 <sup>+0.14</sup> <sub>-0.14</sub>	G21	-
NGC 2617	cRM	6.38 <sup>+0.44</sup> <sub>-0.50</sub>	F17	2424 ± 91	F17	6.86 <sup>+0.06</sup> <sub>-0.07</sub>	7.51 <sup>+0.47</sup> <sub>-0.47</sub>	this work	* 0.65
IC 4329 A	CAMEL	16.33 <sup>+2.35</sup> <sub>-2.28</sub>	B23b	2112 ± 93	B23b	7.15 <sup>+0.10</sup> <sub>-0.11</sub>	7.64 <sup>+0.53</sup> <sub>-0.38</sub>	B23b	0.49 <sup>+0.54</sup> <sub>-0.27</sub>
	GRAVITY	-	-	-	-	-	7.15 <sup>+0.38</sup> <sub>-0.26</sub>	G24	-
Mrk 1044	cRM	10.50 <sup>+3.30</sup> <sub>-2.70</sub>	D15	†831 ± 43	D15	6.15 <sup>+0.15</sup> <sub>-0.19</sub>	6.45 <sup>+0.12</sup> <sub>-0.10</sub>	this work	* 0.65
NGC 5548	CAMEL	4.17 <sup>+0.36</sup> <sub>-0.36</sub>	P17	4115 ± 513	P17	7.14 <sup>+0.14</sup> <sub>-0.13</sub>	7.64 <sup>+0.21</sup> <sub>-0.18</sub>	W20	0.37 <sup>+0.25</sup> <sub>-0.24</sub>
NGC 7469	cRM	8.00 <sup>+0.80</sup> <sub>-1.50</sub>	L21	1485 ± 34	L21	6.53 <sup>+0.08</sup> <sub>-0.09</sub>	7.18 <sup>+0.05</sup> <sub>-0.09</sub>	this work	* 0.65
Mrk 1310	CAMEL	3.66 <sup>+0.59</sup> <sub>-0.61</sub>	B09b	755 ± 138	B09b	5.61 <sup>+0.21</sup> <sub>-0.25</sub>	7.42 <sup>+0.27</sup> <sub>-0.27</sub>	P14	1.63 <sup>+0.34</sup> <sub>-0.37</sub>
Mrk 1239	GRAVITY	-	-	-	-	-	7.47 <sup>+0.15</sup> <sub>-0.92</sub>	G24	-
Arp 151	CAMEL	3.99 <sup>+0.49</sup> <sub>-0.68</sub>	B09b	1252 ± 46	B09b	6.08 <sup>+0.09</sup> <sub>-0.10</sub>	6.62 <sup>+0.10</sup> <sub>-0.13</sub>	P14	0.51 <sup>+0.14</sup> <sub>-0.16</sub>
Mrk 50	CAMEL	8.66 <sup>+1.63</sup> <sub>-1.30</sub>	W18	2020 ± 103	B15	6.84 <sup>+0.12</sup> <sub>-0.12</sub>	7.51 <sup>+0.06</sup> <sub>-0.06</sub>	W18	0.72 <sup>+0.13</sup> <sub>-0.14</sub>
Mrk 335	CAMEL	18.86 <sup>+2.84</sup> <sub>-2.84</sub>	G17	1239 ± 78	G17	6.75 <sup>+0.10</sup> <sub>-0.11</sub>	7.25 <sup>+0.10</sup> <sub>-0.10</sub>	G17	0.59 <sup>+0.15</sup> <sub>-0.15</sub>
Mrk 590	cRM	20.50 <sup>+4.50</sup> <sub>-3.00</sub>	P98	-	-	-	7.58 <sup>+0.07</sup> <sub>-0.07</sub>	this work	* 0.65
SBS 1116+583A	CAMEL	2.31 <sup>+0.69</sup> <sub>-0.45</sub>	B09b	1528 ± 184	B09b	6.02 <sup>+0.19</sup> <sub>-0.23</sub>	6.99 <sup>+0.32</sup> <sub>-0.25</sub>	P14	0.96 <sup>+0.37</sup> <sub>-0.34</sub>
Zw 229-015	CAMEL	3.86 <sup>+0.90</sup> <sub>-0.90</sub>	B11	1590 ± 47	B11	6.28 <sup>+0.13</sup> <sub>-0.13</sub>	6.94 <sup>+0.14</sup> <sub>-0.14</sub>	W18	0.66 <sup>+0.18</sup> <sub>-0.18</sub>
Mrk 279	CAMEL	16.00 <sup>+5.80</sup> <sub>-5.80</sub>	W18	1778 ± 7	B15	6.99 <sup>+0.13</sup> <sub>-0.19</sub>	7.58 <sup>+0.08</sup> <sub>-0.08</sub>	W18	0.78 <sup>+0.16</sup> <sub>-0.21</sub>
Ark 120	CAMEL	18.70 <sup>+5.90</sup> <sub>-5.90</sub>	U22	1882 ± 42	U22	7.11 <sup>+0.16</sup> <sub>-0.16</sub>	8.26 <sup>+0.12</sup> <sub>-0.12</sub>	V22	1.15 <sup>+0.23</sup> <sub>-0.23</sub>
3C 120	CAMEL	25.90 <sup>+2.30</sup> <sub>-2.30</sub>	G12	1514 ± 65	G12	7.06 <sup>+0.07</sup> <sub>-0.07</sub>	7.84 <sup>+0.14</sup> <sub>-0.14</sub>	G17	0.75 <sup>+0.16</sup> <sub>-0.16</sub>
MCG +04-22-042	CAMEL	13.30 <sup>+2.10</sup> <sub>-2.10</sub>	U22	977 ± 29	U22	6.39 <sup>+0.09</sup> <sub>-0.12</sub>	7.59 <sup>+0.42</sup> <sub>-0.28</sub>	V22	1.06 <sup>+0.43</sup> <sub>-0.28</sub>
Mrk 1511	CAMEL	5.44 <sup>+0.69</sup> <sub>-0.69</sub>	W18	1506 ± 42	B15	6.38 <sup>+0.15</sup> <sub>-0.17</sub>	7.11 <sup>+0.20</sup> <sub>-0.17</sub>	W18	0.63 <sup>+0.29</sup> <sub>-0.28</sub>
PG 1304-108	CAMEL	7.20 <sup>+2.41</sup> <sub>-3.11</sub>	W18	†1978 ± 104	B15	6.74 <sup>+0.19</sup> <sub>-0.26</sub>	6.48 <sup>+0.24</sup> <sub>-0.16</sub>	W18	-0.26 <sup>+0.28</sup> <sub>-0.33</sub>
Mrk 509	GRAVITY	-	-	-	-	-	8.00 <sup>+0.23</sup> <sub>-0.15</sub>	G24	-
Mrk 110	CAMEL	27.80 <sup>+4.30</sup> <sub>-5.10</sub>	U22	1314 ± 69	U22	6.97 <sup>+0.11</sup> <sub>-0.13</sub>	7.17 <sup>+0.67</sup> <sub>-0.26</sub>	V22	0.74 <sup>+0.68</sup> <sub>-0.29</sub>
Mrk 1392	CAMEL	26.70 <sup>+3.50</sup> <sub>-3.90</sub>	U22	1501 ± 38	U22	7.07 <sup>+0.08</sup> <sub>-0.09</sub>	8.16 <sup>+0.11</sup> <sub>-0.11</sub>	V22	1.01 <sup>+0.16</sup> <sub>-0.16</sub>
Mrk 841	CAMEL	11.20 <sup>+4.80</sup> <sub>-4.80</sub>	U22	2278 ± 96	U22	7.05 <sup>+0.17</sup> <sub>-0.17</sub>	7.62 <sup>+0.50</sup> <sub>-0.30</sub>	V22	0.60 <sup>+0.53</sup> <sub>-0.38</sub>
Zw 535-012	cRM	20.30 <sup>+8.10</sup> <sub>-8.10</sub>	U22	1259 ± 112	U22	6.80 <sup>+0.19</sup> <sub>-0.22</sub>	7.57 <sup>+0.15</sup> <sub>-0.15</sub>	this work	* 0.65
Mrk 141	CAMEL	5.63 <sup>+2.64</sup> <sub>-2.64</sub>	W18	†2473 ± 125	B15	6.83 <sup>+0.22</sup> <sub>-0.22</sub>	7.46 <sup>+0.19</sup> <sub>-0.19</sub>	W18	0.70 <sup>+0.27</sup> <sub>-0.30</sub>
RBS 1303	CAMEL	18.70 <sup>+3.80</sup> <sub>-4.30</sub>	U22	1292 ± 156	U22	6.78 <sup>+0.33</sup> <sub>-0.21</sub>	6.79 <sup>+0.19</sup> <sub>-0.21</sub>	V22	0.04 <sup>+0.40</sup> <sub>-0.24</sub>
Mrk 1048	CAMEL	7.40 <sup>+0.70</sup> <sub>-0.40</sub>	U22	1726 ± 76	U22	-	7.79 <sup>+0.44</sup> <sub>-0.41</sub>	V22	0.74 <sup>+0.36</sup> <sub>-0.36</sub>
Mrk 142	CAMEL	2.74 <sup>+0.73</sup> <sub>-0.83</sub>	B09b	859 ± 102	B09b	5.59 <sup>+0.21</sup> <sub>-0.26</sub>	6.23 <sup>+0.30</sup> <sub>-0.30</sub>	L18	0.77 <sup>+0.39</sup> <sub>-0.39</sub>
RX J2044.0+2833	CAMEL	14.40 <sup>+1.60</sup> <sub>-1.90</sub>	U22	870 ± 50	U22	6.33 <sup>+0.10</sup> <sub>-0.11</sub>	7.09 <sup>+0.17</sup> <sub>-0.17</sub>	V22	0.66 <sup>+0.20</sup> <sub>-0.20</sub>
IRAS 09149-6206	GRAVITY	-	-	-	-	-	8.00 <sup>+0.30</sup> <sub>-0.40</sub>	G20	-
PG 2130+099	CAMEL	9.60 <sup>+1.20</sup> <sub>-1.20</sub>	G12	1825 ± 65	G12	6.79 <sup>+0.08</sup> <sub>-0.09</sub>	6.92 <sup>+0.24</sup> <sub>-0.25</sub>	G17	0.00 <sup>+0.25</sup> <sub>-0.25</sub>
NPM 1G+27.0587	CAMEL	8.00 <sup>+4.70</sup> <sub>-4.30</sub>	U22	1735 ± 136	U22	6.67 <sup>+0.26</sup> <sub>-0.34</sub>	7.64 <sup>+0.40</sup> <sub>-0.38</sub>	V22	0.93 <sup>+0.48</sup> <sub>-0.46</sub>
RBS 1917	CAMEL	11.90 <sup>+3.80</sup> <sub>-3.80</sub>	U22	851 ± 154	U22	6.22 <sup>+0.08</sup> <sub>-0.08</sub>	7.04 <sup>+0.38</sup> <sub>-0.38</sub>	V22	0.54 <sup>+0.36</sup> <sub>-0.36</sub>
PG 2209+184	CAMEL	13.70 <sup>+3.80</sup> <sub>-2.90</sub>	U22	1353 ± 64	U22	6.69 <sup>+0.36</sup> <sub>-0.14</sub>	7.53 <sup>+0.35</sup> <sub>-0.20</sub>	V22	0.72 <sup>+0.35</sup> <sub>-0.20</sub>
PG 1211+143	cRM	103.00 <sup>+52.00</sup> <sub>-44.00</sub>	K00	†981 ± 120	K00	7.28 <sup>+0.24</sup> <sub>-0.31</sub>	8.07 <sup>+0.11</sup> <sub>-0.15</sub>	this work	* 0.65
PG 1426+015	cRM	115.00 <sup>+68.00</sup> <sub>-49.00</sub>	K00	†3345 ± 471	K00	8.40 <sup>+0.29</sup> <sub>-0.44</sub>	9.02 <sup>+0.11</sup> <sub>-0.15</sub>	this work	* 0.65
Mrk 1501	CAMEL	15.50 <sup>+2.20</sup> <sub>-1.80</sub>	G12	3321 ± 107	G12	7.52 <sup>+0.08</sup> <sub>-0.08</sub>	7.86 <sup>+0.20</sup> <sub>-0.17</sub>	G17	0.34 <sup>+0.22</sup> <sub>-0.19</sub>
PG 1617+175	cRM	34.30 <sup>+6.80</sup> <sub>-6.80</sub>	H21	1288 ± 347	H21	7.04 <sup>+0.27</sup> <sub>-0.35</sub>	7.69 <sup>+0.21</sup> <sub>-0.35</sub>	this work	* 0.65
PG 0026+129	cRM	126.80 <sup>+37.50</sup> <sub>-32.50</sub>	P04	1719 ± 495	P04	7.86 <sup>+0.33</sup> <sub>-0.44</sub>	8.50 <sup>+0.07</sup> <sub>-0.11</sub>	this work	* 0.65
3C 273	GRAVITY	170.00 <sup>+96.00</sup> <sub>-14.00</sub>	Z19	1099 ± 40	Z19	7.60 <sup>+0.06</sup> <sub>-0.06</sub>	9.06 <sup>+0.21</sup> <sub>-0.27</sub>	L22	1.52 <sup>+0.22</sup> <sub>-0.28</sub>

**Notes.** AGNs are listed in order of increasing redshift. (1) Most common identifier. (2) Sample based on  $M_{\text{BH}}$ -measurement. (3) Cross-correlation H $\beta$  emission line lag. (4) Reference for H $\beta$  lag. (5) Velocity indicator. Values marked with (†) are estimated from  $\sigma_{\text{line}}^{\text{mean}}$  or FWHM $^{\text{mean}}$  (6) Reference for velocity indicator. (7) Virial Product as calculated from eq. 5.1. (8) Black hole mass  $M_{\text{BH}}$ . (9) Reference for  $M_{\text{BH}}$ . "this work" indicates that we have standardized the  $f$ -factor. (10) Independent  $f$ -factor inferred from dynamical modelling. (\*) indicates the sample-average for cRM. Reference keys are P98: Peterson et al. (1998), K00: Kaspi et al. (2000), P04: Peterson et al. (2004), B09b: Bentz et al. (2009b), B11: Barth et al. (2011), G12: Grier et al. (2012), P14: Pancoast et al. (2014), B15: Barth et al. (2015), D15: Du et al. (2015), F17: Fausnaugh et al. (2017), G17: Grier et al. (2017), P17: Pei et al. (2017), L18: Li et al. (2018), W18: Williams et al. (2018), Z19: Zhang et al. (2019), G20: GRAVITY Collaboration et al. (2020), W20: Williams et al. (2020), B21a: Bentz et al. (2021b), B21b: Bentz et al. (2021a), G21: GRAVITY Collaboration et al. (2021), H21: Hu et al. (2021), L21: Lu et al. (2021), L22: Li et al. (2022), V22: Villafañã et al. (2022), U22: U et al. (2022), B23a: Bentz et al. (2023a), B23b: Bentz et al. (2023b), G24: GRAVITY Collaboration et al. (2024).

### 5.2.2 Quiescent Galaxy Sample

To compare the AGN scaling relations between  $M_{\text{BH}}$  and  $\sigma$  to those of quiescent galaxies, we adopt the sample from [Kormendy & Ho \(2013; KH13](#) in the following). This sample includes 8 local galaxies with  $M_{\text{BH}}$  measurements based on dynamical modeling of spatially resolved stellar kinematics. Of 86 galaxies in total, we include 44 elliptical galaxies, 20 spiral and S0 galaxies with classical bulges, and 21 spiral and S0 galaxies with pseudobulges. While more recent compilations extend to lower galaxy masses, definition of host galaxy parameters in the KH13 sample is closest to our properties used in the following analysis. In particular the bulge dynamical mass derived from the spheroid effective radius, allowing for a consistent comparison. We have tested that changing the quiescent sample to those from [McConnell & Ma \(2013\)](#) or [van den Bosch \(2016\)](#) does qualitatively not affect the conclusions.

## 5.3 Observations and Data Reduction

### 5.3.1 IFU Observations

Our team has carried out IFU observations for 33/44 of the AGNs in our sample. For the remaining objects, archival IFU observations are available from public repositories. In the following, we describe data acquisition and reduction.

#### Keck/KCWI Observations

Many of the AGNs were initially monitored in the LAMP2011 and LAMP16 RM campaigns to study BLR dynamics and measure ([Barth et al., 2015](#); [U et al., 2022](#)). We followed up with 3D spectroscopy of their host galaxies using the Keck Cosmic Web Imager (KCWI, [Morrissey et al., 2018](#)) on Keck II under several programs. Key diagnostic features were the stellar absorption lines, in particular the Mg Ib  $\lambda\lambda 5167, 5173, 5184$  triplet (hereafter Mg Ib), and the Fe I+Fe II complex. KCWI was configured with the medium IFU slicer and medium-resolution blue grating, providing a  $16''.5 \times 20''.4$  FoV and  $0''.69$  spatial sampling, covering the 4700–5700 Å range optimized for H $\beta$ , [O III], and Mg Ib +Fe lines.

Our observing programs followed the same general strategy: Given the rectangular shape of the KCWI FoV we chose its position angle (PA) such that the FoV major axis matches that of the galaxy as estimated from archival images. For each object, we first took a short exposure (60-120 s, depending on redshift and AGN luminosity) guaranteeing that at least one exposure is available, for which the AGN emission lines in the center are not saturated. We used this exposure to scale up the exposure time of the following frames such that the continuum in the center is close to saturation. For most objects, except nearby bright AGNs, this resulted in 600 s or 990 s science exposures, which we dither-offset by  $1''$  along the FoV major axis in between adjacent exposures. In between every other science exposure, we took sky frames by nodding away from the target (T) to obtain external sky exposures (S) e.g., sequence TSTTSTTST. We chose sky pointings carefully such that they are at least  $1$  arcmin away from the AGN, in blank patches of the sky as verified by SDSS, DSS and 2MASS images.

The pilot program 2018B\_U171 began on Feb 8 2018, with observations under photometric conditions and  $1.5$ - $2''$ . We observed during three more nights on Aug 7, Aug 15 and Oct 3 2018 under Prog.ID 2018B\_U012. In total, our observations during 2018B\_U171 and 2018B\_U012 yielded data of eight AGNs from the LAMP2016 campaign (4200-5400 s on-source times) and for Mrk 50 from the the LAMP2011 campaign (900 s on-source). During program 2023B\_U114, conducted on four nights between October 2023 and January 2024, the BM setup was maintained while using the novel KCWI red arm. We observed 10 AGNs from the LAMP16 campaign under mostly clear conditions, with total integration times from 1800 s to 7200 s. Under program 2024A\_U118, we conducted two consecutive runs, observing the last seven objects from the LAMP2016 campaign with total integration times from 1800 s to 7200 s. In addition, we collecting some more integration on RXJ 2044.0+2833 and NPM1G+27.0587 to improve S/N. Although KCRM observations since 2023 cover the Ca II  $\lambda\lambda 8498, 8542, 8662$  (hereafter CaT), temporal variation in strong sky emission lines, made their accurate subtraction difficult. We tried methods like CubePCA and other PCA-based approaches like the one from Gannon et al. (2020), but these were hindered by the absence of empty sky regions in the science exposure, or strong spatial variation of the science spectra. As a result, we decided to rely solely on KCWI blue spectra for consistent analysis across the AGN sample.

Table 5.2: *Observational parameters for the IFU data.*

AGN Name (1)	$\alpha$ (J2000) (2)	$\delta$ (J2000) (3)	Instrument (4)	UT Date (5)	$t_{\text{exp}}$ [s] (6)	$\theta$ FWHM (7)	Prog. ID (8)
NGC 3227	10:23:30.57	+19:51:54.28	VLT/MUSE	2022-03-31	2660	0.96	0108.B-0838(A)
NGC 6814	19:42:40.64	-10:19:24.60	Keck/KCWI	2023-10-17	1650	1.06	2023B_U114
NGC 4593	12:37:04.67	-05:04:10.79	VLT/MUSE	2019-04-28	4750	0.62	099.B-0242(B)
NGC 3783	11:39:01.70	-37:44:19.01	VLT/MUSE	2015-04-19	3600	0.90	095.B-0532(A)
NGC 2617	08:35:38.80	-04:05:18.00	VLT/MUSE	2020-12-23	2300	1.04	0106.B-0996(B)
IC 4329 A	13:49:19.26	-30:18:34.21	VLT/MUSE	2022-04-01	2200	0.81	60.A-9100(A)
Mrk 1044	02:30:05.52	-08:59:53.20	VLT/MUSE	2019-08-24	1200	1.20	094.B-0345(A)
NGC 5548	14:17:59.54	+25:08:12.60	Keck/KCWI	2024-04-29	3305	0.83	2024A_U118
NGC 7469	23:03:15.67	+08:52:25.28	VLT/MUSE	2014-08-19	2400	0.84	60.A-9339(A)
Mrk 1310	12:01:14.36	-03:40:41.10	Keck/KCWI	2024-04-29	3840	1.02	2024A_U118
Mrk 1239	09:52:19.16	-01:36:44.10	VLT/MUSE	2021-01-27	4600	1.14	0106.B-0996(B)
Arp 151	11:25:36.17	+54:22:57.00	Keck/KCWI	2024-01-04	1890	1.22	2023B_U114
Mrk 50	12:20:50.69	+02:57:21.99	Keck/KCWI	2018-02-08	900	1.62	2018B_U171
Mrk 335	00:06:19.52	+20:12:10.50	Keck/KCWI	2023-10-17	2570	0.69	2023B_U114
Mrk 590	02:14:33.56	-00:46:00.18	VLT/MUSE	2017-10-28	9900	0.76	099.B-0294(A)
SBS 1116+583A	11:18:57.69	+58:03:23.70	Keck/KCWI	2024-01-04	2840	1.22	2023B_U114
Zw 229-015	19:03:50.79	+42:23:00.82	Keck/KCWI	2018-08-15	3600	1.01	2018B_U012
Mrk 279	13:53:03.45	+69:18:29.60	Keck/KCWI	2024-04-30	5400	0.84	2024A_U118
Ark 120	05:13:37.87	-00:12:15.11	Keck/KCWI	2018-02-08	4800	1.75	2018B_U171
3C 120	04:33:11.09	+05:21:15.61	Keck/KCWI	2024-01-04	2760	1.12	2023B_U114
MCG +04-22-042	09:23:43.00	+22:54:32.64	Keck/KCWI	2018-02-08	5400	1.87	2018B_U171
Mrk 1511	15:31:18.07	+07:27:27.90	Keck/KCWI	2024-04-29	5910	0.84	2024A_U118
PG 1310-108	13:13:05.79	-11:07:42.40	Keck/KCWI	2024-04-29	5810	1.03	2024A_U118
Mrk 509	20:44:09.75	-10:44:24.70	Keck/KCWI	2024-04-29	4830	1.18	2024A_U118
Mrk 110	09:21:44.37	+52:30:07.63	Keck/KCWI	2018-02-08	5400	2.09	2018B_U171
Mrk 1392	15:05:56.55	+03:42:26.33	Keck/KCWI	2018-02-08	4200	1.71	2018B_U171
Mrk 841	15:01:36.31	+10:37:55.65	Keck/KCWI	2018-02-08	5400	2.01	2018B_U171
Zw 535-012	00:36:20.98	+45:39:54.08	Keck/KCWI	2018-10-03	4500	1.13	2018B_U012
Mrk 141	10:19:12.56	+63:58:02.80	Keck/KCWI	2024-01-04	3770	1.25	2023B_U114
RBS 1303	13:41:12.88	-14:38:40.24	VLT/VIMOS	2009-04-27	2000	1.19	083.B-0801(A)
Mrk 1048	02:34:37.88	-08:47:17.02	VLT/MUSE	2015-01-12	1200	1.21	094.B-0345(A)
Mrk 142	10:25:31.28	+51:40:34.90	Keck/KCWI	2024-04-30	6690	0.76	2024A_U118
RX J2044.0+2833	20:44:04.50	+28:33:12.10	Keck/KCWI	2018-08-07	5400	0.85	2018B_U012
IRAS 09149-6206	09:16:09.36	-62:19:29.56	VLT/MUSE	2024-05-08	1600	1.01	113.26SK.001(B)
PG 2130+099	21:30:01.18	+09:55:00.84	VLT/MUSE	2019-06-09	2440	0.53	0103.B-0496(B)
NPM 1G+27.0587	18:53:03.87	+27:50:27.70	Keck/KCWI	2023-10-20	6000	0.96	2023B_U114
RBS 1917	22:56:36.50	+05:25:17.20	Keck/KCWI	2023-10-17	5550	0.83	2023B_U114
PG 2209+184	22:11:53.89	+18:41:49.90	Keck/KCWI	2023-10-20	6960	0.78	2023B_U114
PG 1211+143	12:14:17.67	+14:03:13.18	VLT/MUSE	2016-04-01	2800	0.66	097.B-0080(A)
PG 1426+015	14:29:06.57	+01:17:06.15	VLT/MUSE	2016-04-04	2800	0.45	097.B-0080(A)
Mrk 1501	00:10:31.01	+10:58:29.00	Keck/KCWI	2023-11-03	4050	0.82	2023B_U114
PG 1617+175	16:20:11.27	+17:24:27.51	VLT/MUSE	2016-04-04	2800	0.52	097.B-0080(A)
PG 0026+129	00:29:13.70	+13:16:03.94	VLT/MUSE	2016-07-31	2250	0.62	097.B-0080(A)
3C 273	12:29:06.69	+02:03:08.59	VLT/MUSE	2016-03-31	4750	0.47	097.B-0080(A)

**Notes.** AGNs are listed in order of increasing redshift (as in Table 5.1). (1) IFU instrument used to conduct the observations for a given target. (2) Observing night during which the observations were acquired. (3) Total on source exposure time combined for the final cube after rejecting low-quality individual exposures. (4) Seeing in the final combined cubes inferred from 2D Moffat modeling of the broad  $H\beta$  intensity maps. (5) Proposal ID of the data set under which the program was executed at the respective observatories. Our team has carried out the observations with VLT/MUSE and Keck/KCWI of under the Prog. IDs 097.B-0080(A) and U114, U118, U171 respectively. For approximately a quarter of the sample we collect archival data.

We reduced the data using the Python KCWI Data Reduction Pipeline, including bias subtraction, flat field correction, and flux calibration. Additionally, we aligned science frames, replaced saturated pixels, and coadded reduced data cubes as described in our companion paper (Remigio et al., 2024, in prep.). The [O I] $\lambda$ 5577 sky emission line indicates an instrumental resolution of  $\text{FWHM} = 0.95 \text{ \AA}$  ( $\sim 32 \text{ km/s}$ ), with a common wavelength coverage of  $\sim 4700\text{-}5600 \text{ \AA}$  and  $0.28 \text{ \AA/pix}$  sampling.

### VLT/MUSE Observations

We acquired IFU observations for 8/44 AGNs using the Multi-Unit Spectroscopic Explorer (MUSE) at the Very Large Telescope (VLT). All observations were taken in MUSE wide field mode (WFM), covering a  $1' \times 1'$  FoV at  $0''.2$  sampling, and  $4750\text{-}9300 \text{ \AA}$  spectral coverage at a spectral resolution of  $R \sim 2500$ . Observations were conducted across various programs with consistent strategies. Mrk 1044 and Mrk 1048 had already been observed as part of the Close AGN Reference Survey (CARS) (Husemann et al., 2022), while five luminous cRM AGNs were observed under Prog.ID 097.B-0080(A) with integration times between 2800 s and 4500 s, employing standard dither-offset strategies. Observations were conducted in March, April, and July 2016 under gray moon and clear conditions with seeing of  $0''.4\text{-}1''.0$ . In addition, IRAS 09149-6206 was observed under Prog.ID 113.26SK.001(B), with 260 s exposures split into three observing blocks. Observations on May 4 and 8, and June 8, 2024, achieved a total integration time of 3360 s. For another nine CAMEL AGNs and two cRM AGNs, we retrieved phase 3 archival data from the ESO archive.

We processed the data using MUSE pipeline v2.8.3-1 with ESO Reflex v2.11.0, following standard reduction procedures including bias frames, continuum lamp frames, arc lamp frames for wavelength calibration, standard star frames for flux calibration, and twilight flats. For AGN host galaxies covering only a small part of the FoV, we created a mean sky spectrum from the lowest 20% flux in white light images and subtracted it from the cube. When the host galaxy filled the FoV, we used dedicated sky exposures from the archive. Telluric absorption bands were corrected by dividing the spectra by normalized transmission from standard star exposures taken close in time. Residuals in spectra arose from sky-line subtraction issues due to the timing of standard stars and spatial variations in the line spread function. To address these, we used CubePCA.

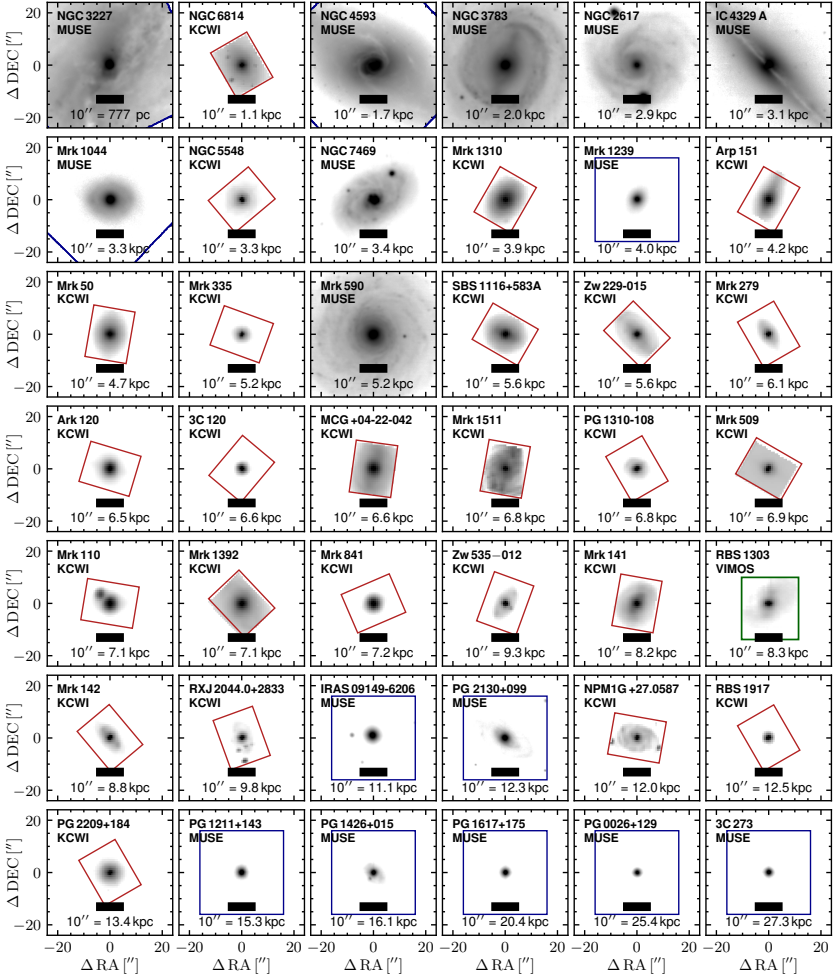


Figure 5.1: *Gallery of V-band images.* Images were reconstructed from the IFU data cubes (Table 5.2) with frames centered on the AGN position. North is up and east is to the left. Rectangles indicate the FoV covered by the IFU instrument, VLT/MUSE (blue), Keck/KCWI (red), VLT/VIMOS (green). For more distant AGNs observed with MUSE, cutouts are shown. AGN luminosity, host-galaxy sizes, IFU field coverage and depth of the observations vary substantially between the datasets.

This tool identifies the principal components (PCs) in the sky line residuals by fitting orthogonal eigenspectra to the individual spectra, and then subtracts the PCs.

### VLT/VIMOS Observations

Three of the 30 CAMEL AGNs (RBS 1303, PG 1310-108, and NGC 5548) were observed with the Visible Multi-Object Spectrograph IFU (VIMOS) (Le Fèvre et al., 2003). The VIMOS blue and orange cubes cover wavelengths of 3700-5222 Å and 5250-7400 Å, respectively, with a  $27'' \times 27''$  FoV and  $0''.6$  pixel sampling. While PG 1310-108 and NGC 5548 have higher-resolution, deeper data from Keck/KCWI, RBS 1303 was only observed with VIMOS. We used reduced data cubes from the Close AGN Reference Survey DR1 (CARS, Husemann et al., 2022), which were initially processed with the Py3D package and included standard reduction steps. For specific details on data reduction, including exposure alignment and drizzling, see Husemann et al. (2022). Our analysis focuses on the blue cubes, as they cover the essential Mg Ib and Fe I absorption lines for measuring stellar kinematics.

### AGN - Host Galaxy Deblending

The AGN featureless continuum and broad emission lines (in the wavelength range covered H $\beta$  and He I and Fe II) can easily outshine the underlying host-galaxy spectrum. It is therefore essential, to subtract the unresolved AGN emission before analyzing the faint host-galaxy emission. For this task, we use the approach outlined by Husemann et al. (2022): (1) We first estimate the empirical point spread function (PSF) at and from the broad wavelengths available in each dataset, using QDeblend<sup>3D</sup> (Husemann et al., 2013, 2014). (2) We model the PSFs with a 2D Moffat profile to suppress noise at large distances from the center. (3) If multiple broad lines are available, we interpolate the PSF as a function of wavelength. (4) We reconstruct the intrinsic host-galaxy surface brightness profile from 2D image modeling. (5) Finally, we iteratively subtract the point-like AGN emission from the extended host-galaxy emission combining the wavelength-dependent PSF with the host-galaxy surface brightness profile.

Deblending is crucial for accurately extracting host-galaxy stellar kinematics, as shown in Appendix 5.7.2. Without deblending, the stellar velocity dispersion  $\sigma$  can be overestimated by up to a factor of two, particularly near the AGN, which severely biases the luminosity-weighted mean  $\sigma$  due to poorly fitted spaxels. An alternative is to fit the AGN spectrum simultaneously with the host-galaxy emission, as used for a subset of the LAMP AGNs by (Remigio et al., 2024, in prep.). This method, compared in Appendix 5.7.8, generally provides results consistent with our deblending approach within the nominal uncertainties.

### 5.3.2 HST Imaging

Considering the large range of AGN parameters in our sample, the host galaxies are also likely to cover a large range in stellar masses, sizes and morphologies. To enable a consistent calibration of the scaling relations, we need a consistent measurement of the host-galaxy kinematics. This can be achieved by measuring the kinematics of different host-galaxy morphological components and separating their contributions to the galaxy-integrated kinematics. We characterize the host-galaxy morphologies from high-resolution images obtained with HST. For 33/44 of AGNs in the sample, archival wide-field imaging data exist which were acquired with either WFC3/UVIS, ACS/HRC or WFPC2/PC1 in optical broad or medium bands. The program HST-GO 17103 (PI: Bennert) acquired broad-band imaging from WFC3/UVIS for the remaining 11 objects of the CAMEL AGN sample. A detailed description of the data acquisition, data reduction, PSF subtraction, host-galaxy decomposition, 2D surface photometry and derived host-galaxy parameters will be presented in our companion paper (Bennert et al., 2024, in prep.).

#### Special handling of individual objects

The host galaxy decomposition based on HST/WFC3 images did not yield stable solutions for three objects at the very low- and high-redshift end. For the nearby galaxy NGC 3227, the WFC3 FoV covers only a small fraction of its  $5.4' \times 3.6'$  size. For NGC 3227's galaxy effective radius, we adopt the scale radius from an exponential fit to the Sloan Digital Sky Survey (SDSS) photometry in the r-band (*exrad\_r*). Although this approach assumes that the PSF has a minimal impact on NGC 3227's light profile,

it provides a quantity closest to the  $R_{\text{eff}}^{\text{gal}}$  definition used for the other objects. We encountered the same challenge for IC 4329A, where the highly inclined galaxy extends beyond the HST ACS/HRC FoV. While structural decomposition allows fitting the bulge, we adopt the galaxy scale length of  $25''2$  from NED, that was fitted to the  $k$ -band photometry from 2MASS.

For PG 0026+129, an extremely bright quasar, the host galaxy parameters recovered using `lenstronomy` and our library of model PSFs did not converge to stable solutions. Therefore, we adopted  $R_{\text{eff}}^{\text{gal}} = 2''6$  from [McLeod & McLeod \(2001\)](#), which was estimated based on HST/NIC2 F160W imaging. We encountered the same issue with the HST/WFC3 image of the bright quasar 3C 273. We adopt an effective radius of  $2''3$  for the host galaxy, as reported by [Bahcall et al. \(1997\)](#). Their measurement is based on HST/WFPC F606W imaging and is consistent with the  $2''3 - 2''6$  range reported by [Martel et al. \(2003\)](#), measured from coronagraphic imaging with HST/ACS in the  $V$  and  $I$  bands, respectively.

## 5.4 Analysis

### 5.4.1 Surface Photometry

For the purpose of this work, we are exclusively interested in the stellar kinematics of different host-galaxy components for which we adopt effective radii derived by fitting the 2D surface brightness profiles. For this task, we used the public code `lenstronomy` ([Birrer & Amara, 2018](#)), as outlined by [Bennert et al. \(2021\)](#). We measure the host-galaxy effective radius  $R_{\text{eff}}^{\text{gal}}$ , from the PSF-subtracted host-galaxy surface profile. A universal parameterization of a single spheroidal component (s), i.e. using a single-Sérsic component as input for `lenstronomy`, as it is often done for marginally resolved high-redshift galaxies or massive elliptical galaxies.

In reality, however, only a minority of galaxies in our sample are well-described by a spheroidal model. The majority of our AGN hosts are late-type galaxies, with a large morphological diversity including bars, bulges and disks, which can be seen in the reconstructed continuum images in Fig. 5.1. The HST imaging allows us to decompose the host galaxy into its morphological components. For many nearby AGNs, morphological classifications are available in the literature, Based on the high-quality imaging data collected for this project (Bennert et al., 2024, in prep.), we complemented (or revised) literature classifications, and standardized the nomenclature to the de Vaucouleurs system (see column (5) of Table. 5.3). We use this information as prior for parameterizing the host model, listed in Table 5.3. Models include bulge-only (s), bulge+disk (sd) or bulge+disk+bar (sdb) components. The best-fitting effective radii of the entire galaxy and bulge-only,  $R_{\text{eff}}^{\text{gal}}$  and  $R_{\text{eff}}^{\text{disk}}$ , serve as standardized measure as across which stellar kinematics are extracted. After running a minimum of ten decompositions for each object using different starting parameters, we estimate 0.1 dex systematic uncertainty for effective radii, and 0.2 dex if strong residuals from the PSF subtraction are present on scales of the spheroid. More details on the HST imaging data, the fitting process, and the full set of parameters will be presented in our companion paper (Bennert et al., 2024, in prep.).

### Disk axis ratio as proxy for inclination

The inclination of a galaxy disk can be estimated from its axis ratio as  $i_{b/a} = \arccos(b/a)$ . However, structural decomposition carried out with `lenstronomy` is sensitive to the parameterization defined by the user. While we are careful to check the parameterization, systematic uncertainties from limited FoV, prominent dust lanes crossing the galaxy center, and PSF mismatches likely contribute systematic uncertainties to the structural decomposition (Bennert et al., 2024, in prep., see also Sec. 5.5.1). To test whether the disk axis ratio is a good proxy for the galaxy inclination, we compare  $i_{b/a}$  with a visual estimate of the galaxy inclination  $i_{\text{vis}}$ . In general, it is possible to estimate the inclination if the host galaxy can be robustly separated from the PSF, and a disk component is clearly visible. For the majority of the sample, we based our estimate on the original HST images. However, for NGC 3227 and NGC 4593, the WFC3 FoV covers only a fraction of the galaxy, so that we used the PanSTARRS  $i$ -band images. We were able to estimate  $i_{\text{vis}}$  for each of the 29 disk galaxies,

Table 5.3: *Host galaxy parameters.*

AGN Name	Alt. Name	$z$	scale	Morph.	Morph.	Model	$R_{\text{eff}}^{\text{gal}}$	$R_{\text{eff}}^{\text{bulge}}$	$i$	Comment
(1)	(2)	(3)	[kpc $''$ ] (4)	(5)	Ref. (6)	(7)	[ $''$ ] (8)	[ $''$ ] (9)	[ $^{\circ}$ ] (10)	
NGC 3227		0.004	0.08	SAc	this work	sd	28.6	1.7	65	
NGC 6814		0.005	0.11	SABc	S11	sdb	45.1	1.3	22	
NGC 4593	Mrk 1330	0.008	0.17	SABb	S11	sdb	16.9	6.2	46	
NGC 3783		0.010	0.20	SABb	V91	sdb	14.0	2.2	33	
NGC 2617	LEDA 24141	0.014	0.29	SAA	this work	sd	12.1	1.2	18	CLAGN
IC 4329 A	RBS 1319	0.015	0.31	SA	V91	sd	35.2	$\wedge$ 2.9	20	
Mrk 1044	HE 0227-0913	0.016	0.33	SABc	this work	sdb	6.0	0.8	28	
NGC 5548	Mrk 1509	0.016	0.33	SAA	this work	sd	11.3	8.4	28	asym. morph.
NGC 7469	Mrk 1514	0.017	0.34	SABc	this work	sd	9.3	8.3	65	
Mrk 1310	RBS 1058	0.019	0.39	SAc	B19	sd	4.1	4.2	43	
Mrk 1239	LEDA 28438	0.020	0.40	S0A	this work	s	3.2	3.2		
Arp 151	Mrk 40	0.021	0.42	S0	S11	s	3.2	3.2		interacting
Mrk 50	RBS 1105	0.023	0.47	S0A	N10	s	4.0	4.0		
Mrk 335	PG 0003+199	0.026	0.52	E	K21	s	2.6	2.6		
Mrk 590	NGC 863	0.026	0.52	SAA	S11	sdb	2.0	1.4	35	CLAGN
SBS 1116+583A	Zw 291-51	0.028	0.56	SABa	this work	sdb	4.1	0.6	28	
Zw 229-015		0.028	0.56	SBd	K21	sdb	7.3	0.8	49	
Mrk 279		0.030	0.61	SAA	this work	sd	4.2	2.3	50	companion
Ark 120	Mrk 1095	0.033	0.65	SAA	this work	sd	5.7	2.0	30	asym. morph.
3C 120	Mrk 1506	0.033	0.66	S0A	S11	s	2.7	2.7		tidal tails
MCG +04-22-042	Zw 121-75	0.033	0.66	SABb	this work	sdb	11.7	0.9	56	
Mrk 1511	NGC 5940	0.034	0.68	SABc	B19	sd	11.6	0.5	40	
PG 1310-108	HE 1310-1051	0.034	0.68	SABa	this work	sdb	3.2	0.4	24	tidal tails
Mrk 509		0.035	0.69	*E2	B09a	s	2.4	2.4		
Mrk 110	PG 0921+525	0.035	0.71	*S0	this work	s	1.5	1.5		
Mrk 1392	Zw 48-115	0.036	0.71	SBb	this work	sdb	10.4	0.7	59	
Mrk 841	PG 1501+106	0.036	0.72	E	this work	s	3.6	3.6		
Zw 535-012	LEDA 2172	0.048	0.93	SBb	this work	sdb	5.7	0.6	58	
Mrk 141	Zw 313-11	0.042	0.82	SABa	B19	sdb	5.6	0.4	40	companion
RBS 1303	HE 1338-1423	0.042	0.83	SBA	this work	sdb	7.1	0.9	53	
Mrk 1048	NGC 985	0.043	0.84	SBc	S02	sd	11.9	2.7	46	interacting
Mrk 142	PG 1022+519	0.045	0.88	SBa	this work	sdb	5.6	0.4	34	
RX J2044.0+2833		0.050	0.98	SBd	K21	sdb	4.2	0.2	46	
IRAS 09149-6206		0.057	1.11	S0	this work	s	5.2	5.2		
PG 2130+099	Mrk 1513	0.064	1.23	Sa	B09a	sd	2.5	0.3	52	
NPM 1G+27.0587		0.062	1.20	SAB	this work	sd	6.5	0.6	38	companion
RBS 1917		0.065	1.25	SB	this work	sdb	1.7	0.1	23	
PG 2209+184		0.070	1.34	S	this work	sd	2.9	2.9	30	
PG 1211+143		0.081	1.53	E2	B09a	s	0.2	0.2		
PG 1426+015	Mrk 1383	0.086	1.61	E2	B09a	s	2.0	2.0		
Mrk 1501	PG 0007+107	0.087	1.63	*S0	S11	s	5.3	5.3		companion
PG 1617+175	Mrk 877	0.112	2.04	E2	B09a	s	1.2	1.2		
PG 0026+129	RBS 68	0.145	2.54	E1	B09a	s	*2.3	*2.3		
3C 273	PG 1226+023	0.158	2.73	E3	B09a	s	$\dagger$ 2.3	$\dagger$ 2.3		

**Notes.** AGNs are listed in order of increasing redshift (as in Table 5.1). (1) Most common identifier. (2) Alternative identifier. (3) Source redshift from NED. (4) Physical scale of  $1''$ . (5) Host Galaxy morphological classification, simplified to the de Vaucouleurs system. Values marked with (\*) are uncertain due to strong AGN blending. (6) Reference key for morphological classification. (7) Adopted parameterization for the host-galaxy morphology (s = Sérsic only, sd = Sérsic + Disk (n=1) fit; sdb = Sérsic + Disk (n=1) + Bar (n=0.5) fit, a detailed presentation will be outlined in Bennert et al. 2024). (8) Galaxy effective radius from fitting a single Sérsic component. (9) Bulge effective radius. (10) Inclination based on disk axis ratio  $a/b$  that is retrieved from the best-fitting  $\text{lenstronomy}$  model. ( $\wedge$ ) Adopted from NED. (\*) Adopted from McLeod & McLeod (2001). ( $\dagger$ ) Adopted from Bahcall et al. (1997). Reference keys are V91: de Vaucouleurs et al. (1991), S02: Salvato (2002), J04: Jahnke et al. (2004), N10: Nair & Abraham (2010), B09a: Bentz et al. (2009a), S11: Slavcheva-Mihova & Mihov (2011), A15: Ann et al. (2015), B19: Buta (2019), K21: Kim et al. (2021).

which are preferentially located at lower-redshift and show a prominent disk component. Depending on how well the galaxy is resolved, and how dominant the PSF is, we estimate that the associated uncertainties of  $i_{\text{vis}}$  range from approximately  $10^\circ$  to  $20^\circ$ . Overall, the visual estimates agree with the `lenstronomy` measurements within these uncertainties. We conclude that  $i_{b/a}$ , derived from the disk axis ratio, is a suitable indicator for the galaxy inclination. In the following, we adopt  $i_{b/a}$  as proxy for the galaxy inclination, and refer to it as  $i$  as listed in Table 5.3. As a side note, the consistent inclination values provide further evidence that the `lenstronomy` fits have resulted in realistic physical parameters of the host galaxy.

## 5.4.2 AGN Parameters

The AGNs in our sample were exclusively selected based on their spectral properties, more precisely the ability to temporally resolve the broad emission line lags. Considering that only a fraction of AGNs show the required variability to monitor them in RM campaigns, we are interested in quantifying to what extent our sample is representative of the overall AGN population. Important properties that can be easily compared are the AGN bolometric luminosity  $L_{\text{bol}}$ , the BH mass  $M_{\text{BH}}$  and the Eddington ratio  $\lambda_{\text{Edd}}$ . They can be directly estimated from the unobscured AGN spectra available in the host-subtracted IFU data.

We constrain the AGN spectral modeling to the  $\text{H}\beta$ -[O III] wavelength range, for which various studies have provided calibrations (e.g. Kaspi et al., 2000; Peterson et al., 2004; Greene & Ho, 2005a; Vestergaard & Peterson, 2006; Bentz et al., 2013; Woo et al., 2015). A detailed description of our fitting methodology is given in Appendix 5.7.1. We estimated the bolometric luminosity from the  $5100 \text{ \AA}$  continuum luminosity using a bolometric correction factor:  $L_{\text{bol}} = 10 \times L_{5100}$  (Richards et al., 2006). The Eddington ratio is  $\lambda_{\text{Edd}} = L_{\text{bol}}/L_{\text{Edd}}$ , where  $L_{\text{Edd}}/\text{erg s}^{-1} = 1.26 \times 10^{38} M_{\text{BH}}/M_{\odot}$  with  $M_{\text{BH}}$  taken from Table 5.1. The AGN parameters are shown in Fig. 5.2, where we compare our sample with the properties of the overall local AGN population in the flux-limited Hamburg ESO survey (Wisotzki et al., 2000; Schulze & Wisotzki, 2010). The unimodal distribution of our AGNs in  $M_{\text{BH}}$  (and  $\lambda_{\text{Edd}}$  analogously) can be explained by the primary sample selection criteria. At low  $M_{\text{BH}}$ , the distribution is incomplete due to the low S/N of the AGN spectral fea-

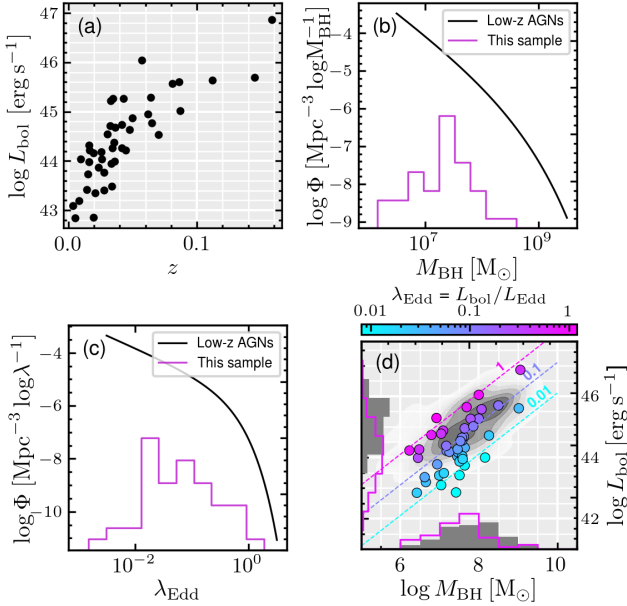


Figure 5.2: *Properties of our AGN sample.* From left to right the panels show the AGN sample in (a) AGN bolometric luminosity as a function of galaxy redshift, (b) distribution of BH masses (purple) the compared to BH mass function (BHMF) obtained from the local AGN population in the Hamburg/ESO survey and (d) Eddington ratio distribution compared with the global Eddington ratio distribution function (ERDF) from HES. Panels (b) and (c) show that our sample’s distribution in  $M_{\text{BH}}$  (and  $\lambda_{\text{Edd}}$ ) is mostly shaped luminosity bias at the low- $M_{\text{BH}}$  end and the cut-off of the BHMF (ERDF) the at the massive end.

tures, whereas at high  $M_{\text{BH}}$  the number of AGNs decreases due the cut-off of the SMBH mass function. The selection effects are discussed in more detail in Sect. 5.5.4.

### 5.4.3 Spectral Synthesis Modeling

To determine the host-galaxy stellar kinematics, We used the first and second moments of the line-of-sight velocity distribution (LOSVD) obtained by fitting the stellar continuum after subtracting AGN emission

(see Sect. 5.3.1). However, data from Keck/KCWI, VLT/MUSE, and VLT/VIMOS vary in wavelength coverage, field coverage, and resolution. Additionally, the depth of observations and the brightness of the central AGN limit the mapping of stellar kinematics. To ensure a consistent analysis across datasets, we developed a common methodology.

The extraction of stellar kinematics involves several interconnected steps, each affecting the kinematic parameters. We tested various approaches to optimize results and maintain general applicability, with details provided in the Appendix.

- (1) We tested stellar kinematics extraction with pPXF (Cappellari & Emsellem, 2004; Cappellari, 2017), PyParadise (Husemann et al., 2016a), and BADASS (Sexton et al., 2021), all yielding consistent results despite differing methodologies. A detailed comparison is in Appendix 5.7.8.
- (2) We tested fitting different wavelength regions ( $[4750\text{--}5300\text{ \AA}]$ ,  $[5150\text{--}5200\text{ \AA}]$ ,  $[8450\text{--}8650\text{ \AA}]$ ), each containing key diagnostic features for stellar kinematics. A comparison is detailed in Appendix 5.7.5.
- (3) We tested the robustness of our results using various stellar and SSP template libraries: the 2009 Galaxy Spectral Evolution Library (CB09, Bruzual & Charlot, 2003b), the high-resolution SSP library from ELODIE (M11, Maraston & Strömbäck, 2011), the X-shooter Spectral Library (XSL, Verro et al., 2022), and the Indo-U.S. Library of Coudé Feed Stellar Spectra (Valdes et al., 2004). A comparison of the impact on stellar kinematics is detailed in Appendix 5.7.7.
- (4) For AGNs observed with multiple IFU instruments (e.g., VLT/MUSE plus Keck/KCWI or VLT/VIMOS), we verified the consistency of our method by analyzing them with the same procedures. Details are provided in Appendix 5.7.4.

After evaluating the options detailed in the appendices, we summarize our findings:

- (1) Template Comparison: PyParadise is superior with large wavelength coverage, e.g., for MUSE spectra, while pPXF offers more robust stellar kinematics extraction for smaller wavelength ranges.

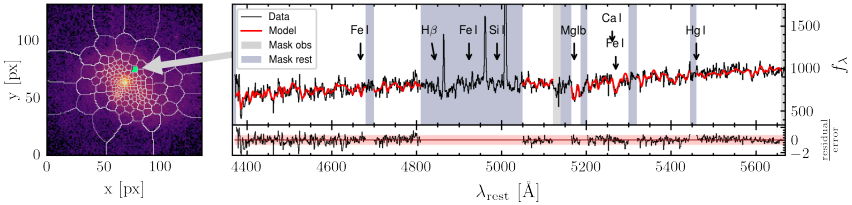


Figure 5.3: *Spatially resolved spectral synthesis modeling, demonstrated for PG 1426+015.* The left panel shows a continuum image from integrating the wavelength range 5100-5200 Å of the AGN-subtracted MUSE data cube. The overlaid grid depicts the Voronoi cells, within which spectra are coadded to achieve a minimum S/N of 20. The example spectrum from the arbitrary cell (highlighted green) is shown as a black line in the upper right panel. We constrain the spectral fitting to regions in the rest frame that are free from contamination from broad emission lines and strong narrow emission lines residuals (blue stripes). In the observed frame, we mask sky line residuals (gray stripes). The best-fit stellar continuum model (red line) closely reproduces the continuum emission within the  $1\sigma$  error, as illustrated by the normalized residuals shown in the bottom right panel.

(2) Wavelength Range: A larger wavelength range provides more diagnostic features and better kinematic constraints. However, CaT cleaned from sky line contamination is covered for objects observed with MUSE. We adopted the 4750–5200 Å range, which is covered by all datasets and contains key absorption features.

(3) Template Resolution: Higher spectral resolution reduces statistical uncertainties. Among higher-resolution templates, XSL and M11 yield consistent results, but XSL’s greater number of spectra (130 versus 10) offers more robust absorption line reproduction and better kinematic fits.

(4) Instrumental Comparison: For objects observed with multiple instruments, deep MUSE observations generally provide the highest S/N stellar continuum and superior spatial resolution and field coverage compared to Keck/KCWI and VLT/VIMOS. Thus, we prefer VLT/MUSE data for our analysis when available.

For all objects, we adopt the following universal strategy: After subtracting the point-like AGN emission as described in Sect. 5.3.1, we increase the S/N of the host-galaxy emission either by taking aperture-integrated spectra (see Sec. 5.4.4), or by binning the cube using

Voronoi tessellation to a spectral S/N of 20 in the rest-frame wavelength range 5100–5200 Å. Next, we fit the stellar continuum emission in the 4750–5200 Å range using the pPXF code (Cappellari & Emsellem, 2004; Cappellari, 2017), typically with 5<sup>th</sup>-order polynomials to account for non-physical continuum variations from 3D-PSF subtraction. We mask the Na I  $\lambda\lambda$ 5890, 5896 sky lines, as well as H $\gamma$ , H $\beta$ , [O III]  $\lambda\lambda$ 4960, 5007 emission lines (hereafter [O III]), and the [O I]  $\lambda$ 5577 night sky line. An example spectrum from a MUSE data cube is shown in Fig. 5.3, along with the best-fit stellar continuum model and residuals.

#### 5.4.4 Host-Galaxy Stellar Kinematics

Most previous studies investigating the  $M_{\text{BH}}-\sigma_*$  relation have used aperture-integrated spectra to measure the AGN host-galaxy properties for large datasets (e.g., Treu et al., 2004; Graham et al., 2011; Grier et al., 2013; Woo et al., 2015; Caglar et al., 2020, 2023, and many more). The statistical power for calibrating scaling relations comes at the cost of larger uncertainties, for example, due to the unknown fraction of the host galaxy covered by the fibers. Long-slit spectroscopy in combination with high-resolution imaging has enabled resolving the host-galaxy kinematics along their photometric major axis (Bennert et al., 2015). Thanks to IFU observations, we can now spatially resolve the host-galaxy kinematics in two dimensions, and differentiate them for different host-galaxy morphological components.

For a 32/44 AGNs, the IFU observations are deep enough to spatially map the host-galaxy stellar kinematics. As illustrated in Fig. 5.4, sub-kpc kinematic structures can be resolved in nearby systems. Examples are nuclear disks in NGC 3227, NGC 2617, or the counter-rotating disk in Mrk 1310. Such features are commonly identified from photometric decomposition of barred galaxies (Comerón et al., 2010; Gadotti et al., 2020) and have been referred to as "pseudobulges" (Kormendy & Kennicutt, 2004b). Due to lower spatial resolution, kinematic substructures remain unresolved in more distant galaxies. In addition, by selection those distant galaxies tend to host more luminous AGNs. Their blending emission can hamper an accurate mapping of the host galaxy stellar kinematics, so that for 12/44 galaxies, the galaxy kinematics cannot be spatially mapped. AGNs for which this is the case are typically high specific-accretion-rate AGNs like Mrk 335, Mrk 1239 3C 120 or the PG quasars contained in our

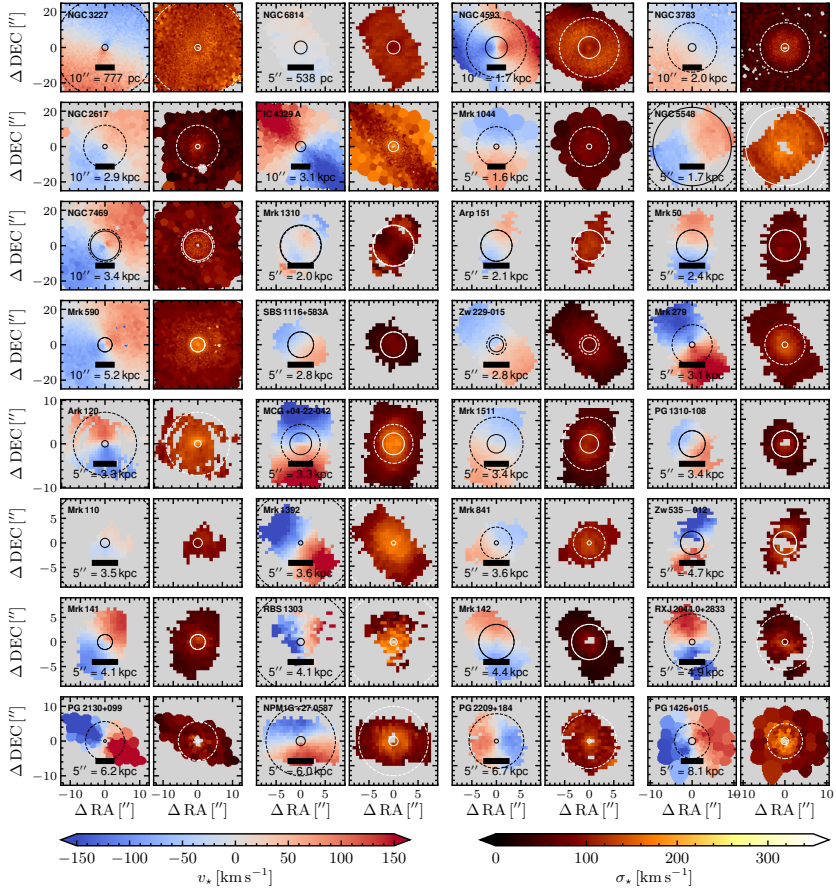


Figure 5.4: *Spatially resolved stellar kinematic maps of the AGN host galaxies.* Kinematic maps are available for 32/44 AGNs object that have spatially resolved stellar continuum with  $S/N > 20$ . We show the first moment (line-of-sight-velocity  $v$ ) and second moment (dispersion  $\sigma$ ), measured from 2D continuum modeling of the AGN-subtracted data cubes (see Sect. 5.4.3). Two neighboring panels belong to the same objects and the velocity and dispersion colormaps share a common scaling which is indicated by the colorbars at the bottom. Black (left panels) or white (right panels) circles indicate  $R_{\text{eff}}^{\text{bulge}}$  (continuous line) and  $R_{\text{eff}}^{\text{gal}}$  (dashed line), as described in Sect. 5.4.1. The AGN host galaxies show a large diversity in their kinematic structures. In some cases, either the kinematics in  $R_{\text{eff}}^{\text{bulge}}$  cannot be resolved, or  $R_{\text{eff}}^{\text{gal}}$  is larger than the FoV covered by the IFU.

sample. Furthermore, we note that accessing the kinematics within  $R_{\text{eff}}^{\text{bulge}}$  and  $R_{\text{eff}}^{\text{gal}}$  can be limited by spatial resolution close to the AGN, or size of the FoV respectively. Given these limitations, establishing a consistent method for extracting  $\sigma$  is essential. This consistency will enable us to fully leverage the strength of this AGN sample, covering a broad range of  $M_{\text{BH}}$ ,  $L_{\text{bol}}$ ,  $z$ , and host morphologies.

## Two Methods For Measuring $\sigma$

There is no standard definition for measuring the stellar velocity dispersion  $\sigma$  from the spatially resolved first and second moments of the LOSVD. As a result, it is unclear over what fraction of  $R_{\text{eff}}^{\text{gal}}$  the kinematics should be averaged or how this averaging should be performed. The literature presents two different approaches for measuring stellar velocity dispersion. For measuring the kinematics within the *bulge* effective radius of quiescent galaxies, several studies have favored including rotational broadening by explicitly combining the first and second velocity moments through eq. 5.8 (KH13 refer to this technique as Nuker team practice, e.g., Pinkney et al. 2003; Gültekin et al. 2009; Cappellari et al. 2013; van den Bosch 2016, for AGNs also Bennert et al. 2015, 2021). This approach is motivated by the equipartition of energy in the dynamically relaxed bulge, where the combination of  $v_{\text{spat}}$  and  $\sigma_{\text{spat}}$  accurately traces the gravitational potential imposed by the stellar mass. However, the bulge component is often barely resolved in AGN host galaxies, resulting in substantial contributions from disk rotation to dispersion being measured from aperture-integrated spectra. When removing rotational broadening through spatially resolving the LOSVD, Batiste et al. (2017b) reported that  $\sigma$  on average is 13 km/s lower  $\sigma$ . They underscore that the difference is strongest for inclined spiral galaxies with significant substructure, highlighting the necessity of maintaining a consistent definition. We briefly review the details of both methods for measuring  $\sigma$  specific to our sample.

### Spatially resolved kinematics

For the first method, we average the spatially resolved velocity dispersion  $\sigma$  within a chosen aperture. In the following, we refer to this quantity as the *spatially resolved* stellar velocity dispersion  $\sigma_{\text{spat}}$ . We note that this quantity is different from the definition used by Bennert et al. (2015),

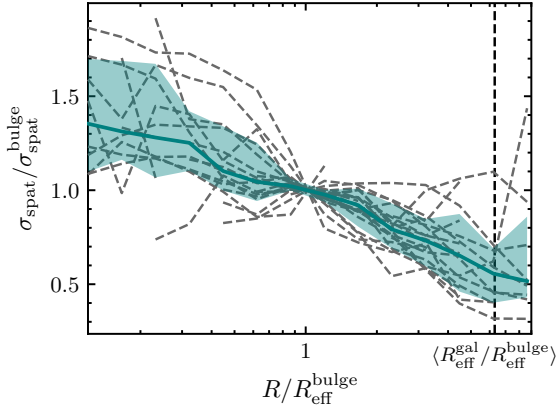


Figure 5.5: *Radial profile of the spatially resolved stellar velocity dispersion  $\sigma_{\text{spat}}$  across AGN host-galaxy bulges.* We measure the spatially resolved stellar dispersion  $\sigma_{\text{spat}}$  in concentric annuli centered on the AGN position. Values of  $\sigma_{\text{spat}}$  are normalized to the value measured at the bulge effective radius  $R_{\text{eff}}^{\text{bulge}}$ . Dashed lines show the spatially resolved  $\sigma_{\text{spat}}$  of individual AGN host galaxies, shaded green regions the 16<sup>th</sup> to 84<sup>th</sup> percentile range of the stacked profile.

who reconstructed the aperture-integrated dispersion from the spatially resolved first and second velocity moment. We have defined a similar quantity  $\sigma_{\text{spat}}^{\text{recon}}$  and explain its behavior relative to  $\sigma_{\text{ap}}$  more detail in Appendix 5.7.3. In short, the definition from Bennert et al. (2015) explicitly includes rotational broadening, whereas our  $\sigma_{\text{spat}}$  implicitly removes rotational broadening from kinematic structures down to the spatial scales that are resolved. We estimate the uncertainties of  $\sigma_{\text{spat}}$  from the scatter, half of the 16<sup>th</sup> to 84<sup>th</sup> percentile range, divided by the square root of the number of independent  $\sigma$  measurements. To account for the systematic uncertainties from limited spectral resolution (see Appendix 5.7.7), we quadratically add the resolution limit to the respective template used to determine the statistical uncertainties. Due to the number of individual spectra, the resulting uncertainties of the  $\sigma_{\text{spat}}$  are typically much smaller than what we get from fitting a single aperture-integrated spectrum.

In Fig. 5.5 we show the radial profile of the spatially resolved dispersion component  $\sigma_{\text{spat}}$ , as a function of distance from the center  $R$ . While all late-type galaxies (LTGs) in the sample are displayed, measuring  $\sigma_{\text{spat}}$  in

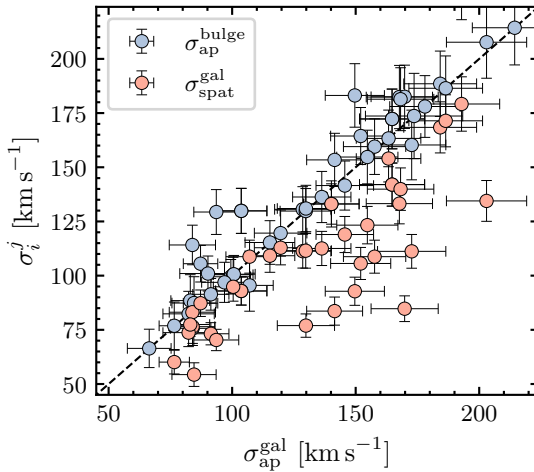


Figure 5.6: *Comparing methods for measuring stellar velocity dispersion.* Aperture-integrated dispersion measured over  $R_{\text{eff}}^{\text{gal}}$  is shown on the x-axis. On the y-axis, we show the aperture integrated dispersion over  $R_{\text{eff}}^{\text{bulge}}$  (blue) and the spatially resolved dispersion over  $R_{\text{eff}}^{\text{gal}}$  (orange), respectively. Compared to the one-to-one correlation, denoted by the dash-dotted line, the mean bulge dispersion is on average slightly higher than the dispersion measured across the galaxy. In contrast, spatially resolving the kinematics results in significantly lower dispersion.

early-type galaxies (ETGs) is often not possible or only sparsely samples the  $R$  range, and therefore, these are not included. The spatially resolved stellar dispersion of LTGs exhibits a steep radial profile. For individual galaxies, the offset between  $\sigma_{\text{spat}}$  measured at  $R_{\text{eff}}^{\text{gal}}$  and  $R_{\text{eff}}^{\text{bulge}}$ , can be as large as a factor of three. While on average, the offset is a factor of  $1.9 \pm 0.4$ , for individual galaxies, the factor can be as large as 3.1. This underscores the importance of considering the aperture size over which  $\sigma_{\text{spat}}$  is measured.

### Aperture-integrated kinematics

Another approach is to coadd the spectra in a given aperture, providing a rotationally broadened spectrum, from which the aperture-integrated kinematics can be derived. We refer to this quantity as the *aperture-integrated* stellar velocity dispersion  $\sigma_{\text{ap}}$ . Since the most luminous AGNs are typically hosted by ETGs, which do not exhibit a detectable disk component, disk rotational broadening is expected to contribute a minor contamination in  $\sigma_{\text{ap}}$ . Varying the aperture size allows us to study the radial behavior of  $\sigma_{\text{ap}}$  across different morphological components. More precisely, we trace bulge velocity dispersion  $\sigma_{\text{ap}}^{\text{bulge}}$  or galaxy-wide velocity dispersion  $\sigma_{\text{ap}}^{\text{gal}}$  by aligning the aperture with the bulge’s luminosity-weighted centroid and matching its size to  $R_{\text{eff}}^{\text{bulge}}$ . More details on comparing aperture-integrated with spatially resolved measurements of  $\sigma$  are described in Appendix 5.7.3. While this approach reduces the spatial resolution of the radial axis, coadding the spectra has the advantage of substantially higher S/N. This is particularly beneficial for luminous AGNs, where extracting  $\sigma_{\text{spat}}$  is often hampered by the poor contrast between the AGN continuum and the underlying stellar absorption lines. Moreover, using aperture-integrated spectra diminishes the contribution from systematic artifacts caused by PSF subtraction, which can be especially severe near the galaxy center.

The results of measuring dispersion using the two methods are summarized in Table 5.4, and illustrated in Fig. 5.6. Overall, the values of  $\sigma_{\text{ap}}^{\text{bulge}}$  tend to be higher than those of  $\sigma_{\text{ap}}^{\text{gal}}$ . Averaged over the entire sample, this offset is small (7 km/s, or 5%), likely related to  $\sigma_{\text{ap}}^{\text{gal}}$  capturing significant rotational broadening from galaxy disk that flattens any aperture-size dependence if the galaxy disk is viewed at high inclination (see Sect. 5.5.1). More notably, on galaxy scales  $\sigma_{\text{spat}}^{\text{gal}}$  is smaller than  $\sigma_{\text{ap}}^{\text{gal}}$  by, on average, 25 km/s, or 12%. Comparing the same for the bulge,  $\sigma_{\text{spat}}^{\text{bulge}}$  versus  $\sigma_{\text{ap}}^{\text{bulge}}$ , yields similar but less pronounced offset of 9%, suggesting an increased contribution from rotational broadening when using galaxy-integrated kinematics. The stellar velocity dispersion measurements reported in the literature often differ substantially from our measurements for individual objects. These discrepancies may arise not only from the different diagnostic features used to constrain the stellar kinematics, e.g., Mg Ib  $\lambda\lambda$ 5167, 5173, 5184 (Batiste et al., 2017a; Husemann et al., 2019),

Table 5.4: *Stellar velocity dispersion measurements.*

AGN Name	$\sigma_{\text{ap}}^{\text{gal}}$	$\sigma_{\text{ap}}^{\text{bulge}}$	$\sigma_{\text{spat}}^{\text{gal}}$	$\sigma_{\text{spat}}^{\text{bulge}}$	lit. $\sigma$	lit. $\sigma$	$M_{\text{bulge, dyn}}$	$M_{\text{gal, dyn}}$
(1)	[ $\text{km s}^{-1}$ ] (2)	[ $\text{km s}^{-1}$ ] (3)	[ $\text{km s}^{-1}$ ] (4)	[ $\text{km s}^{-1}$ ] (5)	[ $\text{km s}^{-1}$ ] (6)	Ref. (7)	[ $\log M_{\odot}$ ] (8)	[ $\log M_{\odot}$ ] (9)
NGC 3227	140 ± 11	133 ± 11	133 ± 9	118 ± 8	92 ± 6	W13	9.23 ± 0.23	10.49 ± 0.23
NGC 6814	107 ± 10	95 ± 12	109 ± 8	92 ± 6	69 ± 3	B17	8.96 ± 0.32	10.59 ± 0.25
NGC 4593	146 ± 12	142 ± 11	119 ± 8	110 ± 8	144 ± 5	B17	10.18 ± 0.23	10.64 ± 0.23
NGC 3783	104 ± 10	130 ± 10	93 ± 7	122 ± 9	95 ± 10	O04	9.72 ± 0.23	10.32 ± 0.27
NGC 2617	84 ± 9	114 ± 9	83 ± 6	109 ± 8	128 ± 9	C23	9.52 ± 0.23	10.24 ± 0.29
IC 4329 A	165 ± 13	172 ± 14	142 ± 10	166 ± 12	-	-	10.27 ± 0.23	11.32 ± 0.23
Mrk 1044	84 ± 9	76 ± 8	76 ± 8	-	-	-	9.01 ± 0.28	9.99 ± 0.28
NGC 5548	163 ± 13	163 ± 13	154 ± 11	154 ± 11	162 ± 12	B17	10.72 ± 0.23	10.85 ± 0.23
NGC 7469	129 ± 11	131 ± 10	111 ± 8	113 ± 8	131 ± 5	N04	10.53 ± 0.23	10.56 ± 0.25
Mrk 1310	82 ± 10	82 ± 10	74 ± 6	74 ± 6	84 ± 5	W10	9.90 ± 0.32	9.89 ± 0.32
Mrk 1239	99 ± 8	†99 ± 8	-	-	-	-	9.95 ± 0.33	9.95 ± 0.33
Arp 151	120 ± 11	†120 ± 11	113 ± 8	†113 ± 8	118 ± 4	W10	10.13 ± 0.35	10.13 ± 0.35
Mrk 50	91 ± 7	†91 ± 7	73 ± 5	†73 ± 5	109 ± 14	B11	10.05 ± 0.33	10.05 ± 0.33
Mrk 335	66 ± 9	†66 ± 9	-	-	-	-	9.63 ± 0.44	9.63 ± 0.44
Mrk 590	184 ± 15	189 ± 15	168 ± 12	178 ± 12	189 ± 6	N04	10.28 ± 0.23	10.40 ± 0.23
SBS 1116+583A	77 ± 6	77 ± 11	60 ± 5	74 ± 6	92 ± 4	W10	9.13 ± 0.35	9.98 ± 0.23
Zw 229-015	83 ± 8	88 ± 12	77 ± 5	70 ± 5	-	-	9.37 ± 0.34	10.30 ± 0.26
Mrk 279	158 ± 13	160 ± 13	109 ± 8	129 ± 9	156 ± 17	B17	10.41 ± 0.23	10.65 ± 0.23
Ark 120	168 ± 13	182 ± 15	133 ± 9	160 ± 11	192 ± 8	W13	10.48 ± 0.23	10.87 ± 0.23
3C 120	178 ± 14	†178 ± 14	-	-	162 ± 20	N95	10.59 ± 0.33	10.59 ± 0.33
MCG +04-22-042	170 ± 14	183 ± 15	85 ± 6	173 ± 12	-	-	10.16 ± 0.23	11.20 ± 0.23
Mrk 1511	87 ± 7	106 ± 8	87 ± 6	104 ± 7	115 ± 9	C23	9.39 ± 0.23	10.62 ± 0.23
PG 1310-108	94 ± 9	129 ± 10	70 ± 5	-	-	-	9.53 ± 0.23	10.13 ± 0.26
Mrk 509	130 ± 10	†130 ± 10	112 ± 8	†112 ± 8	184 ± 12	G13	10.29 ± 0.33	10.29 ± 0.33
Mrk 110	100 ± 8	†100 ± 8	95 ± 7	†95 ± 7	91 ± 9	C23	9.89 ± 0.33	9.89 ± 0.33
Mrk 1392	168 ± 13	181 ± 15	140 ± 10	-	161 ± 9	C23	10.09 ± 0.23	11.17 ± 0.23
Mrk 841	115 ± 10	†115 ± 10	109 ± 8	†109 ± 8	-	-	10.39 ± 0.34	10.39 ± 0.34
Zw 535-012	152 ± 12	164 ± 13	106 ± 7	-	-	-	10.01 ± 0.23	10.94 ± 0.23
Mrk 141	130 ± 12	131 ± 11	77 ± 5	-	135 ± 5	C23	9.59 ± 0.23	10.74 ± 0.25
RBS 1303	203 ± 16	208 ± 17	134 ± 9	176 ± 12	-	-	10.37 ± 0.23	11.23 ± 0.23
Mrk 1048	193 ± 15	237 ± 19	179 ± 13	223 ± 16	-	-	10.95 ± 0.23	11.42 ± 0.23
Mrk 142	85 ± 9	87 ± 12	54 ± 5	-	-	-	9.29 ± 0.35	10.39 ± 0.28
RX J2044.0+2833	141 ± 11	153 ± 12	84 ± 6	-	-	-	10.14 ± 0.23	10.76 ± 0.23
IRAS 09149-6206	155 ± 12	†155 ± 12	123 ± 9	†123 ± 9	-	-	10.99 ± 0.33	10.99 ± 0.33
PG 2130+099	173 ± 14	160 ± 16	111 ± 8	-	163 ± 19	G13	9.88 ± 0.27	10.80 ± 0.23
NPM 1G+27.0587	150 ± 12	183 ± 15	93 ± 6	-	-	-	10.24 ± 0.23	11.09 ± 0.23
RBS 1917	90 ± 11	101 ± 8	-	-	-	-	8.99 ± 0.23	10.08 ± 0.32
PG 2209+184	136 ± 12	136 ± 12	113 ± 8	113 ± 8	-	-	10.70 ± 0.24	10.70 ± 0.24
PG 1211+143	101 ± 9	†101 ± 9	-	-	-	-	9.24 ± 0.34	9.24 ± 0.34
PG 1426+015	186 ± 15	†186 ± 15	171 ± 12	†171 ± 12	217 ± 15	W08	10.89 ± 0.33	10.89 ± 0.33
Mrk 1501	97 ± 9	†97 ± 9	-	-	-	-	10.76 ± 0.36	10.76 ± 0.36
PG 1617+175	174 ± 20	†174 ± 20	-	-	201 ± 37	G13	10.72 ± 0.40	10.72 ± 0.40
PG 0026+129	233 ± 21	†233 ± 21	-	-	-	-	11.35 ± 0.35	11.35 ± 0.35
3C 273	214 ± 17	†214 ± 17	-	-	210 ± 10	H19	11.31 ± 0.33	11.31 ± 0.33

**Notes.** (1) AGN Name. (2) Aperture-integrated  $\sigma$  over  $R_{\text{eff}}^{\text{gal}}$ . (3) Aperture-integrated  $\sigma$  over  $R_{\text{eff}}^{\text{bulge}}$ . Values marked with (†) are ETGs, for which  $R_{\text{eff}}^{\text{bulge}} = R_{\text{eff}}^{\text{gal}}$ . (4) Spatially-resolved  $\sigma$  over  $R_{\text{eff}}^{\text{gal}}$ . (5) Spatially-resolved  $\sigma$  over  $R_{\text{eff}}^{\text{bulge}}$ . (6) Stellar velocity dispersion reported in the literature. (7) Reference for the lit.  $\sigma$ . (8) Logarithm of the bulge dynamical mass. (9) Logarithm of the galaxy dynamical mass. Reference keys are N95: Nelson & Whittle (1995), N04: Nelson et al. (2004), O04: Onken et al. (2004), W08: Watson et al. (2008), W10: Woo et al. (2010), B11: Barth et al. (2011), G13: Grier et al. (2013), W13: Woo et al. (2013), B17: Batiste et al. (2017a), H19: Husemann et al. (2019), C23: Caglar et al. (2023).

Ca II  $\lambda\lambda 8498, 8542, 8662$  (Onken et al., 2004; Woo et al., 2010; Caglar et al., 2023), Ca II H&K  $\lambda\lambda 3969, 3934$  (Bennert et al., 2015), Mg I+CO (Watson et al., 2008; Grier et al., 2013). For instance, Harris et al. (2012) report that the average differences are  $\langle \sigma_{\text{Mg Ib}} / \sigma_{\text{Ca T}} \rangle = -0.02 \pm 0.01$ , i.e. a 5% bias, that depends on aperture size. Furthermore, varying aperture sizes across which these literature values are reported may introduce additional scatter. While galaxy morphology is often unexplored in previous studies, our method for measuring stellar velocity dispersion controls for these systematic uncertainties, making our measurements more robust.

Aperture-integrated measurements can be reconstructed from spatially resolved measurements, as we demonstrate in Appendix 5.7.3. Based on these results, we conclude that across galaxy disks, we can robustly disentangle the contributions of rotation from those of chaotic motions. However, we note that substructures like fast- or counter-rotating disks, which are often observed on scales of several hundred parsecs (Comerón et al., 2010; Gadotti et al., 2020), below the typical  $\sim$ arcsec sizes of our bulges, remain unresolved in the majority of AGNs in our sample.

### Systematic Uncertainties for Measuring $\sigma$

To achieve a more accurate calibration of the  $M_{\text{BH}}$  host galaxy scaling relations in AGNs, our approach involves the most precise  $M_{\text{BH}}$  and  $\sigma$  measurements available. Although the wide dynamic range of AGN parameters is a strength of the sample, it also presents technical challenges in identifying host-galaxy morphological components (see Bennert et al., 2024, in prep.). At the low- $z$  end, for example, NGC 3227, NGC 4593 and NGC 7469 are cases where plenty of kinematic substructure is resolved, including spiral arms, dust lanes, nuclear rings, nuclear disks, or bulges. In such cases, the simplistic parameterization (s, sd, sdb) is insufficient to describe the morphology accurately (however, the photometry for the main components is adequately recovered even by a simple model). For the more distant and luminous AGNs in the sample, the PSF subtraction often leaves strong residuals that dominate over the host galaxy on arcsecond scales. In cases where these residuals coincide with the typical sizes of the bulges, it is impossible to measure accurate bulge sizes. Also the choice of parameterizing host-galaxy morphology can affect  $R_{\text{eff}}^{\text{bulge}}$  for individual objects. However, for most of the sample, the parameterization is

clear, and even in ambiguous cases, adding a component has little impact on the measured sizes.

Another source of systematic uncertainty comes from measuring the kinematics from the IFU data. For the nearest AGNs, the FoV of the IFU is smaller than  $R_{\text{eff}}^{\text{gal}}$ . In contrast, for the more distant AGNs the lower physical spatial resolution and AGN continuum blending does not allow us to measure  $\sigma$  within  $R_{\text{eff}}^{\text{gal}}$ . Moreover, beam smearing might contribute to smoothing the radial profiles of  $\sigma_{\text{spat}}$  on small scales, e.g. in Fig. 5.5. However, this effect cannot be homogeneously controlled without degrading individual datasets. From the aperture-sizes and methods defined in Sect. 5.4.4,  $\sigma_{\text{ap}}^{\text{gal}}$  provides the measurement that is the least sensitive to systematic effects: We find that only for 4/44 AGNs in the sample (PG 1211+143, PG 1617+175, PG 0026+129, 3C 273), the PSF subtraction might have a non-negligible impact on  $\sigma_{\text{ap}}^{\text{gal}}$ , as  $R_{\text{eff}}^{\text{gal}}$ . When excluding these four objects, the slope and intercept of the spatially resolved  $\sigma_{\text{spat}}^{\text{gal}}$  relation is  $<3\%$ . With such small variation we consider the systematic uncertainty for calibrating the  $M_{\text{BH}}\text{-}\sigma$  relation small.

### 5.4.5 Dynamical Masses

Based on the kinematics recovered in the previous section, we can derive dynamical masses as

$$M_{\text{dyn}} = cR_{\text{eff}}\sigma_{\text{ap}}^2/G, \quad (5.3)$$

where  $c$  is a structural constant that depends on the anisotropy of the system Courteau et al. (2014). While the value of  $M_{\text{dyn}}$  for ETGs is best described by coefficient  $c = 2.5$  Cappellari et al. (2006), we adopt  $c = 3$  for both LTGs and ETGs guaranteeing a consistent comparison with literature (e.g., Bennert et al. 2021). For LTGs specifically, we adopt  $R_{\text{eff}}^{\text{bulge}}$  and  $\sigma_{\text{ap}}^{\text{bulge}}$  to get the dynamical bulge mass  $M_{\text{bulge, dyn}}$ . For ETGs, we adopt the parameters that belong to the spheroid, i.e.  $R_{\text{eff}}^{\text{bulge}}$  and  $\sigma_{\text{ap}}^{\text{bulge}}$ , and also refer to the derived dynamical mass as  $M_{\text{bulge, dyn}}$ . With this definition,  $M_{\text{bulge, dyn}}$  provides a consistent metric for the dynamical mass of the spheroidal component for both LTGs and ETGs.

### 5.4.6 Fitting the $M_{\text{BH}}$ Scaling Relations

The  $M_{\text{BH}}$  scaling relations are parameterized as

$$\log\left(\frac{M_{\text{BH}}}{M_{\odot}}\right) = \alpha + \beta \log X \quad (5.4)$$

where  $X$  is the host-galaxy parameter, in our case either  $\sigma_{\star}/200 \text{ km s}^{-1}$  or  $M_{\text{bulge,dyn}}/10^{11} M_{\odot}$ . We fit the relation using the hierarchical Bayesian model `LINMIX_ERR` from Kelly (2007), which performs a linear regression to observed independent variables  $x_i$  and dependent variables  $y_i$ , accounting for the associated uncertainties of both. We re-scale the variables to the mean of their respective distributions to reduce the covariance between the parameters. Monitoring the convergence to a well-sampled posterior distribution allows us to infer realistic uncertainties of the derived fitting parameters, which also include the intrinsic scatter of the relation  $\epsilon$ . Compared to other regression methods that are often used to constrain the  $M_{\text{BH}}$  scaling relations, namely `BCES` (Akritas & Bershady, 1996), `FITEXY` (Tremaine et al., 2002) or `maximum likelihood` (Gültekin et al., 2009; Woo et al., 2010), `LINMIX_ERR` is more general and produces a larger intrinsic scatter (Park et al., 2012). For our analysis, we assume that the measurement uncertainties of  $M_{\text{BH}}$  and  $\sigma$  are symmetric in log-space, and symmetrize the measurement uncertainties on  $M_{\text{BH}}$  from their upper and lower  $1\sigma$  intervals listed in Table 5.1. We note that the adopted choice of the uncertainties does not significantly impact the results, which has already been reported by Park et al. (2012).

## 5.5 Results and Discussion

### 5.5.1 Host-galaxy Morphologies

If major mergers are responsible for shaping the  $M_{\text{BH}}$  scaling relations, only the host-galaxy morphological components bearing the dynamical imprint of merger history should correlate with  $M_{\text{BH}}$ , i.e., classical bulges (Cisternas et al., 2011a,c; Kormendy & Ho, 2013; Bennert et al., 2015). While the dependence of the  $M_{\text{BH}}$  scaling relations on host morphology has been extensively studied for quiescent galaxies (e.g., Gültekin et al., 2009; Greene et al., 2010; McConnell & Ma, 2013; Savorgnan & Graham,

2015; Sahu et al., 2019; Graham, 2023), they are less well constrained for AGNs due to the bright AGN emission (e.g., Debattista et al., 2013; Hartmann et al., 2014, see also Sect. 5.3.1), or the narrow dynamic range in  $M_{\text{BH}}$  covered (e.g., Bennert et al., 2021).

In our sample, 29/44 (66%) of AGNs are hosted by LTGs. However, disks may remain undetected at high bulge-to-disk ratios, so our estimate should be regarded as an upper limit. Nevertheless, the fraction is comparable to the fraction of Seyfert hosts with disk-like galaxies among the overall AGN population (e.g.,  $\sim 52\%$  in CANDELS (Kocevski et al., 2012), or 74% disk galaxies in CARS (Husemann et al., 2022)), the depth and angular resolution of the HST photometry in our study allow us to identify disk components more robustly than previous studies. Bennert et al. (2021), who used the same methodology as in this work, reported an even higher fraction (95%) of disk galaxies among local AGNs imaged with HST.

Among the sample of AGNs hosted by disk galaxies, 15/29 show a clear sign of a bar, and are better fitted when including a bar component in the model. The intrinsic fraction of bars might be higher, since we used a conservative approach by only including a bar when there are clear signs in the PSF-subtracted images. Moreover, a few galaxies have too high disk inclination to identify a bar (for details, see Bennert et al., 2024, in prep.). Typically, the bar fractions of disk-like AGN hosts are reported to be higher (e.g. Cisternas et al., 2011a; Alonso et al., 2013; Husemann et al., 2022). However, we caution against direct comparisons of the bar incidence rate with other surveys, since identification methods, image quality, and intrinsic bar strengths have a significant impact on these numbers, similar to the disk/non-disk classification. In particular, the bar fraction also depends on wavelength range, where higher bar fractions are observed in the infrared compared to identification based on optical photometry (e.g., Eskridge et al., 2000; Buta et al., 2015; Erwin, 2019).

While 10/44 galaxies have irregular or asymmetric morphologies, only two objects show strong signs of interaction or merger activity (Arp 151, Mrk 1048). This corresponds to 5%, which is consistent with the low fraction of strongly disturbed hosts in the overall AGN population (e.g., Cisternas et al., 2011a; Schawinski et al., 2012; Mechtley et al., 2016; Mariani et al., 2019; Kim et al., 2021). As we will demonstrate in Sect. 5.5.3,

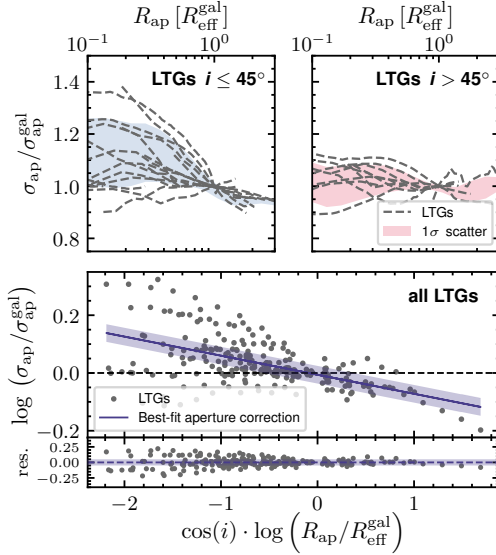


Figure 5.7: *Inclination-dependent aperture correction for stellar velocity dispersion measurements.* (Top) Left and right panels show the behavior of  $\sigma_{\text{spat}}$  as a function of aperture size normalized by the galaxy effective radius, split by disk inclination. Gray dash-dotted lines correspond to individual galaxies, whereas shaded regions denote the scatter (16<sup>th</sup> to 84<sup>th</sup> percentile in bins of  $R_{\text{ap}}$ ). Varying  $R_{\text{ap}}$  significantly affects  $\sigma_{\text{ap}}$  only for the lower-inclination systems. (Bottom) Considering all disk galaxies of the AGN sample, we control for inclination by parameterizing the aperture correction formula with eq. 5.5. A first-order power law describes the overall trend of decreasing  $\sigma_{\text{ap}}$  with increasing  $R_{\text{ap}}$  (top panel), but significant residual structure indicates that galaxy-to-galaxy variation remains likely driven by stellar mass or luminosity.

interacting galaxies do not represent the strongest outliers to the  $M_{\text{BH}}$  scaling relations and are included in the following analysis.

### Correcting Aperture Effects

As spatially resolved studies will remain unavailable for the majority of distant type 1 AGNs in the Universe, aperture-integrated spectra are often the only means to trace stellar kinematics from bulge to galaxy scales. We

therefore investigate the systematic differences induced by the aperture size, depending on host-galaxy morphology. While differences between  $\sigma_{\text{ap}}$  and  $\sigma_{\text{spat}}$  for individual AGNs are detailed in Appendix 5.7.6, we shall here only focus on the sample-integrated behavior and dependencies on morphology.

The spatially resolved kinematics shown in Fig. 5.5 illustrate how galaxy kinematic substructures may impact measurements of  $\sigma$ : for LTGs with spatially resolved kinematics, the sample-averaged normalized  $\sigma_{\text{spat}}$  exhibits a steep radial profile, underscoring the importance of considering the aperture over which  $\sigma_{\text{spat}}$  is extracted.

Aperture correction recipes are often formulated in the form of a power law:

$$\frac{\sigma}{\sigma_{\text{eff}}} = \left( \frac{R}{R_{\text{eff}}} \right)^\gamma \quad (5.5)$$

For quiescent ETGs, it is established that  $\sigma_{\text{ap}}$  typically decreases with increasing aperture size to the center, resulting in  $\alpha = -0.04$  (Jorgensen et al., 1995),  $\alpha = -0.06$  (Mehlert et al., 2003), or  $\alpha = -0.066$  (Cappellari et al., 2006). The few ETGs in our sample are poorly resolved, so that a statistical analysis of the aperture-size dependence is not possible.

For quiescent LTGs, recent studies have shown that aperture correction is more complex, due to multiple kinematic components and their anisotropy. However, compared to galaxy stellar mass and luminosity, we suspect that the galaxy inclination  $i$  has the largest effect on measuring  $\sigma_{\text{ap}}$  in our AGN sample (Sect. 5.5.3). Galaxy-scale kinematics derived from aperture-integrated spectra of highly inclined disk galaxies are more affected by rotational broadening compared to low-inclination disk galaxies. This is reflected in the top panels of Fig. 5.7, where only disk galaxies viewed at lower inclinations exhibit a trend of  $\sigma_{\text{ap}}$  with varying  $R_{\text{ap}}$ , whereas higher-inclination disk galaxies show no significant trend. This is a result of two opposing trends which cancel each other out at high inclination: stellar-velocity dispersion increases towards the center due to either dynamically hotter bulges or spatially unresolved rotating nuclear disks (see discussion in Sect. 5.4.4), but rotational broadening from the galaxy disk only becomes important at larger distance from the galaxy center. Although  $\sigma_{\text{ap}}$  is sometimes measured in elliptical apertures, as for instance in Falc3n-Barroso et al. (2017), measurements in circular apertures are

the default for survey data. To control for inclination, we included the disk inclination  $i$  in the parameterization of the aperture correction:

$$\frac{\sigma}{\sigma_{\text{eff}}} = \left( \frac{R}{R_{\text{eff}}} \right)^{\gamma \cdot \cos(i)} \quad (5.6)$$

Fitting the logarithmic relation with a least-squares minimization provides the best-fitting aperture-correction exponent  $\gamma = 0.063 \pm 0.013$ . This value is surprisingly consistent with the aperture correction suggested for ETGs, indicating that when correcting for disk inclination, the  $\sigma_{\text{ap}}$  correction of disk galaxies is similar to that of pure spheroidals. However, significant residual structure of individual galaxies demonstrate that additional parameters must be considered, such as galaxy stellar mass or luminosity (Falc3n-Barroso et al., 2017; Zhu et al., 2023). For our AGNs, however, the small sample size does not allow us to further constrain second order dependencies on host-galaxy luminosity or stellar mass.

### 5.5.2 The $M_{\text{BH}}$ Scaling Relations of Quiescent Galaxies

The  $M_{\text{BH}}\text{-}\sigma$  relation of the local quiescent galaxy population has been studied across a higher  $M_{\text{BH}}$  dynamic range compared to that of AGNs (G3ltekin et al., 2009; Kormendy & Ho, 2013; McConnell & Ma, 2013). KH13 compiled  $M_{\text{BH}}$  and the "effective dispersion"  $\sigma_{\text{eff}}$ , which they measured within  $R_{\text{eff}}^{\text{gal}}/2$ . Their method involves the intensity-weighted mean of  $v^2 + \sigma^2$ , which close to the definition of our  $\sigma_{\text{ap}}$  (see Appendix 5.7.3). For a consistent analysis, we have re-fit the  $M_{\text{BH}}\text{-}\sigma$  and  $M_{\text{BH}}\text{-}M_{\text{dyn}}$  relation from KH13 with our method (Sect. 5.4.6). The results is listed in row (i) of Table 5.5 and reproduce the parameters that have originally been reported.

However, the KH13 sample mainly covers the high- $M_{\text{BH}}$  regime, where RM AGNs are scarce. For late-type galaxies at the low- $M_{\text{BH}}$  end of the relation, rotational broadening from disk components are non-negligible, and thus the aperture size over which the kinematics are extracted must be considered. Based on a sample of both LTGs and ETGs, Batiste et al. (2017a) have compared using an aperture correction factor to estimate  $\sigma_{\text{ap}}^{\text{gal}}$  versus direct measurements of  $\sigma_{\text{spat}}^{\text{gal}}$ . While the former approach has been widely used in the literature, Batiste et al. (2017a) stress that not only are the effective radii used in the literature uncertain, also the recovered  $\sigma_{\text{spat}}^{\text{gal}}$

are systematically lower by  $13 \text{ km s}^{-1}$  compared to  $\sigma_{\text{ap}}^{\text{gal}}$ . As a consequence,  $M_{\text{BH}}-\sigma$  calibrations using  $\sigma_{\text{ap}}$  are offset towards higher intercepts, and tend to result in steeper slopes (e.g., Woo et al. 2013,  $\beta = 5.31$ , Grier et al. 2013,  $\beta = 5.04$ , Savorgnan & Graham 2015,  $6.34 \pm 0.8$ ). When using the spatially resolved  $\sigma$  measurements of LTGs and ETGs, equivalent to our definition of  $\sigma_{\text{spat}}$ , Batiste et al. (2017a) found  $\alpha = 8.66 \pm 0.09$  and  $\beta = 4.76 \pm 0.60$ , which are more consistent with the KH13 relation.

### 5.5.3 The $M_{\text{BH}}$ Scaling Relations of AGNs

In previous studies, fitting the  $M_{\text{BH}}-\sigma$  relation of type 1 AGNs required an additional free parameter, the unknown virial factor  $f$ . To overcome the limited dynamic range when inferring the AGN relation’s scatter and intercept (and thereby a sample-average  $\langle f \rangle$ ), previous calibrations often required fixing the slope to that of the quiescent galaxies. This implicitly assumes that AGNs and quiescent galaxies follow the same underlying relations, and selection effects are negligible. However, so far this assumption does not have any empirical foundation. In fact, AGNs represent the sites of ongoing SMBH growth, where the present-day SMBH growth may result in different  $M_{\text{BH}}$ -host-galaxy scaling relations. To test this hypothesis, from here on, we will focus on the AGNs in our sample that have independent  $M_{\text{BH}}$  measurements. In contrast to many previous studies, this allows us fitting the AGN  $M_{\text{BH}}-\sigma$  relation without assumptions on any of the parameters. Unlike many previous studies, this approach allows us to fit the AGN  $M_{\text{BH}}-\sigma$  relation without parameter assumptions, control for host-galaxy morphology using  $\sigma$  measured across the bulge or galaxy effective radius, and test how different methods of measuring stellar velocity dispersion impact the  $M_{\text{BH}}-\sigma$  relation.

#### Impact of $\sigma_{\text{ap}}$ versus $\sigma_{\text{spat}}$

The majority (29/44) of AGNs in our sample are hosted by LTGs, for which the best-fitting  $M_{\text{BH}}-\sigma$  relation depends on both the method by which the stellar velocity dispersion is measured (see Sect. 5.4.4), and aperture size. While the galaxy-wide integrated  $\sigma_{\text{ap}}^{\text{gal}}$  is the closest to the definition used in previous studies (e.g., Gültekin et al., 2009; Kormendy & Ho, 2013; Grier et al., 2013),  $\sigma_{\text{spat}}$  results in steeper slopes. This steepening occurs because  $\sigma_{\text{spat}}$  excludes rotational broadening, ef-

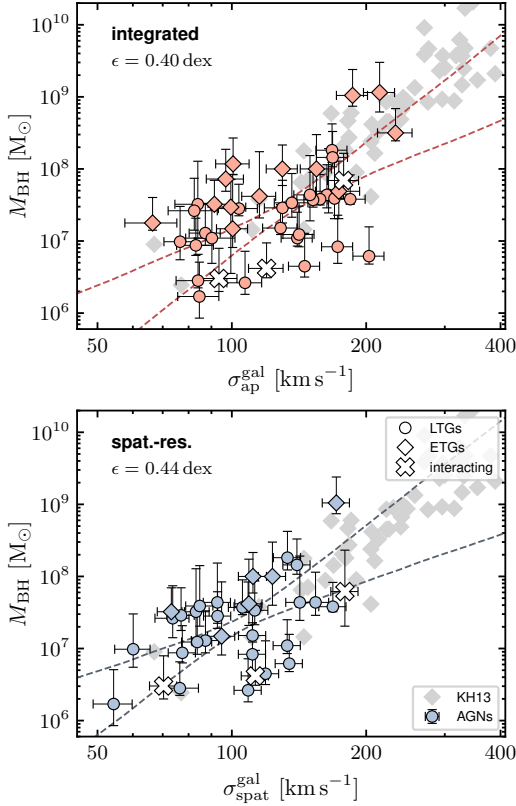


Figure 5.8: *Effect of using aperture-integrated versus spatially resolved  $\sigma$  on the  $M_{\text{BH}}-\sigma$  scaling relation.* (Top) Observed relation of AGNs based on  $\sigma_{\text{ap}}^{\text{gal}}$  (row (iii) in Table 5.5). AGNs show a large scatter, and individual measurements have high uncertainty so that  $\alpha$  and  $\beta$  are not well constrained. Overall, the AGNs in our sample form the extension of quiescent galaxies towards lower  $M_{\text{BH}}$ . Interacting galaxies tend to have lower  $M_{\text{BH}}$ , but they are not the ones that deviate the most from the relation. (Bottom) Observed relation of AGNs based on  $\sigma_{\text{spat}}^{\text{gal}}$  (row (iv) in Table 5.5). Removing rotational broadening reduces the uncertainty of individual measurements. While the resulting  $M_{\text{BH}}-\sigma$  correlation is more significant (larger  $\beta$ ) and has a higher intercept, its intrinsic scatter is the same as when using  $\sigma_{\text{ap}}$ .

fectively shifting many LTGs towards lower  $\sigma$  (see left and middle panels of Fig. 5.8). This primarily affects high-inclination disk galaxies, whereas  $\sigma_{\text{ap}}$  includes this effect (as detailed in Sect. 5.5.1). The  $M_{\text{BH}}-\sigma_{\text{spat}}$  relation is also offset toward lower dispersion, consistent with findings by [Batiste et al. \(2017b\)](#), suggesting that while  $M_{\text{BH}}$  *does* correlate with the velocity dispersion of galaxy discs, but the underlying relations are different (see discussion in Sect. 5.5.3. This observation has been predicted by previous studies, which suggested that rotation effects should be corrected for in case of low-mass, disk-dominant galaxies ([Bennert et al., 2011](#); [Harris et al., 2012](#); [Woo et al., 2013](#)). We note that the inner regions of many distant galaxies with a luminous AGN are dramatically blended by the AGN emission, effectively limiting our ability to resolve  $\sigma_{\text{spat}}$  close to the nucleus. As a result, the bulge size is smaller than  $\sigma_{\text{spat}}$  for 50% of the AGNs in our sample. For those objects, a robust measurement of  $\sigma_{\text{spat}}^{\text{bulge}}$  is not feasible. The effect of fitting the  $M_{\text{BH}}-\sigma$  relation of an incomplete sample is discussed in Sect. 5.5.3.

### Impact of Host-Galaxy Morphology

The dependence of the  $M_{\text{BH}}$  scaling relation on host-galaxy morphology is crucial for understanding its physical drivers (e.g., [Sahu et al., 2019](#); [Graham, 2023](#)). However, studying host galaxies in AGNs, especially at the high- $M_{\text{BH}}$  end, has been challenging. With high-quality spectroscopic data, we can now examine the morphology dependence of the  $M_{\text{BH}}-\sigma$  scaling relation, focusing on the relative behavior of LTGs and ETGs, with best-fitting parameters detailed in rows (vii)-(x) of Table 5.5.

Table 5.5: *Results of fitting the scaling relations of local AGNs and quiescent galaxies.*

$X$ in relation (1)	Sample (2)	$M_{\text{BH}}$ distr. (3)	Aperture (4)	Method (5)	Symbol (6)	$\alpha$ (7)	$\beta$ (8)	$\epsilon$ (9)	Row (10)
$\sigma/200 \text{ km s}^{-1}$	KH13 <sup>†</sup>	KH13	galaxy*	int.	$\sigma_{\text{ap}}^{\text{gal}}$	$8.53 \pm 0.05$	$4.53 \pm 0.32$	$0.34 \pm 0.04$	(i)
	AGN	AGN	bulge	int.	$\sigma_{\text{ap}}^{\text{bulge}}$	<b><math>7.90 \pm 0.16</math></b>	<b><math>2.53 \pm 0.73</math></b>	<b><math>0.47 \pm 0.08</math></b>	(ii)
	AGN	AGN	galaxy	int.	$\sigma_{\text{ap}}^{\text{gal}}$	$7.93 \pm 0.16$	$2.48 \pm 0.72$	$0.47 \pm 0.08$	(iii)
	AGN	AGN	galaxy	spat.-res.	$\sigma_{\text{spat}}^{\text{gal}}$	$8.06 \pm 0.27$	$2.57 \pm 0.89$	$0.45 \pm 0.09$	(iv)
	AGN	KH13	bulge	int.	$\sigma_{\text{ap}}^{\text{bulge}}$	<b><math>8.71 \pm 0.13</math></b>	<b><math>4.10 \pm 0.93</math></b>	<b><math>0.57 \pm 0.09</math></b>	(v)
	AGN	KH13	galaxy	int.	$\sigma_{\text{ap}}^{\text{gal}}$	$8.80 \pm 0.13$	$4.51 \pm 0.88$	$0.53 \pm 0.08$	(vi)
	AGN LTGs	AGN LTGs	bulge	int.	$\sigma_{\text{ap}}^{\text{bulge}}$	$7.72 \pm 0.16$	$2.80 \pm 0.80$	$0.27 \pm 0.11$	(vii)
	AGN LTGs	AGN LTGs	galaxy	int.	$\sigma_{\text{ap}}^{\text{gal}}$	$7.68 \pm 0.18$	$2.17 \pm 0.89$	$0.37 \pm 0.10$	(viii)
	AGN LTGs	AGN LTGs	galaxy	spat.-res.	$\sigma_{\text{spat}}^{\text{gal}}$	$7.88 \pm 0.27$	$2.47 \pm 0.70$	$0.31 \pm 0.10$	(ix)
	AGN ETGs	AGN ETGs	galaxy	int.	$\sigma_{\text{ap}}^{\text{bulge}}$	$8.44 \pm 0.30$	$3.00 \pm 1.28$	$0.54 \pm 0.18$	(x)
$M_{\text{bulge,dyn}}/10^{11} M_{\odot}$	KH13	KH13	bulge	int.	$\sigma_{\text{ap}}^{\text{bulge}}$	$8.78 \pm 0.07$	$1.06 \pm 0.10$	$0.45 \pm 0.05$	(xi)
	AGN	AGN	bulge	int.	$\sigma_{\text{ap}}^{\text{bulge}}$	<b><math>8.11 \pm 0.16</math></b>	<b><math>0.70 \pm 0.14</math></b>	<b><math>0.41 \pm 0.08</math></b>	(xii)
	AGN	AGN	gal	int.	$\sigma_{\text{ap}}^{\text{bulge}}$	$7.80 \pm 0.19$	$0.83 \pm 0.52$	$0.54 \pm 0.10$	(xiii)
	AGN	KH13	bulge	int.	$\sigma_{\text{ap}}^{\text{bulge}}$	<b><math>8.76 \pm 0.11</math></b>	<b><math>0.87 \pm 0.14</math></b>	<b><math>0.49 \pm 0.07</math></b>	(xiv)

**Notes.** All fits were calculated as part of this paper, including those to quiescent galaxies. Relations that are shown in Fig. 5.10 are highlighted in bold-face font. (1) Scaling relation of the form  $\log(M_{\text{BH}}/M_{\odot}) = \alpha + \beta \log X$ , with  $X$  given in the table. (2) Sample for which the  $M_{\text{BH}}-\sigma$  relation was fitted. (3)  $M_{\text{BH}}$  distribution of the sample used for fitting the  $M_{\text{BH}}-\sigma$  relation. The quiescent galaxy sample from KH13 serves as reference. "AGN" refers to the (sub-)sample of AGNs, specified in the column 2. "KH13" refers to the AGN sample being matched to the KH  $M_{\text{BH}}$  distribution, as described in Sect. 5.5.4. (4) Aperture over which the kinematics are evaluated. (5) Method by which the kinematics are measured (see Sect. 5.4.4). (6) Symbol for the stellar dispersion  $\sigma$ , indicating which aperture size and which method we used to measure it. (7) Best-fit intercept of the  $M_{\text{BH}}-\sigma$  relation (eq. 5.4). (8) Best-fit slope of the relation. (9) Best-fit intrinsic scatter of the relation. (10) Row number used to refer to the relation. (†) KH13 data re-fitted with our method. (\*) Galaxy effective radius is poorly constrained from ground-based seeing-limited imaging, as discussed in KH13 and [Batiste et al. \(2017b\)](#).

## Late-type AGN hosts

Only 15/44 AGN host galaxies in our sample are classified as ETGs, whereas the majority 29/44 are hosted by LTGs. In general, constraining the AGN sample to LTGs significantly lowers the intercept and flattens the observed relation, see row (vii)-(iv) of Table 5.5. While this might partially be caused by quiescent LTGs following a shallower  $M_{\text{BH}}-\sigma$  relation compared to ETGs ([Sahu et al., 2019](#)), the smaller  $M_{\text{BH}}$  dynamic range covered may also contribute to the observed shallower slope (see Sect. 5.5.1). Of any method and aperture size used for fitting LTGs, the correlation of  $M_{\text{BH}}$  with  $\sigma_{\text{ap}}^{\text{bulge}}$  has parameters that are the closest to those of quiescent galaxies. This  $M_{\text{BH}}-\sigma_{\text{ap}}^{\text{bulge}}$  relation also shows the least in-

intrinsic scatter of all AGN subsamples. However, this might be driven by selection effects: SMBHs are not detected in every LTGs, whereas here we are only selecting those that harbor one. We might therefore only be sensitive to the upper envelope of the underlying scaling relation. As found for the entire AGN sample in Sect. 5.5.3, the galaxy-wide stellar velocity dispersion  $\sigma^{\text{gal}}$  correlates with  $M_{\text{BH}}$  of LTG AGNs in a relation that shows small intrinsic scatter. Compared to  $\sigma_{\text{spat}}^{\text{gal}}$ , the correlation is slightly more pronounced for  $\sigma_{\text{spat}}^{\text{gal}}$  which is largely rotation-free and thus traces the older, dynamically hot component. Such a correlation is in contradiction to previous studies (e.g., Greene et al., 2010; Kormendy et al., 2011; Kormendy & Ho, 2013), that argued that  $M_{\text{BH}}$  does not correlate with the properties of the disk. These studies suggest that stellar feedback, rather than black hole feedback, plays a more significant role in regulating the growth of galaxy disks. While this might be true for the dynamically cold component, recently formed inside-out through smooth gas accretion (e.g., Pichon et al., 2011; El-Badry et al., 2018), there is no a priori reason to assume that an old disk component should not be affected by early BH feedback, similar to classical bulges. Indeed, recent observations showed that galaxy disk progenitors had already formed at  $z > 3$  (e.g., Lelli et al. 2021; Roman-Oliveira et al. 2023; Ferreira et al. 2023; Jacobs et al. 2023; Robertson et al. 2023), well before the peak of cosmic SMBH growth, potentially carrying information about the SMBH-galaxy coevolution. In this context, the  $M_{\text{BH}}-\sigma_{\text{spat}}^{\text{gal}}$  correlation suggests that SMBHs *do* coevolve with galaxy disks, but this may be limited to early epochs of galaxy disk formation, as traced by the dynamically hot disk component.

### Early-type AGN hosts

Among the ETGs, only Arp 151, Mrk 110 and Mrk 335 have lower  $M_{\text{BH}}$ , comparable to what is typically found in LTGs, whereas the remaining twelve ETGs occupy the high- $M_{\text{BH}}$  end of the scaling relation. Woo et al. (2013) argued that such massive SMBHs are typically hosted by massive galaxies for which the difference between the methods for measuring  $\sigma$  should be minimal. Assuming the  $M_{\text{BH}}-M_{\text{dyn}}$  relation of AGNs from Kormendy & Ho (2013) ( $\alpha = 8.49$ ,  $\beta = 1.16$ ), the average dynamical mass of the ETGs is  $\log(M_{\text{dyn}}/M_{\odot}) \sim 11.1$ , a regime where it is likely that the galaxies are slow rotators (Emsellem et al., 2007). Their stellar kinematics have negligible rotational support ( $\lambda_R < 0.1$ , Emsellem et al., 2011),

so that the contribution from rotational broadening to the kinematics derived from their aperture spectra should be small. We confirm that for ETGs the difference between  $\sigma_{\text{spat}}$  and  $\sigma_{\text{ap}}$  is small: The choice of  $\sigma_{\text{ap}}^{\text{gal}}$  and  $\sigma_{\text{spat}}^{\text{gal}}$  has little effect on the dispersion (see Fig. 5.6). In the  $M_{\text{BH}}-\sigma$  plane, ETGs predominantly fall into the high- $M_{\text{BH}}$  regime where their location aligns with the relation of quiescent galaxies. The observed relation of AGN ETGs is flatter than that of quiescent galaxies, but not as flat as that of LTGs. Since the ETGs sample a broader dynamic range in  $M_{\text{BH}}$ , this flattening likely arises from differences in the  $M_{\text{BH}}$  distribution (see Sect. 5.5.4). Overall, the slope and intercept are similar to those of AGN LTGs within the uncertainties, suggesting that both follow the same underlying  $M_{\text{BH}}-\sigma$  relation.

### Intrinsic Scatter

Constraining the intrinsic scatter of the AGNs'  $M_{\text{BH}}-\sigma$  relation is complicated by the narrow dynamic range in  $M_{\text{BH}}$ . Furthermore, the  $f$ -factor could only historically only be constrained as sample-average value, which intruded additional scatter to the  $M_{\text{BH}}-\sigma$  relation. Individual  $f$  factors can vary due to different BLR geometries and viewing angles by more than an order of magnitude, and scatter by 0.41 dex (Villafaña et al. 2023, see also Sect 5.5.5). Woo et al. (2010), who were the first to simultaneously constrained slope and intrinsic scatter on the RM AGN sample, report  $\epsilon = 0.43$  based on the RM AGN sample. Since then, calibrations for AGNs seem to have converged around this value, e.g., Woo et al. (2015) find  $\epsilon = 0.41 \pm 0.05$ , Bennert et al. (2021) find  $\epsilon = 0.42 \pm 0.08$  and Caglar et al. (2023) determine  $\epsilon = 0.32 \pm 0.06$ . However, previous studies have either suffered from a narrow dynamic range in  $M_{\text{BH}}$  covered (e.g. Woo et al., 2015; Bennert et al., 2021), and/or the use of less precise single-epoch  $M_{\text{BH}}$  estimators (e.g., Grier et al., 2013; Caglar et al., 2023), which increase  $\epsilon$  by about 0.15 dex due to uncertain sample-averaged  $f$  factors (Woo et al., 2015). For individual AGNs, the systematic uncertainties can be as large as  $\sim 0.4$  dex (Pancoast et al., 2014). These  $M_{\text{BH}}$  measurement uncertainties alone may account for a significant portion of the intrinsic scatter in the  $M_{\text{BH}}-\sigma$  relation reported in the literature. Moreover, systematic uncertainties from the host galaxy side may introduce scatter to the  $M_{\text{BH}}-\sigma$  relation. Various apertures have been used for measuring  $\sigma$  in quiescent galaxies, such as  $R_{\text{eff}}/8$  (Ferrarese & Merritt, 2000),  $R_{\text{eff}}/2$

(e.g., Kormendy & Ho, 2013), and  $R_{\text{eff}}$  (e.g., Gültekin et al., 2009). For AGNs the situation is even worse, as aperture size is often ignored (with the exception of e.g., Bennert et al. 2015; Batista et al. 2017b). While there is no physical motivation which spatial scales  $\sigma$  should correlate the closest with  $M_{\text{BH}}$ , the choice of the right aperture size crucial: In our sample we were able to resolve kinematic substructures, such as fast-rotating disks (see Fig. 5.4, NGC 3227, NGC 7469), counter-rotating disks (e.g., Mrk 1310), or circumnuclear spirals (e.g., Mrk 1044). Such complex kinematic substructures will affect  $\sigma$  measurements, depending on what aperture size is used.

### Optimal aperture for minimizing the intrinsic scatter

A generally applicable approach is needed to to define  $\sigma_*$  consistently across different morphological components. We propose using an aperture size in units of the galaxy effective radius,  $R_{\text{eff}}^{\text{gal}}$ , to address varying spatial resolution and morphological complexity, thereby enhancing the consistency of the  $M_{\text{BH}}-\sigma$  relation. This straightforward and self-consistent definition aims to minimize scatter in the  $M_{\text{BH}}-\sigma$  relation. Fig. 5.9 shows the behavior of the best-fitting parameters to the  $M_{\text{BH}}-\sigma_{\text{ap}}$  relation of AGNs hosted by LTGs, as a function of varying aperture size  $R_{\text{ap}}$ . Overall, we observe that the  $M_{\text{BH}}-\sigma$  relation becomes marginally tighter for smaller aperture sizes below  $R_{\text{ap}}/R_{\text{eff}}^{\text{gal}}$ . This may be caused apertures larger than  $R_{\text{ap}}^{\text{gal}}$ , the larger-scale outskirts of galaxies are decoupled from the galaxy-intrinsic processes that shape the  $M_{\text{BH}}-\sigma$  relation. For instance, galaxy interactions, mergers or stellar accretion streams might affect  $\sigma_{\text{ap}}$  at large  $R_{\text{ap}} > R_{\text{eff}}^{\text{gal}}$  of individual galaxies, increasing the scatter of the relation. Within  $R_{\text{eff}}^{\text{gal}}$ , the intrinsic scatter  $\epsilon$  decreases mildly with decreasing  $R_{\text{ap}}$ . Overall, it stays consistent with  $\epsilon = 0.47$  dex, the typical scatter of the relation on galaxy scales (see row (iii) of Table 5.5). For the  $M_{\text{BH}}-M_{\text{gal,dyn}}$  relation, this behavior is slightly more pronounced: The  $M_{\text{BH}}-M_{\text{bulge,dyn}}$  relation shows the more significant slope at has a smaller intrinsic scatter compared to the  $M_{\text{BH}}-M_{\text{gal,dyn}}$  relation (see columns (xii) and (xiii) of Table 5.5, suggesting that the bulge represents the spatial scale on which the correlations are the tightest. However, for many AGNs, stellar kinematics near the galaxy center are often missing, reducing sample completeness from 1 at  $R_{\text{eff}}^{\text{gal}}$  to about 0.5 at  $\langle R_{\text{eff}}^{\text{bulge}} \rangle$ . As  $R_{\text{ap}}$  decreases, the intercept  $\alpha$  varies significantly, indicating substantial effects from sample

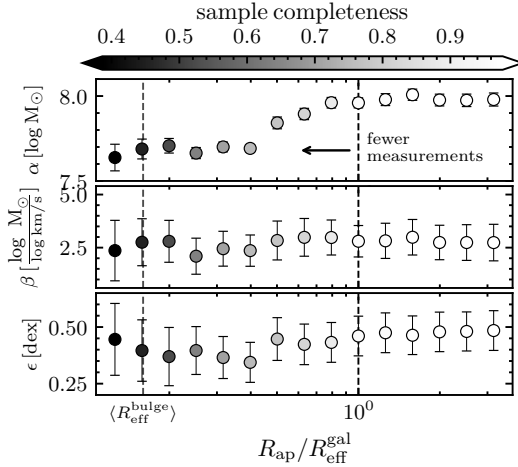


Figure 5.9: *Parameters of the best-fitting observed  $M_{\text{BH}}-\sigma_{\text{ap}}$  relation of AGNs hosted by LTGs, as a function of aperture size  $R_{\text{ap}}$ .* Data points color-coded by the fraction of AGNs for which we can robustly measure  $\sigma_{\text{ap}}$ , which decreases with decreasing  $R_{\text{ap}}$ : While  $\sigma_{\text{ap}}$  is constrained for the full the sample at  $R_{\text{eff}}^{\text{gal}}$ , measuring  $\sigma$  close to the galaxy center becomes increasingly more challenging for more distant and luminous AGNs. The three panels show the parameters of the best-fitting  $M_{\text{BH}}-\sigma_{\text{ap}}$  model parameters to the data, as a function of aperture size. The intrinsic scatter  $\epsilon$  reaches its global minimum close to  $R_{\text{eff}}^{\text{bulge}}$ , also reflected by lowest  $\epsilon$  of the corresponding scaling relation in row (v) of Table 5.5. This  $M_{\text{BH}}-\sigma$  correlation is on scales of the bulge component.

down-selection. Specifically, smaller apertures preferentially exclude distant galaxies, leading to an over-representation of lower-luminosity AGNs hosted by less massive LTGs. We therefore caution to interpret  $\alpha$  and  $\beta$  on scales of the bulge as the "best" parameters for  $M_{\text{BH}}-\sigma$ , as this AGN subsample is likely biased.

#### 5.5.4 Controlling Selection Effects

Lauer et al. (2007) pointed out that flux-limited AGN samples are biased towards over-massive BHs compared to local samples of quiescent galaxies. This introduces a bias because over-massive BHs are preferentially

selected due to the intrinsic scatter of the scaling relations (see also [Treu et al., 2007](#); [Peng, 2007](#)). As such, selection effects can significantly impact black hole mass scaling relations if not properly accounted for. In principle, these biases can be corrected if the selection function is well-defined and based solely on AGN parameters ([Ding et al., 2020, 2023](#)), or if it can be statistically modeled using simple assumptions (e.g. [Li et al., 2021](#)). For AGNs, the biases in the  $M_{\text{BH}}-\sigma$  relation are dominated by two criteria: (i) measuring a reliable  $\sigma_*$  which is often drowned by the bright AGN emission, and (ii) the narrow  $M_{\text{BH}}$  range, limited by the detection of low-luminosity AGNs and scarcity of luminous nearby AGNs. In Sect. 5.4.4, we have directly addressed (i) by using standardized recipe for consistently measuring  $\sigma$  in AGN host galaxies. Regarding (ii), we note that the selection of the AGNs in our sample is purely based on  $M_{\text{BH}}$  measurement technique, with the vast majority (40/44) having been monitored in RM campaigns. The selection for such RM campaigns is, to first order, blind to host-galaxy properties and purely based on AGN properties. As a prerequisite for measuring robust time lags, AGNs must exhibit a broad line that shows sufficient BLR flux variability as well as continuum variability on the relevant timescales. Compared to higher-mass BHs, lower-mass BHs are more likely to be active and thus included in AGN samples ([Schulze & Wisotzki, 2011](#)). This "active fraction bias" is inherent to the RM AGN sample. Additionally, low-luminosity AGNs with weak broad lines ([Greene & Ho, 2007](#); [Chilingarian et al., 2018](#)) are typically excluded from RM campaigns, introducing an additional luminosity bias. As a result, the  $M_{\text{BH}}$  distribution is truncated at both low and high  $M_{\text{BH}}$  ([Schulze & Wisotzki, 2011](#)), reducing the dynamic range in the  $M_{\text{BH}}-\sigma_*$  plane and skewing the relation.

### Matching the $M_{\text{BH}}$ distribution

These selection effects can be addressed by matching  $M_{\text{BH}}$  distributions between AGN and quiescent samples, assuming that differences in  $M_{\text{BH}}$  distributions are the primary driver of varying scaling relations. We correct it by matching the  $M_{\text{BH}}$  distribution function of the quiescent population to that of our AGN sample follow the empirical method outlined by [Woo et al. \(2013\)](#). For the implementation, we use a Monte Carlo approach: For each  $M_{\text{BH}}$  in the quiescent galaxy sample, we assign a random  $\sigma_*$  chosen from AGNs that have the same  $M_{\text{BH}}$  (within a  $\pm 0.15$  dex

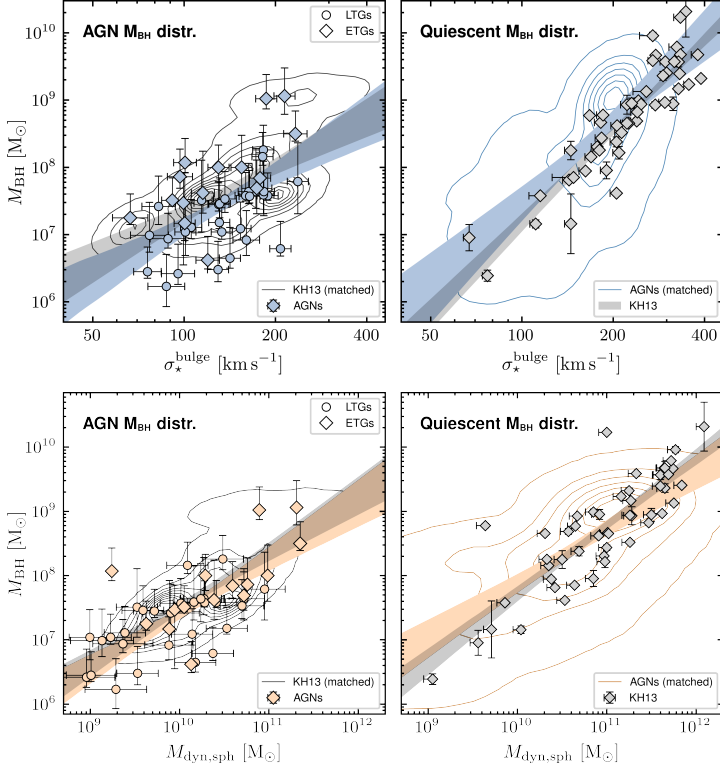


Figure 5.10:  $M_{\text{BH}}$ -host-galaxy scaling relations of AGNs and quiescent galaxies. (Top Left) Colored data points show AGNs hosted by LTGs (circles) and ETGs (squares), with the best-fitting observed relation shown as blue stripe (corresponding to row ii in Table 5.5). For AGNs, no clear distinction between the relations of ETGs and LTGs is observed. The gray contours show the KH13 sample that is resampled in  $M_{\text{BH}}$  to match the AGNs'  $M_{\text{BH}}$ -distribution (see Sect. 5.5.4). with the fitted relations shown as shaded gray stripe. The relation of the  $M_{\text{BH}}$ -matched quiescent sample agrees with the AGNs' observed relation, and is significantly flatter than the observed relation of quiescent galaxies shown in the right panel. (Top right) After empirically matching the  $M_{\text{BH}}$  distribution of AGNs (blue contours) to that of quiescent galaxies (KH13 sample, gray data points), both fall onto the same region of the  $M_{\text{BH}}-\sigma_{\star}$  plane. The best-fitting relations of AGNs are shown as blue and gray stripes, and correspond to the relations in row corresponds to row (v) and (i) respectively, in Table 5.5. (Bottom left) The same for the  $M_{\text{BH}}-M_{\text{bulge,dyn}}$  relation, with the observed AGN listed in row (xii) of Table 5.5. After matching the  $M_{\text{BH}}$  distribution, the relations of AGNs and quiescent galaxies are indistinguishable. (Bottom right) Same for matching the AGNs to the distribution of quiescent. The  $M_{\text{BH}}$  and  $M_{\text{bulge,dyn}}$  relation correspond to row (xiv) of Table 5.5.

bin, the typical uncertainty of  $M_{\text{BH}}$ ). By construction, the resulting mock quiescent sample follows the same  $M_{\text{BH}}$  distribution of the AGN sample. We repeat this step for 1000 Monte Carlo samples, and fit the  $M_{\text{BH}}-\sigma_*$  relation for each, using the method described in Sect. 5.5.3. The left panel of Fig. 5.10 shows the results of this experiment. Indeed, when  $M_{\text{BH}}$  of quiescent galaxies is resampled to the AGNs' distribution (gray contours), their relation (gray shades) is flattened, and the best-fitting parameters  $\beta = 8.02 \pm 0.12$  slope of  $\beta = 2.38 \pm 0.61$ , are consistent with the relation recovered from directly fitting the AGN (Table 5.5, row ii).

By construction, the inverse experiment recovers the AGN  $M_{\text{BH}}-\sigma_{\text{ap}}^{\text{bulge}}$  relation for AGNs if they followed the same  $M_{\text{BH}}$  distribution as the quiescent KH13 galaxy sample. We refer to this quiescent-matched relation, highlighted in Table 5.5, as the *corrected* scaling relation of AGNs. The top right hand panel of Fig. 5.10 illustrates that after the  $M_{\text{BH}}$ -resampling, the AGNs (colored contours) follow the same  $M_{\text{BH}}-\sigma_{\text{ap}}^{\text{bulge}}$  (colored stripes) as quiescent galaxies (gray stripes). The posterior distribution of the best-fitting parameters in Fig. 5.11, confirms that the offsets in  $\alpha$  and  $\beta$  are statistically insignificant (below the  $1\sigma$  confidence level). At our measurement uncertainty, the scaling relations for both populations are indistinguishable. Thus, the observed differences in the  $M_{\text{BH}}-\sigma_*$  relation between AGNs and quiescent galaxies can be attributed to differing  $M_{\text{BH}}$  distributions alone.

The relation of  $M_{\text{BH}}$  with dynamical bulge mass, shown in the bottom panels of Fig. 5.10, confirms what we find for the  $M_{\text{BH}}-\sigma$  relation: AGNs and quiescent galaxies form their own scaling relations that fall in complementary parts of the  $M_{\text{BH}}-M_{\text{bulge,dyn}}$  plane. Fitting the observed  $M_{\text{BH}}-M_{\text{bulge,dyn}}$  of AGNs returns a relation with shallower slope compared to that of quiescent galaxies. After matching their  $M_{\text{BH}}$ -distributions, the relations are indistinguishable, suggesting that both populations share the same underlying scaling relation.

We note that the RM AGN sample might still contain additional biases which were not considered here. Their BLR geometry might sample only a fraction of the parameter space (Richards et al., 2011). From the host-galaxy side, BLR variability may be coupled to gas transport processes on host-galaxy scales, which could entail a secondary correlation with galaxy interactions (Barnes & Hernquist, 1996), or secular processes triggered by e.g., bars (e.g., García-Burillo et al., 2005). Furthermore, is worth noting

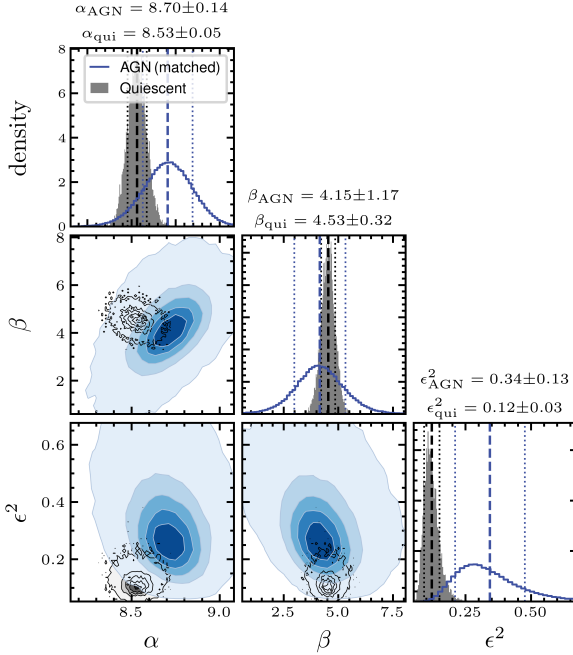


Figure 5.11: *Corner plot of the free parameters of the linear  $M_{\text{BH}}-\sigma$  model after matching the  $M_{\text{BH}}$  distribution.* The posterior distributions of the quiescent population from KH13 are shown as black lines/contours, the AGNs from our sample are shown with blue colors. The intercept  $\alpha$  and both populations are not significantly different, although associated with larger uncertainties for AGNs. While the intercept  $\alpha$  is correlated with  $\beta$  and  $\sigma$ , in particular for AGNs, the covariance cannot account for the offset in  $\alpha$ . This indicates that quiescent galaxies and AGNs follow an intrinsically different  $M_{\text{BH}}-\sigma$  relations.

that also the quiescent sample suffers from selection biases, as pointed out by e.g., [Bernardi et al. \(2007\)](#); [van den Bosch \(2016\)](#): host galaxies with dynamically measured  $M_{\text{BH}}$  tend to have higher  $\sigma$  compared to early type galaxies of the same luminosity, which may artificially increase the normalization  $M_{\text{BH}}-\sigma$  relation by a factor of  $\sim 3$  (see [Shankar et al. 2016, 2020](#), but [Kormendy 2020](#)).

### 5.5.5 The Virial Factor $f$

The classical approach for measuring a sample-average virial factor  $f$  involves matching the  $M_{\text{BH}}\text{-}\sigma$  relation of RM AGNs to that of quiescent galaxies. This is usually done by fitting the VP- $\sigma$  relation with fixed slope, and determining the sample average virial factor via the difference of the intercepts  $\log f = \alpha_{\text{qui}} - \alpha_{\text{AGN}}$ . However, this step implicitly assumes that AGNs and quiescent galaxies follow the same  $M_{\text{BH}}\text{-}\sigma$  relation, which so far has little empirical foundation. Furthermore, the matching is prone to systematic uncertainties introduced by different selection functions between AGN and quiescent galaxy samples;  $\langle f \rangle$  can vary by 0.3 dex depending on what quiescent galaxy sample is used as reference (Ho & Kim, 2014). In addition, individual  $f$  factors vary by one order of magnitude across the sample, limiting the precision of this approach.

To test the implicit assumptions and reduce systematic uncertainties, we used the independently measured individual  $f$  factors from CAMEL modeling. The sample-average  $\langle f \rangle$  can be derived from comparing in the intercept between active and inactive galaxies. We fit the  $M_{\text{BH}}\text{-}\sigma$  relation for the CAMEL sample, this time fixing the slope to that of quiescent galaxies due to the limited dynamic range in  $M_{\text{BH}}$  ( $\alpha_{\text{qui}} = 4.53 \pm 0.32$ , see Sect 5.5.2). This step is justified, since we demonstrated that both share the same underlying relations (see Sect. 5.5.4). As opposed to the classical approach,  $\langle \log f_{\text{dyn}} \rangle$  must be added to account for the sample average virial factor that is already incorporated in the AGNs'  $M_{\text{BH}}$  (i.e., is already included in  $\alpha_{\text{qui}}^{\text{AGN}}$ ):

$$\langle \log f \rangle = \alpha_{\text{qui}} - \alpha_{\text{dyn}}^{\text{AGN}} + \langle \log f_{\text{dyn}} \rangle \quad (5.7)$$

Fitting the AGNs' observed  $M_{\text{BH}}\text{-}\sigma_{\text{ap}}^{\text{bulge}}$  relation with the slope fixed to the KH13 relation yields  $\alpha_{\text{dyn}}^{\text{AGN}} = 8.20 \pm 0.11$  and  $\langle \log f \rangle = 0.65 \pm 0.18$ . This result closely matches  $\langle \log f \rangle = 0.65 \pm 0.12$ , the value obtained from applying the classical method to the RM AGN sample (Woo et al., 2015). It also aligns well with the average of individual  $f$ -factors from dynamically modeling their BLR lags,  $\langle \log f_{\text{dyn}} \rangle = 0.66 \pm 0.07$  (column 11 of Table 5.1). We conclude that the classical approach of determining the sample-average virial factor from matching the  $M_{\text{BH}}\text{-}\sigma$  relation of RM AGNs agrees with the independent measurements of  $M_{\text{BH}}$  in AGNs. Importantly, neither do we find significant dependencies of the sample-average  $f$  on host galaxy

morphology, nor do we observe such a dependency among the  $f_{\text{dyn}}$  (see [Vilafaña et al., 2023](#), for more discussion).

### 5.5.6 Uniform $M_{\text{BH}}$ Scaling Relations of Active and Quiescent Galaxies: Consequences

AGNs represent a special stage of during BH evolution where the ongoing gas accretion may significantly contribute to grow the SMBH. However, AGN lifetime and the associated contribution to SMBH growth are only scarcely constrained, so that it is not clear how this should affect the the AGN  $M_{\text{BH}}$  scaling relations. Regardless, there has been no independent and conclusive observational evidence for whether AGNs follow the same  $M_{\text{BH}}$ -host-galaxy scaling relations as quiescent galaxies. While [Woo et al. \(2013\)](#) demonstrated that selection effects can account for differences in slopes, our independent  $M_{\text{BH}}$  measurements reveal for the first time that both the slope  $\beta$  and intercept  $\alpha$  of the scaling relations for AGNs and quiescent galaxies are the same, indicating that both populations share the same underlying  $M_{\text{BH}}$  scaling relation. This suggests, and we have explicitly tested, that matching the  $M_{\text{BH}}-\sigma$  relation of AGNs with that of quiescent galaxies is justified for constraining the sample-average virial factor  $f$ . In other words, our results reinforce previous calibrations of  $f$  and individual measurements of  $f_{\text{dyn}}$  from dynamical modeling the BLR lags. By covering a larger dynamic range in both host galaxies and BHs, our results also support the use the single-epoch method for estimating  $M_{\text{BH}}$  across the explored parameter range, up to  $\log(M_{\text{BH}}/M_{\odot}) \sim 10^{8.5}$ .

## 5.6 Summary

After more than two decades of study, the  $M_{\text{BH}}$  scaling relations have emerged as essential probes of the coevolution between supermassive black holes and their host galaxies. For AGNs, state-of-the-art observational and computational techniques have enabled more precise measurements of  $M_{\text{BH}}$  and  $\sigma_*$  than were previously possible. In this work, we used spatially resolved stellar kinematics to calibrate the  $M_{\text{BH}}-\sigma_*$  relation of the local AGN population. For a sample of 44 AGNs, the majority of which have precise and independent  $M_{\text{BH}}$  measurements from dynamical modeling, we presented IFU data from Keck/KCWI, VLT/MUSE and VLT/VIMOS.

We tested different AGN deblending and analysis techniques that are required to precisely trace the spatially resolved stellar kinematics. Based on HST imaging data, we spatially resolved  $\sigma$  across different galaxy morphological components, and studied dependencies of the scaling relation  $M_{\text{BH}}$  on morphology and aperture size. Our key findings can be summarized as follows:

1. We find mild evidence that the  $M_{\text{BH}}-\sigma_*$  correlation of AGNs hosted by LTGs is tightest if the kinematics are measured on scales of the galaxy bulge.
2. Rotational broadening from the galaxy disk introduces scatter in the  $M_{\text{BH}}$  host galaxy relations of AGNs hosted by LTGs. Comparative studies based on higher-redshift AGNs hosted by disk galaxies can use the derived aperture-correction method to statistically infer the underlying  $M_{\text{BH}}-\sigma_*$  scaling relation.
3. After removing the contribution from disk rotation, they follow a  $M_{\text{BH}}-\sigma$  relation that is similar to that of quiescent galaxies, but offset to lower  $\sigma_*$  by 0.2 dex. This suggests, that the dynamically hot disk component of LTGs does coevolve with the SMBH.
4. The  $M_{\text{BH}}-\sigma_*$  relation in AGNs is robust, regardless of whether the host galaxies have late-type or early-type morphologies. The intrinsic scatter is primarily driven by galaxy-to-galaxy variations. However, further constraining this scatter is challenging due to the scarcity of AGNs with dynamically measured  $M_{\text{BH}} > 10^8 M_{\odot}$ , and the fact that  $\sigma$  in such luminous AGNs can only be marginally spatially resolved.
5. The observed flattening of both  $M_{\text{BH}}-\sigma$  and  $M_{\text{BH}}-M_{\text{dyn}}$  relations of AGNs is driven by selection biases that limit the  $M_{\text{BH}}$  dynamic range. We demonstrated for the first time that after correcting for this effect, slope *and* intercept of the underlying scaling relations of AGNs match those of quiescent galaxies. This suggests that on average, the current AGN phase does not significantly grow  $M_{\text{BH}}$  compared to  $M_{\text{BH}}$  in quiescent galaxies.
6.  $M_{\text{BH}}$  of our sample was determined independently of the virial factor. Thus, we present a self-consistent empirical calibration of  $\langle f \rangle$

based on spatially resolved kinematics of type-1 AGN. The derived value of  $\log f = 0.65 \pm 0.18$  matches previous calibrations based on the classical RM AGN sample, as well as the average  $\langle f \rangle$  determined from individually measured  $f$ . A robust understanding of the virial factor is essential for estimating  $M_{\text{BH}}$  measurements in the distant Universe via the single epoch method.

Spatially resolving  $\sigma_*$  in AGNs is currently feasible only for the local AGN population, which we used in this study to provide the local reference of the  $M_{\text{BH}}$  scaling relations. It remains an important objective to identify the morphological components and spatial scales across which the  $M_{\text{BH}}-\sigma_*$  relation of the quiescent population is the tightest. This can best be tested on nearby galaxies, for which larger sample size, higher spatial resolution and the lack of a bright AGN PSF make this analysis less sensitive to systematic uncertainties.

## 5.7 Appendix

### 5.7.1 AGN Spectral Fitting

In order to estimate the AGN parameters  $M_{\text{BH}}$ ,  $L_{\text{bol}}$  and  $\lambda_{\text{Edd}}$  as discussed in Sect. 5.4.2, we model the AGN spectrum in the  $\text{H}\beta$ -[O III] wavelength region. As a first step, we correct Galactic foreground extinction which can significantly reduce the observed flux and alter the overall shape of the spectra recorded for our extragalactic targets. We correct all KCWI, MUSE, and VIMOS data cubes for Galactic extinction by dividing with the Cardelli et al. (1989) Milky Way optical extinction curve, before fitting the AGN spectra. The extinction curve is scaled to the line-of-sight V-band extinction as reported by the NASA/IPAC Extragalactic Database (NED) which is based on the far-IR maps presented by Schlegel et al. (1998) or SDSS stars (Schlafly & Finkbeiner, 2011). To get a pure AGN spectrum free from host emission, we take  $3''$  aperture spectrum from the host-deblended AGN data cube, centered on the AGN position. We then subtract the best-fit stellar continuum as determined via pPXF (see Sect. 5.4.3). For a consistent analysis between the data sets that cover different wavelength ranges, we restrict the spectral fitting to the common rest-frame wavelength range  $4750\text{\AA}$  to  $5100\text{\AA}$ . To describe the AGN power-law continuum in this narrow wavelength range, we adopt a linear pseudo-continuum. For the strong emission lines  $\text{H}\beta$  and [O III], we use a superposition of broad and narrow Gaussian line profiles: Two broad components for the  $\text{H}\beta$  line and two broad  $\text{Fe II } \lambda\lambda 4923, 5018$  lines are sufficient to describe the spectral variations across the sample. In addition to the narrow components for each [O III]  $\lambda\lambda 4960, 5007$  and  $\text{H}\beta$ , we often require a wing component to reproduce the typical asymmetry of those lines in AGN (Greene & Ho, 2005b; Mullaney et al., 2013). We kinematically couple the broad narrow and wing components to each other, tie the [O III] doublet line ratio to its theoretical value of 3 (Storey & Zeippen, 2000) and that of Fe II components to their empirical ratio of 0.81. With these constraints, we reduce the number of free parameters and increase the robustness of the fit.

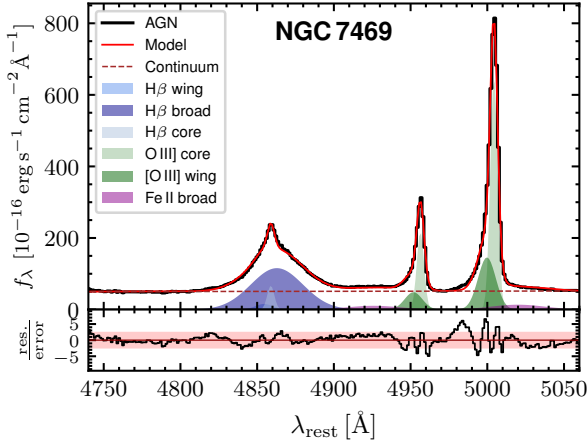


Figure 5.12: *Example of the AGN spectral modeling for the case of NGC 7469.* The modeled wavelength range is limited to the rest-frame wavelength range 4750 Å–5100 Å covering the prominent H $\beta$  and [O III] $\lambda\lambda$ 4960, 5007 emission lines. The spectrum with the full best-fit model and various line components for the BLR and the narrow and core component for H $\beta$  and [O III] are individually shown with different line styles and colors. The residual spectrum and the  $3\sigma$  limiting band are shown in the lower panel.

An example of the modeling is shown in Fig. 5.12. We list the corresponding line fluxes of the broad H $\beta$  and Fe II lines together with their line widths as well as the total [O III] flux in Table 5.6. The corresponding errors are estimated from Monte Carlo sampling, plus an addition a 10% systematic uncertainty introduced from the AGN-host deblending and continuum-subtraction process.

Table 5.6: *AGN parameters estimated from fitting the AGN spectrum.*

AGN name	$\sigma_{H\beta}$	$f_{\lambda}(5100 \text{ \AA})$	$L_{\text{bol}}$	$\log \lambda_{\text{Edd}}$
(1)	[km s <sup>-1</sup> ] (2)	[10 <sup>-15</sup> erg s <sup>-1</sup> cm <sup>-2</sup> \AA <sup>-1</sup> ] (3)	[10 <sup>43</sup> erg s <sup>-1</sup> ] (4)	(5)
NGC 3227	1656 ± 83	7.7 ± 0.4	1.23 ± 0.07	-2.0 ± 0.2
NGC 6814	1466 ± 73	2.3 ± 0.3	0.69 ± 0.09	-1.7 ± 0.3
NGC 4593	1655 ± 83	2 ± 0.4	1.6 ± 0.3	-1.6 ± 0.4
NGC 3783	2170 ± 110	10.2 ± 0.2	10.9 ± 0.2	-1.5 ± 0.2
NGC 2617	2100 ± 110	1.13 ± 0.08	2.6 ± 0.2	-2.2 ± 0.2
IC 4329 A	2860 ± 430	2.08 ± 0.09	5.4 ± 0.2	-2.0 ± 0.2
Mrk 1044	805 ± 40	3.2 ± 0.2	9.6 ± 0.7	-0.6 ± 0.2
NGC 5548	3500 ± 170	6.8 ± 0.2	20.7 ± 0.7	-1.4 ± 0.2
NGC 7469	1046 ± 52	5.2 ± 0.4	16.4 ± 1.2	-1.1 ± 0.3
Mrk 1310	1360 ± 180	0.16 ± 0.03	0.7 ± 0.1	-2.7 ± 0.4
Mrk 1239	1093 ± 55	3.3 ± 0.2	14.7 ± 0.7	-1.4 ± 0.2
Arp 151	1170 ± 350	0.46 ± 0.06	2.3 ± 0.3	-1.4 ± 0.3
Mrk 50	1992 ± 100	1.16 ± 0.1	7.3 ± 0.6	-1.7 ± 0.3
Mrk 335	1800 ± 200	2 ± 0.3	15.2 ± 2.4	-1.2 ± 0.4
Mrk 590	3580 ± 180	1.39 ± 0.07	11 ± 0.5	-1.6 ± 0.2
SBS 1116+583A	1845 ± 92	0.28 ± 0.03	2.6 ± 0.3	-1.7 ± 0.3
Zw 229-015	1386 ± 69	0.65 ± 0.02	5.9 ± 0.2	-1.3 ± 0.2
Mrk 279	2010 ± 100	3.24 ± 0.1	35.3 ± 1.1	-1.1 ± 0.2
Ark 120	1200 ± 60	4.11 ± 0.06	51.8 ± 0.8	-1.6 ± 0.2
3C 120	1658 ± 83	13.1 ± 0.1	168.1 ± 1.9	-0.7 ± 0.2
MCG +04-22-042	1410 ± 70	0.68 ± 0.03	8.9 ± 0.4	-1.7 ± 0.2
Mrk 1511	1906 ± 95	0.22 ± 0.01	3 ± 0.2	-1.7 ± 0.2
PG 1310-108	1589 ± 79	1.31 ± 0.04	18.1 ± 0.6	-0.3 ± 0.2
Mrk 509	2060 ± 100	13 ± 0.1	185 ± 1.8	-0.8 ± 0.2
Mrk 110	1797 ± 90	1.6 ± 0.02	23.8 ± 0.3	-0.9 ± 0.2
Mrk 1392	1983 ± 99	0.65 ± 0.02	9.9 ± 0.3	-2.3 ± 0.2
Mrk 841	2030 ± 100	3.03 ± 0.05	47.6 ± 0.8	-1.0 ± 0.2
Zw 535-012	1916 ± 96	1.6 ± 0.03	43.7 ± 0.8	-1.0 ± 0.2
Mrk 141	2780 ± 140	0.89 ± 0.09	18.5 ± 1.8	-1.3 ± 0.3
RBS 1303	1249 ± 62	2.6 ± 0.08	54.1 ± 1.7	-0.2 ± 0.2
Mrk 1048	2080 ± 100	8.4 ± 0.7	183 ± 15	-0.6 ± 0.3
Mrk 142	1291 ± 65	0.7 ± 0.02	16.8 ± 0.4	-0.1 ± 0.2
RXJ 2044.0+2833	898 ± 45	2.49 ± 0.04	75 ± 1.3	-0.3 ± 0.2
IRAS 09149-6206	2310 ± 120	27.7 ± 1.7	1110 ± 67	-0.1 ± 0.2
PG 2130+099	1690 ± 510	3.85 ± 0.08	194.1 ± 4.1	0.3 ± 0.2
NPM1G+27.0587	1228 ± 61	1.88 ± 0.05	88.8 ± 2.3	-0.8 ± 0.2
RBS 1917	1390 ± 70	1.14 ± 0.08	59.6 ± 4.1	-0.4 ± 0.2
PG 2209+184	1908 ± 95	0.56 ± 0.02	34.2 ± 1.3	-1.1 ± 0.2
PG 1211+143	1736 ± 87	4.5 ± 0.7	375 ± 54	-0.6 ± 0.4
PG 1426+015	2630 ± 140	4.29 ± 0.08	402.8 ± 7.9	-1.5 ± 0.2
Mrk 1501	1870 ± 170	1.08 ± 0.04	103.5 ± 3.4	-0.9 ± 0.2
PG 1617+175	2030 ± 140	2.67 ± 0.08	439 ± 13	-0.1 ± 0.2
PG 0026+129	921 ± 92	1.7 ± 0.2	500 ± 60	-0.9 ± 0.3
3C 273	2120 ± 110	20.9 ± 1.2	7300 ± 420	-0.3 ± 0.2

**Notes.** AGNs are listed in order of increasing redshift (as in Table 5.1). (1) AGN name. (2) Line dispersion of the H $\beta$  BLR component. (3) AGN continuum spectral flux density at 5100 \AA. (4) Approximate AGN bolometric luminosity from using a bolometric correction factor of 10. (5) Eddington ratio  $\lambda_{\text{Edd}}=L_{\text{bol}}/L_{\text{Edd}}$ .

### 5.7.2 The Importance of AGN-host Deblending

Since close to the galaxy center the AGN is typically orders of magnitude brighter than the host-galaxy stellar continuum, the AGN emission blends the kinematic diagnostic features, making an accurate extraction of host-galaxy parameters challenging. This can drastically affect the kinematics measured for any extended host-galaxy component. While this is a well-known problem for tracing ionized gas emission lines of outflows and the extended narrow line region (e.g. Villar-Martín et al., 2016; Husemann et al., 2016b), we here demonstrate the impact of the AGN emission on extracting the host-galaxy stellar kinematics.

The AGN spectrum can be described by a power-law spectrum, with an additional contribution from the BLR clouds. Depending on observational setup, atmospheric conditions, the AGN/host luminosity ratio, and the AGN spectral classification, the AGN spectrum outshines the stellar continuum within the central  $0''.4$  to  $\sim 6''.0$ . Especially for some luminous AGNs, e.g., the narrow-line-Seyfert 1 galaxies Mrk 335, Mrk 1044, with strong Fe II blending the Mg Ib wavelength region. In these cases, an accurate extraction of the stellar kinematics close to their nuclei is limited by the contrast between the AGN emission and the host galaxy, together with the accuracy by which the PSF can be modeled and subtracted.

There are two approaches to handle the AGN contamination: (i) The AGN spectrum can be included in the spectral synthesis modeling, as e.g., performed by (Remigio et al., 2024, in prep.) who use the package `BADASS` for analyzing a subsample of our AGNs. While, this approach is free of parameters, such as, e.g., the host-galaxy surface brightness profile, it requires a sophisticated treatment of the kinematic coupling between the spectral components, plus a well-considered choice of the starting parameters. (ii) We make the well-justified assumption that the broad lines exclusively originate from the spatially unresolved BLR. The package `QDeblend3D` uses this to extract an empirical PSF, whose subtraction is described in Sect. 5.3.1.

Fig. 5.13 shows the results for  $\sigma$  from fitting the stellar continuum emission of Mrk 110 with `pPXF`, before and after the PSF subtraction with `QDeblend3D`. In the AGN-contaminated case, i.e., before PSF subtraction,  $\sigma$  within the central  $3''$  reaches a central value of  $295 \pm 15 \text{ km s}^{-1}$ . These formal errors drastically underestimate the systematic offset that arises from the AGN contamination: After the AGN-host deblending,

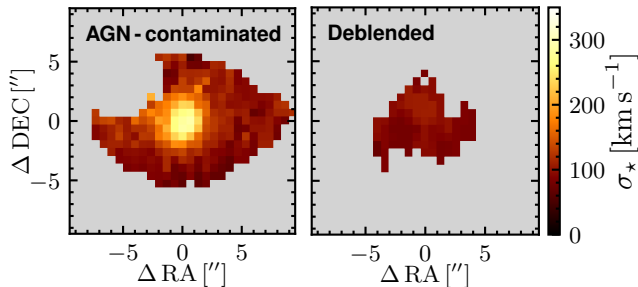


Figure 5.13: *AGN deblending impacts the extraction of  $\sigma$  in Mrk 110.* The left panel shows the spatially resolved  $\sigma_{\text{spat}}$  of Mrk 110 as extracted from the AGN-contaminated cube (left panel). Its profile shows a steep rise of towards the galaxy nucleus, caused by the prominent Fe II broad emission lines blending with important  $\sigma$  diagnostic lines. After carefully subtracting the bright AGN emission, the measured central  $\sigma_{\text{spat}}$  is smaller by a factor of three (right panel).

the spectral synthesis modeling of the faint host-galaxy signal results in a flat radial profile, where the central spaxel at the AGN location has  $\sigma_{\text{spat}} = 103 \pm 4 \text{ km s}^{-1}$ . This value is consistent with the  $95 \pm 8 \text{ km s}^{-1}$  reported by Ferrarese et al. (2001), which were measured from CaT in a  $2'' \times 4''$  long-slit aperture, which is less affected by AGN contamination. We note that Mrk 110 represents an extreme case, where the AGN-contamination offsets the central  $\sigma$  by a factor of three. However, within the bulge effective radii  $R_{\text{eff}}^{\text{bulge}}$ , we observe an average increase of 30% when measuring  $\sigma$  after not properly subtracting the AGN emission.

### 5.7.3 Spatially Resolved vs. Aperture-integrated $\sigma$

In Sect. 5.4.4 we have defined two methods for measuring the stellar velocity dispersion: The dispersion measured from aperture-integrated  $\sigma_{\text{ap}}$  and the spatially resolved  $\sigma_{\text{spat}}$ . As a consistency check, we reconstruct aperture-integrated kinematics from spatially resolved measurements in individual Voronoi cells. To achieve this, both contributions from ordered rotation  $v_{\text{res}}$  and chaotic motion  $\sigma_{\text{res}}$  must be considered, as it has been done e.g., for quiescent galaxies by Pinkney et al. (2003) and Gültekin et al. (2009), and for AGNs by Bennert et al. (2015). In our case of 2D

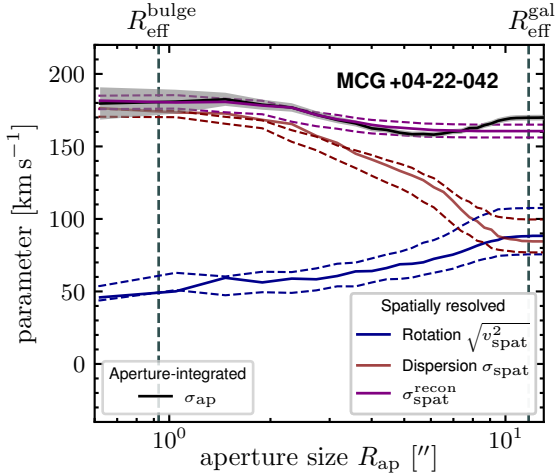


Figure 5.14: Comparing different methods to measure  $\sigma$  in MCG+04-22-042. The black line shows the aperture-integrated stellar velocity dispersion as a function of aperture size  $R_{\text{ap}}$ , with the uncertainty indicated by gray shades. By integrating over the intensity-weighted contributions from the spatially resolved measurements of the rotational component  $v_{\text{spat}}$  and dispersion  $\sigma_{\text{spat}}$ , we can reconstruct the aperture-integrated value across a large dynamical range in aperture sizes ( $\sigma_{\text{spat}}^{\text{recon}}$ , purple line).

kinematic fields, the surface area (i.e., number of spaxels) and the associated surface brightness of the host-galaxy stellar emission varies between different Voronoi cells. To derive consistent flux-weighted kinematics, the spatially resolved values must be weighted by the luminosity of the respective Voronoi cell. Thus, we reconstruct the aperture-integrated kinematics from spatially resolved measurements as

$$(\sigma_{\text{ap}}^{\text{recon}})^2 = \frac{\int_0^{R_{\text{eff}}} [\sigma_{\text{spat}}^2(r) + v_{\text{spat}}^2(r)] \cdot I(r) \cdot dr}{\int_0^{R_e} I(r) \cdot dr} \quad (5.8)$$

with the surface brightness  $I(r)$ . In case of reconstructing the kinematics of the bulge,  $I(r) = I(R_e) \times \exp(-\kappa_n[(r/R_e)^{1/n} - 1])$  is described by a

Sérsic profile, where the  $R_e$  as the bulge effective radius as measured from the photometry presented in (Bennert et al., 2024, in prep.). This approach is equivalent to the prescription of the Nuker team (e.g., Pinkney et al. 2003; Gültekin et al. 2009), but for AGNs has only been applied to long-slit spectra (Bennert et al., 2015). From the ionized gas kinematics (see Remigio et al., 2024, in prep.), we have noticed that  $\sigma_{\text{ap}}^{\text{recon}}$  and  $\sigma_{\text{ap}}$  are not necessarily equal (also see KH13, supplementary material for a discussion), although very complex emission line profiles with high-velocity components are required for the differences to matter. Within the context of stellar kinematics where the gradients are small, we detect no significant differences between  $\sigma_{\text{ap}}^{\text{recon}}$  and  $\sigma_{\text{ap}}$ ; MCG,+04-22-042 is an arbitrarily selected AGN for which we have coverage of  $\sigma_{\text{spat}}$  from scales below  $R_{\text{eff}}^{\text{bulge}}$  to beyond  $R_{\text{eff}}^{\text{gal}}$ . In Fig. 5.14, we show that with increasing distance from the center, the relative contribution from the bulge component ( $\sigma_{\text{spat}}$ ) decreases, while the relative contribution of the ordered disk-like rotation ( $v_{\text{spat}}$ ) increases. When combined, the reconstructed radial profile of  $\sigma_{\text{ap}}^{\text{recon}}$  matches that of  $\sigma_{\text{ap}}$  as directly measured from the coadded spectra corresponding to that aperture size. We have confirmed this behavior for LTGs in the sample, demonstrating the feasibility of disentangling the contributions from random orbital motions versus disk-like galaxy-scale rotation. Therefore, we conclude that our approach of inferring the  $M_{\text{BH}}$  scaling relation from rotation-corrected  $\sigma_{\text{spat}}$  is self-consistent (see Sect. 5.5.3).

However, we note that the spatial resolution in many data sets is too low to spatially resolve the bulge. In addition, the bright AGN emission often prevents measuring robust  $\sigma_{\text{spat}}^{\text{bulge}}$  for 10 out of 38 LTGs. In these cases, the finite spatial resolution impacts also our ability to resolve the stellar kinematics on the relevant scales of the disk (few arcseconds), so that rotational broadening likely contributes even to the spatially resolved quantity  $\sigma_{\text{spat}}^{\text{gal}}$ . As a result, disk rotation is poorly spatially resolved, so that the lower spatial resolution might bias  $\sigma_{\text{spat}}$  of individual AGNs towards higher values if the disk rotation is not resolved.

### 5.7.4 Stellar Kinematics from Different IFU Datasets

A handful of AGNs in our sample (5/44) have been observed with multiple optical IFU instruments, offering different field coverage, depth, spectral and spatial resolution. We have demonstrated in Appendix 5.7.2 that the extraction of the stellar kinematics is limited by the accurate subtraction of the PSF, which is specific to each data set. For the multiply observed objects, observations taken under different conditions with different instruments allow us to obtain independent measurements of the host-galaxy stellar kinematics for consistency checks. MCG +04-22-042 is one of the AGNs that have been observed with both Keck/KCWI and VLT/MUSE. We processed each dataset as outlined in Sect. 5.7.2 and Sect. 5.4.3, and here compare the radial profiles of the aperture-integrated  $\sigma$ , and the spatially resolved  $\sigma_{\text{spat}}$  measurements (described in Sect. 5.4.4). Fig. 5.15 shows the comparison between the radial behavior of the spatially resolved kinematics extracted in MCG +04-22-042. Compared to the relative small FoV of our KCWI setup ( $16'' \times 20''$ ), the MUSE FoV covers a much larger fraction of the host galaxy. Within the overlapping field, the radial profile of  $\sigma_{\text{spat}}$  shows a steep decrease with increasing distance to the center. The radial profiles extracted from the two data sets agree within the uncertainties, out to the radius where the KCWI coverage stops. Different observing conditions and instrumental characteristics are reflected in the PSF width,  $\theta_{\text{FWHM}}^{\text{MUSE}} = 1.2$ , and  $\theta_{\text{FWHM}}^{\text{KCWI}} = 1.8$ . However, this difference does not significantly impact  $\sigma_{\text{spat}}$  on scales of the galaxy bulge  $R_{\text{eff}}^{\text{bulge}}$ ; Analyzing the MUSE and KCWI data sets yields  $\sigma_{\text{spat}}^{\text{bulge}} = 173 \pm 5$  km/s and  $\sigma_{\text{spat}}^{\text{bulge}} = 169 \pm 6$  km/s, respectively.

For the remaining 4 objects (RBS 1303, NGC 5548, NGC 4593, PG 1310-108, all observed with VLT/VIMOS), we have carried out the same test for  $\sigma_{\text{ap}}$ , which is less sensitive to the differences between instrument characteristics. While the results generally agree with each other within the error margin, the depth and resolution of the MUSE and KCWI cubes superior to the VIMOS data sets. We therefore adopted the MUSE and KCWI for the analysis in the main part of this work.

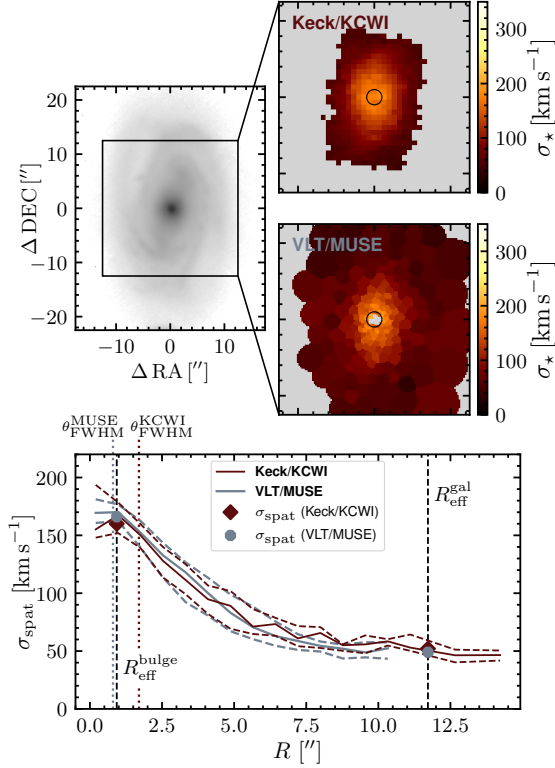


Figure 5.15: Comparing  $\sigma_{\text{spat}}$  in MCG +04-22-042, extracted from two different data sets. (Top panels) The top left panel shows the V-band AGN-subtracted continuum image of MCG +04-22-042, with  $\sigma_{\text{spat}}$  measured from the Keck/KCWI and VLT/MUSE data sets (top right inset panels). While the field coverage of MUSE is superior, we can measure accurate  $\sigma_{\text{spat}}$  at the AGN location only in the KCWI data set. (Bottom panels) The radial profiles of  $\sigma_{\text{spat}}$  measured from the the two data sets are shown, together with the PSF FWHM  $\theta_{\text{FWHM}}$  of the respective data set. Across the entire host galaxy, the spatially resolved radial profiles of  $\sigma_{\text{spat}}$  agree within the uncertainty, which confirms that our method is valid independent of the observational setup.

### 5.7.5 Stellar Kinematics from Fitting Different Diagnostic Features

In Fig. 5.16, we compare how the choice of the wavelength range used for fitting the host galaxy emission affects the extracted stellar kinematics (see Sect. 5.4.3). Specifically, we compare the kinematics obtained from the galaxy aperture-integrated spectra in the wavelength ranges 8400 Å–8750 Å (CaT), 5100 Å–5700 Å (Mg Ib +Fe) and 4700 Å–5700 Å (full). We find that in general, maximizing the wavelength range is favorable to increase the robustness of the parameters inferred through spectral synthesis modeling. However, PSF subtraction required to remove the AGN emission can severely affect the faint host galaxy stellar emission. As a result, spatially coadding spectra can introduce non-physical artifacts in the spectra, especially near the galaxy nucleus, severely impacting the measured stellar kinematics. This effect is pronounced in two of the brightest AGNs, PG 1617+175 or PG 0026+129, where the choice of wavelength range can lead to systematic differences as large as 32 km/s. This is caused by H $\beta$  AGN residual emission swamping the Mg Ib and Fe stellar absorption features, leading to nonphysically high  $\sigma$  (see Appendix 5.7.2). A consistent choice of the wavelength range is therefore a trade-off between narrow wavelength ranges that provide more robust results in bright AGNs, vs. larger wavelength ranges providing the more robust results in faint AGNs. Moreover, the coverage stellar absorption features varies due to varying spectral coverage between the data sets used in this work; While CaT is available for almost all objects observed with MUSE, KCWI only covers the Mg Ib and Fe features. Overall, choosing the maximum common wavelength range between the data sets provides the best compromise between the three constraints. We therefore settled with using the wavelength range 4700 Å–5700 Å for the spectral synthesis modeling in Sect. 5.4.3.

### 5.7.6 Effect of Aperture Size on Aperture-integrated $\sigma$

As a primary objective of this work, we investigate the dependency of the  $M_{\text{BH}}-\sigma_*$  relation on aperture size in Sect. 5.5.3. While the crucial role of aperture-size on the spatially resolved kinematics of LTGs is discussed in Sect. 5.4.4, we here examine the effect of aperture size on measuring the aperture-integrated stellar velocity dispersion  $\sigma_{\text{ap}}$ .

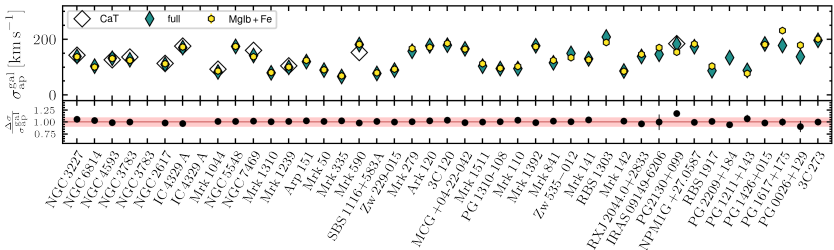


Figure 5.16: *Comparison of extracting stellar velocity dispersion from different spectral windows.* The top panel shows  $\sigma_{\text{ap}}^{\text{gal}}$ , the aperture-integrated dispersion from coadded spectra within and aperture matched to  $R_{\text{eff}}^{\text{gal}}$ , itemized after AGNs in the sample. Colors refer to the different spectral windows within which we measured  $\sigma_{\text{ap}}^{\text{gal}}$ . The bottom row shows the residual dispersion between measurements from MgIb vs. "full" measurements, with the 5% uncertainty, a typical uncertainty of  $\sigma_{\text{ap}}$ , indicated by the shaded red stripe. The differences remain usually below the nominal uncertainties returned by pPXF. MgIb +Fe and full wavelength windows usually provide consistent within the 5% margin, and we consider both to be similarly robust and consistent tracers for the stellar kinematics across the sample.

Fig. 5.17 presents  $\sigma_{\text{ap}}$  for each AGN, measured from aperture-integrated spectra with aperture sizes corresponding to  $R_{\text{eff}}^{\text{bulge}}$ ,  $R_{\text{eff}}^{\text{gal}}$ , or fixed to  $3''$  (corresponding to the SDSS fiber size). The distinction between bulge and galaxy is applicable only for LTGs, which have an identifiable disk component. For ETGs,  $\sigma_{\text{ap}}^{\text{gal}}$  is the sole indicator of morphology-matched kinematics since no substructure is detected in these systems. Additionally, small bulge sizes in several galaxies precluded the measurement of  $\sigma_{\text{ap}}^{\text{bulge}}$  on such small scales (e.g. for Mrk 1044, see also Sect. 5.5.3, and discussion in Sect. 5.5.3).

For the majority of AGNs, changing the aperture size has marginal impact on the stellar kinematics. For ETGs, as long as  $R_{\text{eff}}^{\text{gal}}$  is covered by the aperture, this is to be expected since their bright cores dominate the luminosity and kinematic profiles, which are typically covered by both the  $3''$  and  $R_{\text{eff}}^{\text{gal}}$ -matched aperture. For LTGs, using bulge- vs. galaxy-size apertures makes a significant difference in approximately 50% of the cases. This can be understood from the aperture-size dependent profiles, shown

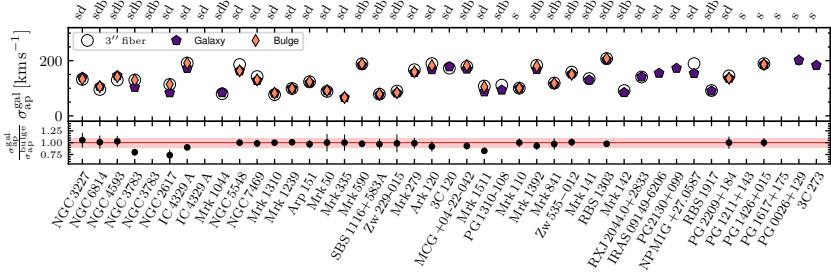


Figure 5.17: Comparing integrated  $\sigma_{ap}$  across different host-galaxy morphological components and aperture sizes. For each object, we show  $\sigma_{ap}$  color-coded by the aperture size over which the host-galaxy emission was integrated prior to spectral synthesis modeling (see Sect. 5.4.1). The bottom panel shows the residual between  $\sigma_{ap}^{\text{bulge}}$  and  $\sigma_{ap}^{\text{gal}}$ , for galaxies where we could robustly measure both quantities. For disk galaxies viewed at low inclination,  $\sigma_{ap}^{\text{bulge}}$  is systematically larger than  $\sigma_{ap}^{\text{gal}}$ , a difference that can be as large as 40%.

in Fig. 5.7. For LTGs viewed at high inclination, rotational broadening compensates for the drop of  $\sigma_{\text{spat}}$  on galaxy scales, resulting in a flat  $\sigma_{ap}$  profile. These are the galaxies for which  $\sigma_{ap}^{\text{gal}} \approx \sigma_{ap}^{\text{bulge}}$ . Conversely, if LTGs are observed at low inclination, e.g., NGC 3783, NGC 26717 or Mrk 1511, the high  $\sigma_{\text{spat}}$  in their centers contributes less and less with increasing aperture size, leading to  $\sigma_{ap}^{\text{gal}} < \sigma_{ap}^{\text{bulge}}$ . For individual AGNs in our sample, this effect can be as large as 30% which is the dominant driver behind differing scaling relation inferred from  $\sigma_{\text{spat}}^{\text{gal}}$  vs.  $\sigma_{\text{spat}}^{\text{bulge}}$  (see Sect. 5.5.3).

### 5.7.7 Comparing Stellar and SSP Libraries

To understand the robustness of our kinematic measurements, we have tested if the stellar kinematics are sensitive to the choice of stellar or SSP libraries used for fitting the spectra. In Fig. 5.18, we show the velocity dispersion obtained from fitting AGNs’ PSF-subtracted aperture-integrated spectra across the restframe 4700Å-5700Å wavelength range. We compared the kinematics recovered with templates from M11, Indo-U.S., and XSL. Motivated by the assumption that the light from the bulges of late-type

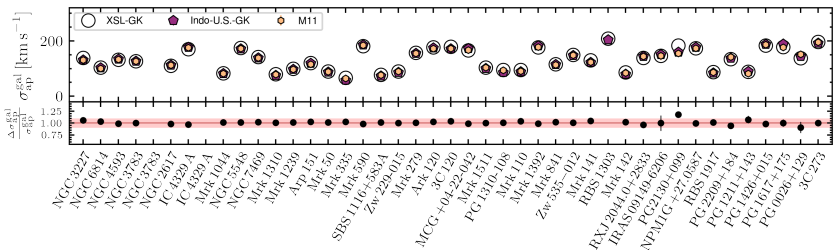


Figure 5.18: *Comparing stellar and SSP libraries for  $\sigma_{ap}$  of individual AGNs.* For each galaxy, we show the aperture-integrated galaxy stellar velocity, color-coded by different template libraries used for the spectral synthesis modeling (see Sect. 5.4.3). The differences between the results small, and typically range between 5 km/s and 10 km/s.

galaxies, and early-type galaxies in general, is dominated by old stars, we also selected subsets of G and K giant stars from the XSL and Indo-U.S. libraries. Specifically, we selected temperatures  $4400 < T_{\text{eff}} < 5000$ , surface gravity  $0.15 < \log(g) < 3.59$ , and metallicity  $-2.5 < [\text{Fe}/\text{H}] < 0.34$ . We refer to these templates as XSL-GK and Indo-U.S.-GK, respectively.

We found that the systematic offsets in  $\sigma$  are typically  $< 10$  km/s and therefore indistinguishable from the nominal uncertainties returned by pPXF. However, we recognized that, on an individual basis, the best-fitting  $\sigma$  can differ by up to 30 km/s. This is predominantly the case for objects for which the spectra have low S/N due to a strong AGN or a faint host galaxy (e.g., PG 2130+099). In these cases, the higher-resolution templates XSL and M11 provide consistent solutions, whereas the lower-resolution template spectra from Indo-U.S. lead to larger uncertainties. Overall, we do not recognize a significant systematic difference when constraining the library to G and K giants, possibly because the aperture covers the entire galaxy disk. However, stellar absorption features of Mg Ib and Fe are better modeled when choosing the full template library. We therefore prefer the XSL library, which we adopted for the spectral synthesis modeling in Sect. 5.4.3.

### 5.7.8 Comparing Spectral Synthesis Modeling Codes

We have tested three different codes for fitting the stellar continuum via stellar population synthesis modeling. We employed `pPXF`, `PyParadise` and `BADASS` which differ in their fitting methodologies. `pPXF` and `PyParadise` fit the stellar continuum emission separately from narrow and broad emission lines, which need to be subtracted first. For the stellar continuum emission, `pPXF` describes large-scale continuum variations with a polynomial, whereas `PyParadise` first normalizes the continuum with a running mean before fitting kinematics with the normalized template spectra. This approach effectively removes non-physical continuum variations caused by PSF subtraction with `QDeblend`<sup>3D</sup>. Since the continuum shape contains important information about the stellar populations (if AGN contamination is negligible), such a normalization removes information contained in the spectra and thus, effectively, reduces the S/N. As expected, we observed that the performance of each code depends on the respective data set. If the dataset covers a large wavelength range, as is the case for the MUSE datasets, `PyParadise` produces more stable results. However, if the analysis is constrained to the wavelength range shared between KCWI, VIMOS, and MUSE, the polynomial used by `pPXF` provides sufficient accuracy to describe the non-physical continuum variations. Moreover, `pPXF` tends to provide better fits at lower S/N compared to `PyParadise`, likely due to the S/N loss during continuum normalization in `PyParadise`. Since our analysis is constrained to the common wavelength range of 4700 Å-5700 Å, we adopted `pPXF` for our study. We note that for individual AGNs, spurious spectral features near the galaxy need to be masked; otherwise, they would dominate the continuum variation modeled with the polynomial (see Fig. 5.3).

The full Bayesian analysis code, `BADASS`, offers a different approach to fitting AGN spectra. Unlike `pPXF` and `PyParadise`, which require the point-like AGN emission to be subtracted first, `BADASS` fits the AGN spectrum, emission line templates and stellar spectra simultaneously. An accurate knowledge of the AGN spectrum, combined with sophisticated coupling of the emission line parameters, allows for the robust inference of emission line and stellar kinematic parameters across the FoV of the IFU. With this method, `BADASS` provides a fundamentally different approach that is independent of the PSF subtraction method. However, running the full MCMC for `BADASS` is time-consuming and fine-tuning for individ-

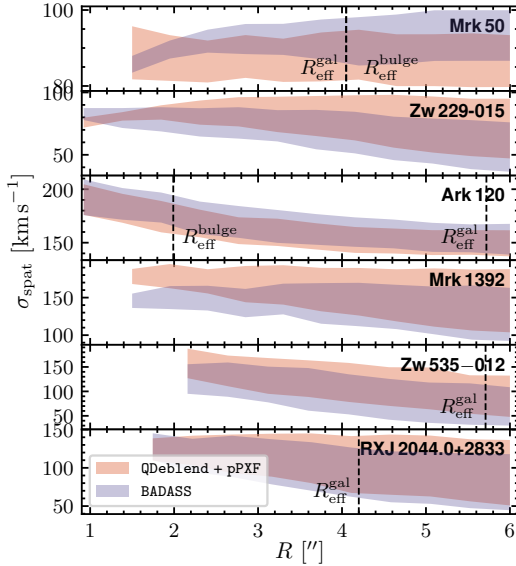


Figure 5.19: *Comparing kinematics extracted using different spectral synthesis modeling codes.* The panels show  $\sigma_{\text{spat}}$  for a subset of AGNs for which the spectra were also fitted by BADASS. Shades indicate the uncertainty range of the kinematic profile, colors indicate the method by which we extracted  $\sigma_{\text{spat}}$ . Dashed lines indicate the bulge and galaxy effective radius. For the range across which we can measure  $\sigma_{\text{spat}}$ , the radial profiles extracted from QDeblend<sup>3D</sup>+pPXF agree within the uncertainties with what we find when using BADASS.

ual AGNs is required, depending on the AGN spectral features, absorption line strength, and spectral masking. The details for individual AGNs will be presented in our companion paper (Remigio et al., 2024, in prep.). Here, we focus solely on the quantitative comparison of the inferred stellar kinematics parameters with those obtained using pPXF. Fig. 5.19 shows the radial behavior of  $\sigma_{\text{spat}}$  for a subset of AGNs (chosen for good coverage within the effective radius to compare radial trends). (Note that the same trends found for this subset also hold for a larger sample which will be presented in (Remigio et al., 2024, in prep.)) Within the range where we can robustly measure  $\sigma_{\text{spat}}$ , the radial profiles extracted from

QDeblend<sup>3D</sup>+pPXF are in agreement within the uncertainties. This suggests that the two independent methods provide consistent results, regardless of the distance from the AGN. We conclude that the method used to measure the stellar kinematics in Sect. 5.4.3 is robust. Furthermore, the nominal uncertainties returned by pPXF do not systematically underestimate the systematic uncertainties induced by the PSF subtraction with QDeblend<sup>3D</sup>

---

# Summary and Outlook

This chapter provides a summary and evaluation of the results presented in this thesis. Based on the exceptional pilot studies, I led a large team with which I submitted observing proposals for VLT/MUSE. They were recently approved for execution beginning in ESO Period 114. I will give a brief overview of the planned observations and discuss the scientific progress that can be expected from these datasets.

## Chapter 6 | Summary and Outlook

### 6.1 Summary and Interpretation of Main Results

In the previous four chapters, I took two different approaches to obtain a comprehensive understanding of the AGN-host-galaxy connection at high black hole accretion rates. Gas in- and outflows and the  $M_{\text{BH}}$ -host-galaxy scaling relations have been investigated using state-of-the-art observational techniques, including optical IFU spectroscopy, high-resolution imaging, and spectroscopic imaging of CO emission.

The pilot studies of two luminous type 1 AGNs, conducted with high angular resolution MUSE NFM setup are among the first objects targeted with this specific instrument configuration. The data reduction and optimisation required special attention, as detailed in Chapter 2. An important lesson learned is that while 3D spectroscopy is a powerful tool, the interpretation of the results necessitates a thorough understanding of the preceding data analysis. Specifically for extracting host galaxy properties in the centre of Mrk 1044, close to the luminous unobscured AGN, a detailed understanding of the 3D PSF shape (Sect. 2.2.4), instrument characteristics (Sect. 2.2.1), and emission line diagnostics (Sect. 2.3.2) is crucial for measuring robust emission line fluxes. As the emission line strengths can significantly impact the diagnostic tools to infer the excitation mechanism, reddening and star formation rates, the scientific conclusions depend on an accurate treatment of the data. Specific to the MUSE NFM data set of Mrk 1044, I developed and tested the spectroastrometric routine `Siena`<sup>3D</sup> to spatially locate kinematic emission-line components with sub-pixel accuracy. This technique revealed a compact outflow that is launched from the highly accreting AGN. However, its exact geometric alignment remains uncertain, as cross-identifying the [O III]-emitters with Ly $\alpha$ -absorbers in a 3D toy model did not resolve the degeneracy. Interestingly, the circumnuclear star formation, even on  $\sim 100$  pc scales, appears unaffected, in contrast to what is usually seen in type 1 AGNs. These findings allowed me to draw a comprehensive picture about Mrk 1044's nature, summarised at the end of Chapter 3, where the small 2D extent of the outflow is either a coincidental projection effect or it is intrinsically

compact. The latter explanation supports the hypothesis of a young AGN, consistent with the often-discussed evolutionary scenario of NLS1 galaxies. Ruling out the former hypothesis, however, can only be done conclusively with larger samples where inclination effects can be corrected statistically.

In Chapter 4, the same observing technique revealed that in NGC 4593 star formation is concentrated along a single-arm spiral. This spiral is also visible in dust absorption, and remarkably pronounced in molecular gas emission. Despite the abundance of gas, star formation is inefficient, possibly due to shear forces acting onto the gas, preventing its dynamical relaxation. A kinematic analysis revealed gas mass inflow rates that are large enough to sustain the central SMBH accretion rate of a few percent of the Eddington limit over several tens of million of years, potentially allowing for substantial growth of the central SMBH. While our team is currently exploring the exact mechanism behind the single-arm structure, it is clear that galaxy-intrinsic processes are responsible for driving the gas inflow on sub-kiloparsec scales. In this context, NGC 4593 provides a compelling example of how secularly evolving galaxies can fuel their AGNs if high gas densities are present in their centres.

The cumulative effects of AGN feeding and feedback are suspected to be reflected in the host galaxy scaling relations, which were the focus of Chapter 5. Based on a sample of type 1 AGNs with dynamically measured BH masses, our team conducted five different observing programs to collect IFU data for a re-calibration of the  $M_{\text{BH}}-\sigma_*$  relation in local AGNs. The uniqueness of this work lies in the sample of independently measured  $M_{\text{BH}}$ , which are free of assumptions regarding the virial factor  $f$ . Moreover, our sample extends to luminous AGNs hosting massive BHs, a regime lacking in previous calibrations. While the inevitable heterogeneity of the observational datasets presents technical challenges, this diversity ultimately turns out as a strength: We were able to demonstrate for the first time, that when selection effects are accounted for, the underlying  $M_{\text{BH}}$ -host-galaxy scaling relations between AGNs and the quiescent galaxy population are identical. Previous calibrations of the AGN's  $M_{\text{BH}}-\sigma_*$  relation *assumed* that AGNs follow the same scaling relations as their quiescent counterparts to determine the sample-average virial factor  $\langle f \rangle$ . In this context, our results reinforces this "classical" approach of using AGNs'  $M_{\text{BH}}-\sigma_*$  relation to estimate a sample-average  $\langle f \rangle$ .

## 6.2 Future Prospects

### 6.2.1 BH-mass-host-galaxy Scaling Relations

#### Host Galaxy Properties

Improved measurements of host galaxy properties in AGNs can be achieved via at least two approaches. First of all, for the Keck subset of AGNs in the sample from Chapter 5, more data are available, as the observations were complemented by the novel KCRM, the red arm of the KCWI instrument. We selected the configuration to cover the CaT lines, which are, in principle, the cleanest diagnostic feature for stellar kinematics, as they typically suffer from less contamination from AGN continuum or broad lines (Greene & Ho, 2006; Harris et al., 2012). However, in practice, the CaT lines in our observations were swamped by sky emission lines, which varied on timescales shorter than a single exposure. Consequently, the sky subtraction left severe residuals that made measurements of  $\sigma_*$  impossible. Accurate subtraction or correction for these issues is not implemented in any of the current data reduction pipelines. While we experimented with different approaches, they were only successful under specific conditions, such as when empty sky region are contained within the science exposure. Since this condition is met only for a few cases, we decided to abandon the use of CaT as a diagnostic for the sake of consistency. In a future project, it can be explored further to what extent sky subtraction can be improved and whether the introduced systematic uncertainties can be minimised. If successful, this might enable more precise  $\sigma_*$  measurements in our AGN sample.

Second, an obvious next step is to extend our analysis presented in Chapter 5 to quiescent galaxies, to address questions such as: What are the spatial scales on which host galaxy properties correlate the closest with BH mass? And does this scale have a physical interpretation? Datasets to address these questions are publicly available from the ATLAS<sup>3D</sup> survey and ESO Prog.ID 094.B-0298(A) (PI: Walcher) and represent an urgent objective that needs to be pursued.

Third, the AGN sample can be expanded by including AGNs that host megamasers. In these galaxies, stimulated emission from Keplerian circumnuclear H<sub>2</sub>O molecular gas traces the motion of material within <1 pc of the BH. If the distance to the galaxy is known, dynamical modelling

of the disc’s motion provides an independent method for measuring  $M_{\text{BH}}$ . Previous studies suggest that megamasers are offset towards lower  $M_{\text{BH}}$  values in the  $M_{\text{BH}}-\sigma_*$  plane (e.g., [Greene et al., 2016](#)). To test this result, our team is currently developing a proposal to follow up on the megamaser sample observed with Keck/KCWI. These galaxies are typically nearby, within several to several tens of Mpc, and are classified as type 2 AGNs. Their angular extent is much larger, and they lack broad line emission, which may present different technical challenges. However, this also offers the opportunity for a more detailed investigation of how aperture sizes affect the  $M_{\text{BH}}-\sigma_*$  scaling relation.

### Black Hole Masses in AGNs

Over the past decade, the primary method for measuring BH masses more precisely has been high-cadence RM. Large-scale RM surveys such as (OzDES [Yuan et al., 2015](#)), or SDSS-RM ([Shen et al., 2015, 2024](#)) continue to increase the  $M_{\text{BH}}$  dynamical range and sample sizes via classical RM, but the data quality is too low to measure velocity-resolved lags. On the other hand, the campaigns dedicated to achieve independent measurements of  $M_{\text{BH}}$  are intensive in terms of observations, organisation and data modelling. Recent progress has been made on the data modelling front, particularly with the development of CAMEL-GAS ([Williams & Treu, 2022](#)), which offers a more physical description of the gas distribution in the BLR by incorporating a photoionization approximation to more accurately reproduce the BLR emissivity distribution, rather than assuming constant emissivity. This represents a first step towards modelling lags from several emission lines simultaneously, obtaining an even better model of the BLR gas properties. Data sets are already available for a few objects e.g., NGC 5548 ([De Rosa et al., 2015](#)) and Mrk 817 ([Kara et al., 2021](#)). Due to the complexity of RM campaigns and the data analysis, independent BH mass estimates have been published slowly, typically one or a few at a time. Consequently, AGNs with independently measured  $M_{\text{BH}}$  from RM are mostly  $10^7 - 10^8 M_{\odot}$  regime, which poses a significant limitation to the calibration of the  $M_{\text{BH}}$  scaling relations. As the BLR lags scale linearly with BH mass ( $\propto M_{\text{BH}}$ ), and with cosmological time dilation  $\propto (1+z)$ , already now RM campaigns devour a lot of resources, including both observational facilities and personnel involved in the projects. Pushing this towards the highest-mass BHs,  $>10^8 M_{\odot}$ , and to higher redshift

requires monitoring over several years, up to decades (Wang et al., 2020; Woo et al., 2024). Extending this to even higher  $M_{\text{BH}}$  for a statistical sample seems unfeasible.

Progress can be anticipated from the GRAVITY+ instrument, which is currently being implemented at the VLTI. The addition of laser guide star facilities and AO systems to all Unit Telescopes, infrastructure developments, and upgrades to the phase reference star system will significantly improve its sensitivity and spatial resolution. This will enable independent  $M_{\text{BH}}$  measurements across cosmic time for a statistical sample of luminous AGNs, complementary to what has been explored with RM so far. While the current sample of six AGNs used the VLTI for approximately 20 nights, the projected number of observable AGNs is expected to be “hundreds for  $z < 0.3$ , a hundred at  $z \approx 0.8 - 1$ , and a good dozen QSOs at  $z \approx 2$ ” (GRAVITY+ white paper, but see also Gravity+ Collaboration et al., 2022). While these objectives will have to compete for time allocation, the AGN-host-galaxy coevolution is one of the key scientific goals for which the instrument was designed. It is expected that there will be significant interest by the community in  $M_{\text{BH}}$  measurements of luminous AGNs, which will directly contribute to refining our understanding of  $M_{\text{BH}}$ -host galaxy scaling relations across cosmic time.

### 6.2.2 Resolving the Role of NLS1s in AGN Evolution

PI: Nico Winkel  
 CoIs: Stefanie Komossa, Vardha N. Bennert, Julia Scharwächter, Knud Jahnke  
 Status: ESO Phase 2 approved

The single-case study of the NLS1 galaxy Mrk 1044 provided many insights. However, the inclination correction needed to obtain intrinsic outflow sizes can only be done statistically, and discussing AGN evolution based on only a single object is inconclusive. Scharwächter et al. (2017) spatially resolved five low-redshift NLS1 galaxies, three of which show lower specific SFRs than typical galaxies. Another three NLS1s have been observed with MUSE WFM as part of CARS. However, a key finding from Chapters 2 and 3 is that fuelling and outflow signatures are likely hidden in the sub-kpc volume, which these observations do not resolve. At this point, high angular resolution IFU observations, of a representative sample are required. The only other object for which this has been obtained

is the NLS1 prototype IZw1, which has also been observed with MUSE NFM (Prog.ID 0103.B-0572A, PI: Kawaguchi).

Based on the two pilot studies, IZw1 and Mrk 1044, I developed a proposal for observing time with VLT/MUSE NFM. The sample size was chosen to distinguish the NLS1 population from the overall AGN population in each of the diagnostic plots (Fig. 6.1). Detecting an offset in the  $M_{\text{BH}}-\sigma$  relation is particularly challenging: To statistically confirm an offset of  $>40\text{km/s}$  from the relation at  $3\sigma$  significance, we require a minimum of 15 objects. We apply a joint homogeneous selection from the 6dFGS NLS1 catalogue (Chen et al., 2018) complemented by nearby NLS1s from Véron-Cetty & Véron (2010), considering atmospheric constraints and target visibility. Both parent samples exclusively contain spectroscopically confirmed nearby NLS1s. Our final sample contains 15 NLS1s, including the well-studied examples like Ton S 180 and Mrk 896. The three main open questions that can be immediately tested with such observations are

1. What are the mechanisms that fuel NLS1s? With MUSE NFM we will systematically constrain the orientation, circumnuclear kinematics, turbulence and SFRs. Our hypothesis is that NLS1s exhibit significant circumnuclear SFR and/or dynamical disturbance to power the high BH accretion rates (see discussion in Chapter 2, Fig. 6.1 a).
2. Do NLS1s show signatures of AGN feedback? With a representative census of NLS1 outflows, we can test whether the present-day high accretion rate of NLS1s can be directly connected to the outflow morphologies, densities, and energetics. As confirmed for Mrk 1044 and IZw1, NLS1s seem to systematically lack or have smaller ENLRs (Husemann et al., 2008). A representative census of their resolved ENLRs allows locating the NLS1s along the ENLR-size-AGN-lifetime relation (Fig. 6.1 b, Husemann et al. 2022).
3. Are NLS1 galaxies offset from the  $M_{\text{BH}}-\sigma_*$  relation? Based on the deep pilot observations of IZw1 and Mrk 1044, I was able to show that it is technically possible to measure  $\sigma_*$  even in the very centres of the brightest NLS1. Achieving this for a statistically meaningful sample would allow comparing the  $M_{\text{BH}}-\sigma_*$  relation of NLS1s with that of the overall AGN population (Fig. 6.1 c), for which conflicting

results have been published in the past (e.g., Komossa & Xu 2007a; Rakshit & Woo 2018 vs. Woo et al. 2015)

Each of the objectives 1-3 directly tests how NLS1s are distinct compared to the overall AGN population. Combined, this will help justifying or rejecting their interpretation as "young" AGNs, with under-massive but rapidly growing SMBHs that have not yet self-regulated the BH accretion through AGN feedback. The proposal was recently accepted by the ESO Observing Programmes Committee (OPC), and 64 hours of observing time at VLT UT4 have been allocated. I recently completed Phase 2 preparations, and service mode observations are scheduled to begin in October 2024.

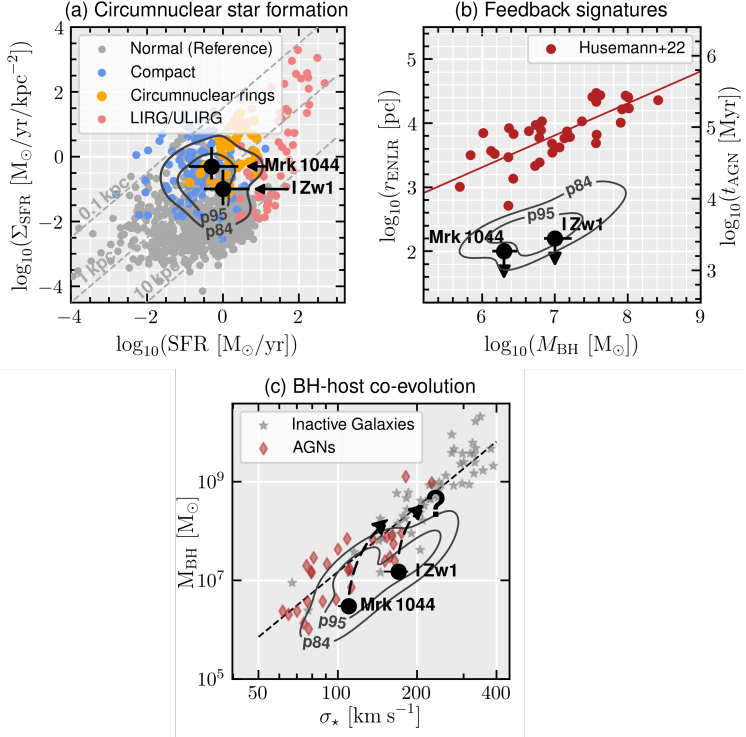


Figure 6.1: Three critical tests for how NLS1s may be different from other AGNs, demonstrated for NFM-pilot-observations of Mrk 1044 and 1 Zw1. (Left) There is tentative evidence for a systematically higher  $\Sigma_{\text{SFR}}$  in the NLS1s’ circumnuclear regions, which requires confirmation and tests against model predictions (e.g. Volonteri et al. (2015)). (Centre) ENLR-size-BH-mass relation, which can be interpreted as relation between AGN-lifetime and BH mass. NLS1s seem to drastically diverge from this relation, which requires confirmation from a representative sample. (Right) Locating and tracking the evolution along the  $M_{\text{BH}}-\sigma$  relation; this programme will statistically confirm whether NLS1s harbour under-massive BHs (e.g. Komossa & Xu (2007b)). The grey contours in each panel show the expected distribution of NLS1s. The proposed sample is required to statistically constrain the offsets, and thereby confirm (or reject) the three hypotheses outlined in the immediate objective.

### 6.2.3 The VLT Large Programme TENSION-QSO: A Comprehensive Census of Gas Flows in Nearby Quasars

PI:	Nico Winkel
CoIs:	Knud Jahnke, Françoise Combes, Montserrat Villar-Martín, Vardha N. Bennert, Vincenzo Mainieri, Enrico Piconcelli, Vivian U. Justus Neumann, Miguel Pérez Torres, Tanya Urrutia, Julia Scharwächter, Massimo Gaspari, Hans-Walter Rix, Rebecca McElroy, Mainak Singha, Bryan Terrazas, Aaron Barth, Grant Tremblay, Timothy Davis, Eric Rohr, Eduardo Bañados
Contributors:	Rationale initiated by Bernd Husemann
Status:	ESO Phase 2 approved

As touched upon in Chapter 1, theory and observations agree that feeding and feedback processes related to SMBH growth are a vital ingredient to galaxy evolution. However, galaxy formation theory is running into a problem: Along with other baryonic processes, AGN feeding and feedback develop on scales that cannot be resolved in cosmological simulations. The complex processes are treated via sub-grid recipes for which numerous implementations in cosmological simulations are degenerate (Hopkins & Quataert, 2010a; Oppenheimer et al., 2021; Habouzit et al., 2021). In recent years, the collaborations behind most cosmological simulations have moved to simulating larger volumes, whereas the development of small-scale baryonic feedback descriptions is limited by missing observational constraints (e.g., Pakmor et al. 2023; Nelson et al. 2023; Schaye et al. 2023). Instead, a bottom-up approach via hydrodynamic simulations resolving micro-scale physical processes, first in isolated boxes and then scaling up, has proven to be a successful strategy (Gaspari et al. 2020, for a review). From an observational perspective, the detailed mechanisms involved in QSO feedback and their relative importance remain highly debated. Resolving AGN feeding and feedback in QSOs, the brightest AGNs, is imperative, but has been difficult due to limited spatial resolution and the overwhelming brightness of the central source. This is unfortunate, since QSOs harbour SMBHs accreting at high rates, thus, they are sites where the phenomena of rapid SMBH growth can be observed. Resolving SMBH feeding and feedback processes and their interplay with star formation and stellar feedback, is crucial for informing the next generation of cosmological and isolated zoom-in simulations. The diversity of processes involved in QSO feeding

and feedback that have been spatially resolved in QSOs are demonstrated by several pilot studies (e.g., Marasco et al. 2021; Travascio et al. 2024, Chapter 2 and 3 of this thesis). Accessing a large number of QSOs observationally across a wide dynamic range of spatial scales is essential to break the current degeneracies between sub-grid models.

To study a sample of highly accreting SMBHs in great detail, I am the PI of a project with 22 international co-investigators: TENSION-QSO is a VLT/MUSE legacy survey of a spectroscopically complete sample of 48 low- $z$  QSOs. While the MUSE WFM will map the entire galaxies, the NFM offers spectroscopy with a unique spatial resolution of 50–100 mas at optical wavelengths (Fig. 6.3). We selected the sample from the Hamburg/ESO Survey (HES) QSO catalogue, which is spectroscopically 99% complete with well-defined  $B$  band flux limits. It represents the most unbiased sample of unobscured QSOs suitable for observations with the VLT (Wisotzki et al., 2000). The selection is further refined by criteria such as low declination from Paranal to ensure the functionality of the adaptive optics system, redshift cuts to achieve the desired spatial resolution and ensure that the critical emission lines remain observable, and the RA range blocked by ongoing large programmes and guaranteed-time observations. The final sample contains 48 QSOs, the largest sample of bright spectroscopically-confirmed low- $z$  QSOs observable with MUSE NFM (Fig. 6.2).

Our immediate scientific objectives related to BH fuelling include resolving gas inflow signatures in individual QSOs using established diagnostic tools such as BPT diagrams, kinematic plots, condensation ratios, and torque profiles. These analyses will help constrain the circumnuclear kinematics, turbulence, sSFR, and geometric orientation of QSOs. Additionally, we aim to assess the presence or absence of dynamic features like nuclear bars, spirals, and chaotic cold accretion that may drive inflows down to parsec scales. The overarching goal is to link these properties with BH accretion rates, providing direct tests for theoretical models and thereby distinguishing between different scenarios that explain QSO spectral properties, such as AGN evolution, or the influence of environment and fuelling mechanisms. In terms of QSO feedback, our goal is to resolve and characterise ionized gas outflows. We will compare their sizes, radial velocity profiles, geometry, and gas densities with predictions from

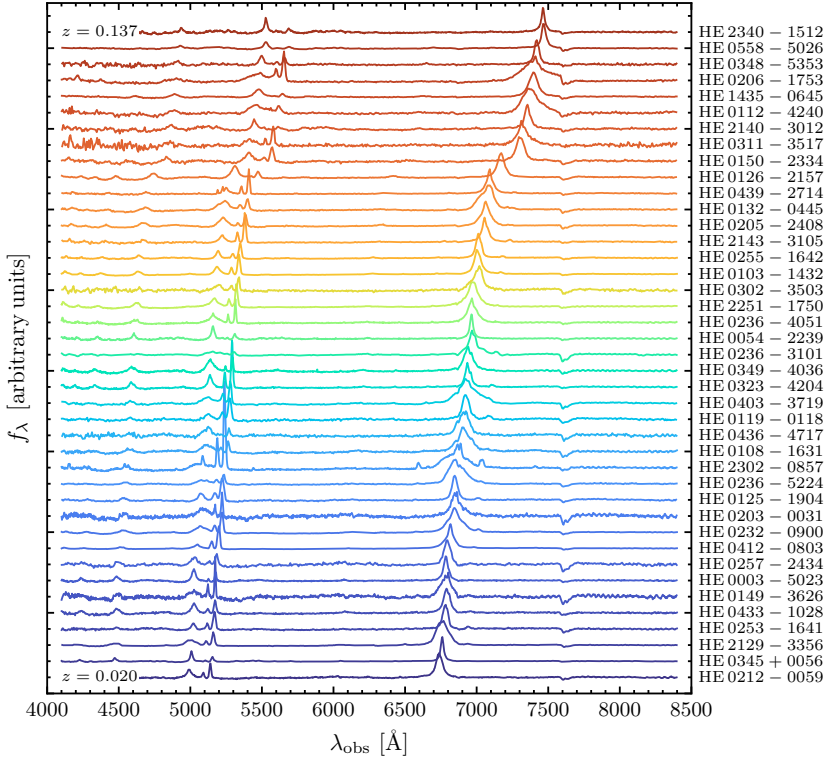


Figure 6.2: *HES Spectroscopy of the TENSION-QSO sample.* QSOs are ordered by redshift. Already in the relatively low spectral resolution and S/N, it is evident that the targets show a variety of broad-line structures, and [O III] strengths, suggesting a large variety in EELR and outflows properties. In some cases the [S II] line doublet is pronounced, indicating star formation. The HES original data has been shared by Dr. Andreas Schulze and Prof. Lutz Wisotzki (priv. communication).

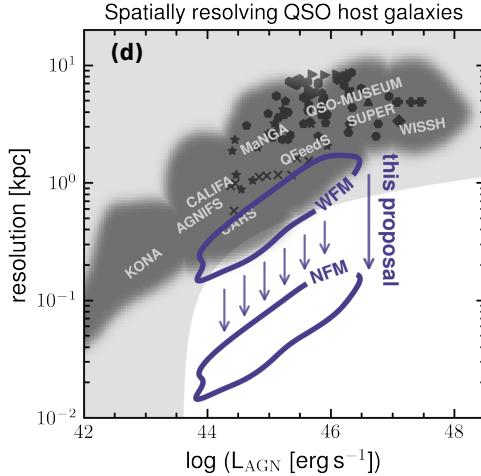


Figure 6.3: *TENSION-QSO* survey versus previous type 1 AGNs studies in AGN luminosity and spatial resolution. Individual object studies (black symbols) and surveys (grey shades) have either resolved nearby low-L AGNs, or higher- $z$  luminous QSOs at substantially lower spatial resolution, which have left more than one order of magnitude uncertainty for essential diagnostics of gas in- and outflows. With the *TENSION-QSO* survey we will access a completely unexplored regime, for the first time resolving QSO host galaxies at  $\sim 100$  pc scales.

theoretical models to better understand outflow propagation through the host galaxy’s ISM. Furthermore, spatially resolved diagnostics will reduce uncertainties in global properties like mass outflow rates and energetics, enabling us to precisely quantify the cumulative impact of the QSO phase on their host galaxies. For systems in which the outflow remains unresolved even by MUSE NFM, a spectroastrometric analysis will enable the measurement of their location, sizes and energetics (see Chapter 3). If contrary to our expectation, multiple QSOs in the sample exhibit similarly compact outflows, the outflow expansion timescales  $< 10^5$  yr allow to statistically constrain the connection between outflow properties and the BH accretion state, and test model predictions for the duration of the QSO phase. In addition to our immediate objectives, the *TENSION-QSO* survey will serve as a benchmark for other QSO studies. Ancillary sci-

ence cases include, e.g., interaction of QSOs with the CGM, identifying changing-look AGN, testing accretion disk and dust torus models, discovery of dual AGN, and interpreting QSOs in the light of recent ALMA and JWST discoveries.

In July 2024, the ESO OPC approved our proposal as a large programme, with 149 h allocated at VLT/UT4 (Yepun). I prepared ESO P114 the Phase 2 material for the first MUSE runs 114.27KU.002 (WFM) and 114.27KU.001 (NFM), which have recently been approved by ESO. Service mode observations will start this autumn, and will extend over the next two years to complete the programme. The TENSION-QSO survey will offer a comprehensive view of QSO feeding and feedback characteristics on scales ranging from 10 pc to several 10 kpc. With such a rich database, I will address long-standing questions of SMBHs growth and their influence on their host galaxies. It will serve as a reference for QSO studies in the coming decade.

### 6.3 Closing

Sixty years after the discovery of supermassive black holes, research has expanded beyond understanding the AGN phenomenon to exploring the origin of black holes and their role in galaxy formation and evolution. The complexity of the physical processes involved requires studies across all spatial scales, including the very centres of AGN host galaxies. We live in an exceptional historical period for pursuing this goal. Rapid technological developments, upgrades to world-leading observatories, and a dedicated scientific community are continuously pushing the boundaries of human understanding. The high-angular resolution spectroscopy explored in this thesis, along with developments in multi-wavelength, multi-messenger, and time-domain observations, pave the way for exciting advances in black hole research. As new ideas continue to emerge, the future holds even greater promise.

# Abbreviations

<b>ACS</b>	Advanced Camera for Surveys
<b>AGN</b>	Active galactic nucleus
<b>ALMA</b>	Atacama Large Millimeter/submillimeter Array
<b>ADC</b>	Atmospheric Dispersion Corrector
<b>AO</b>	Adaptive optics
<b>BAT</b>	Swift-Burst Alert Telescope
<b>BHMF</b>	Black Hole mass function
<b>BLR</b>	Broad line region
<b>BLS1</b>	Broad line Seyfert 1
<b>BH</b>	Black Hole
<b>BHAR</b>	Black Hole accretion rate
<b>BPT</b>	Baldwin, Phillips & Terlevich
<b>CARS</b>	Close AGN Reference Survey
<b>CCA</b>	Chaotic cold accretion
<b>CGM</b>	Circumgalactic medium
<b>CaT</b>	Ca II triplet
<b>CNE</b>	Circumnuclear ellipse
<b>CNR</b>	Circumnuclear region
<b>cRM</b>	Classical reverberation mapping
<b>DAR</b>	Differential atmospheric refraction
<b>EELR</b>	Extended emission line region
<b>ENLR</b>	Extended narrow line region
<b>ESO</b>	European Southern Observatory
<b>ERDF</b>	Eddington ratio distribution function
<b>ETG</b>	Early-type galaxy
<b>EV1</b>	Eigenvector 1
<b>FIR</b>	Far-infrared
<b>FoV</b>	Field of view
<b>FWHM</b>	Full width at half maximum
<b>HES</b>	Hamburg/ESO Survey
<b>HST</b>	Hubble Space Telescope
<b>HRC</b>	High Resolution Channel

- ICM** Intracluster medium
- IGrM** Intergroup medium
- IFU** Integral Field Unit
- ILR** Inner Lindblad resonance
- IMF** Initial mass function
- IR** Infrared
- ISM** Interstellar medium
- JWST** James Webb Space Telescope
- KCWI** Keck Cosmic Web Imager
- LAMP** Lick AGN Monitoring Project
- LINER** Low-ionization nuclear emission region
- LOSVD** Line-of-sight velocity distribution
- LTG** Late-type galaxy
- mas** Milliarsecond
- MCMC** Markov chain Monte Carlo
- MUSE** Multi Unit Spectroscopic Explorer
- NED** NASA/IPAC Extragalactic Database
- NFM** Narrow Field Mode
- NIR** Near-Infrared
- NLR** Narrow line region
- NLS1** Narrow line Seyfert 1
- OPC** Observing Programmes Committee
- PA** Position angle
- PCA** Principle component analysis
- PSD** Power spectral density
- PSF** Point-spread function
- QSO** Quasi-stellar object
- RM** Reverberation mapping
- RMS** Root mean square
- SF** Star formation
- SFE** Star formation efficiency
- SFR** Star formation rate
- SFRD** Star formation rate surface density
- SMBH** Supermassive Black Hole
- SNe** Supernovae

<b>S/N</b>	Signal to noise ratio
<b>SDSS</b>	Sloan Digital Sky Survey
<b>SB</b>	Surface brightness
<b>SE</b>	Single epoch
<b>SED</b>	Spectral energy distribution
<b>SoI</b>	Sphere of influence
<b>SSP</b>	Simple stellar population
<b>STIS</b>	Space Telescope Imaging Spectrograph
<b>UFO</b>	Ultrafast outflow
<b>ULIRG</b>	Ultra-luminous infrared galaxy
<b>UV</b>	Ultraviolet
<b>UT</b>	Unit Telescope
<b>VIMOS</b>	Visible Multi Object Spectrograph
<b>VLA</b>	Karl G. Jansky Very Large Array
<b>VLT</b>	Very Large Telescope
<b>VLTI</b>	Very Large Telescope Interferometer
<b>WFC3</b>	Wide Field Camera 3
<b>WFM</b>	Wide Field Mode
<b>XSL</b>	X-shooter Spectral Library

# List of Figures

1.1	AGN Spectral Energy Distribution	5
1.2	AGN Unification Models	8
1.3	Centaurus A and AGN feedback	14
1.4	Spatial and Temperature Scales of AGN feedback	16
1.5	Outflow Coupling to ISM	17
1.6	BH Growth in the First Gigayear	20
2.1	Mrk 1044 Hots Galaxy Overview	33
2.2	MUSE DAR Correction	34
2.3	MUSE NFM-AO PSF Modelling	37
2.4	Hybrid PSF Construction	39
2.5	AGN-Host Deblending	41
2.6	PyParadise Example Fit	43
2.7	Ionised Gas Fluxes	45
2.8	Ionised Gas Kinematics and BPT	47
2.9	Circumnuclear Star Formation Map	50
2.10	Gas and Stellar Velocity Fields	53
2.11	Gas versus Stellar Residual Velocity Field	56
2.12	Residual Gas Velocity	57
2.13	Tilted Ring Modelling Parameters	58
2.14	Star Formation versus BH Accretion Rate	60
2.15	Gas Phase Metallicity	63
3.1	AGN Spectrum Modelling	76
3.2	Spectroastrometry	79
3.3	Nuclear Host Galaxy Spectrum	82
3.4	Compact Radio Emission	84
3.5	UV Spectrum Modelling	85
3.6	BPT Diagnostics of the Extended Outflow	88
3.7	Illustration of Geometric Outflow Alignment	91
3.8	Kinematic Plot	97
3.9	Outflow Scaling Relations	99
3.10	Outflow Projected Size	105
3.11	Expanding Shell Model Illustration	107
3.12	Behaviour of the Model Parameters with Inclination	108
3.13	Best-fitting Geometric Model	110

---

4.1	NGC 4593 Host Galaxy Overview . . . . .	117
4.2	BPT and Star Formation . . . . .	120
4.3	Kinematic Modelling with KinMS . . . . .	122
4.4	Gas Density and Torque Map . . . . .	126
4.5	Time Evolution of the Torque Field . . . . .	127
4.6	Radial Mass Inflow Rates . . . . .	128
4.7	Radial Gas Depletion Timescales . . . . .	131
4.8	Kinometry Modelling . . . . .	136
5.1	Gallery Continuum Images . . . . .	152
5.2	AGN Parameters of the Sample . . . . .	159
5.3	Spatially Resolved Spectral Synthesis Modelling . . . . .	161
5.4	Gallery Stellar Kinematic Maps . . . . .	163
5.5	Radial Profile of the Resolved Dispersion . . . . .	165
5.6	Comparison of Methods for Measuring $\sigma$ . . . . .	166
5.7	Aperture Correction . . . . .	173
5.8	Aperture-integrated versus Spatially resolved $\sigma$ . . . . .	177
5.9	$M_{\text{BH}} - \sigma$ Parameters as Function of Aperture Size . . . . .	183
5.10	$M_{\text{BH}}$ -host-galaxy scaling relations . . . . .	185
5.11	Corner Plot of the Model Parameter Posterior Distribution . . . . .	187
5.12	Example of AGN Spectral Modelling . . . . .	193
5.13	Effect of AGN-host Deblending . . . . .	196
5.14	Comparing Methods for Measuring $\sigma$ in MCG +04-22-042 . . . . .	197
5.15	Comparison of different Datasets . . . . .	200
5.16	Comparing the Impact of Different Diagnostic Features . . . . .	202
5.17	Testing the Impact of Aperture Size . . . . .	203
5.18	Comparison between SSP and Stellar Libraries . . . . .	204
5.19	Impact of different Spectral Synthesis Modelling Codes . . . . .	206
6.1	Tests for NLS1s versus AGN population . . . . .	216
6.2	TENSION-QSO HES Spectroscopy . . . . .	219
6.3	Comparison TENSION-QSO versus Previous Surveys . . . . .	220

# List of Tables

2.1	PSF Model Parameters	38
3.1	AGN Spectrum Parameters	77
3.2	Spectroastrometry Results	78
3.3	Summary of Diagnosed Outflows	86
3.4	Outflow Energetics	93
4.1	CO Kinematic Modelling with KinMS	123
5.1	Black Hole Masses	147
5.2	IFU Observational Parameters	150
5.3	Host Galaxy Parameters	157
5.4	Stellar Velocity Dispersion Measurements	168
5.5	Scaling Relations Results	179
5.6	AGN Parameters	194

# Publication List

## Author's Publications Included in This Thesis

- Winkel, N., Bennert, V. N., Remigio, R. P., et al. 2024, *ApJ*, submitted to the journal
- Winkel, N., & Singha, M. 2022, *Siena3D*
- Winkel, N., Husemann, B., Davis, T. A., et al. 2022, *A&A*, 663, A104
- Winkel, N., Husemann, B., Singha, M., et al. 2023, *A&A*, 670, A3

## Complete List of Publications

- Brogan, R., Krumpe, M., Homan, D., et al. 2023, *A&A*, 677, A116
- McElroy, R., Singha, M., Husemann, B., et al. 2022, *The Messenger*, 187, 3
- Singha, M., Winkel, N., Vaddi, S., et al. 2023, *ApJ*, 959, 107
- Smirnova-Pinchukova, I., Husemann, B., Davis, T. A., et al. 2022, *A&A*, 659, A125
- Winkel, N., Pasquali, A., Kraljic, K., et al. 2021, *MNRAS*, 505, 4920

# Bibliography

- Akritas, M. G., & Bershady, M. A. 1996, *ApJ*, 470, 706
- Alonso, M. S., Coldwell, G., & Lambas, D. G. 2013, *A&A*, 549, A141
- Angel, J. R. P., & Stockman, H. S. 1980, *ARA&A*, 18, 321
- Anglés-Alcázar, D., Faucher-Giguère, C.-A., Quataert, E., et al. 2017, *MNRAS*, 472, L109
- Ann, H. B., Seo, M., & Ha, D. K. 2015, *ApJS*, 217, 27
- Antonucci, R. 1993, *ARA&A*, 31, 473
- Athanassoula, E., Romero-Gómez, M., Bosma, A., & Masdemont, J. J. 2009, *MNRAS*, 400, 1706
- Azadi, M., Aird, J., Coil, A. L., et al. 2015, *ApJ*, 806, 187
- Baade, W., & Minkowski, R. 1954, *ApJ*, 119, 206
- Bacon, R., Accardo, M., Adjali, L., et al. 2010, *SPIE Conf. Ser.*, 7735, 8
- Bacon, R., Vernet, J., Borisova, E., et al. 2014, *The Messenger*, 157, 13
- Bacon, R., Conseil, S., Mary, D., et al. 2017, *A&A*, 608, A1
- Bae, H.-J., & Woo, J.-H. 2016, *ApJ*, 828, 97
- Bahcall, J. N., Kirhakos, S., Saxe, D. H., & Schneider, D. P. 1997, *ApJ*, 479, 642
- Bailey, J. 1998, *MNRAS*, 301, 161
- Baldi, R. D., Capetti, A., Robinson, A., Laor, A., & Behar, E. 2016, *MNRAS*, 458, L69
- Baldwin, J. A., Phillips, M. M., & Terlevich, R. 1981, *PASP*, 93, 5
- Barnes, J. E., & Hernquist, L. 1996, *ApJ*, 471, 115
- Barth, A. J., Nguyen, M. L., Malkan, M. A., et al. 2011, *ApJ*, 732, 121
- Barth, A. J., Bennert, V. N., Canalizo, G., et al. 2015, *ApJS*, 217, 26
- Baskin, A., & Laor, A. 2005, *MNRAS*, 358, 1043
- Batiste, M., Bentz, M. C., Manne-Nicholas, E. R., Onken, C. A., & Bershady, M. A. 2017a, *ApJ*, 835, 271
- Batiste, M., Bentz, M. C., Raimundo, S. I., Vestergaard, M., & Onken, C. A. 2017b, *ApJ*, 838, L10
- Baum, S. A., Gallimore, J. F., O’Dea, C. P., et al. 2010, *ApJ*, 710, 289
- Beifiori, A., Courteau, S., Corsini, E. M., & Zhu, Y. 2012, *MNRAS*, 419, 2497
- Bellovary, J. M., Holley-Bockelmann, K., Gültekin, K., et al. 2014, *MNRAS*, 445, 2667
- Bennert, V. N., Auger, M. W., Treu, T., Woo, J.-H., & Malkan, M. A. 2011, *ApJ*, 726, 59
- Bennert, V. N., Winkel, N., U, V., et al. 2024, in prep.
- Bennert, V. N., Treu, T., Auger, M. W., et al. 2015, *ApJ*, 809, 20

- Bennert, V. N., Treu, T., Ding, X., et al. 2021, *ApJ*, 921, 36
- Benson, A. J., Bower, R. G., Frenk, C. S., et al. 2003, *ApJ*, 599, 38
- Bentz, M. C., Markham, M., Rosborough, S., et al. 2023a, *ApJ*, 959, 25
- Bentz, M. C., Onken, C. A., Street, R., & Valluri, M. 2023b, *ApJ*, 944, 29
- Bentz, M. C., Peterson, B. M., Netzer, H., Pogge, R. W., & Vestergaard, M. 2009a, *ApJ*, 697, 160
- Bentz, M. C., Street, R., Onken, C. A., & Valluri, M. 2021a, *ApJ*, 906, 50
- Bentz, M. C., Williams, P. R., Street, R., et al. 2021b, *ApJ*, 920, 112
- Bentz, M. C., Williams, P. R., & Treu, T. 2022, *ApJ*, 934, 168
- Bentz, M. C., Walsh, J. L., Barth, A. J., et al. 2009b, *ApJ*, 705, 199
- Bentz, M. C., Denney, K. D., Grier, C. J., et al. 2013, *ApJ*, 767, 149
- Bernardi, M., Sheth, R. K., Tundo, E., & Hyde, J. B. 2007, *ApJ*, 660, 267
- Berton, M., Congiu, E., Ciroi, S., et al. 2019, *AJ*, 157, 48
- Berton, M., Peluso, G., Marziani, P., et al. 2021, *A&A*, 654, A125
- Bertram, T., Eckart, A., Fischer, S., et al. 2007, *A&A*, 470, 571
- Best, P. N., & Heckman, T. M. 2012, *MNRAS*, 421, 1569
- Bigiel, F., Leroy, A., Walter, F., et al. 2008, *AJ*, 136, 2846
- Binette, L., Magris, C. G., Stasińska, G., & Bruzual, A. G. 1994, *A&A*, 292, 13
- Binney, J., & Tabor, G. 1995, *MNRAS*, 276, 663
- Birrer, S., & Amara, A. 2018, *Physics of the Dark Universe*, 22, 189
- Bischetti, M., Piconcelli, E., Vietri, G., et al. 2017, *A&A*, 598, A122
- Bittner, A., Sánchez-Blázquez, P., Gadotti, D. A., et al. 2020, *A&A*, 643, A65
- Blandford, R. D., & McKee, C. F. 1982, *ApJ*, 255, 419
- Bogdán, Á., Lovisari, L., Volonteri, M., & Dubois, Y. 2018, *ApJ*, 852, 131
- Bolatto, A. D., Wolfire, M., & Leroy, A. K. 2013, *ARA&A*, 51, 207
- Boller, T. 2000, *New A Rev.*, 44, 387
- Bonfield, D. G., Jarvis, M. J., Hardcastle, M. J., et al. 2011, *MNRAS*, 416, 13
- Booth, C. M., & Schaye, J. 2009, *MNRAS*, 398, 53
- Boroson, T. 2005, *AJ*, 130, 381
- Boroson, T. A. 2002, *ApJ*, 565, 78
- Boroson, T. A., & Green, R. F. 1992, *ApJS*, 80, 109
- Bowyer, C. S., Lampton, M., Mack, J., & de Mendonca, F. 1970, *ApJ*, 161, L1
- Brewer, B. J., Treu, T., Pancoast, A., et al. 2011, *ApJ*, 733, L33
- Brinchmann, J., Charlot, S., White, S. D. M., et al. 2004, *MNRAS*, 351, 1151
- Bruzual, G., & Charlot, S. 2003a, *MNRAS*, 344, 1000
- Bruzual, G., & Charlot, S. 2003b, *MNRAS*, 344, 1000
- Buta, R., & Combes, F. 1996, *Fund. Cosmic Phys.*, 17, 95
- Buta, R. J. 2019, *MNRAS*, 488, 590
- Buta, R. J., Sheth, K., Athanassoula, E., et al. 2015, *ApJS*, 217, 32
- Caccianiga, A., Severgnini, P., Della Ceca, R., et al. 2007, *A&A*, 470, 557
- Caglar, T., Burtscher, L., Brandl, B., et al. 2020, *A&A*, 634, A114

- Caglar, T., Koss, M. J., Burtscher, L., et al. 2023, *ApJ*, 956, 60
- Calzetti, D., Armus, L., Bohlin, R. C., et al. 2000, *ApJ*, 533, 682
- Calzetti, D., Kennicutt, R. C., Engelbracht, C. W., et al. 2007, *ApJ*, 666, 870
- Cano-Díaz, M., Maiolino, R., Marconi, A., et al. 2012, *A&A*, 537, L8
- Cappellari, M. 2017, *MNRAS*, 466, 798
- Cappellari, M., & Copin, Y. 2003, *MNRAS*, 342, 345
- Cappellari, M., & Emsellem, E. 2004, *PASP*, 116, 138
- Cappellari, M., Bacon, R., Bureau, M., et al. 2006, *MNRAS*, 366, 1126
- Cappellari, M., McDermid, R. M., Alatalo, K., et al. 2013, *MNRAS*, 432, 1862
- Cardelli, J. A., Clayton, G. C., & Mathis, J. S. 1989, *ApJ*, 345, 245
- Castelló-Mor, N., Barcons, X., Ballo, L., et al. 2012, *A&A*, 544, A48
- Chen, C.-T. J., Hickox, R. C., Alberts, S., et al. 2013, *ApJ*, 773, 3
- Chen, S., Berton, M., La Mura, G., et al. 2018, *A&A*, 615, A167
- Chilingarian, I. V., Katkov, I. Y., Zolotukhin, I. Y., et al. 2018, *ApJ*, 863, 1
- Cicone, C., Brusa, M., Ramos Almeida, C., et al. 2018, *Nature Astronomy*, 2, 176
- Cicone, C., Maiolino, R., Sturm, E., et al. 2014, *A&A*, 562, A21
- Cid Fernandes, R., Stasińska, G., Schlickmann, M. S., et al. 2010, *MNRAS*, 403, 1036
- Ciotti, L., & Ostriker, J. P. 1997, *ApJ*, 487, L105
- Circosta, C., Mainieri, V., Padovani, P., et al. 2018, *A&A*, 620, A82
- Cisternas, M., Sheth, K., Salvato, M., et al. 2015, *ApJ*, 802, 137
- Cisternas, M., Jahnke, K., Bongiorno, A., et al. 2011a, *ApJ*, 741, L11
- Cisternas, M., Jahnke, K., Inskip, K. J., et al. 2011b, *ApJ*, 726, 57
- Cisternas, M., Jahnke, K., Inskip, K. J., et al. 2011c, *ApJ*, 726, 57
- Collin, S., & Kawaguchi, T. 2004, *A&A*, 426, 797
- Combes, F. 1996, in *Astronomical Society of the Pacific Conference Series*, Vol. 91, IAU Colloq. 157: Barred Galaxies, ed. R. Buta, D. A. Crocker, & B. G. Elmegreen, 286
- Combes, F., García-Burillo, S., Casasola, V., et al. 2014, *A&A*, 565, A97
- Combes, F., García-Burillo, S., Audibert, A., et al. 2019, *A&A*, 623, A79
- Comerón, S., Knapen, J. H., Beckman, J. E., et al. 2010, *MNRAS*, 402, 2462
- Condon, J. J. 1992, *ARA&A*, 30, 575
- Courteau, S., Cappellari, M., de Jong, R. S., et al. 2014, *Reviews of Modern Physics*, 86, 47
- Crain, R. A., Schaye, J., Bower, R. G., et al. 2015, *MNRAS*, 450, 1937
- Crenshaw, D. M., Kraemer, S. B., & Gabel, J. R. 2003, *AJ*, 126, 1690
- Crenshaw, D. M., Schmitt, H. R., Kraemer, S. B., Mushotzky, R. F., & Dunn, J. P. 2010, *ApJ*, 708, 419
- Cresci, G., Mainieri, V., Brusa, M., et al. 2015, *ApJ*, 799, 82
- Croton, D. J. 2006, *MNRAS*, 369, 1808

- Curtis, H. D. 1918, Publications of Lick Observatory, 13, 9
- Dalla Bontà, E., Peterson, B. M., Bentz, M. C., et al. 2020a, *ApJ*, 903, 112
- Dalla Bontà, E., Peterson, B. M., Bentz, M. C., et al. 2020b, *ApJ*, 903, 112
- Das, V., Crenshaw, D. M., Kraemer, S. B., & Deo, R. P. 2006, *AJ*, 132, 620
- Davies, R., Baron, D., Shimizu, T., et al. 2020, *MNRAS*, 498, 4150
- Davies, R. I., Maciejewski, W., Hicks, E. K. S., et al. 2009, *ApJ*, 702, 114
- Davies, R. I., Müller Sánchez, F., Genzel, R., et al. 2007, *ApJ*, 671, 1388
- Davies, R. I., Thomas, J., Genzel, R., et al. 2006, *ApJ*, 646, 754
- Davies, R. L., Kewley, L. J., Ho, I. T., & Dopita, M. A. 2014, *MNRAS*, 444, 3961
- Davies, R. L., Förster Schreiber, N. M., Übler, H., et al. 2019, *ApJ*, 873, 122
- Davis, B. L., Graham, A. W., & Seigar, M. S. 2017, *MNRAS*, 471, 2187
- Davis, S. W., & Laor, A. 2011, *ApJ*, 728, 98
- Davis, T. A., Alatalo, K., Bureau, M., et al. 2013, *MNRAS*, 429, 534
- de Nicola, S., Marconi, A., & Longo, G. 2019, *MNRAS*, 490, 600
- De Robertis, M. M., & Osterbrock, D. E. 1986, *ApJ*, 301, 727
- De Rosa, G., Peterson, B. M., Ely, J., et al. 2015, *ApJ*, 806, 128
- de Vaucouleurs, G., de Vaucouleurs, A., Corwin, Herold G., J., et al. 1991, Third Reference Catalogue of Bright Galaxies (Springer, New York, NY (USA))
- Debattista, V. P., Kazantzidis, S., & van den Bosch, F. C. 2013, *ApJ*, 765, 23
- Deo, R. P., Crenshaw, D. M., & Kraemer, S. B. 2006, *AJ*, 132, 321
- Dewangan, G. C., Griffiths, R. E., Dasgupta, S., & Rao, A. R. 2007, *ApJ*, 671, 1284
- Di Matteo, T., Springel, V., & Hernquist, L. 2005, *Nature*, 433, 604
- Diamond-Stanic, A. M., & Rieke, G. H. 2012, *ApJ*, 746, 168
- Díaz-García, S., Lisenfeld, U., Pérez, I., et al. 2021, *A&A*, 654, A135
- Dimitrijević, M. S., Popović, L. Č., Kovačević, J., Dačić, M., & Ilić, D. 2007, *MNRAS*, 374, 1181
- Ding, X., Silverman, J. D., & Onoue, M. 2022, *ApJ*, 939, L28
- Ding, X., Silverman, J., Treu, T., et al. 2020, *ApJ*, 888, 37
- Ding, X., Onoue, M., Silverman, J. D., et al. 2023, *Nature*, 621, 51
- Doi, A., Asada, K., Fujisawa, K., et al. 2013, *ApJ*, 765, 69
- Dopita, M. A., Kewley, L. J., Sutherland, R. S., & Nicholls, D. C. 2016, *Ap&SS*, 361, 61
- Dopita, M. A., Pereira, M., Kewley, L. J., & Capaccioli, M. 2002, *ApJS*, 143, 47
- Dopita, M. A., & Sutherland, R. S. 1996, *ApJS*, 102, 161
- Downes, D., & Solomon, P. M. 1998, *ApJ*, 507, 615
- Downes, D., & Solomon, P. M. 2003, *ApJ*, 582, 37
- Du, P., Hu, C., Lu, K.-X., et al. 2014, *ApJ*, 782, 45
- Du, P., Hu, C., Lu, K.-X., et al. 2015, *ApJ*, 806, 22

- Du, P., Zhang, Z.-X., Wang, K., et al. 2018, *ApJ*, 856, 6
- Dubois, Y., Devriendt, J., Slyz, A., & Teyssier, R. 2012, *MNRAS*, 420, 2662
- Dubois, Y., Peirani, S., Pichon, C., et al. 2016, *MNRAS*, 463, 3948
- Dubois, Y., Pichon, C., Devriendt, J., et al. 2013, *MNRAS*, 428, 2885
- Eilers, A.-C., Simcoe, R. A., Yue, M., et al. 2023, *ApJ*, 950, 68
- El-Badry, K., Quataert, E., Wetzel, A., et al. 2018, *MNRAS*, 473, 1930
- Ellison, S. L., Patton, D. R., Mendel, J. T., & Scudder, J. M. 2011, *MNRAS*, 418, 2043
- Elvis, M., Maccacaro, T., Wilson, A. S., et al. 1978, *MNRAS*, 183, 129
- Emsellem, E., Cappellari, M., Krajnović, D., et al. 2007, *MNRAS*, 379, 401
- Emsellem, E., Cappellari, M., Krajnović, D., et al. 2011, *MNRAS*, 414, 888
- Erwin, P. 2019, *MNRAS*, 489, 3553
- Eskridge, P. B., Frogel, J. A., Pogge, R. W., et al. 2000, *AJ*, 119, 536
- Esparza-Arredondo, D., González-Martín, O., Dultzin, D., et al. 2018, *ApJ*, 859, 124
- Esquej, P., Alonso-Herrero, A., González-Martín, O., et al. 2014, *ApJ*, 780, 86
- Euclid Collaboration, Scaramella, R., Amiaux, J., et al. 2022, *A&A*, 662, A112
- Event Horizon Telescope Collaboration, Akiyama, K., Alberdi, A., et al. 2019, *ApJ*, 875, L1
- Fabian, A. C. 2012, *ARA&A*, 50, 455
- Falcón-Barroso, J., Lyubenova, M., van de Ven, G., et al. 2017, *A&A*, 597, A48
- Fath, E. A. 1909, *Lick Observatory Bulletin*, 149, 71
- Fausnaugh, M. M., Grier, C. J., Bentz, M. C., et al. 2017, *ApJ*, 840, 97
- Ferrarese, L., & Ford, H. 2005, *Space Sci. Rev.*, 116, 523
- Ferrarese, L., & Merritt, D. 2000, *ApJ*, 539, L9
- Ferrarese, L., Pogge, R. W., Peterson, B. M., et al. 2001, *ApJ*, 555, L79
- Ferreira, L., Conselice, C. J., Sazonova, E., et al. 2023, *ApJ*, 955, 94
- Feruglio, C., Maiolino, R., Piconcelli, E., et al. 2010, *A&A*, 518, L155
- Fétick, R. J. L., Fusco, T., Neichel, B., et al. 2019, *A&A*, 628, A99
- Fields, D. L., Mathur, S., Pogge, R. W., Nicastro, F., & Komossa, S. 2005a, *ApJ*, 620, 183
- Fields, D. L., Mathur, S., Pogge, R. W., et al. 2005b, *ApJ*, 634, 928
- Fiore, F., Feruglio, C., Shankar, F., et al. 2017, *A&A*, 601, A143
- Fluetsch, A., Maiolino, R., Carniani, S., et al. 2019, *MNRAS*, 483, 4586
- Fonseca Alvarez, G., Trump, J. R., Homayouni, Y., et al. 2020, *ApJ*, 899, 73
- Fontanot, F., De Lucia, G., Hirschmann, M., et al. 2020, *MNRAS*, 496, 3943
- Foschini, L. 2011, in *Narrow-Line Seyfert 1 Galaxies and their Place in the Universe*, ed. L. Foschini, M. Colpi, L. Gallo, D. Grupe, S. Komossa, K. Leighly, & S. Mathur, 24
- Foschini, L., Berton, M., Caccianiga, A., et al. 2015, *A&A*, 575, A13
- Fryer, C. L., Belczynski, K., Wiktorowicz, G., et al. 2012, *ApJ*, 749, 91

- Gadotti, D. A., Bittner, A., Falcón-Barroso, J., et al. 2020, [A&A](#), 643, A14
- Gannon, J. S., Forbes, D. A., Romanowsky, A. J., et al. 2020, [MNRAS](#), 495, 2582
- García-Burillo, S., Combes, F., Schinnerer, E., Boone, F., & Hunt, L. K. 2005, [A&A](#), 441, 1011
- García-Burillo, S., Fernández-García, S., Combes, F., et al. 2009, [A&A](#), 496, 85
- Gaspari, M., Brighenti, F., & Temi, P. 2015, [A&A](#), 579, A62
- Gaspari, M., Ruszkowski, M., & Sharma, P. 2012, [ApJ](#), 746, 94
- Gaspari, M., & Sądowski, A. 2017, [ApJ](#), 837, 149
- Gaspari, M., Temi, P., & Brighenti, F. 2017, [MNRAS](#), 466, 677
- Gaspari, M., Tombesi, F., & Cappi, M. 2020, [Nature Astronomy](#), 4, 10
- Gaspari, M., McDonald, M., Hamer, S. L., et al. 2018, [ApJ](#), 854, 167
- Gaspari, M., Eckert, D., Etori, S., et al. 2019, [ApJ](#), 884, 169
- Gebhardt, K., Bender, R., Bower, G., et al. 2000, [ApJ](#), 539, L13
- Genzel, R., Tacconi, L. J., Gracia-Carpio, J., et al. 2010, [MNRAS](#), 407, 2091
- Giacconi, R., Murray, S., Gursky, H., et al. 1974, [ApJS](#), 27, 37
- Giustini, M., & Proga, D. 2019, [AAP](#), 630, A94
- Glozzi, M., Papadakis, I. E., Grupe, D., et al. 2010, [ApJ](#), 717, 1243
- Glozzi, M., & Williams, J. K. 2020, [MNRAS](#), 491, 532
- Gnerucci, A., Marconi, A., Capetti, A., Axon, D. J., & Robinson, A. 2010, [A&A](#), 511, A19
- Gnerucci, A., Marconi, A., Capetti, A., et al. 2011, [A&A](#), 536, A86
- Gofford, J., Reeves, J. N., Tombesi, F., et al. 2013, [MNRAS](#), 430, 60
- González Delgado, R. M., Cerviño, M., Martins, L. P., Leitherer, C., & Hauschildt, P. H. 2005, [MNRAS](#), 357, 945
- Goodrich, R. W. 1989, [ApJ](#), 342, 224
- Goulding, A. D., Forman, W. R., Hickox, R. C., et al. 2014, [ApJ](#), 783, 40
- Graham, A. W. 2008, [ApJ](#), 680, 143
- Graham, A. W. 2016, in [Astrophysics and Space Science Library](#), Vol. 418, [Galactic Bulges](#), ed. E. Laurikainen, R. Peletier, & D. Gadotti, 263
- Graham, A. W. 2023, [MNRAS](#), 518, 6293
- Graham, A. W., Onken, C. A., Athanassoula, E., & Combes, F. 2011, [MNRAS](#), 412, 2211
- Graham, A. W., & Sahu, N. 2023, [MNRAS](#), 520, 1975
- GRAVITY Collaboration, Sturm, E., Dexter, J., et al. 2018, [Nature](#), 563, 657
- GRAVITY Collaboration, Amorim, A., Bauböck, M., et al. 2020, [A&A](#), 643, A154
- GRAVITY Collaboration, Amorim, A., Bauböck, M., et al. 2021, [A&A](#), 654, A85
- Gravity+ Collaboration, Abuter, R., Alarcon, P., et al. 2022, [The Messenger](#), 189, 17

- GRAVITY Collaboration, Amorim, A., Bourdarot, G., et al. 2024, [arXiv e-prints](#), [arXiv:2401.07676](#)
- Greene, J. E., & Ho, L. C. 2005a, [ApJ](#), 630, 122
- Greene, J. E., & Ho, L. C. 2005b, [ApJ](#), 630, 122
- Greene, J. E., & Ho, L. C. 2006, [ApJ](#), 641, 117
- Greene, J. E., & Ho, L. C. 2007, [ApJ](#), 670, 92
- Greene, J. E., Strader, J., & Ho, L. C. 2020, [ARA&A](#), 58, 257
- Greene, J. E., Zakamska, N. L., Ho, L. C., & Barth, A. J. 2011, [ApJ](#), 732, 9
- Greene, J. E., Peng, C. Y., Kim, M., et al. 2010, [ApJ](#), 721, 26
- Greene, J. E., Seth, A., Kim, M., et al. 2016, [ApJ](#), 826, L32
- Grier, C. J., Pancoast, A., Barth, A. J., et al. 2017, [ApJ](#), 849, 146
- Grier, C. J., Peterson, B. M., Pogge, R. W., et al. 2012, [ApJ](#), 755, 60
- Grier, C. J., Martini, P., Watson, L. C., et al. 2013, [ApJ](#), 773, 90
- Grupe, D. 2004, [AJ](#), 127, 1799
- Grupe, D., Komossa, S., Leighly, K. M., & Page, K. L. 2010, [ApJS](#), 187, 64
- Guérou, A., Krajnović, D., Epinat, B., et al. 2017, [A&A](#), 608, A5
- Gültekin, K., Richstone, D. O., Gebhardt, K., et al. 2009, [ApJ](#), 698, 198
- Gupta, A., Mathur, S., Krongold, Y., & Nicastro, F. 2013, [ApJ](#), 772, 66
- Haan, S., Schinnerer, E., Emsellem, E., et al. 2009, [ApJ](#), 692, 1623
- Haardt, F., & Maraschi, L. 1991, [ApJ](#), 380, L51
- Habouzit, M., Li, Y., Somerville, R. S., et al. 2021, [MNRAS](#), 503, 1940
- Habouzit, M., Onoue, M., Bañados, E., et al. 2022, [MNRAS](#), 511, 3751
- Håring, N., & Rix, H.-W. 2004, [ApJ](#), 604, L89
- Harris, C. E., Bennert, V. N., Auger, M. W., et al. 2012, [ApJS](#), 201, 29
- Harrison, C. M. 2017, [Nature Astronomy](#), 1, 0165
- Harrison, C. M., Alexander, D. M., Mullaney, J. R., & Swinbank, A. M. 2014, [MNRAS](#), 441, 3306
- Harrison, C. M., Alexander, D. M., Rosario, D. J., Scholtz, J., & Stanley, F. 2021, in [Nuclear Activity in Galaxies Across Cosmic Time](#), ed. M. Pović, P. Marziani, J. Masegosa, H. Netzer, S. H. Negu, & S. B. Tessema, Vol. 356, 199
- Harrison, C. M., & Ramos Almeida, C. 2024, [Galaxies](#), 12, 17
- Harrison, C. M., Alexander, D. M., Mullaney, J. R., et al. 2016, [MNRAS](#), 456, 1195
- Hartmann, M., Debattista, V. P., Cole, D. R., et al. 2014, [MNRAS](#), 441, 1243
- Heckman, T. M. 1980, [A&A](#), 500, 187
- Heckman, T. M., & Best, P. N. 2014, [ARA&A](#), 52, 589
- Heckman, T. M., Miley, G. K., van Breugel, W. J. M., & Butcher, H. R. 1981, [ApJ](#), 247, 403
- Hickox, R. C., & Alexander, D. M. 2018, [ARA&A](#), 56, 625
- Hickox, R. C., Mullaney, J. R., Alexander, D. M., et al. 2014, [ApJ](#), 782, 9

- Hickox, R. C., Jones, C., Forman, W. R., et al. 2009, *ApJ*, 696, 891
- Hirschmann, M., Khochfar, S., Burkert, A., et al. 2010, *MNRAS*, 407, 1016
- Ho, L. C., & Kim, M. 2014, *ApJ*, 789, 17
- Holt, J., Tadhunter, C., Morganti, R., et al. 2006, *MNRAS*, 370, 1633
- Holt, J., Tadhunter, C. N., & Morganti, R. 2008, *MNRAS*, 387, 639
- Hönig, S. F., & Kishimoto, M. 2017, *ApJ*, 838, L20
- Hopkins, P. F., & Quataert, E. 2010a, *MNRAS*, 407, 1529
- Hopkins, P. F., & Quataert, E. 2010b, *MNRAS*, 407, 1529
- Hopkins, P. F., Robertson, B., Krause, E., Hernquist, L., & Cox, T. J. 2006, *ApJ*, 652, 107
- Hopkins, P. F., Torrey, P., Faucher-Giguère, C.-A., Quataert, E., & Murray, N. 2016, *MNRAS*, 458, 816
- Horne, K., Peterson, B. M., Collier, S. J., & Netzer, H. 2004, *PASP*, 116, 465
- Hornschemeier, A. E., Heckman, T. M., Ptak, A. F., Tremonti, C. A., & Colbert, E. J. M. 2005, *AJ*, 129, 86
- Hu, C., Li, S.-S., Yang, S., et al. 2021, *ApJS*, 253, 20
- Hu, J. 2008, *MNRAS*, 386, 2242
- Humason, M. L. 1932, *PASP*, 44, 267
- Husemann, B., Bennert, V. N., Scharwächter, J., Woo, J. H., & Choudhury, O. S. 2016a, *MNRAS*, 455, 1905
- Husemann, B., Jahnke, K., Sánchez, S. F., et al. 2014, *MNRAS*, 443, 755
- Husemann, B., Scharwächter, J., Bennert, V. N., et al. 2016b, *A&A*, 594, A44
- Husemann, B., Wisotzki, L., Sánchez, S. F., & Jahnke, K. 2008, *A&A*, 488, 145
- Husemann, B., Wisotzki, L., Sánchez, S. F., & Jahnke, K. 2013, *A&A*, 549, A43
- Husemann, B., Scharwächter, J., Davis, T. A., et al. 2019, *A&A*, 627, A53
- Husemann, B., Singha, M., Scharwächter, J., et al. 2022, *A&A*, 659, A124
- Imanishi, M., & Wada, K. 2004, *ApJ*, 617, 214
- Isbell, J. W., Burtscher, L., Asmus, D., et al. 2021, *ApJ*, 910, 104
- Izumi, T., Kawakatu, N., & Kohno, K. 2016, *ApJ*, 827, 81
- Jacobs, C., Glazebrook, K., Calabrò, A., et al. 2023, *ApJ*, 948, L13
- Jahnke, K., Kuhlbrodt, B., & Wisotzki, L. 2004, *MNRAS*, 352, 399
- Jahnke, K., & Macciò, A. V. 2011, *ApJ*, 734, 92
- Järvelä, E., Berton, M., & Crepaldi, L. 2021, *Frontiers in Astronomy and Space Sciences*, 8, 147
- Järvelä, E., Lähteenmäki, A., & Berton, M. 2018, *A&A*, 619, A69
- Järvelä, E., Lähteenmäki, A., Lietzen, H., et al. 2017, *A&A*, 606, A9
- Jarvis, M. E., Harrison, C. M., Mainieri, V., et al. 2021, *MNRAS*, 503, 1780
- Jorgensen, I., Franx, M., & Kjaergaard, P. 1995, *MNRAS*, 276, 1341
- Kakkad, D., Stalevski, M., Kishimoto, M., et al. 2023, *MNRAS*, 519, 5324
- Kakkad, D., Sani, E., Rojas, A. F., et al. 2022, *MNRAS*, 511, 2105
- Kara, E., Mehdipour, M., Kriss, G. A., et al. 2021, *ApJ*, 922, 151

- Kaspi, S., Smith, P. S., Netzer, H., et al. 2000, *ApJ*, 533, 631
- Kauffmann, G., Heckman, T. M., Tremonti, C., et al. 2003, *MNRAS*, 346, 1055
- Kawakatu, N., & Wada, K. 2008, *ApJ*, 681, 73
- Keel, W. C., Lintott, C. J., Maksym, W. P., et al. 2017, *ApJ*, 835, 256
- Kelly, B. C. 2007, *ApJ*, 665, 1489
- Kennicutt, Robert C., J. 1998, *ApJ*, 498, 541
- Kennicutt, Robert C., J., & De Los Reyes, M. A. C. 2021, *ApJ*, 908, 61
- Kennicutt, Robert C., J., Calzetti, D., Walter, F., et al. 2007, *ApJ*, 671, 333
- Kewley, L. J., Dopita, M. A., Sutherland, R. S., Heisler, C. A., & Trevena, J. 2001, *ApJ*, 556, 121
- Kewley, L. J., & Ellison, S. L. 2008, *ApJ*, 681, 1183
- Khachikian, E. Y., & Weedman, D. W. 1974, *ApJ*, 192, 581
- Kim, M., Barth, A. J., Ho, L. C., & Son, S. 2021, *ApJS*, 256, 40
- Kim, W.-T., & Elmegreen, B. G. 2017, *ApJ*, 841, L4
- King, A. 2003, *ApJ*, 596, L27
- Knapen, J. H., Comerón, S., & Seidel, M. K. 2019, *A&A*, 621, L5
- Kocevski, D. D., Faber, S. M., Mozena, M., et al. 2012, *ApJ*, 744, 148
- Kollatschny, W., & Fricke, K. J. 1985, *A&A*, 143, 393
- Komossa, S. 2018, in *Revisiting Narrow-Line Seyfert 1 Galaxies and their Place in the Universe*, 15
- Komossa, S., Voges, W., Xu, D., et al. 2006, *AJ*, 132, 531
- Komossa, S., & Xu, D. 2007a, *ApJ*, 667, L33
- Komossa, S., & Xu, D. 2007b, *ApJl*, 667, L33
- König, S., Eckart, A., García-Marín, M., & Huchtmeier, W. K. 2009, *A&A*, 507, 757
- Kormendy, J. 2020, in *IAU Symposium, Vol. 353, Galactic Dynamics in the Era of Large Surveys*, ed. M. Valluri & J. A. Sellwood, 186
- Kormendy, J., Bender, R., & Cornell, M. E. 2011, *Nature*, 469, 374
- Kormendy, J., & Ho, L. C. 2013, *ARA&A*, 51, 511
- Kormendy, J., & Kennicutt, Robert C., J. 2004a, *ARA&A*, 42, 603
- Kormendy, J., & Kennicutt, Robert C., J. 2004b, *ARA&A*, 42, 603
- Kormendy, J., & Richstone, D. 1995, *ARA&A*, 33, 581
- Kosec, P., Buisson, D. J. K., Parker, M. L., et al. 2018, *MNRAS*, 481, 947
- Koss, M., Mushotzky, R., Veilleux, S., & Winter, L. 2010, *ApJ*, 716, L125
- Koss, M., Trakhtenbrot, B., Ricci, C., et al. 2017, *ApJ*, 850, 74
- Krajnović, D., Cappellari, M., de Zeeuw, P. T., & Copin, Y. 2006, *MNRAS*, 366, 787
- Kreckel, K., Faesi, C., Kruijssen, J. M. D., et al. 2018, *ApJ*, 863, L21
- Kristian, J. 1973, *ApJ*, 179, L61
- Krolik, J. H., & Begelman, M. C. 1988, *ApJ*, 329, 702
- Krongold, Y., Dultzin-Hacyan, D., & Marziani, P. 2001, *AJ*, 121, 702

- Krongold, Y., Longinotti, A. L., Santos-Lleó, M., et al. 2021, *ApJ*, 917, 39
- Kumar, P., & Johnson, J. L. 2010, *MNRAS*, 404, 2170
- Lanzuisi, G., Delvecchio, I., Berta, S., et al. 2017, *A&A*, 602, A123
- Lauer, T. R., Tremaine, S., Richstone, D., & Faber, S. M. 2007, *ApJ*, 670, 249
- Lawrence, A. 1991, *MNRAS*, 252, 586
- Le Fèvre, O., Saisse, M., Mancini, D., et al. 2003, in *Society of Photo-Optical Instrumentation Engineers (SPIE) Conference Series*, Vol. 4841, *Instrument Design and Performance for Optical/Infrared Ground-based Telescopes*, ed. M. Iye & A. F. M. Moorwood, 1670
- Leitherer, C., Schaerer, D., Goldader, J. D., et al. 1999, *ApJS*, 123, 3
- Lelli, F., Davis, T. A., Bureau, M., et al. 2022, *MNRAS*, 516, 4066
- Lelli, F., Di Teodoro, E. M., Fraternali, F., et al. 2021, *Science*, 371, 713
- Leroy, A. K., Walter, F., Brinks, E., et al. 2008, *AJ*, 136, 2782
- Li, J., Silverman, J. D., Ding, X., et al. 2021, *ApJ*, 922, 142
- Li, Y., & Bryan, G. L. 2014, *ApJ*, 789, 153
- Li, Y.-R., Wang, J.-M., Ho, L. C., Du, P., & Bai, J.-M. 2013, *ApJ*, 779, 110
- Li, Y.-R., Wang, J.-M., Songsheng, Y.-Y., et al. 2022, *ApJ*, 927, 58
- Li, Y.-R., Songsheng, Y.-Y., Qiu, J., et al. 2018, *ApJ*, 869, 137
- Lintott, C. J., Schawinski, K., Keel, W., et al. 2009, *MNRAS*, 399, 129
- Lister, M. L., Aller, M. F., Aller, H. D., et al. 2016, *AJ*, 152, 12
- Liu, G., Zakamska, N. L., Greene, J. E., Nesvadba, N. P. H., & Liu, X. 2013, *MNRAS*, 436, 2576
- Lotz, J. M., Jonsson, P., Cox, T. J., et al. 2011, *ApJ*, 742, 103
- Lu, K.-X., Wang, J.-G., Zhang, Z.-X., et al. 2021, *ApJ*, 918, 50
- Ludwig, R. R., Wills, B., Greene, J. E., & Robinson, E. L. 2009, *ApJ*, 706, 995
- Lusso, E., Hennawi, J. F., Comastri, A., et al. 2013, *ApJ*, 777, 86
- Maccagni, F. M., Serra, P., Gaspari, M., et al. 2021, *A&A*, 656, A45
- Maciejewski, W. 2004, *MNRAS*, 354, 892
- Magorrian, J., Tremaine, S., Richstone, D., et al. 1998, *AJ*, 115, 2285
- Maiolino, R., Scholtz, J., Witstok, J., et al. 2024, *Nature*, 627, 59
- Mallick, L., Alston, W. N., Parker, M. L., et al. 2018, *MNRAS*, 479, 615
- Mallmann, N. D., Riffel, R., Storchi-Bergmann, T., et al. 2018, *MNRAS*, 478, 5491
- Marasco, A., Cresci, G., Posti, L., et al. 2021, *MNRAS*, 507, 4274
- Maraston, C., & Strömbäck, G. 2011, *MNRAS*, 418, 2785
- Marconi, A., & Hunt, L. K. 2003, *ApJ*, 589, L21
- Marian, V., Jahnke, K., Mechtley, M., et al. 2019, *ApJ*, 882, 141
- Marin, F., & Antonucci, R. 2016, *ApJ*, 830, 82
- Martel, A. R., Ford, H. C., Tran, H. D., et al. 2003, *AJ*, 125, 2964
- Martínez-Aldama, M. L., Czerny, B., Kawka, D., et al. 2019, *ApJ*, 883, 170
- Massonneau, W., Volonteri, M., Dubois, Y., & Beckmann, R. S. 2023, *A&A*,

670, A180

- Mathur, S. 2000, *MNRAS*, 314, L17
- Matsuoka, Y., Oyabu, S., Tsuzuki, Y., & Kawara, K. 2007, *ApJ*, 663, 781
- Matthews, T. A., & Sandage, A. R. 1963, *ApJ*, 138, 30
- Mayall, N. U. 1934, *PASP*, 46, 134
- Mazzalay, X., Rodríguez-Ardila, A., Komossa, S., & McGregor, P. J. 2013, *MNRAS*, 430, 2411
- Mazzuca, L. M., Knapen, J. H., Veilleux, S., & Regan, M. W. 2008, *ApJS*, 174, 337
- McConnell, N. J., & Ma, C.-P. 2013, *ApJ*, 764, 184
- McElroy, R., Croom, S. M., Pracy, M., et al. 2015, *MNRAS*, 446, 2186
- McHardy, I. M., Connolly, S. D., Horne, K., et al. 2018, *MNRAS*, 480, 2881
- McKinney, J. C., Dai, L., & Avara, M. J. 2015, *MNRAS*, 454, L6
- McLeod, K. K., & McLeod, B. A. 2001, *ApJ*, 546, 782
- McMullin, J. P., Waters, B., Schiebel, D., Young, W., & Golap, K. 2007, in *Astronomical Society of the Pacific Conference Series*, Vol. 376, *Astronomical Data Analysis Software and Systems XVI*, ed. R. A. Shaw, F. Hill, & D. J. Bell, 127
- Mechtley, M., Jahnke, K., Windhorst, R. A., et al. 2016, *ApJ*, 830, 156
- Mehlert, D., Thomas, D., Saglia, R. P., Bender, R., & Wegner, G. 2003, *A&A*, 407, 423
- Merloni, A. 2004, *MNRAS*, 353, 1035
- Merloni, A., Bongiorno, A., Brusa, M., et al. 2014, *MNRAS*, 437, 3550
- Merritt, D., & Ferrarese, L. 2001, *ApJ*, 547, 140
- Mingozzi, M., Cresci, G., Venturi, G., et al. 2019, *A&A*, 622, A146
- Mo, H., Chen, Y., & Wang, H. 2024, *MNRAS*, arXiv:2311.05030 [astro-ph.GA]
- Morrissey, P., Matuszewski, M., Martin, D. C., et al. 2018, *ApJ*, 864, 93
- Mullaney, J. R., Alexander, D. M., Fine, S., et al. 2013, *MNRAS*, 433, 622
- Mullaney, J. R., Daddi, E., Béthermin, M., et al. 2012, *ApJ*, 753, L30
- Müller Sánchez, F., Davies, R. I., Genzel, R., et al. 2009, *ApJ*, 691, 749
- Müller-Sánchez, F., Hicks, E. K. S., Malkan, M., et al. 2018, *ApJ*, 858, 48
- Müller-Sánchez, F., Prieto, M. A., Hicks, E. K. S., et al. 2011, *ApJ*, 739, 69
- Murphy, E. J., Condon, J. J., Schinnerer, E., et al. 2011, *ApJ*, 737, 67
- Nair, P. B., & Abraham, R. G. 2010, *ApJS*, 186, 427
- Nandra, K., O'Neill, P. M., George, I. M., & Reeves, J. N. 2007, *MNRAS*, 382, 194
- Nelson, C. H., Green, R. F., Bower, G., Gebhardt, K., & Weistrop, D. 2004, *ApJ*, 615, 652
- Nelson, C. H., & Whittle, M. 1995, *ApJS*, 99, 67
- Nelson, D., Pillepich, A., Ayromlou, M., et al. 2023, *arXiv e-prints*, arXiv:2311.06338

- Nenkova, M., Sirocky, M. M., Nikutta, R., Ivezić, Ž., & Elitzur, M. 2008, *ApJ*, **685**, 160
- Nesvadba, N. P. H., Lehnert, M. D., De Breuck, C., Gilbert, A., & van Breugel, W. 2007, *A&A*, **475**, 145
- Netzer, H. 2015, *ARA&A*, **53**, 365
- North, E. V., Davis, T. A., Bureau, M., et al. 2021, *MNRAS*, **503**, 5179
- O'Donnell, J. E. 1994, *ApJ*, **422**, 158
- Ohsuga, K., Mori, M., Nakamoto, T., & Mineshige, S. 2005, *ApJ*, **628**, 368
- Ohta, K., Aoki, K., Kawaguchi, T., & Kiuchi, G. 2007, *ApJS*, **169**, 1
- Onken, C. A., Ferrarese, L., Merritt, D., et al. 2004, *ApJ*, **615**, 645
- Onken, C. A., Valluri, M., Peterson, B. M., et al. 2007, *ApJ*, **670**, 105
- Onodera, S., Kuno, N., Tosaki, T., et al. 2010, *ApJ*, **722**, L127
- Oppenheimer, B. D., Babul, A., Bahé, Y., Butsky, I. S., & McCarthy, I. G. 2021, *Universe*, **7**, 209
- Orban de Xivry, G., Davies, R., Schartmann, M., et al. 2011, *MNRAS*, **417**, 2721
- Osterbrock, D. E. 1989, *Astrophysics of gaseous nebulae and active galactic nuclei* (University Science Books)
- Osterbrock, D. E., & Koski, A. T. 1976, *MNRAS*, **176**, 61P
- Osterbrock, D. E., & Pogge, R. W. 1985, *ApJ*, **297**, 166
- Pacholczyk, A. G., & Weymann, R. 1968, *AJ*, **73**, 836
- Padovani, P., Alexander, D. M., Assef, R. J., et al. 2017, *A&A Rev.*, **25**, 2
- Pakmor, R., Springel, V., Coles, J. P., et al. 2023, *MNRAS*, **524**, 2539
- Paliya, V. S., Parker, M. L., Jiang, J., et al. 2019, *ApJ*, **872**, 169
- Pan, H.-W., Yuan, W., Yao, S., Komossa, S., & Jin, C. 2018, *ApJ*, **866**, 69
- Pancoast, A., Brewer, B. J., & Treu, T. 2011, *ApJ*, **730**, 139
- Pancoast, A., Brewer, B. J., Treu, T., et al. 2014, *MNRAS*, **445**, 3073
- Pancoast, A., Barth, A. J., Horne, K., et al. 2018, *ApJ*, **856**, 108
- Panessa, F., Baldi, R. D., Laor, A., et al. 2019, *Nature Astronomy*, **3**, 387
- Park, D., Kelly, B. C., Woo, J.-H., & Treu, T. 2012, *ApJS*, **203**, 6
- Parker, M. L., Alston, W. N., Buisson, D. J. K., et al. 2017, *MNRAS*, **469**, 1553
- Pasha, I. I., & Smirnov, M. A. 1982, *Ap&SS*, **86**, 215
- Pei, L., Fausnaugh, M. M., Barth, A. J., et al. 2017, *ApJ*, **837**, 131
- Peng, C. Y. 2007, *ApJ*, **671**, 1098
- Pérez-Torres, M., Mattila, S., Alonso-Herrero, A., Aalto, S., & Efstathiou, A. 2021, *A&A Rev.*, **29**, 2
- Pessa, I., Schinnerer, E., Belfiore, F., et al. 2021, *A&A*, **650**, A134
- Peters, T., Naab, T., Walch, S., et al. 2017, *MNRAS*, **466**, 3293
- Peterson, B. M. 1993, *PASP*, **105**, 247
- Peterson, B. M., Wanders, I., Bertram, R., et al. 1998, *ApJ*, **501**, 82
- Peterson, B. M., Ferrarese, L., Gilbert, K. M., et al. 2004, *ApJ*, **613**, 682

- Pichon, C., Pogosyan, D., Kimm, T., et al. 2011, *MNRAS*, 418, 2493
- Pinkney, J., Gebhardt, K., Bender, R., et al. 2003, *ApJ*, 596, 903
- Planck Collaboration, Ade, P. A. R., Aghanim, N., et al. 2016, *A&A*, 594, A13
- Ponti, G., Fender, R. P., Begelman, M. C., et al. 2012, *MNRAS*, 422, L11
- Powell, M. C., Husemann, B., Tremblay, G. R., et al. 2018, *A&A*, 618, A27
- Puerari, I., & Dottori, H. A. 1992, *A&AS*, 93, 469
- Querejeta, M., Meidt, S. E., Schinnerer, E., et al. 2016, *A&A*, 588, A33
- Rakshit, S., Stalin, C. S., Chand, H., & Zhang, X.-G. 2017, *ApJS*, 229, 39
- Rakshit, S., & Woo, J.-H. 2018, *ApJ*, 865, 5
- Ramírez-Olivencia, N., Varenius, E., Pérez-Torres, M., et al. 2022, *A&A*, 658, A4
- Ramos Almeida, C., & Ricci, C. 2017, *Nature Astronomy*, 1, 679
- Ramos Almeida, C., Alonso-Herrero, A., Esquej, P., et al. 2014, *MNRAS*, 445, 1130
- Ramos Almeida, C., Bischetti, M., García-Burillo, S., et al. 2022, *A&A*, 658, A155
- Reeves, J. N., & Braitto, V. 2019, *ApJ*, 884, 80
- Reeves, J. N., Braitto, V., Nardini, E., et al. 2018, *ApJ*, 854, L8
- Remigio, R., U, V., Barth, A., et al. 2024, in prep.
- Rennehan, D., Babul, A., Moa, B., & Davé, R. 2023, *arXiv e-prints*, [arXiv:2309.15898](https://arxiv.org/abs/2309.15898)
- Revalski, M., Crenshaw, D. M., Kraemer, S. B., et al. 2018, *ApJ*, 856, 46
- Ricci, C., Trakhtenbrot, B., Koss, M. J., et al. 2017, *ApJS*, 233, 17
- Richards, G. T., Lacy, M., Storrie-Lombardi, L. J., et al. 2006, *ApJS*, 166, 470
- Richards, G. T., Kruczek, N. E., Gallagher, S. C., et al. 2011, *AJ*, 141, 167
- Richardson, C. T., Allen, J. T., Baldwin, J. A., Hewett, P. C., & Ferland, G. J. 2014, *MNRAS*, 437, 2376
- Riffel, R. A., Storchi-Bergmann, T., Riffel, R., et al. 2017, *MNRAS*, 470, 992
- Riffel, R. A., Storchi-Bergmann, T., Zakamska, N. L., & Riffel, R. 2020, *MNRAS*, 496, 4857
- Robertson, B., Hernquist, L., Cox, T. J., et al. 2006, *ApJ*, 641, 90
- Robertson, B. E., Tacchella, S., Johnson, B. D., et al. 2023, *ApJ*, 942, L42
- Roman-Oliveira, F., Fraternali, F., & Rizzo, F. 2023, *MNRAS*, 521, 1045
- Romano, P., Vercellone, S., Foschini, L., et al. 2018, *MNRAS*, 481, 5046
- Rosario, D. J., Santini, P., Lutz, D., et al. 2012, *A&A*, 545, A45
- Rosario, D. J., Trakhtenbrot, B., Lutz, D., et al. 2013, *A&A*, 560, A72
- Rosario, D. J., Burtscher, L., Davies, R. I., et al. 2018, *MNRAS*, 473, 5658
- Rose, T., Edge, A. C., Combes, F., et al. 2019, *MNRAS*, 489, 349
- Rupke, D. S., Veilleux, S., & Sanders, D. B. 2005, *ApJS*, 160, 115
- Rupke, D. S. N., Gültekin, K., & Veilleux, S. 2017, *ApJ*, 850, 40
- Ruschel-Dutra, D., Rodríguez Espinosa, J. M., González Martín, O., Pastoriza,

- M., & Riffel, R. 2017, *MNRAS*, 466, 3353
- Sadowski, A., & Gaspari, M. 2017, *MNRAS*, 468, 1398
- Saglia, R. P., Opitsch, M., Erwin, P., et al. 2016, *ApJ*, 818, 47
- Sahu, N., Graham, A. W., & Davis, B. L. 2019, *ApJ*, 887, 10
- Sakamoto, K., Okumura, S. K., Ishizuki, S., & Scoville, N. Z. 1999, *ApJ*, 525, 691
- Salvato, M. 2002, PhD thesis, University of Potsdam, Germany
- Sameshima, H., Kawara, K., Matsuoka, Y., et al. 2011, *MNRAS*, 410, 1018
- Sánchez, S. F., Barrera-Ballesteros, J. K., Colombo, D., et al. 2021, *MNRAS*, 503, 1615
- Savorgnan, G. A. D., & Graham, A. W. 2015, *MNRAS*, 446, 2330
- Schartmann, M., Meisenheimer, K., Camenzind, M., et al. 2008, *A&A*, 482, 67
- Schartmann, M., Mould, J., Wada, K., et al. 2018, *MNRAS*, 473, 953
- Scharwächter, J., Husemann, B., Busch, G., Komossa, S., & Dopita, M. A. 2017, *ApJ*, 848, 35
- Schawinski, K., Koss, M., Berney, S., & Sartori, L. F. 2015, *MNRAS*, 451, 2517
- Schawinski, K., Simmons, B. D., Urry, C. M., Treister, E., & Glikman, E. 2012, *MNRAS*, 425, L61
- Schaye, J., Kugel, R., Schaller, M., et al. 2023, *MNRAS*, 526, 4978
- Schlafly, E. F., & Finkbeiner, D. P. 2011, *ApJ*, 737, 103
- Schlegel, D. J., Finkbeiner, D. P., & Davis, M. 1998, *ApJ*, 500, 525
- Schmidt, M. 1963, *Nature*, 197, 1040
- Schulze, A., & Wisotzki, L. 2010, *A&A*, 516, A87
- Schulze, A., & Wisotzki, L. 2011, *A&A*, 535, A87
- Schulze, A., Bongiorno, A., Gavignaud, I., et al. 2015, *MNRAS*, 447, 2085
- Sellwood, J. A., & Wilkinson, A. 1993, *Reports on Progress in Physics*, 56, 173
- Severgnini, P., Caccianiga, A., Braitto, V., et al. 2003, *A&A*, 406, 483
- Sexton, R. O., Matzko, W., Darden, N., Canalizo, G., & Gorjian, V. 2021, *MNRAS*, 500, 2871
- Seyfert, C. K. 1943, *ApJ*, 97, 28
- Shangguan, J., Ho, L. C., Bauer, F. E., Wang, R., & Treister, E. 2020, *ApJ*, 899, 112
- Shankar, F., Bernardi, M., Sheth, R. K., et al. 2016, *MNRAS*, 460, 3119
- Shankar, F., Bernardi, M., Richardson, K., et al. 2019, *MNRAS*, 485, 1278
- Shankar, F., Weinberg, D. H., Marsden, C., et al. 2020, *MNRAS*, 493, 1500
- Shen, J., Vanden Berk, D. E., Schneider, D. P., & Hall, P. B. 2008, *AJ*, 135, 928
- Shen, Y., & Liu, X. 2012, *ApJ*, 753, 125
- Shen, Y., Brandt, W. N., Dawson, K. S., et al. 2015, *ApJS*, 216, 4
- Shen, Y., Grier, C. J., Horne, K., et al. 2024, *ApJS*, 272, 26
- Sheth, K., Vogel, S. N., Regan, M. W., Thornley, M. D., & Teuben, P. J. 2005, *ApJ*, 632, 217

- Shimizu, T. T., Davies, R. I., Lutz, D., et al. 2019, *MNRAS*, 490, 5860
- Shlosman, I., Begelman, M. C., & Frank, J. 1990, *Nature*, 345, 679
- Shlosman, I., Frank, J., & Begelman, M. C. 1989a, *Nature*, 338, 45
- Shlosman, I., Frank, J., & Begelman, M. C. 1989b, *Nature*, 338, 45
- Silk, J. 2013, *ApJ*, 772, 112
- Silk, J., & Rees, M. J. 1998a, *A&A*, 331, L1
- Silk, J., & Rees, M. J. 1998b, *A&A*, 331, L1
- Silverman, J. D., Kampczyk, P., Jahnke, K., et al. 2011, *ApJ*, 743, 2
- Singha, M., Husemann, B., Urrutia, T., et al. 2022, *A&A*, 659, A123
- Skjelboe, A., Pancoast, A., Treu, T., et al. 2015, *MNRAS*, 454, 144
- Slavcheva-Mihova, L., & Mihov, B. 2011, *A&A*, 526, A43
- Smirnova-Pinchukova, I., Husemann, B., Davis, T. A., et al. 2022, *A&A*, 659, A125
- Somerville, R. S., Hopkins, P. F., Cox, T. J., Robertson, B. E., & Hernquist, L. 2008, *MNRAS*, 391, 481
- Sormani, M. C., Barnes, A. T., Sun, J., et al. 2023, *MNRAS*, 523, 2918
- Springel, V., Di Matteo, T., & Hernquist, L. 2005, *MNRAS*, 361, 776
- Stalevski, M., Fritz, J., Baes, M., Nakos, T., & Popović, L. Č. 2012, *MNRAS*, 420, 2756
- Stalevski, M., Ricci, C., Ueda, Y., et al. 2016, *MNRAS*, 458, 2288
- Stalevski, M., Tristram, K. R. W., & Asmus, D. 2019, *MNRAS*, 484, 3334
- Stanley, F., Harrison, C. M., Alexander, D. M., et al. 2015, *MNRAS*, 453, 591
- Stanley, F., Alexander, D. M., Harrison, C. M., et al. 2017, *MNRAS*, 472, 2221
- Stasińska, G., Vale Asari, N., Cid Fernandes, R., et al. 2008, *MNRAS*, 391, L29
- Stemo, A., Comerford, J. M., Barrows, R. S., et al. 2020, *ApJ*, 888, 78
- Storchi-Bergmann, T., & Schnorr-Müller, A. 2019, *Nature Astronomy*, 3, 48
- Storey, P. J., & Zeppen, C. J. 2000, *MNRAS*, 312, 813
- Ströbele, S., La Penna, P., Arsenault, R., et al. 2012, in *Society of Photo-Optical Instrumentation Engineers (SPIE) Conference Series*, Vol. 8447, *Adaptive Optics Systems III*, ed. B. L. Ellerbroek, E. Marchetti, & J.-P. Véran, 844737
- Stuber, S. K., Saito, T., Schinnerer, E., et al. 2021, *A&A*, 653, A172
- Sulentic, J. W., Zwitter, T., Marziani, P., & Dultzin-Hacyan, D. 2000, *ApJ*, 536, L5
- Tadhunter, C., Rodríguez Zaurín, J., Rose, M., et al. 2018, *MNRAS*, 478, 1558
- Temì, P., Gaspari, M., Brighenti, F., et al. 2022, *ApJ*, 928, 150
- Terrazas, B. A., Bell, E. F., Pillepich, A., et al. 2020, *MNRAS*, 493, 1888
- Thompson, T. A., Quataert, E., & Murray, N. 2005, *ApJ*, 630, 167
- Tombesi, F., Cappi, M., Reeves, J. N., et al. 2013, *MNRAS*, 430, 1102
- Tombesi, F., Cappi, M., Reeves, J. N., et al. 2010, *A&A*, 521, A57
- Toomre, A. 1981, in *Structure and Evolution of Normal Galaxies*, ed. S. M. Fall & D. Lynden-Bell, 111

- Travascio, A., Piconcelli, E., Bischetti, M., et al. 2024, *A&A*, 686, A250
- Treister, E., Krolik, J. H., & Dullemond, C. 2008, *ApJ*, 679, 140
- Treister, E., Schawinski, K., Urry, C. M., & Simmons, B. D. 2012, *ApJ*, 758, L39
- Tremaine, S., Gebhardt, K., Bender, R., et al. 2002, *ApJ*, 574, 740
- Tremonti, C. A., Heckman, T. M., Kauffmann, G., et al. 2004, *ApJ*, 613, 898
- Treu, T., Malkan, M. A., & Blandford, R. D. 2004, *ApJ*, 615, L97
- Treu, T., Woo, J.-H., Malkan, M. A., & Blandford, R. D. 2007, *ApJ*, 667, 117
- Treuthardt, P., Seigar, M. S., Sierra, A. D., et al. 2012, *MNRAS*, 423, 3118
- Tristram, K. R. W., Burtscher, L., Jaffe, W., et al. 2014, *A&A*, 563, A82
- Trump, J. R., Impey, C. D., Taniguchi, Y., et al. 2009, *ApJ*, 706, 797
- Tumlinson, J., Peebles, M. S., & Werk, J. K. 2017, *ARA&A*, 55, 389
- U, V., Barth, A. J., Vogler, H. A., et al. 2022, *ApJ*, 925, 52
- Umehura, M., Fukue, J., & Mineshige, S. 1997, *ApJ*, 479, L97
- Urrutia, T., Lacy, M., & Becker, R. H. 2008, *ApJ*, 674, 80
- Urry, C. M., & Padovani, P. 1995, *PASP*, 107, 803
- Utomo, D., Sun, J., Leroy, A. K., et al. 2018, *ApJ*, 861, L18
- Valdes, F., Gupta, R., Rose, J. A., Singh, H. P., & Bell, D. J. 2004, *ApJS*, 152, 251
- van den Bosch, R. C. E. 2016, *ApJ*, 831, 134
- van den Bosch, R. C. E., Gebhardt, K., Gültekin, K., Yıldırım, A., & Walsh, J. L. 2015, *ApJS*, 218, 10
- Veilleux, S., Bolatto, A., Tombesi, F., et al. 2017, *ApJ*, 843, 18
- Veilleux, S., Cecil, G., & Bland-Hawthorn, J. 2005, *ARA&A*, 43, 769
- Veilleux, S., Maiolino, R., Bolatto, A. D., & Aalto, S. 2020, *A&A Rev.*, 28, 2
- Veilleux, S., Meléndez, M., Sturm, E., et al. 2013, *ApJ*, 776, 27
- Venturi, G., Nardini, E., Marconi, A., et al. 2018, *A&A*, 619, A74
- Véron-Cetty, M. P., Joly, M., & Véron, P. 2004, *A&A*, 417, 515
- Véron-Cetty, M. P., & Véron, P. 2010, *A&A*, 518, A10
- Verro, K., Trager, S. C., Peletier, R. F., et al. 2022, *A&A*, 660, A34
- Vestergaard, M., & Peterson, B. M. 2006, *ApJ*, 641, 689
- Villafaña, L., Williams, P. R., Treu, T., et al. 2022, *ApJ*, 930, 52
- Villafaña, L., Williams, P. R., Treu, T., et al. 2023, *ApJ*, 948, 95
- Villar-Martín, M., Arribas, S., Emonts, B., et al. 2016, *MNRAS*, 460, 130
- Villar-Martín, M., Humphrey, A., Delgado, R. G., Colina, L., & Arribas, S. 2011, *MNRAS*, 418, 2032
- Villforth, C., Hamann, F., Rosario, D. J., et al. 2014, *MNRAS*, 439, 3342
- Villforth, C., Hamilton, T., Pawlik, M. M., et al. 2017, *MNRAS*, 466, 812
- Vogelsberger, M., Genel, S., Springel, V., et al. 2014, *Nature*, 509, 177
- Vollmer, B., Schartmann, M., Burtscher, L., et al. 2018, *A&A*, 615, A164
- Volonteri, M., Capelo, P. R., Netzer, H., et al. 2015, *MNRAS*, 449, 1470

- Volonteri, M., & Natarajan, P. 2009, *MNRAS*, 400, 1911
- Wada, K., Papadopoulos, P. P., & Spaans, M. 2009, *ApJ*, 702, 63
- Walcher, C. J., Coelho, P. R. T., Gallazzi, A., et al. 2015, *A&A*, 582, A46
- Walter, F., Neeleman, M., Decarli, R., et al. 2022, *ApJ*, 927, 21
- Wang, F., Yang, J., Hennawi, J. F., et al. 2023, *ApJL*, 951, L4
- Wang, J.-M., Songsheng, Y.-Y., Li, Y.-R., Du, P., & Zhang, Z.-X. 2020, *Nature Astronomy*, 4, 517
- Wang, J.-M., Du, P., Hu, C., et al. 2014, *ApJ*, 793, 108
- Wang, T., Brinkmann, W., & Bergeron, J. 1996, *A&A*, 309, 81
- Watabe, Y., Kawakatu, N., & Imanishi, M. 2008, *ApJ*, 677, 895
- Watson, L. C., Martini, P., Dasyra, K. M., et al. 2008, *ApJ*, 682, L21
- Weilbacher, P. M., Streicher, O., Urrutia, T., et al. 2012, in *Society of Photo-Optical Instrumentation Engineers (SPIE) Conference Series*, Vol. 8451, *Software and Cyberinfrastructure for Astronomy II*, ed. N. M. Radziwill & G. Chiozzi, 84510B
- Weilbacher, P. M., Palsa, R., Streicher, O., et al. 2020, *A&A*, 641, A28
- Weinberger, R., Springel, V., Hernquist, L., et al. 2017, *MNRAS*, 465, 3291
- Weston, M. E., McIntosh, D. H., Brodwin, M., et al. 2017, *MNRAS*, 464, 3882
- Williams, P. R., & Treu, T. 2022, *ApJ*, 935, 128
- Williams, P. R., Pancoast, A., Treu, T., et al. 2018, *ApJ*, 866, 75
- Williams, P. R., Pancoast, A., Treu, T., et al. 2020, *ApJ*, 902, 74
- Winkel, N., Bennert, V. N., Remigio, R. P., et al. 2024, *ApJ*, submitted to the journal
- Winkel, N., & Singha, M. 2022, *Siena3D*
- Winkel, N., Husemann, B., Davis, T. A., et al. 2022, *A&A*, 663, A104
- Winkel, N., Husemann, B., Singha, M., et al. 2023, *A&A*, 670, A3
- Wisotzki, L., Christlieb, N., Bade, N., et al. 2000, *A&A*, 358, 77
- Wittor, D., & Gaspari, M. 2020, *MNRAS*, 498, 4983
- Woo, J.-H., Bae, H.-J., Son, D., & Karouzos, M. 2016, *ApJ*, 817, 108
- Woo, J.-H., Schulze, A., Park, D., et al. 2013, *ApJ*, 772, 49
- Woo, J.-H., Yoon, Y., Park, S., Park, D., & Kim, S. C. 2015, *ApJ*, 801, 38
- Woo, J.-H., Treu, T., Barth, A. J., et al. 2010, *ApJ*, 716, 269
- Woo, J.-H., Wang, S., Rakshit, S., et al. 2024, *ApJ*, 962, 67
- Wutschik, S., Schleicher, D. R. G., & Palmer, T. S. 2013, *A&A*, 560, A34
- Wylezalek, D., Flores, A. M., Zakamska, N. L., Greene, J. E., & Riffel, R. A. 2020, *MNRAS*, 492, 4680
- Xiao, T., Barth, A. J., Greene, J. E., et al. 2011, *ApJ*, 739, 28
- Xu, L., Rieke, G. H., Egami, E., et al. 2015, *ApJ*, 808, 159
- Xu, Y., Pinto, C., Kara, E., et al. 2022, *MNRAS*, 513, 1910
- Yip, C. W., Connolly, A. J., Vanden Berk, D. E., et al. 2004, *AJ*, 128, 2603
- Yuan, F., Lidman, C., Davis, T. M., et al. 2015, *MNRAS*, 452, 3047

- Yuan, W., Zhou, H. Y., Komossa, S., et al. 2008, *ApJ*, 685, 801
- Zakamska, N. L., Strauss, M. A., Krolik, J. H., et al. 2003, *AJ*, 126, 2125
- Zhang, Z.-X., Du, P., Smith, P. S., et al. 2019, *ApJ*, 876, 49
- Zhou, H., Wang, T., Yuan, W., et al. 2006, *ApJS*, 166, 128
- Zhu, K., Li, R., Cao, X., et al. 2023, *Research in Astronomy and Astrophysics*, 23, 085001
- Zhuang, M.-Y., & Ho, L. C. 2020, *ApJ*, 896, 108
- Zubovas, K., & King, A. 2012, *ApJ*, 745, L34
- Zubovas, K., Nayakshin, S., King, A., & Wilkinson, M. 2013, *MNRAS*, 433, 3079